



UNIVERSITAT POLITÈCNICA
DE CATALUNYA
BARCELONATECH

Advanced GNSS-R instruments for altimetric and scatterometric applications

Raul Onrubia Ibáñez

ADVERTIMENT La consulta d'aquesta tesi queda condicionada a l'acceptació de les següents condicions d'ús: La difusió d'aquesta tesi per mitjà del repositori institucional UPCommons (<http://upcommons.upc.edu/tesis>) i el repositori cooperatiu TDX (<http://www.tdx.cat/>) ha estat autoritzada pels titulars dels drets de propietat intel·lectual **únicament per a usos privats** emmarcats en activitats d'investigació i docència. No s'autoritza la seva reproducció amb finalitats de lucre ni la seva difusió i posada a disposició des d'un lloc aliè al servei UPCommons o TDX. No s'autoritza la presentació del seu contingut en una finestra o marc aliè a UPCommons (*framing*). Aquesta reserva de drets afecta tant al resum de presentació de la tesi com als seus continguts. En la utilització o cita de parts de la tesi és obligat indicar el nom de la persona autora.

ADVERTENCIA La consulta de esta tesis queda condicionada a la aceptación de las siguientes condiciones de uso: La difusión de esta tesis por medio del repositorio institucional UPCommons (<http://upcommons.upc.edu/tesis>) y el repositorio cooperativo TDR (<http://www.tdx.cat/?locale-attribute=es>) ha sido autorizada por los titulares de los derechos de propiedad intelectual **únicamente para usos privados enmarcados** en actividades de investigación y docencia. No se autoriza su reproducción con finalidades de lucro ni su difusión y puesta a disposición desde un sitio ajeno al servicio UPCommons No se autoriza la presentación de su contenido en una ventana o marco ajeno a UPCommons (*framing*). Esta reserva de derechos afecta tanto al resumen de presentación de la tesis como a sus contenidos. En la utilización o cita de partes de la tesis es obligado indicar el nombre de la persona autora.

WARNING On having consulted this thesis you're accepting the following use conditions: Spreading this thesis by the institutional repository UPCommons (<http://upcommons.upc.edu/tesis>) and the cooperative repository TDX (<http://www.tdx.cat/?locale-attribute=en>) has been authorized by the titular of the intellectual property rights **only for private uses** placed in investigation and teaching activities. Reproduction with lucrative aims is not authorized neither its spreading nor availability from a site foreign to the UPCommons service. Introducing its content in a window or frame foreign to the UPCommons service is not authorized (*framing*). These rights affect to the presentation summary of the thesis as well as to its contents. In the using or citation of parts of the thesis it's obliged to indicate the name of the author.



UNIVERSITAT POLITÈCNICA DE CATALUNYA
BARCELONATECH

Departament de Teoria del Senyal
i Comunicacions

Advanced GNSS-R Instruments for Altimetric and Scatterometric Applications

Author

Raul Onrubia Ibáñez

Thesis Advisors

Prof. Adriano José Camps Carmona

and

Dr. Hyuk Park

A thesis submitted to the
Universitat Politècnica de Catalunya - BarcelonaTech (UPC)
in partial fulfillment of the requirements for the degree of
DOCTOR OF PHILOSOPHY

PhD program on Signal Theory and Communications
Remote Sensing Laboratory (RSLAB) Group
Barcelona, November 2019

Advanced GNSS-R Instruments for Altimetric and Scatterometric Applications, *R. Onrubia*, PhD thesis, UPC, Barcelona, 2019.

Copyright ©2019 by Raul Onrubia and UPC-BarcelonaTech.

Author IDs:

IEEE Member 90873129

ORCID 0000-0001-6636-1587

Scopus 56041090700

Researcher L-4628-2014

Google Scholar 3AwUCvoAAAAJ

Social:

GitHub onrubia

Email onrubia@tsc.upc.edu

The author of this Ph.D. thesis has received financial support from the grant FI-DGR 2015 of the AGAUR / Generalitat de Catalunya, and by the “Beca La Caixa de Mobilitat International” for an almost 4-month visiting research stay at Monash University, Australia, and by the Spanish grant with project ref. AYA2011-29183-C02-01 “AROSA-Advanced Radio Occultations and Scatterometry Applications using GNSS and other opportunity signals”, of the Spanish Ministry of Economy and Competitiveness (MICINN), and by Spanish grant with project ref. No ESP2015-70014-C2-1-R “AGORA: Técnicas Avanzadas en Teledetección Aplicada Usando Señales GNSS y Otras Señales de Oportunidad” of the Spanish Ministerio de Economía y Competitividad (MINECO/FEDER), and by the Unidad de Excelencia María de Maeztu MDM-2016-0600, and to Prof. Camps ICREA Academia 2015 award of the Generalitat de Catalunya, and by the Australian GRDC (Grains Research & Development Corporation) with project UMO-0004.

*“I would rather have questions that can’t be answered than
answers that can’t be questioned.”*

RICHARD FEYNMAN

Acknowledgements

In this section I would like to express my gratitude to all people who helped me and supported me during these 8 years. Without them, I could not have gone that far.

First, I would like to thank Professor Adriano Camps for his support, trust, guidance, and help since the very first day we met 10 years ago. Thank you for the opportunity to develop myself and grow as a researcher with your advise.

Special thanks to Daniel Pascual for all the time we have spent together since we met in the research group. I am glad of having shared this thesis with you. Thanks for those great memories, specially the year we spent in the rooftop office together, for all the support in the lowest moments, and for coming to Australia, even if it was for such a short period of time. I will never forget all I learned from you.

Thanks to Alberto, Hyuk and Jorge for their help in the development of my Ph.D. thesis, and for the time spent together “fixing the World” during the coffee time. Also thanks Jorge for all we learnt together when doing the PID controller, I enjoyed like a kid that month. I also want to thank to my lab colleagues Adrià, Alessio, Dongliang, Estefany, Fran, Jordi, JuanFran, Joan Adrià, Lara, and Roger. Special thanks also to Lidia, the student I co-directed her bachelor thesis, for your dedication and your help with the MIR software. It was a pleasure to work together.

Thanks Chris and Sandra for trusting me and for giving me the chance to visit Australia twice, both, but the last one in particular, were life-changing experiences. Also thanks Jeff, Jon, Frank, and Richard for your help during the field campaigns and the experiments.

Thanks to Sebastià Blanch for his help in the anechoic chamber calibrating the arrays. Thanks also to Albert Aguasca for all doubts he answered. Thanks to Albert, Eric, Joaquim, Josep and Rubén for their help building the MIR instrument and their technical support. Thanks to Aynie, Teresa, Cristina, Pere, and Alicia for the administrative support, and thanks Josep Maria and Ferran for the IT support.

Also thanks to Francisco, Alessio, and Isaac for all the time they dedicated to review my manuscript. I really appreciate the time you dedicated to read it and all the comments you sent me.

Thanks for all the support and love I received from family, friends, partners, and all people I shared my path with during this period. Thanks for encouraging me to not give up. Special thanks to Brianna for reviewing my thesis and for the jokes you left in the reviewed manuscript, the revision was way more enjoyable this way.

Abstract

This work is the result of more than eight years during a bachelor thesis, a master thesis, and the Ph.D. thesis dedicated to the development of the Microwave Interferometric Reflectometer (MIR) instrument. During this time, the instrument was designed, built, tested, and calibrated. A field campaign was carried out in Australia between May 2018 and June 2018 to determine the instrument's accuracy in sensing soil moisture and sea altimetry. This work describes each of these steps in detail, summarizes all the knowledge acquired, and aims to be helpful for those who decide to keep working with the instrument.

MIR is a Global Navigation Satellite System - Reflectometer (GNSS-R), that is, an instrument that uses Global Navigation Satellite System (GNSS) signals scattered on the Earth's surface to retrieve geophysical parameters. These signals are received below the noise level, but since they have been spread in the frequency domain using spread-spectrum techniques, and in particular using the so-called Pseudo-Random Noise (PRN) codes, it is still possible to retrieve them because of the large correlation gain achieved.

In GNSS Reflectometry (GNSS-R), two main techniques are used for this purpose: the conventional technique (cGNSS-R) and the interferometric one (iGNSS-R), each with its pros and cons. In the former technique, the reflected signal is cross-correlated against a locally generated clean-replica of the transmitted signal. In the latter technique the reflected signal is cross-correlated with the direct one. Nowadays multiple GNSS systems coexist, transmitting narrow and wide, open and private signals. A comparison between systems, signals, and techniques in fair conditions is necessary.

The MIR instrument has been designed as an airborne instrument for that purpose: the instrument has two arrays, an up-looking one, and a down-looking one, each with 19 dual-band antennas in a hexagonal distribution. The instrument is able to form 2 beams at each frequency band (L1/E1, and L5/E5A), which are pointing continuously to the desired satellites taking into account their position, as well as the instrument's position and attitude. The data is sampled and stored for later post-processing. Last but not least, MIR is auto-calibrated using similar signals to the ones transmitted by the GNSS satellites.

During the instrument development, the Distance Measurement Equipment/TACTical Air Navigation (DME/TACAN) signals from the Barcelona airport threatened to disrupt the interferometric technique. These signals were also studied, and it was concluded that the use of a mitigation systems were as strongly recommended. The interferometric technique was also affected by the unwanted contribution of other satellites. The impact of these contributions was studied using real data gathered during this Ph.D. thesis.

Contents

Abstract	iii
List of Tables	ix
List of Figures	xi
Acronyms	xix
I Introduction and State of the Art	1
1 Introduction	3
1.1 Remote Sensing for Earth Observation	3
1.2 Motivation	5
1.3 Passive Remote Sensing Laboratory Background	6
1.4 Goals	7
1.5 Outline	8
2 State of the Art	11
2.1 Introduction	11
2.2 Global Navigation Satellite Systems	11
2.3 Global Navigation Satellite System - Reflectometry	14
2.3.1 Global Navigation Satellite System - Reflectometry Observables . .	18
2.3.2 Global Navigation Satellite System - Reflectometry Applications .	21
2.3.3 Global Navigation Satellite System - Reflectometry Instruments .	21
2.4 Distance Measurement Equipment/TACTial Air Navigation Signals	27
2.5 Conclusions	28
3 Instrument Precursors	31
3.1 Introduction	31
3.2 P(Y) C/A ReflectOmeter at BEXUS 17/19 Stratospheric Balloon Experiment	31
3.3 L band RAdiometer and Radio Occultations	34
3.4 Multiband Airborne L band reflectometrY with GNSS-R	38
3.5 Conclusions	41

II Instrument Design, Implementation, Calibration, and Characterization	43
4 Instrument Principles of Operation	45
4.1 Introduction	45
4.2 Satellite Selection Algorithm	45
4.3 Satellite Position and Specular Reflection Point Determination	47
4.3.1 Coordinate systems	48
4.3.2 Satellite Position and Specular Reflection Point Determination	50
4.4 Array Pointing	53
4.5 Phase and Amplitude Setting Using Vector Modulators	59
4.6 Airplane Dynamics Analysis	62
4.7 Conclusions	63
5 Instrument Description	65
5.1 Introduction	65
5.2 Antenna Arrays	66
5.2.1 Antenna Elements	66
5.2.2 RF Front-ends	68
5.2.3 Antenna Array Integration	72
5.3 Beam-former	74
5.3.1 Phase Shifters	75
5.3.2 19-way Power Splitters/Combiners	78
5.3.3 Motherboards	79
5.3.4 Beamformer Integration	81
5.3.5 Extra RF Amplifiers in the Down-looking RF Chains	84
5.3.6 RF Front-ends and Beamformer Connection Test	85
5.4 Data Sampling and Processing	85
5.5 Calibration System	87
5.6 Position and Attitude Determination System	90
5.7 Linux Embedded System	92
5.8 Instrument Integration	94
5.9 Instrument Software	96
5.9.1 Main Thread	100
5.9.2 Log Thread	101
5.9.3 IMU Thread	101
5.9.4 GetDataFromBD982 Thread	101
5.9.5 RequestSVDData Thread	102
5.9.6 GetSVLookAngles Thread	103
5.9.7 RT27 Thread	104
5.10 Conclusions	104
6 Instrument Calibration and Characterization	105
6.1 Introduction	105
6.2 Instrument Calibration	105
6.2.1 Pre-calibration Step 1: Calibration Through the Antenna	109
6.2.2 Pre-calibration Step 2: Calibration Through the Calibration Port	112
6.2.3 Pre-calibration Step 3: Obtaining the Compensation Parameters	113

6.2.4	Pre-calibration Step 4: Re-calibrating the Instrument	113
6.2.5	In-flight Calibration	113
6.2.6	Noise Characterization of the USRPs and SNR Mapping	120
6.3	Validation Results	125
6.3.1	Calibration impact and Measured Radiation Patterns	125
6.3.2	Outdoor Experiments	132
6.4	Conclusions	133
III Experimental Results		135
7	DME/TACAN Impact Analysis in GNSS-R	137
7.1	Introduction	137
7.2	Radio Frequency Interference in GNSS/GNSS-R Systems	138
7.3	DME/TACAN Signal Properties	139
7.4	DME/TACAN Traffic Properties	144
7.5	Application to GNSS-R from a LEO Orbit	145
7.6	Conclusions	149
8	Field Campaign Description, Data Processing Considerations, and Preliminary Results	153
8.1	Introduction	153
8.2	Field Campaign Description	154
8.2.1	Sea Flight in Port Phillip Bay	154
8.2.2	Sea Flight in the Bass Strait	154
8.2.3	Land Flights in Yanco	156
8.3	Calibration data	161
8.4	Data Processing Considerations to Avoid the Effect of Secondary Codes	162
8.5	Preliminary Results	165
8.5.1	Soil Moisture in the Yanco Flights	169
8.5.2	Sea Altimetry	170
8.5.3	Topography	172
8.5.4	Land-Water Transitions	173
8.6	Conclusions	174
9	Satellite Cross-talk	179
9.1	Methodology	179
9.2	Results	183
9.3	Conclusions	187
IV Conclusions and Future Work		189
10	Conclusions and Future Work	191
10.1	Conclusions	191
10.2	Future work	192

V	Appendices	195
A	Subsystem Schematics, PCBs, and Housing CADs	197
A.1	Antennas	197
A.2	RF Front-ends	198
A.3	Phase shifters	202
A.4	19-Way Combiners	208
A.5	Motherboard	214
A.6	Calibration System	217
A.7	Position and Attitude Determination System	221
A.8	Embedded System	224
A.9	Extra RF Amplifiers	225
B	Subsystems Characterization	227
B.1	RF Front-ends	227
B.2	19-way Power Combiner	228
B.3	Beamformer Integration	229
C	PLMR and Cabin Specifications for the MIR Instrument Design	237
D	Integration CADs	239
D.1	Arrays	239
D.2	Beamformer	246
D.3	Rack Integration	247
E	Coordinate Systems Transformations	249
E.1	LLA Coordinates to ECEF Coordinates	249
E.2	ECEF Coordinates to LLA Coordinates	250
E.3	ECEF Vector from LLA Point to Vehicle Carried NED Coordinates	250
E.4	Vehicle Carried NED Coordinates to BODY Coordinates	251
F	Satellite Position Determination	253
G	Satellite Overpass Analysis	257
H	Instrument Setup	263
VI	Bibliography and List of Publications	267
	Bibliography	269
	List of Publications	289
	Granted Patents	289
	Open-source software	289
	Journal Articles	289
	Conference Proceedings	291
	Co-directed Bachelor Final Degree Projects	294

List of Tables

2.1	Main characteristics of the broadcasted GPS signals.	16
2.2	Main characteristics of the broadcasted Galileo signals.	17
2.3	Summary of state of the art GNSS-R instruments.	25
2.4	DME transmitting and receiving frequencies.	28
5.1	Measured parameters of the antenna elements.	68
5.2	Gain and Phase statistics from the calibration port of all the RF Front-ends by array.	71
5.3	Summary of the required cables per array.	75
5.4	S-parameters statistics of a 19-way power combiner.	80
5.5	Beamformer power consumption budget.	80
5.6	Summary of the required cables per beamformer.	81
5.7	S-parameters summary of the two manufactured beamformers.	85
5.8	Chosen values for the configurable parameters of the frequency synthesizers.	88
5.9	MIR instrument weight, size, and power consumption.	95
5.10	Power supplies in the MIR instrument and subsystems fed by them.	96
5.11	Data sources used by the MIR instrument for the satellite tracking.	99
5.12	GOSF packets sent by the GNSS receiver, information that contain, and transmission rate.	103
6.1	Measured noise power at the USRP inputs.	121
6.2	Beamformer inaccuracy impact in the array directivity before and after calibration.	126
6.3	MIR arrays measured cross-polarization after calibration. The data from the up-looking was lost.	127
6.4	MIR arrays measured directivities after calibration pointing to the boresight.	129
7.1	Mean degradation in iGNSS-R caused by each interference cross-correlation term in L5 and E5, in the worst and best pointing cases.	151
8.1	Mean and standard deviation of the computed calibration parameters.	163
9.1	Effect of cross-talk in three different delay estimators and in the peak amplitude in the flight over the Bass Strait.	187

A.1 Phase shifter address setting as function of the resistors mounted. 202

List of Figures

1.1	Electromagnetic spectrum, and electromagnetic wave source examples. . .	4
2.1	Signals being broadcasted by the currently deployed systems.	12
2.2	GPS and Galileo Woodward Ambiguity Functions, Auto Correlation Functions and Cross Correlation Functions.	14
2.3	Shared spectrum by GPS and Galileo at L1/E1, and L5/E5 frequency bands.	15
2.4	Reflection scenario.	18
2.5	DDM examples over ocean and ice in airborne and spaceborne missions. .	19
2.6	Simulated waveforms over the ocean.	20
2.7	Series of processed data over Ukraine at L1 contaminated by RFI.	23
2.8	Simplified DME concept, and DME pulse shape.	27
2.9	DME channel allocation and GNSS spectra.	28
2.10	DME station's locations.	29
3.1	Bexus up-looking antenna.	32
3.2	Bexus down-looking antenna.	33
3.3	PYCARO simplified schematic in the BEXUS 17 experiment.	33
3.4	Measurement of the BEXUS antennas temperature matching response. . .	34
3.5	BEXUS antenna temperature response.	34
3.6	BEXUS measured radiation patterns.	35
3.7	L-RARO radiation patterns.	36
3.8	L-RARO block schematic.	37
3.9	L-RARO instrument photos.	37
3.10	L-RARO PID temperature performance.	38
3.11	L-RARO measured transfer functions.	39
3.12	MALYGNSS instrument block diagram.	39
3.13	Aircraft and antennas used in the MALYGNSS experiments.	41
3.14	First sampling region of the HUMIT field campaign.	42
3.15	Delay difference between the correlation peaks of the direct and the reflected signals in L1 C/A, and L2CM.	42
4.1	Algorithm developed to choose the best satellites available.	46
4.2	Selection algorithm simulation.	47
4.3	Satellite elevation difference after 10 minutes for GPS, and Galileo satellites.	48

4.4	ECEF, ENU, and LLA coordinate systems over the WGS-84 reference ellipsoid surface.	48
4.5	Body coordinate systems and rotation angles with respect to the NED coordinate system.	50
4.6	Vector pointing to a GNSS satellite, and to its specular reflection point assuming flat Earth model in NED coordinate system.	51
4.7	Azimuth and elevation angle for the specular reflection point pointing vector and for the up-looking equivalent pointing vector in NED coordinates.	52
4.8	Satellite and specular reflection point pointing vectors in the NED and BODY coordinate systems.	53
4.9	Array distribution with the element coordinates, and definition of the propagation angles θ and ϕ	54
4.10	Simulated current distributions.	55
4.11	Array factor pointing to the boresight at L1/E1 frequency band with different current distributions.	56
4.12	Simulated side lobes with uniform current distribution pointing at $\theta = 75^\circ$ and at different φ directions.	57
4.13	Beamwidth as function of the off-boresight pointing angle θ	58
4.14	Side lobe level as a function of the off-boresight pointing angle θ	58
4.15	Used model for a whole MIR RF chain.	59
4.16	Ideal gain circle, and modeled gain ellipsoid in the IQ gain plane	61
4.17	Flight height and ground speed of the three analyzed flights.	63
4.18	Mean and maximum angle deviation for all possible pointing directions caused by the airplane movement in three different flights.	64
5.1	Block diagram of the MIR instrument.	66
5.2	Array baseline and block diagram.	67
5.3	3D model and photo of the antenna elements.	68
5.4	Antenna matching of one of the manufactured antennas.	68
5.5	Measured antenna elements full radiation patterns.	69
5.6	Temperature effect in the calibration switch coupling.	69
5.7	Block diagram and manufactured RF Front-end picture.	70
5.8	Transmission gain curves of all RF Front-ends by array.	70
5.9	Modified RF Front-end to measure gain vs. input power.	71
5.10	Gain response of the RF Front-end to a power sweep to find the P_{1dB} point.	72
5.11	Array pictures.	73
5.12	Structural elements to hold the down-looking array in the airplane.	73
5.13	Radome pictures.	74
5.14	Array connector panel pictures.	75
5.15	Beamformer block diagram and pictures.	76
5.16	Manufactured phase shifter.	77
5.17	Block diagram of the I2C network.	78
5.18	Gain response of the phase shifter as a function of the input power.	78
5.19	Block diagram and picture of a 19-way power combiner.	79
5.20	Measured total insertion losses of one of the manufactured 19-way power combiners.	80
5.21	Manufactured beamformer pictures.	81

5.22 Thermal images before adding forced ventilation.	82
5.23 Thermal simulation with non-forced and forced ventilation.	82
5.24 Modified beamformer including forced ventilation.	83
5.25 Measured I and Q gains of one of the beamformers at a) L1/E1, and b) L5/E5A frequency bands.	83
5.26 Measured I and Q phase differences of one of the beamformers at a) L1/E1, and b) L5/E5A frequency bands.	84
5.27 Gain response to a power sweep of the RF Front-end and the phase shifter combined.	85
5.28 Block diagram of the data sampling system.	86
5.29 Simplified block diagram of the USRP x310 with two DBSRX2 daughter- boards.	86
5.30 Data sampling subsystem pictures.	87
5.31 Calibration system block diagram.	88
5.32 Measured up-conversion transfer function and calibration signal spectrum. L1/E1 band.	89
5.33 Measured up-conversion transfer function and calibration signal spectrum. L5/E5A band.	90
5.34 Calibration system pictures.	91
5.35 Transmitted calibration signal spectrum.	92
5.36 Embedded system picture.	93
5.37 Embedded system expansion port mapping.	93
5.38 MIR rack with the data sampling subsystem attached during the integra- tion of the calibration block.	94
5.39 Finished MIR instrument rack.	96
5.40 MIR array with attached beamformer prior to calibration in anechoic cham- ber.	97
5.41 Interactions between threads.	98
5.42 Data structure storing all position and attitude information coming from the GNSS receiver.	99
5.43 Data structure storing the attitude coming from the IMU.	99
5.44 Data structure storing the satellite position and orbital information. . . .	100
5.45 Data structure storing the selected satellites required information for the data processing.	100
5.46 Data structure used to parse the RT27 packets.	100
5.47 Data structure to be stored for post-processing and debugging purposes .	101
5.48 Main thread flow diagram.	101
5.49 Flow diagram of the thread in charge of writing the log information to a file.	101
5.50 Flow diagram of the thread in charge of getting the attitude and heading information from the IMU.	101
5.51 Flow diagram of the thread in charge of receiving the GSOF, ephemeris and almanac packets from the GNSS receiver.	102
5.52 Flow diagram of the thread in charge of requesting the ephemeris or the almanac to the GNSS receiver.	103
5.53 Flow diagram of the thread in charge of computing the pointing angles and to program the beamformers.	104

5.54	Flow diagram of the thread in charge of receiving the RT27 packets from the GNSS receiver.	104
6.1	Simplified model of the blocks to be calibrated in the MIR instrument. . .	106
6.2	Received and calibration signals' paths to the receiver in one of the bands and beams.	110
6.3	Cross-correlation peak phase before and after frequency error compensation.	117
6.4	Detailed blocks of the in-flight calibration.	118
6.5	Estimated channel transfer function.	119
6.6	Estimated frequency error difference between the up-looking and down-looking RF channels throughout time for a single USRP.	119
6.7	Estimated phase difference between the up-looking and down-looking RF channels throughout time for a single USRP.	120
6.8	Estimated group delay difference between the up-looking and down-looking RF channels throughout time for a single USRP.	120
6.9	Estimated gain between the up-looking and down-looking RF channels throughout time for a single USRP.	121
6.10	Phase noise histograms for the four USRPs after the frequency error compensation.	122
6.11	Used USRPs noise source model.	122
6.12	Measured peak power value as function of the signal input power.	123
6.13	MIR down-looking array being calibrated and measured at the UPC anechoic chamber.	125
6.14	IQ gain circles before, and after calibration.	126
6.15	Effect of the calibration in the radiation patterns.	127
6.16	Planar cuts of the radiation pattern when tilting the beam.	128
6.17	Directivity loss of the down-looking array as a function of the pointing direction.	128
6.18	Fore hemisphere of the up-looking array cross-polarization.	129
6.19	Azimuthal cuts of the full radiation pattern pointing to the boresight of the antenna.	130
6.20	Fore hemisphere of the measured radiation pattern of the down-looking array.	130
6.21	Side lobes for different azimuthal cuts of the antenna pattern when pointing to an off-boresight angle of 35°	131
6.22	MIR up-looking array and rack, and retrieved waveforms from GPS and Galileo satellites during the rooftop experiments.	132
6.23	Tracked C/N0 during the experiment in the laboratory rooftop.	133
7.1	Experiment on the rooftop that lead to the discovery of the Distance Measurement Equipment/TACTical Air Navigation (DME/TACAN) interferences at L5/E5A frequency band.	138
7.2	Cross-correlation waveform, and CAF of the sampled data at L5/E5A frequency band under presence of in-band DME/TACAN signals.	138
7.3	DME Woodward Ambiguity Function.	140
7.4	Resulting WAF for "non-delayed cross-correlation".	141
7.5	Resulting WAF for "delayed cross-correlation".	141
7.6	L5, E5, DME and Noise auto- and cross-correlations.	143

7.7	SNR degradation in the presence of a single DME pulse in the coherent integration time: a) 1 msec data without DME pulses, and b) 1 msec data with a single pair of DME.	144
7.8	Sample of the captured data from the Barcelona Airport, and PDF of the measured time between arrivals.	145
7.9	Array used for the interference power simulation.	146
7.10	Maximum expected SINR degradation for cGNSS-R.	149
7.11	Maximum expected SINR degradation for iGNSS-R.	150
7.12	CDF of the relative degradation of the height precision in sea altimetry in the worst pointing case. Note that for ocean altimetry results will be significantly reduced since the worst degradation happens over land.	151
8.1	Geoid height of Australia, and southern Australia.	154
8.2	Flight altitude and ground speed during the Port Phillip Bay flight.	155
8.3	Flight path, altitude, and ground speed during the Bass Strait flight.	156
8.4	Accumulated geoid gradient and geoid gradient in the Cryosat-2 overpasses in May 2018 and June 2018.	157
8.5	Flight path over the Yanco area YB in the dry wet flights.	158
8.6	Flight path over the Yanco area YA in the dry wet flights.	159
8.7	OzNet soil moisture measurements the days around the dry, and wet flights.	159
8.8	Flight altitude and ground speed in the flights over land.	160
8.9	Estimated group delay difference for the flight over the Bass Strait and flights over land.	161
8.10	Estimated phase difference for the flight over the Bass Strait and flights over land.	162
8.11	Estimated gain difference for the flight over the Bass Strait and flights over land.	162
8.12	Coherent, and incoherent waveforms when the secondary codes are not aligned with the coherent integration window.	164
8.13	Modulation effect caused by the cross-correlation window misalignment.	164
8.14	L5 I+Q WAF when a secondary code bit change happens at different moments of the sequence.	165
8.15	Power loss and Doppler shift as function of the correlation window misalignment with the secondary codes.	166
8.16	Zero padding strategy for cross-correlation window alignment.	166
8.17	Coherent, and incoherent waveforms when the secondary codes are aligned with the coherent integration window.	166
8.18	GPS L5 direct signal normalized coherent peak power with and without code alignment.	167
8.19	First condition for specular reflection.	167
8.20	Second condition for specular reflection.	168
8.21	First and second conditions for specular reflection.	168
8.22	Third condition for specular reflection.	169
8.23	All combined condition for specular reflection.	170
8.24	Uncalibrated reflectivity in the Yanco flights.	170
8.25	Uncalibrated soil moisture histograms in the Yanco flights per frequency band and flight.	171

8.26	Delays of the direct and the reflected signals in altimetry.	172
8.27	Uncalibrated sea height in the L1 beams in the Bass Strait flight.	173
8.28	Uncalibrated topography at the beginning of the Bass Strait flight.	173
8.29	Uncalibrated retrieved height and expected height in the Port Phillip Bay flight.	174
8.30	Uncalibrated retrieved height and expected height in the Port Phillip Bay flight over Point Nepean National Park.	175
8.31	Uncalibrated retrieved height and expected height in the Port Phillip Bay flight over Mornington Peninsula.	176
8.32	Retrieved reflectivity at GPS L1 and GPS L5 in a land-sea transition.	177
9.1	Retrieved interferometric contaminated waveform, conventional tracked and interfering waveforms, and reconstructed waveform.	180
9.2	Skyplot of the tracked satellites in the Australian field campaign.	184
9.3	Cumulative histogram of the probability of having cross-talk in the Australian campaign.	185
9.4	Probability density functions of the delay and amplitude estimators errors.	186
A.1	Antenna layer stack representation.	197
A.2	Antenna PCB layers.	198
A.3	RF Front-end schematic.	200
A.4	RF Front-end PCB layers.	201
A.5	RF Front-end box CAD design.	201
A.6	Phase shifter schematic.	203
A.7	Vector modulator subschematic.	204
A.8	Phase shifter PCB layers.	205
A.9	Phase shifter box CAD design.	206
A.10	Fan holding pieces CAD design.	207
A.11	19-way power splitter/combiner schematic.	209
A.12	19-way power splitter/combiner subschematics.	210
A.13	19-way power splitter/combiner PCB layers (1/2).	211
A.14	19-way Power splitter/combiner PCB layers (2/2).	212
A.15	19-way power splitter/combiner box CAD design.	213
A.16	Motherboard schematic.	214
A.17	Motherboard PCB layers.	215
A.18	Motherboard box 3D model.	216
A.19	Calibration system blocks schematics.	217
A.20	Calibration system PCBs.	218
A.21	Base-band power splitter and low-pass filter box CAD design.	218
A.22	Mixer and band-pass filter box CAD design.	219
A.23	SPI controlled local oscillators box CAD design.	219
A.24	RF power combiner box CAD design.	220
A.25	Calibration system mounted over the USRP N210 CAD design.	220
A.26	GNSS signal power splitter schematic.	221
A.27	GNSS signal power splitter PCB and box CAD design.	222
A.28	DAC sampling board schematic.	222
A.29	ADC sampling board PCB layers.	223

A.30	Inclinometer and ADC sampling board holding system CAD design.	223
A.31	Expansion board schematic.	224
A.32	Expansion board PCB layers.	225
A.33	Extra RF amplifiers schematic.	225
A.34	Extra RF amplifiers PCB top layer.	226
A.35	Extra RF Amplifiers box CAD design.	226
B.1	S-Parameters of the 19 RF Front-ends of the up-looking array.	228
B.2	S-Parameters of the 19 RF Front-ends of the down-looking array.	228
B.3	Measured gain, and phase of the transmission S-Parameters of a 19-way Power combiner.	229
B.4	Measured input and output matching of a 19-way Power combiner.	230
B.5	Measured coupling between ports in of one of the 19-way Power combiners.	230
B.6	Beamformers measured input matching.	231
B.7	Beamformers measured output matching.	231
B.8	Beamformers measured transfer function in beam L1-1.	231
B.9	Beamformers measured transfer function in beam L1-2.	232
B.10	Beamformers measured transfer function in beam L5-1.	232
B.11	Beamformers measured transfer function in beam L5-2.	232
B.12	Beamformer 1 measured I and Q gain.	233
B.13	Beamformer 2 measured I and Q gain.	233
B.14	Beamformer 1 measured gain unbalance.	234
B.15	Beamformer 2 measured gain unbalance.	234
B.16	Beamformer 1 measured I component phase.	235
B.17	Beamformer 2 measured I component phase.	235
B.18	Beamformer 1 measured phase unbalance.	236
B.19	Beamformer 2 measured phase unbalance.	236
C.1	Cabin sketch used to design the up-looking array and the rack instrument (from [1]).	237
C.2	PLMR specifications used to design the down-looking array. Dimensions are in inches.	238
D.1	Back view of CAD Design of the up-looking array with the calibration power splitter attached.	240
D.2	CAD design ground plane of the up-looking array.	241
D.3	Back view of CAD Design of the down-looking array and the support holds.	242
D.4	CAD design ground plane of the down-looking array.	243
D.5	Designed radome to cover the down-looking array.	244
D.6	Detail of one of the sides of the down-looking array radome.	244
D.7	CAD design of the slide that hold the SMA connectors in one of the sides of each array.	245
D.8	3D model of the slide used to manufacture the pieces.	245
D.9	CAD design of the integrated beamformer.	246
D.10	CAD design of the integrated rack.	248
G.1	Accumulated geoid gradient and geoid gradient in the Jason 2 overpasses in May 2018 and June 2018.	258

G.2	Accumulated geoid gradient and geoid gradient in the Jason 3 overpasses in May and June 2018.	259
G.3	Accumulated geoid gradient and geoid gradient in the Cryosat-2 overpasses in May 2018 and June 2018.	260
G.4	Accumulated geoid gradient and geoid gradient in the Sentinel-3a overpasses in May 2018 and June 2018.	261
H.1	Down-looking RF chain calibration connector in the MIR rack.	264
H.2	USB switch, power connector, and SPI connector.	264
H.3	GNSS receiver USB connector.	264
H.4	GNSS receiver input SMA connectors.	265

Acronyms

ACF Auto-Correlation Function.

ADC Analog-to-Digital Converter.

ADS-B Automatic Dependent Surveillance-Broadcast.

AM Amplitude Modulation.

AWGN Additive White Gaussian Noise.

BOC Binary Offset Carrier.

BPSK Binary Phase-Shift Keying.

C/N₀ Carrier to Noise ratio.

CAD Computer-Aided Design.

CAF Cross Ambiguity Function.

CCF Cross-Correlation Function.

CDF Cumulative Distribution Function.

CDMA Code Division Multiple Access.

cGNSS-R conventional GNSS-R.

CNC Computer Numerical Control.

COTS Commercial Off-The-Shelf.

CS Chip Select.

CYGNSS Cyclone Global Navigation Satellite System.

DAC Digital-to-Analog Converter.

DAFIF Digital Aeronautical Flight Information File.

DDM Delay-Doppler Map.

DDMI Delay Doppler Mapping Instrument.

DEM Digital Elevation Model.

DLR Deutsches Zentrum für Luft- und Raumfahrt - German Aerospace Center.

DME Distance Measurement Equipment.

DME/N Distance Measurement Equipment - Navigation.

DME/P Distance Measurement Equipment - Precise.

DME/TACAN Distance Measurement Equipment/TACTical Air Navigation.

DMR Delay Mapping Receiver.

DODEREC DOPpler-Delay Receiver.

DUT Device Under Test.

ECEF Earth-Centered, Earth-Fixed.

EGNOS European Geostationary Navigation Overlay Service.

EIRP Equivalent Isotropic Radiated Power.

ENU East-North-Up.

EO Earth Observation.

ESA European Space Agency.

FDMA Frequency Division Multiple Acces.

FENIX Front-End GNSS Interference eXcisor.

FM Frequency Modulation.

FOG Fiber Optic Gyros.

FPGA Field Programmable Gate Array.

GEROS-ISS GNSS REflectometry, Radio Occultation and Scatterometry onboard ISS.

GLONASS Global'naya Navigatsionnaya Sputnikovaya Sistema.

GNSS Global Navigation Satellite System.

GNSS-R GNSS Reflectometry.

GNSS-RO GNSS-Radio Occultation.

GOLD-RTR GPS Open Loop Differential Real-Time Receiver.

GORS GNSS Occultation, Reflectometry and Scatterometry.

GPIO General Purpose Input/Output.

GPS Global Position System.

GPS-DO Global Positioning System Disciplined Oscillator.

GriPAU GPS Receiver Instrument for PAU.

GSM Global System for Mobile communications.

GSSC Generalized Spectral Separation Coefficient.

I2C Inter-Integrated Circuit.

ICF Interferometric Complex Field.

ICGC Institut Cartogràfic i Geogràfic de Catalunya.

IF intermediate Frequency.

iGNSS-R interferometric GNSS-R.

IMU Inertial Measurement Unit.

INTA Instituto Nacional de Técnica Aeroespacial.

IPT Interference Pattern Technique.

IR InfraRed.

IRNSS Indian Regional Navigation Satellite System.

ISS International Space Station.

L-RARO L band RAdiometer and Radio Occultations.

LARGO Light Airborne Reflectometer for GNSS Observations.

LDO Low-DropOut regulator.

LEiMON Land Monitoring with Navigation Signals.

LEO Low Earth Orbit.

LHCP Left Hand Circular Polarization.

LIDAR Light Detection And Ranging.

LLA Latitude, Longitude, Altitude.

LNA Low-Noise Amplifier.

LO Local Oscillator.

LoS Line-of-Sight.

MALYGNSS Multiband Airborne L-Band reflectometry with GNSS-r.

MCGIVER Monitoring of the Canopy using a GNSS-T Instrument for VEgetation Research.

MERITXELL Multifrequency Experimental Radiometer with Interference Tracking for Experiments over Land and Littoral.

MIR Microwave Interferometric Reflectometer.

NASA National Aeronautics and Space Administration.

NEB Noise Equivalent Bandwidth.

NED North-East-Down.

NRCS Normalized Radar Cross Section.

OBA Off-Boresight Angle.

OS Open Service.

PARIS Passive Reflectometry and Interferometry System.

PARIS IoD Passive Reflectometry and Interferometry System In-orbit Demonstrator.

PAU Passive Advanced Unit.

PAU-GNSS-R PAU-GNSS-Reflectometry.

PAU-RAD PAU-RADiometer.

PAU-SA PAU-Synthetic Aperture.

PCB Printed Circuit Board.

PDF Probability Density Function.

PID Proportional–Integral–Derivative.

PIR Paris Interferometric Receiver.

PLL Phase-Locked Loop.

PLMR Polarimetric L-band Multibeam Radiometer.

PPS Pulses Per Second.

PRN Pseudo-Random Noise.

PRS Public Regulated Service.

PWM Pulse Width Modulation.

PYCARO P(Y) C/A ReflectOmeter.

QZSS Quasi-Zenith Satellite System.

RADAR RAdio Detection And Ranging.

RF Radio-Frequency.

RFI Radio Frequency Interference.

RHCP Right Hand Circular Polarization.

SAW Surface Acoustic Wave.

SBAS Satellite Based Augmentation System.

SDR Software Defined Radio.

SGR Space GNSS Receiver.

SGR-ReSI Space GNSS Receiver - Remote Sensing Instrument.

SINR Signal to Interference-plus-Noise Ratio.

SLL Side Love Level.

SM Soil Moisture.

SMIGOL Soil Moisture IPT GNSS Observations at L-band.

SMOS Soil Moisture and Ocean Salinity.

SNR Signal to Noise Ratio.

SNSA Swedish National Space Agency.

SONAR SOund Navigation And Ranging.

SPI Serial Peripheral Interface.

SPIR Software Paris Interferometric Receiver.

SRP Specular Reflection Point.

SSD Solid State Disk.

SSS Sea Surface Salinity.

SST Sea Surface Temperature.

TACAN TACTical Air Navigation.

TCIP/IP Transmission Control Protocol/Internet Protocol.

TDS-1 TechDemoSat-1.

TOA Time Of Arrival.

TPR Total Power Radiometer.

UART Universal Asynchronous Receiver-Transmitter.

UDP User Datagram Protocol.

UK-DMC UK Disaster Monitor Constellation.

UPC Universitat Politècnica de Catalunya.

USB Universal Serial Bus.

USRP Universal Software Radio Peripheral.

VNA Vector Network Analyzer.

VWC Vegetation Water Content.

WAAS Wide Area Augmentation System.

WAF Woodward Ambiguity Function.

WVS Wigner-Ville Spectrum.

Part I

Introduction and State of the Art

1

Chapter 1

Introduction

1.1 Remote Sensing for Earth Observation

Remote sensing is the ability to acquire information about an object or phenomenon without physically contact to it. The term was coined in the 1950s by Evelyn Pruitt when she was working at the US Office of Naval Research, but remote sensing originates in the early part of the 19th century, when Louis Daguerre created the first photographic plate: the daguerreotype. Later in 1858, the first aerial picture attempts were undertaken from a balloon. The first practical use of aerial photographs goes back to the American Civil War, where photographs were used to assess Confederate positions [2]. In 1935, the Explorer II balloon took photos from more than a 20 km height, showing the curvature of Earth, and later in 1960 TIROS-1 was the first satellite mission with a camera onboard [3].

Common photographs are the result of photons in the visible range of the electromagnetic spectrum being emitted by a natural source of light, scattered then in an object, and finally colliding into a photographic plate, or nowadays an optical sensor. These photons induce an electromagnetic charge that is later collected by a circuit and converted into counts, which after calibration is converted into physical units. In proper light conditions, the camera only needs to receive the light from the target and does not need to transmit any energy; thus cameras are cataloged as passive systems. Similar sensors can be found at the infrared, ultraviolet, and X-rays part of the spectrum (see Fig. 1.1). In order to capture electromagnetic waves with longer wavelengths, antennas are used. Analogously to cameras, the instruments called radiometers capture the electromagnetic radiation coming from a target. Nevertheless, this electromagnetic radiation is spontaneously generated by the target itself as it is at a temperature higher than 0 K, and does not require an external “light” source as the sun or a light bulb at the visible part of the electromagnetic spectrum.

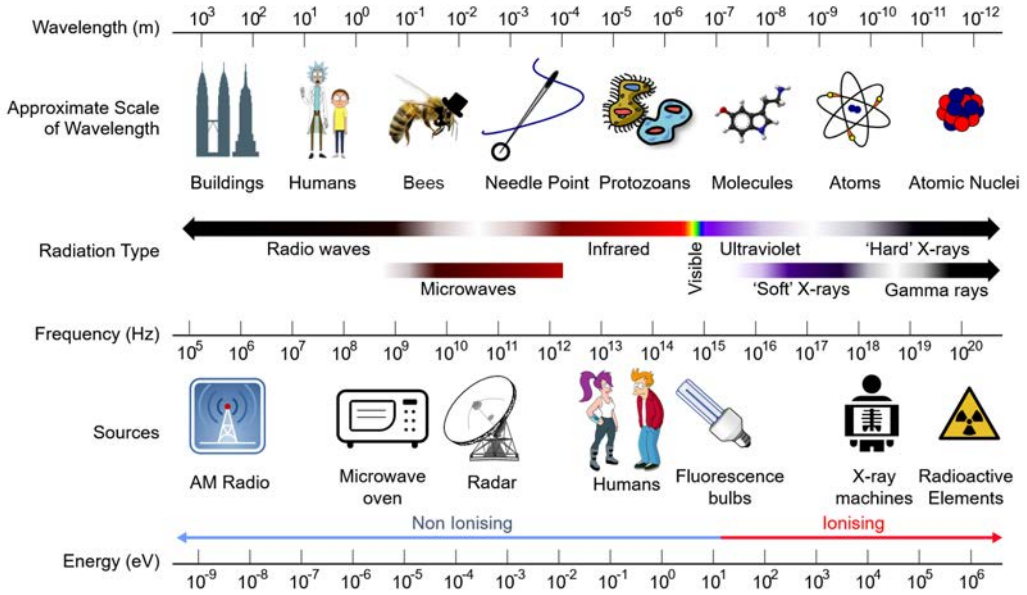


Figure 1.1: Electromagnetic spectrum, and electromagnetic wave source examples (from [4]).

In 1914 the first echo-locator, known as SOund Navigation And Rangings (SONARs), proved the detection of icebergs at a distance of 3.2 km, but they were still unable to estimate their course. The system transmitted a sound pulse at 500 Hz that reflected on the target and was then received by the system [5]. The time delay between the pulse transmission and the echo reception is proportional to the distance to the target. Remote sensing systems that require to transmit energy to later capture its echo are called active systems. Similar systems exist in the visible and near infrared part of the spectra. The former are called LIDARs (LIGHT Detection And Ranging), and use a laser to transmit a light pulse that is later received by an optical sensor. The latter, in the microwave region of the spectra, are called RADARs (RADIO Detection And Ranging).

Remote sensing systems have been widely used both for military and scientific purposes, which include a wide diversity of applications such as medical imaging, new material research, astronomy, and Earth Observation (EO) for weather forecasting or climate change study among others.

This Ph.D. thesis is devoted to the development of a novel remote sensing instrument for EO using radio waves at L band. L band is the frequency band that ranges from 1 to 2 GHz, and is suitable for Earth observation for several reasons. First, the atmosphere is transparent in that frequency band, which allows distant measurements such as satellite missions. Second, L band radio waves have already been proven to be useful to estimate soil moisture, an essential climate variable needed for desertification, flood assessment, crop yield estimation, etc. [2, 6–9]. In addition, Global Navigation Satellite System (GNSS) satellites transmit globally their signals in this radio frequency band and have been proved useful as opportunity signals for remote sensing [10–12].

1.2 Motivation

Starting a Ph.D. was a consequence of my passion on working hands on and building things. I found that most of the engineering courses lacked a practical part, and others had practical sessions but were pure simulations, so the hardware courses were the ones I found more interesting. To be able to build something, to touch it, and to measure it fascinated me.

Commonly, the communication courses use blocks to describe the different parts of the systems. In my courses there was one of these blocks that I felt curious about, a mixer, which stuck two simple questions in my mind: what does a mixer look like, and how does it work? I thought I would find the answer in one of the elective courses, but instead of using a “mixer” to demodulate an Amplitude Modulation (AM) signal, I used a power detector to recover the envelope of the signal. I could not unravel the mystery of mixers! I found later the answer in another elective course, where I had to design a mixer myself. I have to admit it was one of the courses that fulfilled me the most, designing blocks, connecting them. It was simply fun. During my antenna and propagation course I found antenna arrays interesting, but I arrived to a similar question: what does a phase shifter look like and how does it work?

Right after finishing my bachelor courses I had to choose a project for my bachelor thesis. I met Professor Adriano Camps in a CubeSat project, and he was teaching me Remote Sensing in an elective course, a topic that also got my interest. My bachelor thesis topic was going to be CubeSats under his supervision, but that would had not fulfilled me. Professor Camps proposed me to design two antenna arrays with beam steering for GNSS Reflectometry (GNSS-R): the Microwave Interferometric Reflectometer (MIR) instrument. During the project I had time design and manufacture the antenna elements currently used in the MIR instrument (later patented), sketch the instrument system block diagram, design some of the subsystems, and even prototype one I had particular interest with: the phase shifter. I had finally got the answer to the second question.

After finishing, Professor Camps offered me the option then to do a Ph.D. to finish what I started. I wanted to see it finished; I felt interested in research, so I accepted. In the next seven years I kept developing the MIR instrument while I also worked in other side projects mainly developing hardware for other students’ thesis, such as the antenna array for a GNSS-R instrument onboard a stratospheric balloon, or the antennas and the hardware setup to test the data sampling subsystem of the MIR instrument onboard an airplane. I enrolled in most of these side projects because they were somehow to the MIR instrument, but others were just for fun.

While doing this Ph.D. thesis I have had the chance to grow in many aspects of my life. From a professional point of view, I have gotten in touch with all of the aspects of the development of complex systems: design, manufacture, test, and calibration. I also had the chance to get to know the research community, and to travel and meet researchers from different countries. From a personal point of view, this thesis allowed me to visit Australia twice, and despite being there for research, I had one of the most enlightening experiences of my life.

1.3 Passive Remote Sensing Laboratory Background

The research group where this Ph.D. thesis has been carried out, the Passive Remote Sensing group, has its origin in the Soil Moisture and Ocean Salinity (SMOS) mission [13]. In his Ph.D. thesis [14], Professor Camps developed the basic principles of Synthetic Aperture Radiometry for EO and built a simple technological demonstrator at X band, what it turned to be later the European Space Agency (ESA) SMOS mission.

In 2001 the first GNSS-R instrument of the research group was developed: the DOppler-Delay Receiver (DODEREC) [15]. In 2004, Professor Camps was awarded with an EURYI Award to develop “Passive Advanced Unit (PAU): A Hybrid L band Radiometer, GNSS-Reflectometer, and InfraRed (IR)-radiometer for Passive Remote Sensing of the Ocean,” which consisted of a family of instruments for remote sensing: an L band radiometer to measure Sea Surface Salinity (SSS), an IR-radiometer for Sea Surface Temperature (SST) estimation, and a GNSS-Reflectometer to correct the effect of the sea surface roughness. Two L band radiometers were developed: PAU-Synthetic Aperture (PAU-SA), a synthetic aperture radiometer based in the SMOS concept [16], and PAU-RADiometer (PAU-RAD), a real aperture radiometer with digital beamforming [17]. The developed GNSS-R instrument was called GPS Receiver Instrument for PAU (GriPAU), and was able to compute Delay-Doppler Map (DDM) in real time and included an L band Total Power Radiometer (TPR) to measure the brightness temperature [18]. GriPAU was a prototype for a spaceborne instrument for which a flight model was built for the Instituto Nacional de Técnica Aeroespacial (INTA) MicroSat-1 mission [19], which unfortunately was canceled due to budgetary restrictions.

In parallel to PAU-RAD and PAU-SA, the Multifrequency Experimental Radiometer with Interference Tracking for Experiments over Land and Littoral (MERITXELL) radiometer [20], a real aperture multiband radiometer designed for Radio Frequency Interference (RFI) detection, was developed. This radiometer was the starting point of the RFI detection and mitigation branch of the research group, followed by the development of the Front-End GNSS Interference eXcisor (FENIX), a RFI detector and mitigator system for GNSS, GNSS-R and Radiometric systems [21]. In 2007, the first Cubesat mission (³Cat-1) started being developed [22], which became the seed of a laboratory devoted to space technologies: the NanosatLab. As of now, two cubesats have been launched (³Cat-2 on 15 August 2016, and ³Cat-1 on 29 November 2018), two ready to be launched (³Cat-5/A and ³Cat-5/B, expected during the first quarter of 2020), one being manufactured (³Cat-4, with an expected launch date within 2020), and one more under study (³Cat-3) [23].

Just after GriPAU, many GNSS-R instruments were developed, such as the Soil Moisture IPT GNSS Observations at L-band (SMIGOL) [24], and the Light Airborne Reflectometer for GNSS Observations (LARGO) [25] and its smallest version CORTO, all built using Commercial Off-The-Shelf (COTS) components, the P(Y) C/A ReflectOmeter (PYCARO) [26], which flew onboard a stratospheric balloon (ESA Academy BEXUS 17 and 19 experiments), and later was put into orbit onboard the ³Cat-2 mission, the Monitoring of the Canopy using a GNSS-T Instrument for VEgetation Research (MCGIVER) [27], among others.

This Ph.D. thesis is a natural evolution of the GNSS-R instruments developed by the research group, and was conceived a technological demonstrator of the Passive Reflectometry and Interferometry System In-orbit Demonstrator (PARIS IoD) mission [28]: a

multiband (L1/E1 and L5/E5A) GNSS-R, multi-constellation (U.S. Global Position System (GPS) and European Galileo positioning system), multi-beam (two beams at each frequency band) instrument capable of applying the two main GNSS-R techniques (conventional GNSS-R (cGNSS-R) and interferometric GNSS-R (iGNSS-R)) and with beam steering capabilities. This instrument, and some of the other instruments developed in parallel to this Ph.D. thesis, are described in the following chapters.

1.4 Goals

The main objective of this Ph.D. thesis is to develop all the Radio-Frequency (RF) hardware of MIR mimicking the PARIS IoD instrument. The digital processing unit has been developed in the frame of Daniel Pascual Ph.D. thesis [29]. The instrument requirements are:

- **Multi-constellation:** GPS and Galileo.
- **Dual band:** GPS L1 and L5 bands, and Galileo E1 and E5 bands.
- **Analog Beam Steering:** The instrument must have analog beamsteering. Digital beam steering was discarded due to the excessive amount of data generated, power consumption, and hardware complexity.
- **Single Polarization:** Performing polarimetric measurements was discarded in order to simplify the instrument. Therefore the up-looking antenna must be Right Hand Circular Polarization (RHCP), and the down-looking one must be Left Hand Circular Polarization (LHCP).
- **Multiple beams:** At least 2 beams per band are desirable.
- **Conventional and Interferometric GNSS-R:** Both techniques must be used to compare their performances in fair conditions (same antennas and receivers).
- **Computation of complex waveforms in real time:** Data must be processed in real time to provide scientifically valuable data without human intervention and long processing time. Complex waveforms must be provided without incoherent averaging. This part corresponds to the back-end of the instrument, which was developed in parallel in Daniel Pascual Ph.D. thesis [29].
- **Airborne instrument:** As the instrument should be placed in a small airplane, the system must refresh the beams fast enough to properly track the satellites and the specular reflection point compensating the flight dynamics.
- **Centimetric precision in altimetric applications:** The optimum bandwidths determined in [30] must be achieved (30 MHz at L1/E1, 40 MHz at L5/E5A).

The instrument was planned to sample data at 16 bits, compute complex waveforms in real time, and then store the waveforms. However, this part could not be finished on time for the field campaign, and only raw data was stored instead. In order to fulfill the bandwidth requirement and be supported by the chosen hardware, the data had to be sampled at 1 bit I+Q, which limited some of the instrument capabilities as explained

is [29]. Initially, the instrument should also have included an RFI detection and mitigation system [31, p. 73-100], but the instrument was finished too close to the shipment due date for the field campaign, and it was preferred to use that time to test the instrument rather than to add an extra functionality.

1.5 Outline

This Ph.D. thesis is divided into 6 parts which contain a total of 10 Chapters, plus 8 Appendices. The outline of this PhD is the following:

- Part I: Introduction and State of the Art.
 - Chapter 1 introduces the use of remote sensing techniques for EO. Then the background of this work and previous works carried out in the research group are stated. The motivations and goals of this work are drawn before this outline is stated.
 - Chapter 2 explains the different GNSS systems, their use as opportunity signals for reflectometry (GNSS-R), and states the main applications, observables and instruments up to the date. Lastly, radio navigation signals DME/TACAN are explained and why they can be a threat for GNSS-R.
 - Chapter 3 summarizes all the instruments developed in parallel to the thesis that were useful to it, and explains the lessons learned.
- Part II: Instrument Design, Implementation, Calibration, and Characterization
 - Chapter 4 explains how the MIR instrument chooses which satellites to track, and all the steps to point them based on the position and attitude of the satellites and the airplane.
 - Chapter 5 describes in depth all the MIR hardware and software, and shows some measurements of the integration and validation of the subsystems.
 - Chapter 6 explains the calibration procedure of the MIR instrument, and evaluates its impact in the antenna pattern and in the beam directivity.
- Part III: Experimental Results
 - Chapter 7 analyzes how the DME/TACAN signals may affect a GNSS-R instrument in orbit.
 - Chapter 8 describes the field campaign carried out in Australia between May 2018 and June 2018. Then, it shows some preliminary results over land and sea. Data processing continues now in the frame of Juan Francisco Muñoz Ph.D. thesis.
 - Chapter 9 analyzes how satellite cross-talk affected interferometric measurements in one of the flights over sea in the Australian campaign.
- Part IV: Conclusions and future work

– Chapter 10 draws conclusions about this work and suggests future lines of work derived from the data gathered during the field campaign.

- Part V: Appendices
- Part VI: Bibliography and list of publications

This dissertation is not just a summary of all the research done along the Ph.D., but also aims to be a helpful guide to those who will continue the MIR legacy. One does not simply turn on the instrument; Appendix H should be followed for that purpose. The author will appreciate if the reader notifies by email typos, errors, comments, or anything unusual found in the manuscript.

2

Chapter 2

State of the Art

2.1 Introduction

This chapter first explains what are GNSS in section 2.2, which ones are currently operational, the transmitted signals, and their characteristics. Then, section 2.3 explains how these signals can be used as opportunity signals for remote sensing, the main observables, applications, and instruments. Next, DME/TACAN signals are explained in section 2.4, and why do they may interfere with GNSS-R instruments. Last, conclusions are drawn in section 2.5.

2.2 Global Navigation Satellite Systems

GNSS are radio navigation systems originally designed to provide accurate position, navigation, and timing. There are currently four operational systems: the American GPS, the Russian Global'naya Navigatsionnaya Sputnikovaya Sistema (GLONASS), the European Galileo, and the Chinese Beidou-2. Additionally, there is a regional system Indian Regional Navigation Satellite System (IRNSS), and several Satellite Based Augmentation Systems (SBASs) used to increase the system accuracy in certain regions, such as Wide Area Augmentation System (WAAS) in North America, European Geostationary Navigation Overlay Service (EGNOS) in Europe, or Quasi-Zenith Satellite System (QZSS) in Japan.

All the current systems are based on the Time Of Arrival (TOA) estimation of the transmitted signals from satellites, which is converted to the distance to the satellite by multiplying it by the speed of light. When four satellites are available, the position and time of the receiver can be triangulated. Each user receives the signals transmitted from different satellites, frequency bands, and systems at the same time (see the whole GNSS

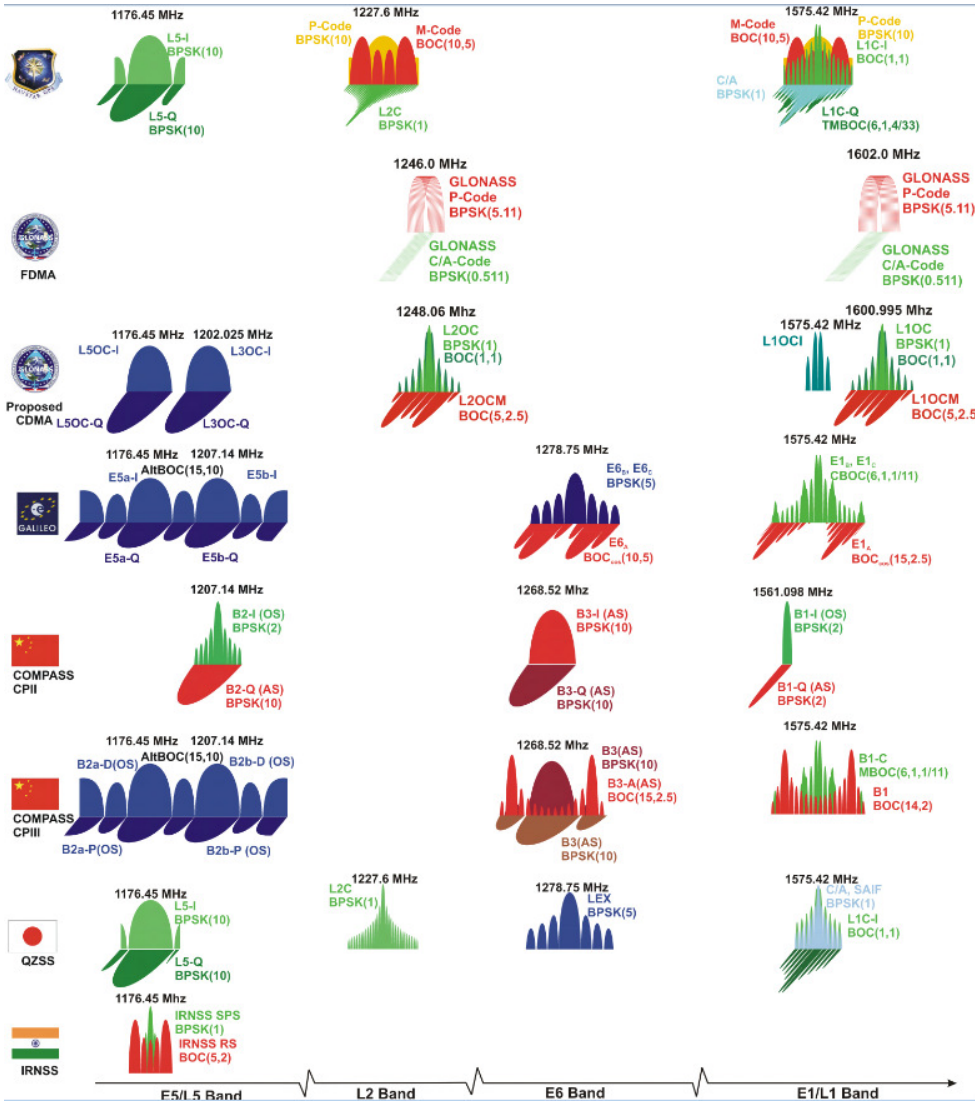


Figure 2.1: Signals being broadcasted by the currently deployed systems (from [32]).

spectrum allocation in Fig. 2.1).

Except GLONASS, which uses Frequency Division Multiple Acces (FDMA), the rest of systems use Code Division Multiple Access (CDMA) [33]. The codes must be orthogonal between satellites, signals, and systems, and they must correlate only at the origin to avoid ambiguity. The so-called Pseudo-Random Noise (PRN) codes fulfill the three first properties, however most of the signals are periodic in the range 1-20 ms (see tables 2.1 and 2.2), thus introducing an ambiguity in the order of 300-6000 km. Some signals are modulated to increase the robustness against other signals and systems; for instance the Galileo E1 Open Service (OS) signal is modulated so its spectrum does not match

the GPS one. CDMA not only multiplexes the signals, but also spreads the energy of the signal in the electromagnetic spectrum. When the signal is cross-correlated with the desired code, the signal is despread, thus obtaining the so-called correlation gain. Any received interfering signal in the system is also cross-correlated with the code, being its energy spread in the electromagnetic spectrum, that is, CDMA also adds robustness against RFI. Hardware receivers only compute the cross-correlation in the delay domain since the Doppler frequency created by the relative velocity between the satellite and the receiver is compensated with Phase-Locked Loops (PLLs); software receivers, whereas, also cross-correlate in the Doppler domain with the so-called Cross Ambiguity Function (CAF):

$$Y_{xy}(\tau, \nu) = \frac{1}{T_c} \int_0^{T_c} x(t)y^*(t - \tau)e^{-j2\pi\nu t} dt, \quad (2.1)$$

where y is the received signal, x is the transmitted code, T_c is the coherent integration time, and τ and ν are the delay and Doppler differences between the received signal and the code. Note that Eqn. (2.1) is Woodward Ambiguity Function (WAF) when $x = y$ [34], or the CAF if $x \neq y$. Figures 2.2a and 2.2b show the WAF of a GPS L1 C/A signal, and a Galileo E1 OS signal. In the Doppler domain, the WAF can be approximated by a sinc function, whose main lobe is $2/T_c$ wide; therefore, the Galileo E1 OS WAF in the Doppler domain is four times narrower than the L1 C/A signal since the coherent integration time is four times longer.

The WAF and the CAF become the unidimensional functions called ACF and CCF, respectively, if the Doppler difference is totally compensated, that is when $\nu = 0$. Figures 2.2c and 2.2d show the ACF and CCF of GPS and Galileo signals at L1/E1 and L5/E5 frequency bands. In time, the GPS L1 C/A, GPS L5, Galileo E5A, and Galileo E5B ACFs can be approximated by a triangle whose width is $2/R_c$, where R_c is the chip rate. The signals modulated with Binary Offset Carrier (BOC) modulations such as Galileo E1 OS and Galileo E5 can be approximated by many of them, with an envelope whose width is $2/R_c$. Note also that the Galileo E1 OS ACF is narrower than the GPS L1 C/A due to the larger signal bandwidth (see tables 2.1 and 2.2). The three triangles in the Galileo ACF are caused by the modulation of the signal. GPS L5 and Galileo E5A ACFs have the same shape than GPS L1 C/A, and are also narrower because of the larger bandwidth (20 MHz vs. 1 MHz).

Not all transmitted signals by each system are open, for instance L1 C/A and L1C are public, while the private L1 P(Y) and the military M are restricted. Analogously, the Galileo E1 OS is open, while the Public Regulated Service (PRS) signal is also restricted. Besides, each system transmits in different frequency bands, mainly to compensate the random delay introduced by the ionosphere. GPS transmits at L2 to compensate the ionospheric delay, but also in the L5 for life-critical applications. Galileo can be used with single frequency receivers at E1, E5A, or E5B. If more than one band is used, ionospheric corrections can be applied. Besides, the third band E6 is used for life-critical applications. A list of all the signals transmitted by GPS and Galileo is shown in tables 2.1, and 2.2, respectively. Figures 2.3a , 2.3b show how GPS and Galileo signals share the L1/E1 and the L5/E5 frequency bands, respectively, which are the bands of interest in this Ph.D thesis.

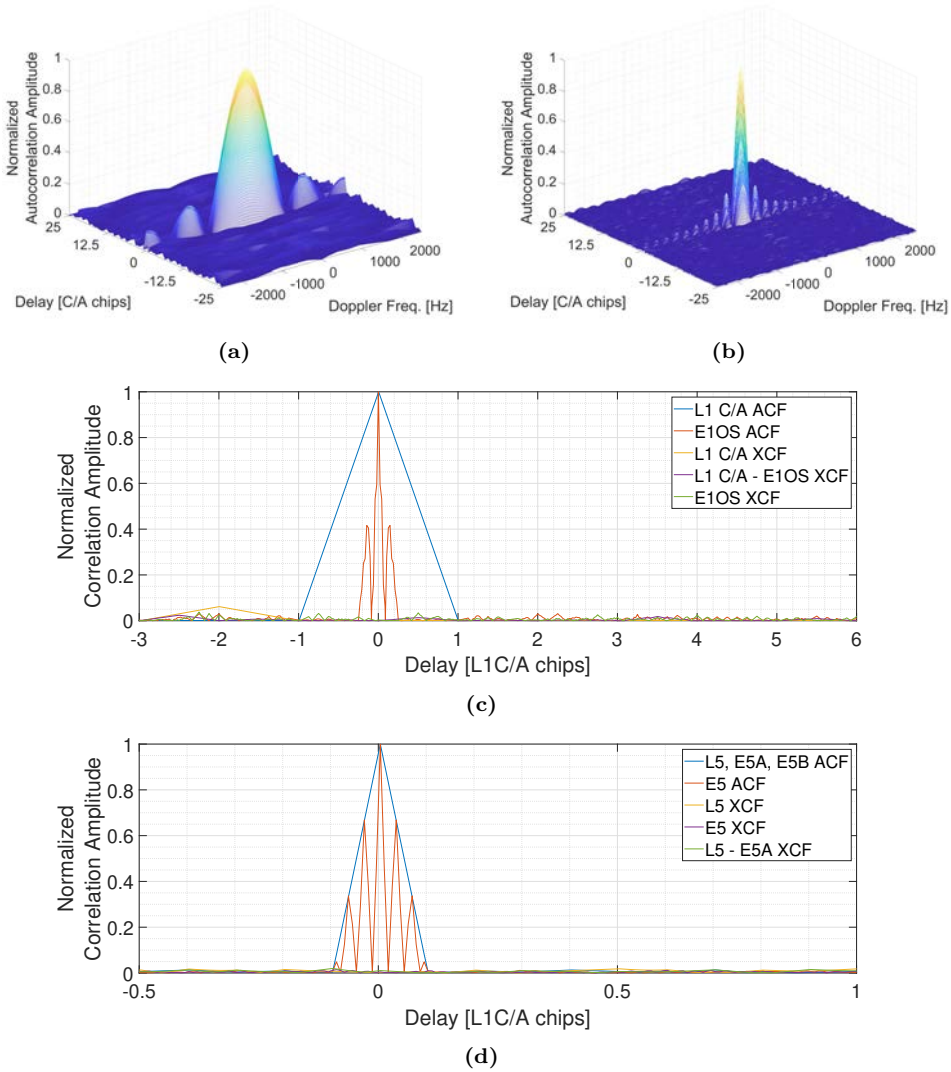
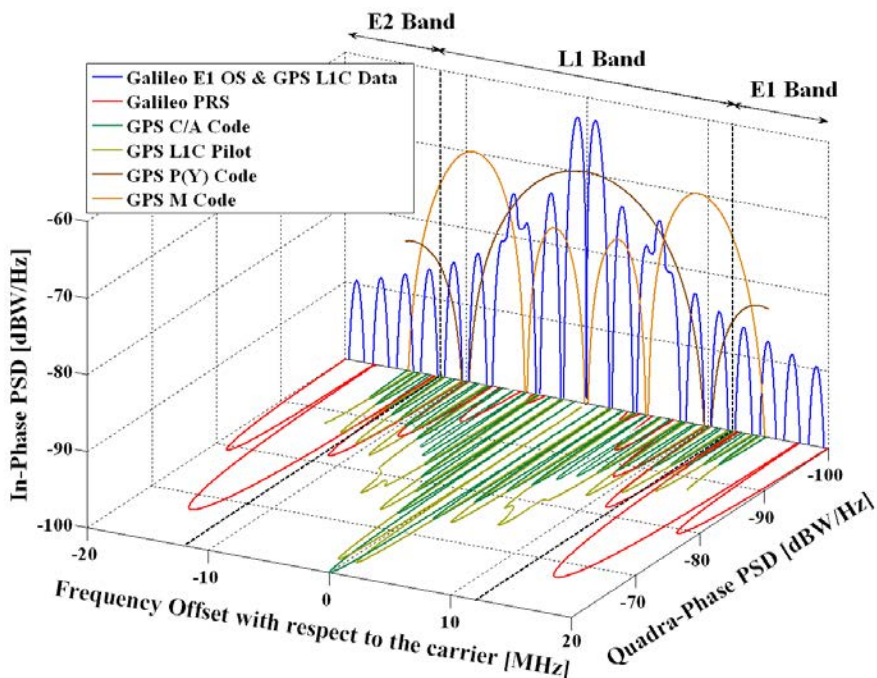


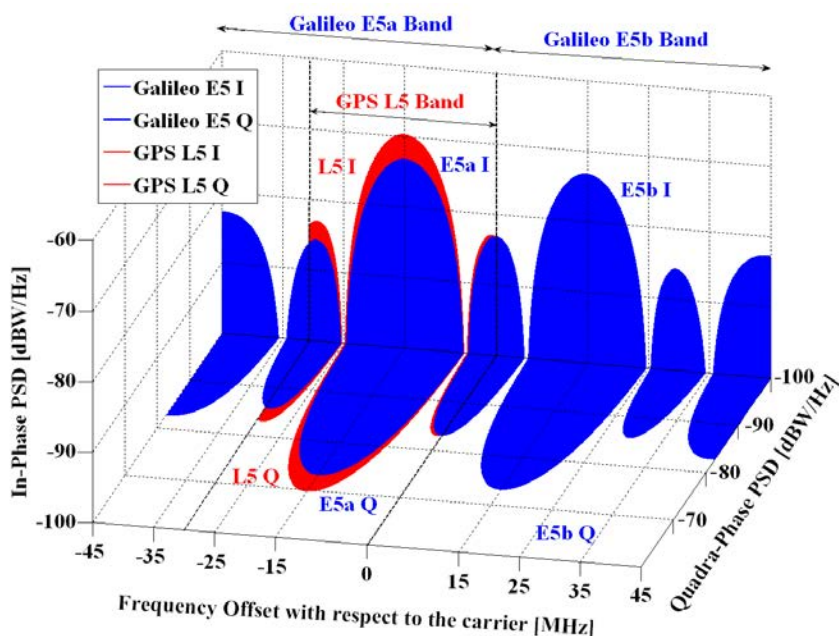
Figure 2.2: a) WAF of a GPS L1 C/A code, b) WAF of a Galileo E1 OS code, c) Auto-Correlation Function (ACF) and Cross-Correlation Function (CCF) at L1/E1, and d) ACF and CCF at L5/E5.

2.3 Global Navigation Satellite System - Reflectometry

Besides the original purposes of GNSS, multiple indirect applications have been derived [37–39]. In Remote Sensing, GNSS provides opportunity signals for GNSS-Radio Occultation (GNSS-RO) [40, 41], and for reflectometry (GNSS-R). The concept of GNSS-R was first proposed for multistatic scatterometry in 1988 [42], and later in 1993 for



(a)



(b)

Figure 2.3: Shared spectrum by GPS and Galileo at a) L1/E1, and b) L5/E5 frequency bands (From [36]).

Table 2.1: Main characteristics of the broadcasted GPS signals (from [35]).

Service Name	L1 C/A	L1C		P(Y)	M-Code
Frequency Band	L1			L1 & L2	
Signal Component	Data	Data	Pilot	Data	N.A.
Modulation	BPSK(1)	TMBOC(6,1,1/11)		BPSK(10)	BOC _{sin} (10,5)
Code Freq.	1.023 MHz	1.023 MHz		10.23 MHz	5.115 MHz
Code Family	Gold	Weil		Combination of short-cycling of M-sequences	N.A.
Primary PRN Length	1023 (1 ms)	10230 (10 ms)		$6.19 \cdot 10^{12}$ (1 week)	N.A.
Sec. PRN Length	-	-	1800	-	N.A.
Data Rate	50 bps	50 bps	-	50 bps	N.A.
Public/Private	Public	Public		Private	Private

Service Name	L2 CM	L2 CL	L5 I	L5 Q
Frequency Band	L2		L5	
Signal Component	Data	Pilot	Data	Pilot
Modulation	BPSK(1)		BPSK(10)	BPSK(10)
Code Freq.	511.5 kHz	511.5 kHz	10.23 MHz	10.23
Code Family	M-sequence from a maximal polynomial degree of 27		Combination of short-cycling of M-sequences	
Primary PRN Length	10230 (20 ms)	767250 (1.5 sec)	10230 (1 ms)	10230 (1 ms)
Sec. PRN Length	-	-	10	20
Data Rate	50 bps	-	50 bps	-
Public/Private	Public	Public	Public	Public

mesoscale sea altimeter called Passive Reflectometry and Interferometry System (PARIS) [43]. The latter proposed the so-called interferometric technique iGNSS-R, which is based on the cross-correlation of the direct signal received from the satellite, and the same signal once it is reflected on the Earth's surface. Later, in 1996, cGNSS-R was proposed [44], which is based on the correlation of the reflected signal with a locally generated clean replica of the desired code. As the clean replica has no noise, the cross-correlation in cGNSS-R has a higher Signal to Noise Ratio (SNR) than in iGNSS-R, but only open codes can be used, which have typically narrower bandwidths.

The conventional technique achieved thus higher SNR at the expense of a precision reduction. The interferometric technique took advantage of the whole bandwidth of the signals being correlated regardless of the codes allocated, but with lower SNR. The conventional technique only shows the correlation peak corresponding to the satellite associated to the code used, while the interferometric technique shows the peaks of all the cross-correlations simultaneously (satellite cross-talk) [45]. Last but not least, as iGNSS-

Table 2.2: Main characteristics of the broadcasted Galileo signals (from [36]).

Service Name	E1 OS		PRS		E6 CS		E6 PRS
Frequency Band	E1				E6		
Signal Component	Data	Pilot	Data		Data	Pilot	Data
Modulation	CBOC(6,1,1/11)		BOC _{cos} (6,1,1/11)		BPSK(5)		BOC _{cos} (10,5)
Code Freq.	1.023 MHz		2.5575 MHz		5.115 MHz		
Code Family	Random Codes		N.A.		Memory Codes		N.A.
Primary PRN Length	4092 (1 ms)		N.A.		5115 (1 ms)		N.A.
Sec. PRN Length	-	25	N.A.			100	N.A.
Data Rate	250 bps	-	N.A.		1000 sps		N.A.
Public/Private	Public		Private		Public		Private

Service Name	E5A		E5B	
Frequency Band	E5			
Signal Component	Data	Pilot	Data	Pilot
Modulation	AltBOC(15,10)			
Code Freq.	10.23 MHz			
Code Family	Combination and short-cycling of M-sequences			
Primary PRN Length	10230 (1 ms)			
Sec. PRN Length	20	100	4	100
Data Rate	50 bps	-	250 sps	-
Public/Private	Public		Public	

R cross-correlates two signals, it is prone to be affected by RFI [46]. The conventional technique is also more difficult to process: the codes have to be generated at the proper frequency, and the Doppler of the reflected signal has to be compensated. The interferometric technique does not required to know the codes, and in ground-based and airborne experiments, where the Doppler frequency of the direct and the reflected signals are almost identical, the data processing becomes even easier since the Doppler difference between both signals is null. On the contrary, if the drawbacks of iGNSS-R must be overcome, large arrays with steerable beams are required, that is, complex hardware systems. Nowadays, the newly broadcasted GPS L5 and Galileo E5 signals have bandwidths even larger than the private codes P(Y) and M. Therefore, the main drawback of cGNSS-R is not the narrower bandwidths and lower accuracy anymore, but the data processing complexity.

In-between cGNSS-R and iGNSS-R the codeless and semi-codeless techniques exist [47]. The P(Y) code is an encrypted 20 MHz code, but the encryption can be overcome by using models of the P(Y) code. This approach results in high SNR, and high precision, but at the expense of a high complexity processing, which in 21014 was considered “*impractical*”

for an orbiting remote-sensing mission” [48].

2.3.1 Global Navigation Satellite System - Reflectometry Observables

Once a GNSS signal is reflected on the ground, multiple scattered wave fronts reach the antenna. Each one has a different delay and Doppler that depends on the scenario geometry and the satellite and the receiver conditions [49]. The point that has the minimum path between the transmitting satellite, the surface, and the receiving antenna is called the Specular Reflection Point (SRP). When the surface is flat, only the wave reflected on this point is received (see Fig. 2.4). As the surface becomes rougher, more wave fronts scattered around the specular point are received in the antenna. The area from where these reflected wavefronts are received is the so-called Glistening Zone, and it depends not only on the roughness, but also on the height, the elevation angle, and the signal wavelength [44].

All the wave fronts received with a given delay are geometrically distributed around the specular point in ellipsoids (equi-range lines) called annulus. As the radius of the annulus increases, the scattered power decreases. Similarly, all wave fronts are received with a Doppler frequency that depends on the relative speed between the scenario, the satellite, and the receiver. However, in this case the wave fronts received with the same Doppler are distributed in the scenario in hyperbolae (equi-Doppler lines).

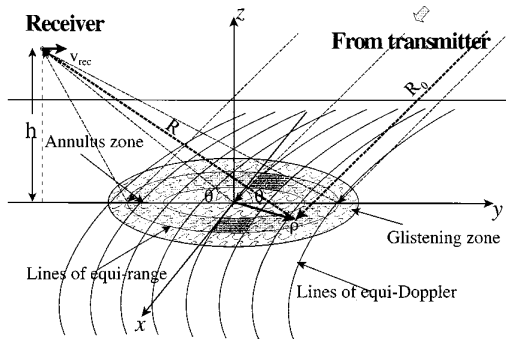


Figure 2.4: Reflection scenario (from [49]).

The distribution of the received signals in the delay and Doppler domains can be studied with the DDM, which is the incoherently averaged CAF between the reflected signal and the direct signal or the desired code [49]:

$$\left\langle |Y_{xy}(\tau, \nu)|^2 \right\rangle = \left\langle \left| \frac{1}{T_c} \int_0^{T_c} x(t)y^*(t - \tau)e^{-j2\pi\nu t} dt \right|^2 \right\rangle, \quad (2.2)$$

where x and y are the signals to be cross-correlated, and T_c is the coherent integration time. In cGNSS-R, the reflected signal $x = s_r$ is correlated against the code $y = c$, while in iGNSS-R, the reflected signal $x = s_r$ is correlated against the direct signal $y = s_d$.

Figure 2.5 shows 4 examples of DDM from airborne and spaceborne instruments, and over different scattering surfaces.

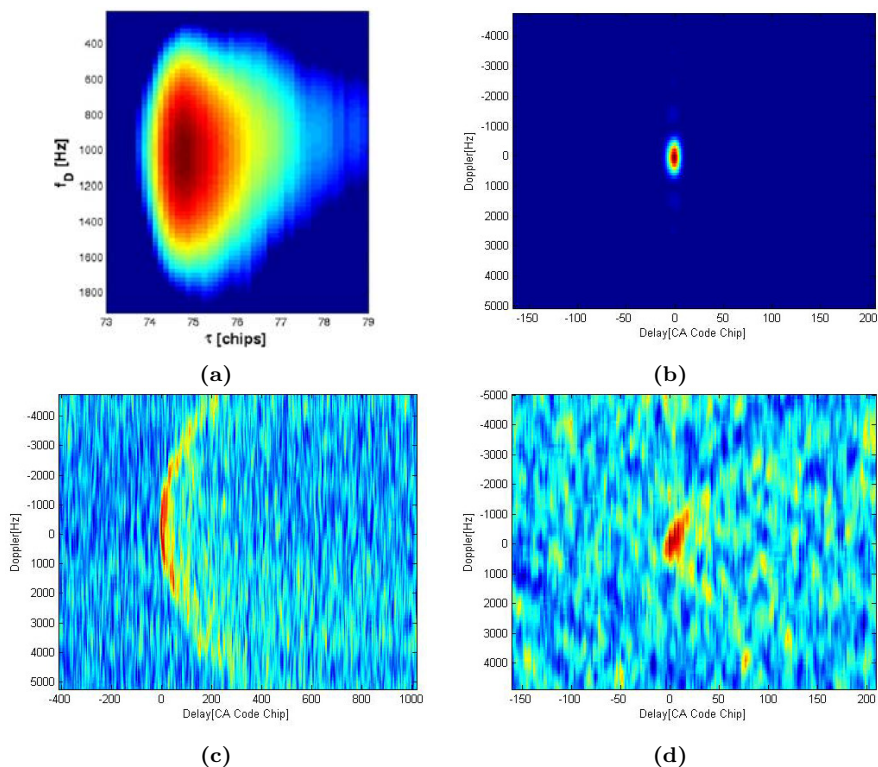


Figure 2.5: DDM examples: a) over ocean, from an airplane, wind speed of $U_{10} = 10$ m/s, coherent integration time of 1 ms, incoherent averaging time of 20 s (from [50]), and from the UK-DMC satellite with coherent integration time of 1 ms, incoherent averaging time of 200 ms (from [51]) b) over ice, c) over ocean, with wind speed of $U_{10} = 7.8$ m/s, and d) over land.

If the surface is flat, that is, there is no wind or no surface roughness, the reflection is specular and the DDM is the product of a triangle in the delay axis with a sinc in the Doppler axis [49] (e.g. Fig. 2.5b, corresponding to a specular reflection over ice received from space). As surface roughness increases, the reflections become less coherent, and spread in the delay and Doppler plane. For low heights and incoherent scattering, the maximum Doppler and delay in the glistening zone is limited, and the power is concentrated in the DDM as a bump elongated in the increasing direction of the delay axis (e.g. Fig. 2.5a, corresponding to a DDM over the sea received from an aircraft). As the height increases, the glistening zones also does. From space, this is seen as a horseshoe or a *croissant* (e.g. Fig. 2.5c, corresponding to a reflection over sea with a wind speed of $U_{10} = 7.8$ m/s received from space). It must be emphasized that as the power spreads, the SNR of the peak decreases. Last, Fig. 2.5d shows a reflection over land received from space, where the low reflection coefficient and the topography reduce the SNR, showing

a degraded version of the DDM peak.

The other main GNSS-R observable is the “waveform”, which is a cut in the delay direction that passes through the DDM peak. Figure 2.6 shows several waveforms simulated in [49] for different wind speeds. An increase in the wind speed not only reduces the slope of the tail of the waveform, but also the peak amplitude. The higher the receiver, the faster the peak amplitude decreases with an increase of the wind speed.

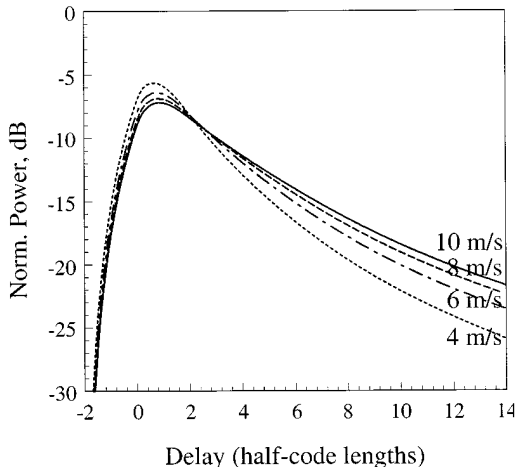


Figure 2.6: Simulated waveforms over the ocean at $h=10$ km, with an elevation angle of 45° , for different wind speeds (from [49]).

The comparison of the complex value of the direct and reflected DDM peaks, also called Interferometric Complex Field (ICF) [52], has information on the sea state, and as well between the reflected DDM peaks of two perpendicular linear polarized antennas (GNSS-R polarimetry) [53].

DDMs and waveforms are versatile and powerful for remote sensing, but require a complex sampling and processing system, whereas other useful observables can be obtained from COTS GNSS receivers in a reasonable time.

One of the most extended techniques using this type of observables is the Interference Pattern Technique (IPT), which was first proposed in 1998 [54]. It was discovered in static ground-based GPS receivers for positioning that for low elevation angles, the tracked power showed a periodical fading, which turned out to be multipath coming. For a vertically polarized antenna pointing to the horizon, the amplitude of this interference pattern reduces to 0 at the Brewster angle, which depends on the dielectric permittivity of the ground, which is related to several geophysical parameters such as the Soil Moisture (SM), or the Vegetation Water Content (VWC). At the same time, the periodicity of the interference pattern depends on the receiver height, which can be used to infer the height of the surface with respect to the receiver. In 2008, the use of GNSS receiver networks was proposed for a soil moisture network [55], and to improve it by pointing the antenna to the horizon to retrieve a clearer and longer interference pattern [56]. Later, two linear polarizations were used instead of a single one [57], and multiple frequency bands were used [58].

Another observable that can be obtained from the GNSS receivers are the pseudo-ranges, the raw estimated distances from the receiver to the satellite. These distances have contributions from clock biases, and ionospheric errors among other that must be removed prior to estimate correctly the position. For reflectometers at low altitudes, the direct and reflected signals are affected equally by the ionosphere, and the troposphere, and if they are sampled simultaneously by the same system, all the errors are equally present in both pseudo-ranges. The difference between the two pseudo-ranges thus removes most of these errors, and the difference is proportional to the receiver height and the incidence angle with high precision [59]. The pseudo-ranges can be measured by correlating sampled raw data or can be provided by commercial two-channel receivers, which can be enhanced by using GNSS receivers that use codeless and semi-codeless techniques [48].

In 2007, [60] proved that it was possible to track the phase of the peak of the DDM of the reflected signal. This is not only possible for specular reflections, such as over ice, land, and calmed water bodies, but also over rough surfaces such as the sea surface with wind speeds up to 8 m/s [61]. This technique has been used to determine ice thickness with a static receiver [62], and to estimate water height over a lake with a dynamic receiver on-board a Zeppelin [63].

2.3.2 Global Navigation Satellite System - Reflectometry Applications

GNSS-R was originally proposed for scatterometry [42], but multiple applications for remote sensing were soon found. Over ocean, reflectometry has been proposed for sea state and wind speed determination [64], wind direction [50], sea state corrections for salinity estimation in the SMOS mission [65], oil slick detection [66], and tropical cyclone monitoring [11]. Ocean altimetry was originally proposed to study the ocean mesoscale flows and the interaction sea-ice [43], and later [67] claimed that GNSS-R would be able to detect tsunamis. Water body altimetry can be used to monitor river floods [68], river and reservoir water levels [63, 69–71], sea level and tides [58, 72], and Significant Wave Height (SWH) [73].

A wide variety of applications over land have been proved: soil moisture has been widely studied both with scatterometry [25, 74–76], polarimetry [77], and IPT [56, 57, 78]; topography has been estimated with IPT [79]; vegetation growing has been successfully monitored with IPT in wheat [24] and maize fields [80], and biomass estimations with polarimetry [81].

Reflection over ice have been used to characterize the ice layers [62, 82], and to monitor snow depth [83], which can be useful to calculate frozen water reserves, monitor the thawing caused by climate change, and to forecast the risk of avalanches.

2.3.3 Global Navigation Satellite System - Reflectometry Instruments

The first GNSS-R instrument proposed was PARIS IoD in 1993: an In Orbit Demonstrator for a constellation of satellites for mesoscale altimetry. PARIS IoD would have had two arrays, analog beamforming, two frequency band (L1/E1 + L5/E5), and would have been an interferometric reflectometer [43].

The first GNSS reflection ever captured was in 1991 when a military French aircraft got locked by accident to a GNSS signal scattered over the sea [84], but the incident was not published until 1994. Then, in 1996, the first dedicated airborne experiment was carried out by [85] using a commercial GPS receiver, an up-looking RHCP antenna, and a down-looking LHCP antenna to track the Carrier to Noise ratio (C/N0) and pseudoranges of the reflected signals. The instrument, called Delay Mapping Receiver (DMR) was later used in 1998 to study wind speed over sea [64] and later in 2000 to study soil moisture [74], both using the L1 C/A signal. In 1998 the first experiment with the IPT technique was conducted to study the electric permittivity of the ground using a commercial GPS receiver and an up-looking RHCP antenna: grass and asphalt were successfully differentiated [54]. Later in 2000 the same technique was used to measure sea height [72]. In 2001, a modified TurboRogue GPS receiver was used to retrieve a lake surface height with centimetric accuracy using phase altimetry with L1 C/A from ground, and later on from an airplane using the L1 and L2 frequency bands in 2002 [86]. This same receiver was used in 2014 to propose the semi-codeless techniques (sGNSS-R) [48]. This last experiment also was the first one to be affected by satellite cross-talk (see Chapter 9).

So far all the experiments correlated the received signals with the desired codes inside the GPS receiver. In 2001 the first ground-based experiment that sampled raw data was carried out near Rotterdam to retrieve sea height [12]. This was the first of a series of technological demonstrators of the PARIS concept. Later in 2004, Eddy, the first airborne software GNSS-R instrument, was used to retrieve significant sea height and mean sea level [87]. In October 2003, the UK Disaster Monitor Constellation (UK-DMC) satellite was launched [88]. It had a 1x3 array antenna made of L1 patches with a total gain of 12 dBi (with a footprint of approximately 1000 km x 200 km) pointing 10° with respect to nadir. The receiver was a modified GPS receiver that sampled 40 seconds of raw data at 5.714 MHz with 2 bits [89]. The sampled data could be either correlated on-board or transmitted without any processing. This mission proved not only that it was possible to retrieve reflected GNSS signals from space over ocean, ground and ice, but also to estimate wind direction and speed [90], and to track the signal phase over ice [88].

In 2007 GNSS Occultation, Reflectometry and Scatterometry (GORS) used Galileo and GLONASS signals for the first time for altimetry [91]. The same year, the use of already deployed geodetic GNSS receivers was proposed for soil moisture mapping [78]. One year later, in 2008, [56] proposed to use a horizon-looking antenna using vertical and horizontal polarization to improve the IPT performance for soil moisture estimation. With it, the SMIGOL instrument also retrieved vegetation height [24], snow depth [83], water height [69], and wave height [92]. Also, in 2014, the soil moisture estimation accuracy was improved by studying the phase difference between the vertical and horizontal interference patterns [57].

In 2007, the GPS Open Loop Differential Real-Time Receiver (GOLD-RTR) and PAU-GNSS-Reflectometry (PAU-GNSS-R) instruments claimed to be the firsts to compute DDMs in real time [93, 94]. GOLD-RTR was also the first instrument to use the polarization ratio between two down-looking antennas with different circular polarizations (RHCP and LHCP) to estimate the sea electrical permittivity [95], and the first non-IPT instrument to study sea ice [96], snow layers [82], and phase altimetry over ice [97].

In 2011, the Paris Interferometric Receiver (PIR) instrument made the first sea al-

timetry interferometric measurement from ground [98] again in the Zealand Bridge, in the Netherlands, as a demonstrator of the PARIS concept. Then, in 2012, the Land Monitoring with Navigation Signals (LEiMON) project was the first instrument to have two down-looking antennas with different polarizations to infer soil moisture [77] and biomass [99] using polarimetry, which one year later was improved by the PYCARO instrument by using polarimetry in GPS L1, L2, Galileo E1, and GLONASS L1 and L2 also for biomass estimation [26]. The PYCARO instrument also presented the reconstructed GNSS-R (rGNSS-R).

Back in 2014, the first altimeter using the GPS L5 band was conceived [100]. The same year, the LARGO was the first low-cost, low-size, and low-weight reflectometer using commercial components that measured the DDM peak in real-time [25]. Two years later a GPS L1 and L5, and Galileo E1 and E5 conventional and interferometric instrument for altimetry with digital beamforming was presented: Software Paris Interferometric Receiver (SPIR) [101].

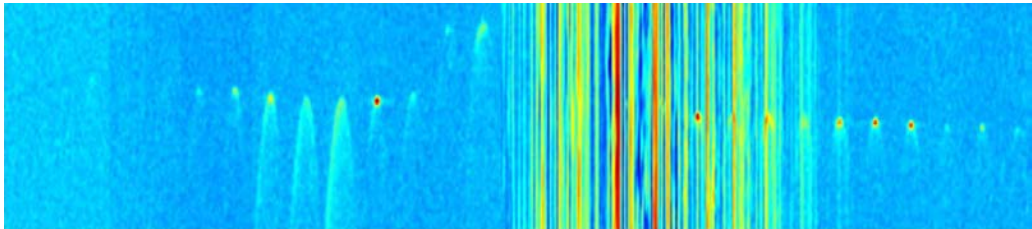


Figure 2.7: Series of processed data over Ukraine at L1 contaminated by RFI (from [102]).

In 2014, the UK launched TechDemoSat-1 (TDS-1), a microsatellite with a 2x2 array with 13 dBi directivity and a modified version of the Space GNSS Receiver (SGR) onboard the UK-DMC called Space GNSS Receiver - Remote Sensing Instrument (SGR-ReSI) that allowed the use of L1, L2 and L5 bands with 16 MHz of sampling frequency and real time processing. It is also capable of recording raw data for further studies. TDS-1 has been the first GNSS-R mission directly affected by RFI (see Fig. 2.7) [103], a problem already foreseen in 2014 [104]. TDS-1 was a technological demonstrator of the Cyclone Global Navigation Satellite System (CYGNSS) mission, a constellation of microsatellites at 500 km height with 35° orbit inclination focused on the study of tropical cyclones using GNSS-R with an expected average and median revisit times of 4 h and 1.5 h respectively [11, 105]. The constellation was proposed in 2012 and finally launched at the end of 2016. Each micro-satellite has two 2x3 L1 nadir-looking LHCP arrays pointing towards the cross-track of the satellite motion, rolled approximately 20°, one in each side direction. The arrays have 14.5 dB directivity, and a half-power beamwidth of 37° in the cross-track direction and 24° in the along-track direction. The satellites use a modified version of the SGR-ReSI receiver in the TDS-1, called Delay Doppler Mapping Instrument (DDMI) [106], that samples continuously and computes up to 4 DDMs with 1 ms of coherent integration time and 1 second of incoherent averaging time in units of counts [107]. Then, they are converted to units of Watts (L1a product) using a calibration method similar to the used in microwave radiometry, and later to Normalized Radar Cross Section (NRCS) σ^0 (L1b product) [108, 109]. Afterwards, wind speed is retrieved (L2 product) [110–112]. If a particularly interesting location is detected, the

DDMI can change to raw data sampling mode, accumulating up to 60 seconds of recorded data (L0 product) [106].

All the aforementioned instruments are summarized in table 2.3. The instrument developed along this thesis has been added at the end: a GPS L1 and L5, and Galileo E1 and E5 software airborne reflectometer that can apply both the conventional and interferometric techniques that has analog beamsteering.

Table 2.3: Summary of state of the art GNSS-R instruments. The receiver type indicates how the correlations are computed: Software (Sw, raw data stored) or Hardware (Hw, computed in real time). The antennas can be Direct (D), Reflected (R), or Horizontal (H). BS stands for Beam Steering. sGNSS-R stands for semi-codeless GNSS-R, and rGNSS-R stands for reconstructed GNSS-R.

Instrument Name	Type	Receiver Type	Technique	Bands	Antennas	Application
DMR	Air	Hw	cGNSS-R	L1	D: RHCP R: LHCP	Wind Speed [64] Soil Moisture [74]
-	Ground	Hw	IPT	L1	D: RHCP	Elec. Permittivity [54] Sea Height [72]
TurboRogue GPS	Ground Air	Hw	cGNSS-R, sGNSS-R	L1, L2	D: RHCP R: LHCP	Phase Altimetry [113] Sea Height [86] Semicodeless Processing [48]
-	Ground	Sw	cGNSS-R	L1	D: RHCP R: LHCP	Sea Altimetry [12]
Eddy	Air	Sw	cGNSS-R	L1	D: RHCP R: LHCP	Significant Sea Height [87] Mean Sea Level [87]
SGR (UK-DMC)	Space	Hw/Sw	cGNSS-R	L1, L2	D: RHCP R: LHCP	Wind Speed [88]
GORS	Ground Air	Hw	cGNSS-R	L1, L2, L5, E1	D: RHCP R: LHCP	Altimetry [91]
-	Ground	Hw	IPT	L1	D: RHCP	Soil Moisture [78]
SMIGOL	Ground	Hw	IPT	L1	H: V,H	Soil Moisture [56] Vegetation Height [24] Snow Monitoring [83] Water Height [69] Wave height [92]
GOLD-RTR	Air Ground	Hw	cGNSS-R	L1	D: RHCP R: LHCP, RHCP	Polarimetry [95] Sea Ice, Dry Snow [96] Snow Layers [82] Phase Altimetry [97]

Table 2.3 continued from previous page

Instrument Name	Type	Receiver Type	Technique	Bands	Antennas	Application
PIR	Ground	Hw	iGNSS-R	L1	D: RHCP R: LHCP	Sea Altimetry [98]
LEiMON	Ground	Hw	cGNSS-R	L1	D: RHCP R: LHCP, RCHP	Soil Moisture [77] Biomass [99]
-	Ground	Sw	cGNSS-R	L1, L5	D: RHCP R: LHCP	Altimetry [100]
PYCARO	Ground Air	Hw	cGNSS-R, rGNSS-R	L1, L2, E1	D: RHCP R: LHCP, RCHP	Biomass [26]
SGR-ReSI (TDS-1)	Space	Hw	cGNSS-R	L1, L2, L5	D: RHCP R: LHCP	Wind Speed [112] Phase altimetry [114]
SPIR	Air	Sw	cGNRR-R, iGNRR-R	L1, E1, L5, E5	D: RHCP R: LHCP BS	Altimetry [101]
DDMI (CYGNSS)	Space	Hw	cGNSS-R	L1, L2	D: RHCP R: LHCP	Wind Speed [115]
MIR	Air	Sw	cGNRR-R, iGNRR-R	L1, E1, L5, E5	D: RHCP R: LHCP BS	-

2.4 Distance Measurement Equipment/TACTial Air Navigation Signals

GPS L5, and the Galileo E5 bands (1,164 MHz - 1,217 MHz) are shared with two wide extended aerial radio navigation systems: the Distance Measurement Equipment (DME) (civilian), and TACTical Air Navigation (TACAN) (military), both transmitting in the band from 962 MHz to 1,213 MHz, divided in 1 MHz channels [116]. Both systems are based on the time delay to determine the distance between an aircraft, and a transponder. When a plane interrogates a station, it transmits a sequence of pairs of pulses with an average pulse repetition frequency of 27 pulses per second at the frequency channel assigned to the transponder. When a pair of pulses reaches the DME/TACAN station, it is retransmitted at a different frequency channel after a given delay, depending on the channel and the coding assigned to each transponder. The distance to the station is then estimated from the elapsed time between the transmission and the reception of the pulse t_0 , the plane height, and the delay at the station t_D , as illustrated in Fig. 2.8a.

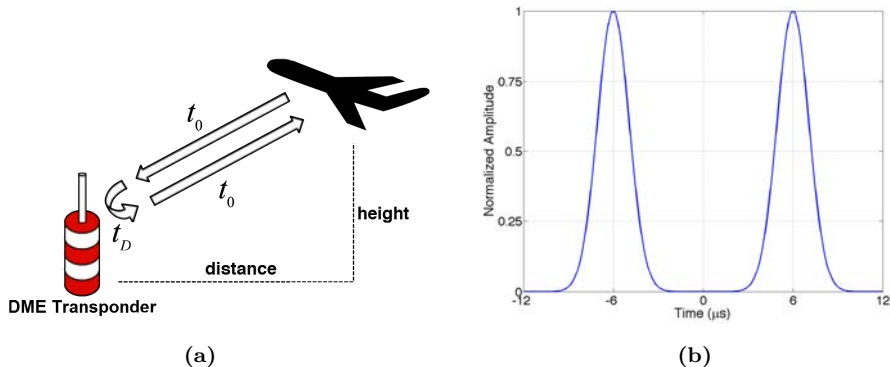


Figure 2.8: a) Simplified DME concept, and b) DME pulse shape.

DME signals (see Fig. 2.8b) consist of pairs of Gaussian pulses of $12 \mu s$ length with the following expression:

$$s(t) = \left(e^{-\frac{\alpha}{2}(t-\frac{\Delta t}{2})^2} + e^{-\frac{\alpha}{2}(t+\frac{\Delta t}{2})^2} \right) \cdot \cos(2\pi f_c t + \phi) \quad (2.3)$$

where $\alpha = 4.5 \cdot 10^{11} s^{-2}$, f_c is the channel frequency, and Δt is the time separation between pulses, which is determined by the operation mode and the coding. The operation modes, Distance Measurement Equipment - Navigation (DME/N) and Distance Measurement Equipment - Precise (DME/P), are used to provide different levels of accuracy appropriate for each flying operation. DME/N is used for on route navigation, and has an accuracy of 370 meters. DME/P is used for precise operations such as airport approaching (Initial Approach or DME/P IA, with an accuracy from 370 to 85 meters), and landing (Final Approach, or DME/P FA, with an accuracy down to 12 meters). The codes, X and Y, allow to reuse each frequency channel. DME transponders have an assigned channel from among the 126 existing, and a coding. The assigned transmitting and receiving

Table 2.4: DME transmitting and receiving frequencies (from the airplane point of view).

Coding	Channel	Transmitting Frequency (MHz)	Receiving Frequency (MHz)
X	1 → 63	1,025 → 1,087	962 → 1,024
	64 → 126	1,088 → 1,150	1,151 → 1,213
Y	1 → 63	1,025 → 1,087	1,088 → 1,150
	64 → 126	1,088 → 1,150	1,025 → 1,087

frequencies are fixed and can be seen in Table 2.4. Stations using the X coding and channels from 77 to 126 retransmit the received signals at frequencies from 1,164 MHz to 1,213 MHz, where the L5 and E5 bands are allocated. The time separation between pulses for the interfering transponders is $\Delta t = 12 \mu s$ [116]. Airplanes transmit out of the GNSS band (1,025 - 1,150 MHz), as well as stations with Y coding.

According to [117]¹, from a total of 4,000 DME/TACAN stations, more than 2,500 are assigned to the 77 - 126 channels in X mode (see Fig. 2.9).

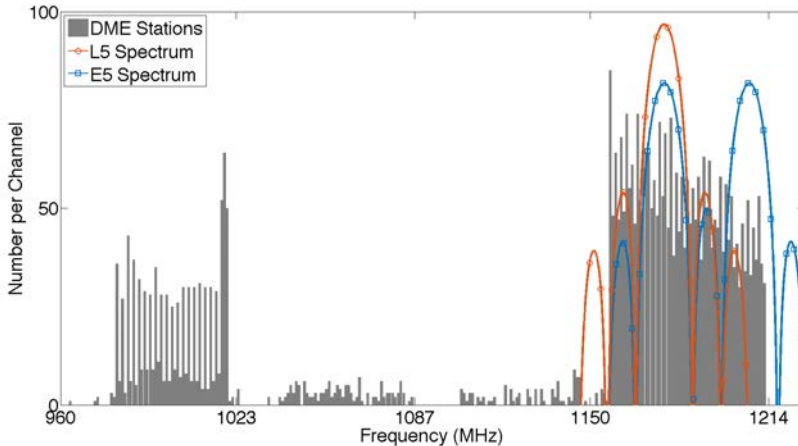
**Figure 2.9:** DME channel allocation (grey), L5 spectrum (orange) and E5 spectrum (blue).

Figure 2.10 shows that North America, Europe, and the East Asia are the regions with the highest density of DME/TACAN stations; therefore these regions are specially susceptible to RFI.

2.5 Conclusions

This chapter has summarized how GNSS work, the signals that they use and their characteristics. Then, since these signals were proposed for Earth Observation for first

¹There are no official public world databases of Radio Navigation Aids since the Digital Aeronautical Flight Information File (DAFIF) was closed in 2006. However, several unofficial databases have appeared, such as OurAirports, which mixes multiple official regional sources in a single database.

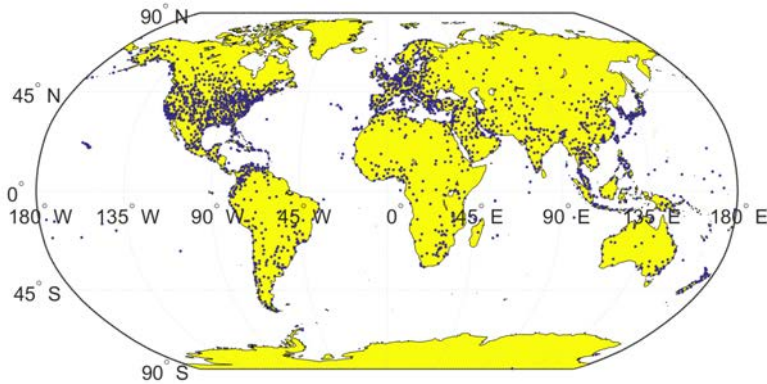


Figure 2.10: DME station's locations (from [117]).

time, many applications have been proposed: from soil moisture estimation, to snow thickness determination, or sea altimetry. All the instruments that presented a novelty, or at least the ones that the author is aware of, have been listed. Last, the DME/TACAN radio navigation systems have been explained and why they might interfere with GNSS-R instruments.

3

Chapter 3

Instrument Precursors

3.1 Introduction

This chapter presents the main contributions to other instruments developed in parallel to the MIR instrument. The first experiment was a GNSS-R instrument called PYCARO developed during 2013. The author was in charge of designing, manufacturing, and testing the antenna arrays and the RF conditioning system. This experiment was the first time the author was able to compare the simulated and measured patterns of an antenna array. Then, an RFI detector and locator for GNSS/GNSS-R was developed during 2016-2017 to obtain experience about RFI detection and mitigation in order to later apply it to the MIR instrument data, however the data processing of the instrument did not advance enough to be applied. Last, during 2017 the author contributed to the HUMIT project from Institut Cartogràfic i Geogràfic de Catalunya (ICGC) by setting up the CORTO reflectometer for a field campaign and designing the structural element to hold the down-looking antennas fuselage. The ICGC offered the author to carry onboard the plane other GNSS-R instruments if desired, so Multiband Airborne L-Band reflectometry with GNSS-r (MALYGNSS), a L1 and L2 GNSS-R instrument, was developed to test the data sampling blocks of the MIR instrument. The flight was also useful to acquire experience about field campaign planning.

3.2 P(Y) C/A Reflectometer at BEXUS 17/19 Stratospheric Balloon Experiment

PYCARO was a L1 C/A and L1 P(Y) GNSS-R instrument part of the Ph.D. thesis of Dr. Hugo Carreño-Luengo “Contributions to GNSS-R Earth remote sensing from

nano-satellites” [118, p. 133-156]. It was carried onboard the BEXUS 17 and BEXUS 19 stratospheric balloons, an educational project from the ESA, the Deutsches Zentrum für Luft- und Raumfahrt - German Aerospace Center (DLR), and the Swedish National Space Agency (SNSA). This experiment was a proof of concept for a later cubesat mission called ³Cat-2 that was finally launched on 15 August 2016. The author contributed to the antennas and the RF part of the experiment carried on the BEXUS 17. The up-looking antenna (see Fig. 3.1) was made of a L1 RHCP patch [119] and a L2 RHCP patch combined and then amplified. The down-looking array (see Fig. 3.2) was made of six L1 LHCP patches and six L2 LHCP patches combined by frequency band, then amplified, and then both bands were combined as shown in Fig. 3.3. The antennas were mounted inside extruded polystyrene foam radomes, and both the Printed Circuit Boards (PCBs) and the antennas had temperature sensors and heaters due to expected temperatures below -40 °C. The GNSS receiver had two inputs. The main one was connected to the up-looking RHCP antenna, while the secondary input was connected to a switch that allowed to select the up-looking antenna or the down-looking LHCP array. First, the auxiliary channel of the GNSS receiver received the up-looking signal. When it got locked to it, the system switched to the down-looking signal, thus easing the receiver to get locked to the reflected signal.

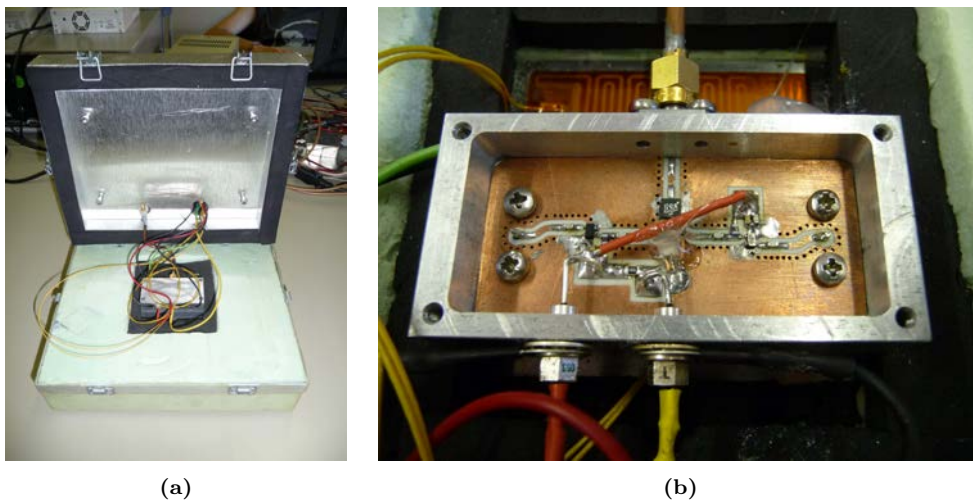


Figure 3.1: a) Back part of the Bexus up-looking antenna, and b) detail of the PCB.

The temperature response of the antennas was measured from ambient temperature down to -58 °C by covering the back part of the antenna ground plane with dry ice (see Fig. 3.4) and then measuring the S-Parameters. Figure 3.5 shows how the antenna resonance drifts to higher frequencies at L1, but seems not to change at L2.

Once built, the radiation patterns of both antennas were measured at the anechoic chamber (see Fig. 3.6). The measured directivities for the up-looking antenna are 6.3 dB and 5.7 dB at L1 and L2 frequency bands, respectively, and for the down-looking array are 13.4 dB and 11.5 dB at L1 and L2 frequency bands, respectively.

The stratospheric balloon was launched on 10 October 2013, from the Erange space

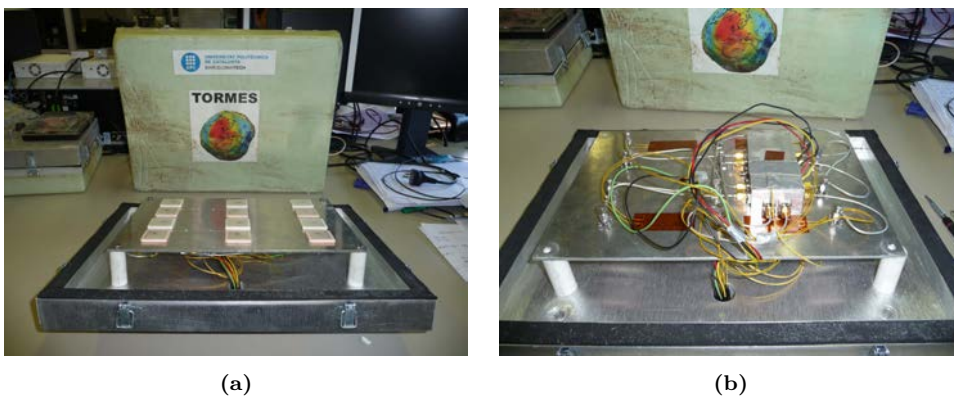


Figure 3.2: a) Front part of the Bexus down-looking antenna, and b) detail of the combiner box attached behind the ground plane.

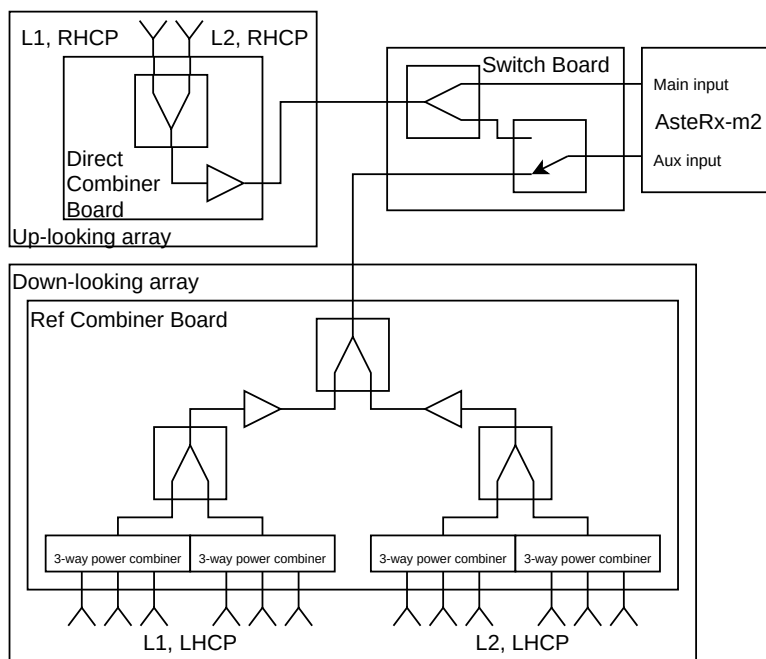


Figure 3.3: PYCARO simplified schematic in the BEXUS 17 experiment.

facilities in northern Sweden. A technical issue in the balloon-ground link prevented the full exploitation of the instrument, but still some results were obtained [120,121].



Figure 3.4: Measurement of the BEXUS antennas temperature matching response.

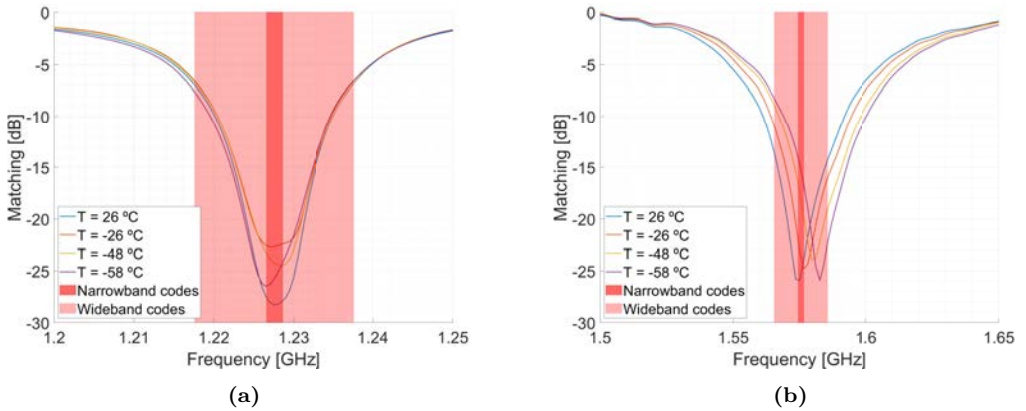


Figure 3.5: BEXUS antenna temperature response at a) L2, and b) L1 frequency bands. In dark red, the narrow band code allocation. In clear red, the wide band code allocation.

3.3 L band RAdiometer and Radio Occultations

The L band RAdiometer and Radio Occultations (L-RARO) instrument is an L band instrument meant to be used both as a radiometer for RFI detection and location, and for GNSS-RO, but that finally was used just for the first use. The RFI detector required high sensitivity, so a radiometer architecture was chosen. It also required temperature control since high accurate radiometers do. It is part of the Ph.D. thesis of Dr. Jorge Querol Borrás “Radio frequency interference detection and mitigation techniques for navigation and Earth observation” [31, p. 103-123].

The instrument consisted of an array of two GPS L1 patch antennas like the ones used in the PYCARO instrument (see Section 3.2) separated $\lambda/2$ connected to RF Front-ends followed by a low-cost COTS Software Defined Radios (SDRs). The antennas were summed in phase for the detection, and in counter-phase for the location using a 180° hybrid coupler made of a 90° hybrid coupler with a 90° transmission lines in of the inputs. The resulting radiation patterns can be seen in Fig. 3.7. The in-phase output of the hybrid

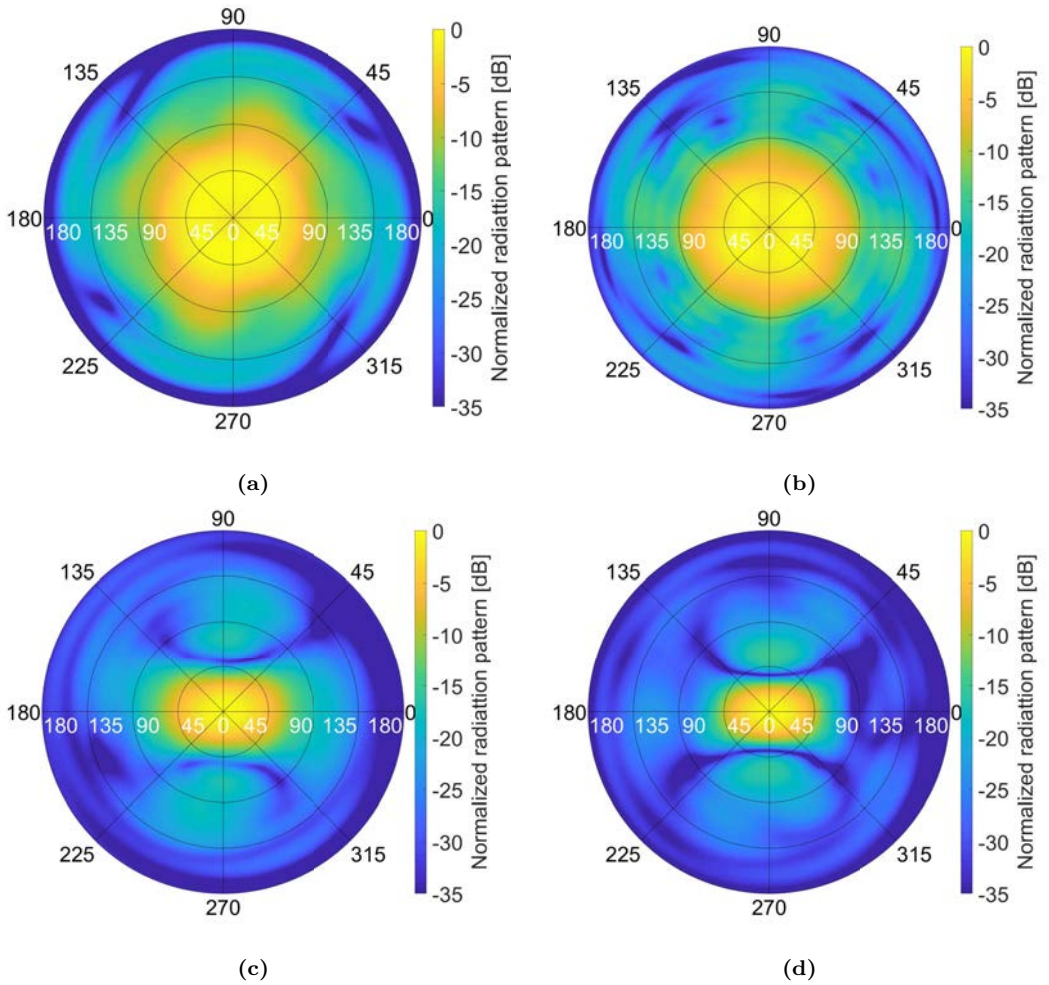


Figure 3.6: BEXUS measured radiation patterns: a) up-looking antenna at L2, b) up-looking antenna at L1, c) down-looking array at L2, and d) down-looking array at L2 frequency bands.

(see Fig. 3.7a) creates a beam with 53.3° beamwidth at -3 dB, and a directivity of $D \approx 8.2$ dB. The counter-phase output of the hybrid (see Fig. 3.7b) has a sharp null at the boresight of the antenna with a width of approximately 8.2° at -20 dB.

Each output of the 180° hybrid coupler is connected to a RF Front-end, whose schematic can be seen in Fig. 3.8. The Front-end (see Fig. 3.9b) has an absorptive calibration switch at the input with $IL \approx 0.8$ dB of insertion losses, which allows to commute to a match load at the ambient temperature. Then, the signal is amplified with an Low-Noise Amplifier (LNA) with $G \approx 19$ dB and $NF \approx 0.65$ dB. The signal is then band-pass filtered at L1 frequency band with 2 MHz bandwidth, amplified again, and split using a directional coupler. The direct line is used for the radiometric measure-

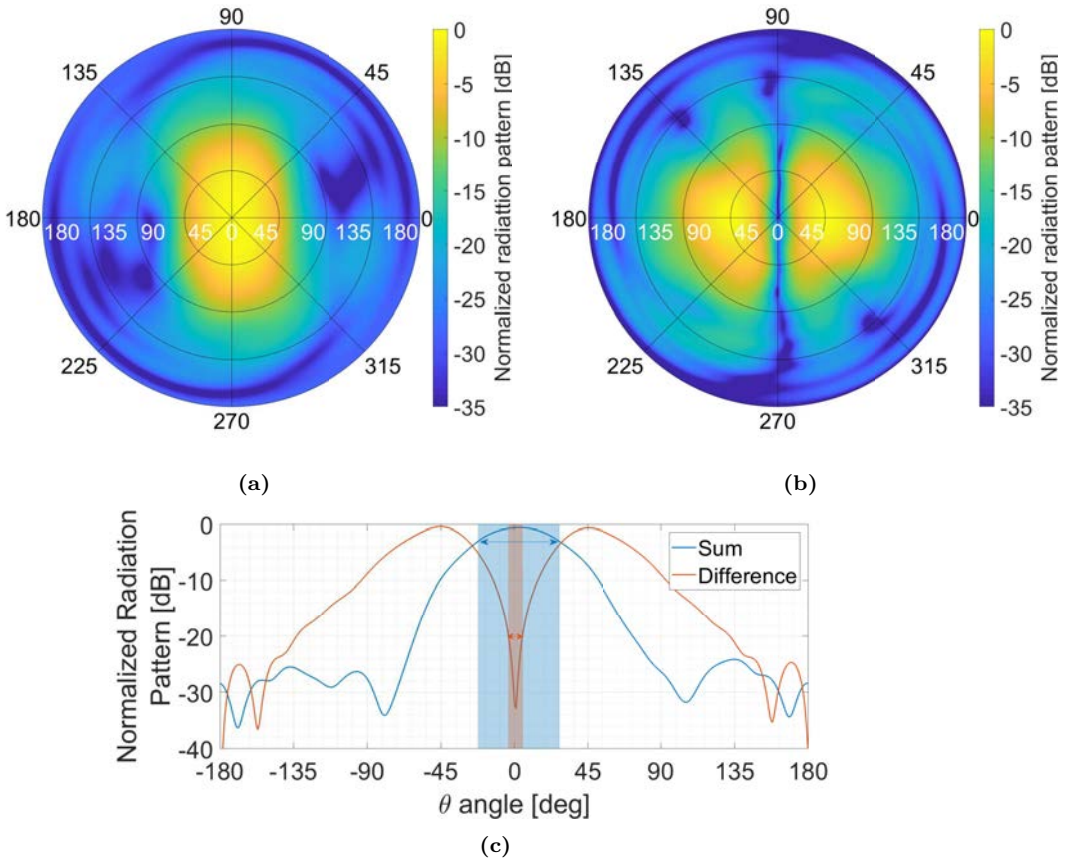


Figure 3.7: a) Detection radiation pattern, b) Geo-location radiation pattern, and c) cut $\varphi = 0^\circ$ in both radiation patterns to measure the beam and null widths.

ments, while the coupled line was supposed to be used for the radio occultations, but is finally unused and is currently connected to a matched load. The radiometric output is sampled at 2.048 Msps with 8 bits I/Q using a COTS TV tuner hacked to be used as an SDR.

The instrument blocks are mounted behind the antenna ground plane as shown in Fig. 3.9a (the ground plane has been turned upside down to show the back part), which is mounted inside an extruded polystyrene foam radome reused from an older L band radiometer. The instrument has several temperature sensors in the RF Front-ends in the ground plane, and in the SDRs; a 220 V 60 W heater; and a fan over the heater used to distribute the generated heat, thus homogenizing the temperature gradient along the instrument.

A customized Arduino Proportional–Integral–Derivative (PID) controller stabilized the instrument temperature switching a heater with a 220 V relay controlled by the Pulse Width Modulation (PWM) output of the Arduino board. The temperature controller

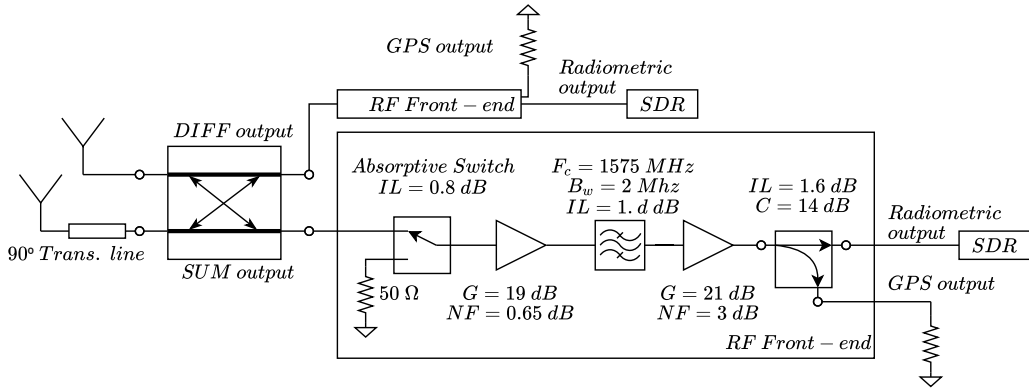
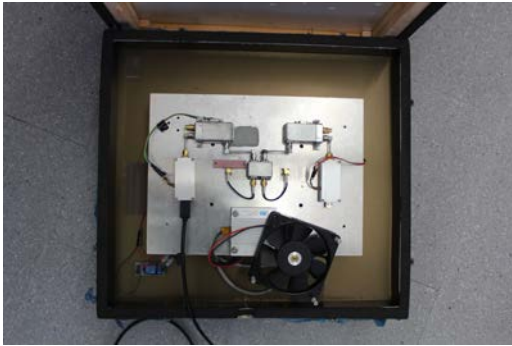
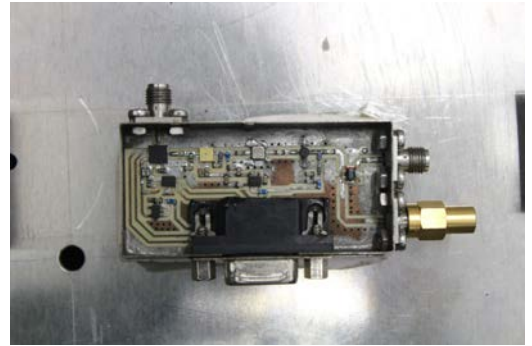


Figure 3.8: L-RARO block schematic.



(a)



(b)

Figure 3.9: a) L-RARO back part of the antenna ground plane, and b) one of the RF Front-ends.

performance was analyzed by setting a desired temperature in order to measure how much time it would take to stabilize, and the ripple around that temperature. An experiment was carried out during the winter. Fig. 3.10 shows the temperatures recorded how the PID took less than 15 minutes to stabilize the ground plane temperature at $44\text{ }^{\circ}\text{C}$ with an error lower than $0.25\text{ }^{\circ}\text{C}$. A window was open for 15 minutes 1 hour 26 minutes after the beginning of the experiment in order to suddenly decrease the room temperature and to study the response to sudden variations of the temperature. The instrument temperature was affected, but the PID could compensate it introducing a ripple in the instrument temperature smaller than $\pm 0.5\text{ }^{\circ}\text{C}$.

The instrument was calibrated as a TPR. First, the Noise Equivalent Bandwidth (NEB) of the whole RF chain was estimated by measuring the transfer function of the RF chain. To do so, several chirp signals injected to the input antenna port of the RF Front-ends were sampled by the SDR at 2.048 Msps and at a central frequency of 1575.42 MHz. Three chirps overlapped 50% in the frequency domain were generated: 1573.372 - 1575.42 MHz, 1574.396 - 1576.444 MHz, and 1575.42 - 1577.468 MHz. Figure 3.11 shows

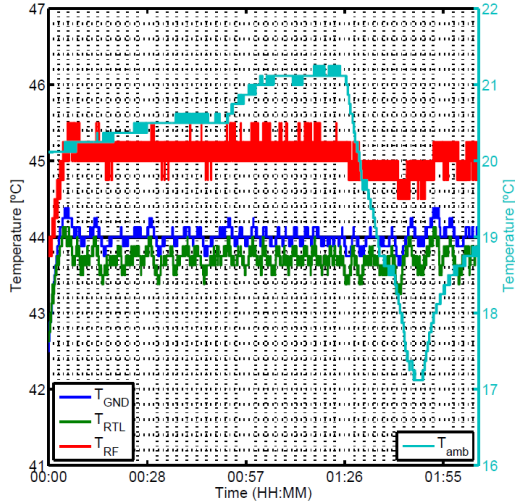


Figure 3.10: L-RARO PID temperature performance. The blue line is the ground plane temperature, the one used as reference by the PID, which is set to be 44°C . The red line is the RF Front-end temperature. The green line is the SDR temperature. The clear blue is the room temperature. From [31, p. 103-123].

the measured transfer functions for both RF chains. The red lines mark the limit without aliasing with respect to the central frequency. Outside the figure limits, the transfer function is flat and approximately -30 dB , therefore it is not shown. The obtained NEB is 1.8 MHz in both RF chains, and the full band sensitivity approximately -108 dBm , with a noise power resolution of approximately -138 dBm [31, p. 103-123]. An external signal generator is used to generate a continuous wave with increasing power which is used to calibrate the linearity of the of the system and remove its offset. Also, during the operation mode, the system periodically samples the calibration matching load, which is used to compensate the transfer function shape of the RF chain. Deeper information in the calibration procedure, tests, and results can be found in [31, p. 105-125].

3.4 Multiband Airborne L band reflectometry with GNSS-R

This section is adapted from the previously published work “Preliminary altimetry results of the MALYGNSS instrument in the HUMIT project” [122].

MALYGNSS is a dual-band reflectometer designed as a preliminary experiment for the MIR instrument flying as an opportunity sensor in the HUMIT project from ICGC, together with the CORTO instrument [123] (a compact and autocalibrated version of the LARGO GNSS reflectometer [25]), a thermal camera (TASI), an hyperspectral camera (AISA), and an L band radiometer at 1.4 GHz (ARIEL) [124]. The MALYGNSS instrument aims to validate different blocks of the MIR instrument, and to gather data to validate the CORTO soil moisture datasets.

The MALYGNSS instrument (see Fig. 3.12) is a dual-channel software defined ra-

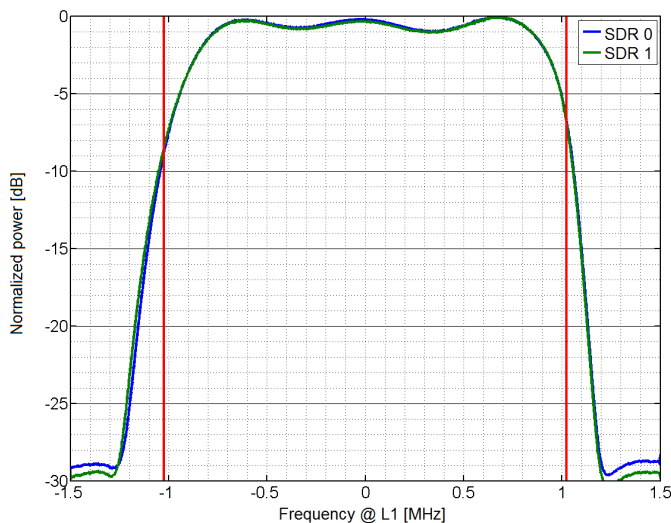


Figure 3.11: L-RARO measured transfer functions (from [31, p. 103-123]). The x-axis shows the frequency difference with respect to the central frequency (1575.42 MHz). The red lines show the limit without aliasing.

dio Universal Software Radio Peripheral (USRP) X310 with DBSR2 daughterboard that samples synchronously the signal from the direct and the reflected antennas, and stores the data for later post-processing. The instrument samples data at 8 Msps and 16 bits in intervals of 60 seconds when it is triggered. It samples data alternating between the GPS L1 and L2 frequency bands. The SDR has a Global Positioning System Disciplined Oscillator (GPS-DO) that provides accurate timestamps, and a 10 MHz reference signal.

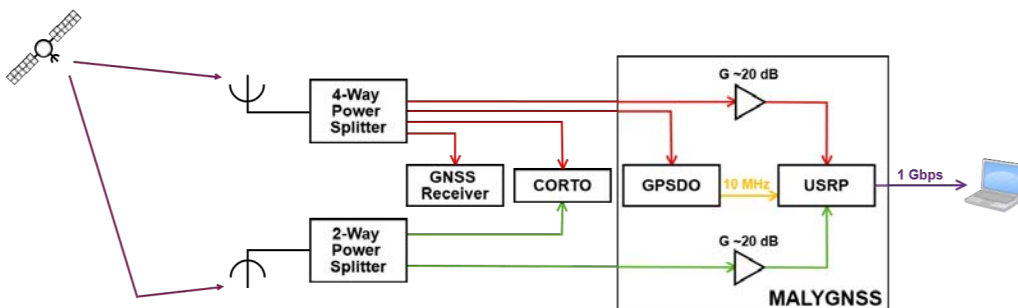


Figure 3.12: MALYGNSS instrument block diagram.

The direct and reflected signals from the satellites are received with two active antennas ($G \sim 40$ dB), one RHCP on the top of the aircraft (Sensors System 67-1575-96 [125]), and one LHCP on the bottom of it (Antcom 42G1215RL-AA-XT-1 [126], see Fig. 3.13b). The direct signal is first split, and then feeds a position and attitude determination GNSS receiver (Trimble BD982 [127]), the GPS-DO, the CORTO direct receiving channel, and the MALYGNSS direct receiving channel (previously amplified with a MAR-6+ $G \sim 20$ dB [128]). The GNSS receiver is used not only to provide accurate positioning but also

the Doppler frequency of the GNSS satellites, which facilitates the post-processing of the L2CM and L2CL signals. The reflected signal is analogously split to feed the CORTO reflected receiving channel, and the MALYGNSS reflected receiving channel after being amplified.

A preliminary field campaign was performed on 30 November 2017 on board a Cessna Caravan (see Fig. 3.13a). Two regions were studied. The first one was in Balaguer (Lleida), 150 km northwest of Barcelona, Spain. There, ten different types of farm fields were studied. From each field, three soil samples were taken with a constant volume probe. Then, the soil moisture and density of each sample was measured. The second area was in Tremp (Lleida), 60 km north of Balaguer. There, four weather stations continuously monitor the soil moisture of different farm fields. Due to bad weather conditions, the latter region was not overflown properly. Last, but not least, data was also sampled over the sea on the way back to the airport. Figure 3.14 shows the first sampling region, with the soil sampling locations (red dots), the flight path when L1 data was captured (green), and the flight path when L2 data was captured (cyan).

A second flight was conducted on October 2019, where the LHCP antenna was replaced by a choke-ring antenna (see Fig. 3.13c) with a higher cross-polar isolation and lower back lobes [129] in order to reduce the direct signal leakage in the reflected antenna, minimizing the chances that the CORTO reflectometer gets locked to the direct signal.

The main goal of the experiment was to test the SDRs to be used in the MIR instrument. The obtained data allowed researchers to start developing the codes for the data processing. Also, the experiment allowed to recognize in advance issues to be addressed in the MIR instrument, such as time stamping, or a Doppler frequency difference between the GNSS receiver and the apparent Doppler frequency in the sampled data. Besides, by testing the processing codes some preliminary results were obtained.

The DDM was computed for the direct and the reflected signal. Then, the difference between the pseudoranges [130] was coarsely estimated as the difference the peak delays of the reflected signal $\tau_{Ref_{MAX}}$ and the direct one $\tau_{Dir_{MAX}}$:

$$\widehat{\Delta\rho_s} = \tau_{Ref_{MAX}} - \tau_{Dir_{MAX}} = 2 \cdot h \cdot \sin(\theta_e), \quad (3.1)$$

The pseudorange difference is proportional to the height h of the receiver over the surface where the wave was scattered, and the sine of the elevation angle θ_e . Figure 3.15 shows the coarse estimation of $\widehat{\Delta\rho_s}$. The upper graph corresponds to the first dataset, which has been cross-correlated with L1 C/A code with 1 ms coherent integration time and two different incoherent averaging times (50 ms in blue, 200 ms in red). The lower graph corresponds to the second dataset, which has been cross-correlated with an L2CM code with 20 ms coherent integration time and two different incoherent averaging times (50 ms in blue, 100 ms in red). The DDM peak has still to be interpolated in order to reduce the ambiguity of the sampling period.

In addition, the results over sea presented in [131] show that reflected signals were received with high SNR, making possible to track the cross-correlation peak phase in both L1 and L2 bands.

RFI was found in all the datasets, and the impact of these signals and how RFI mitigation improve the results is studied in [132].



(a)



(b)



(c)

Figure 3.13: a) Aircraft where the instrument was mounted, down-looking antennas mounted in a fuselage hole in the b) the first flight, and c) second flight.

3.5 Conclusions

This chapter has presented the contributions to three instruments that were developed in parallel to the MIR instrument, and the acquired knowledge that was used later on the main instrument of this Ph.D. thesis: the PYCARO instrument was useful for the antenna array simulation and test, and for the RF design and test; the L-RARO instrument will be useful for RFI detection and mitigation once the data processing advances; and last, the MALYGNSS instrument was useful to test the data sampling system of the MIR instrument. All of them taught valuable lessons for the development of this thesis.

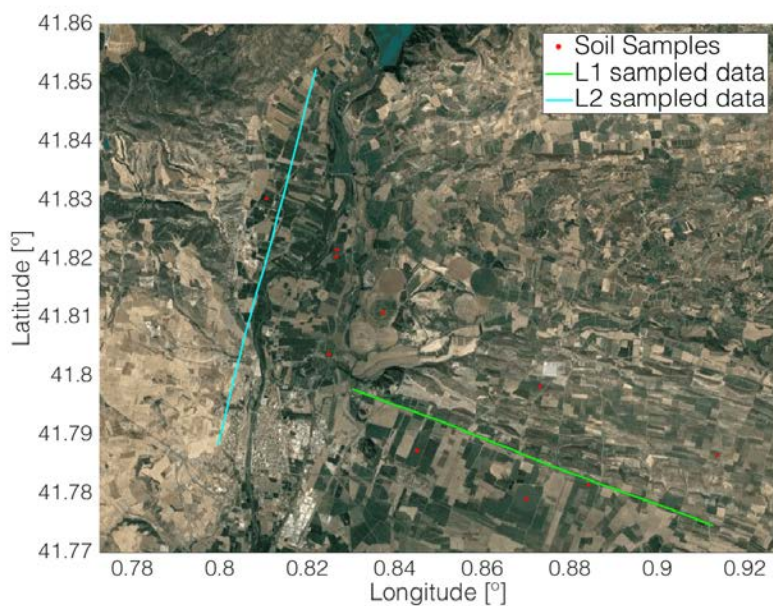


Figure 3.14: First sampling region of the HUMIT field campaign, with the soil sampling locations (red dots), the flight path when L1 data was captured (green), and the flight path when L2 data was captured (cyan).

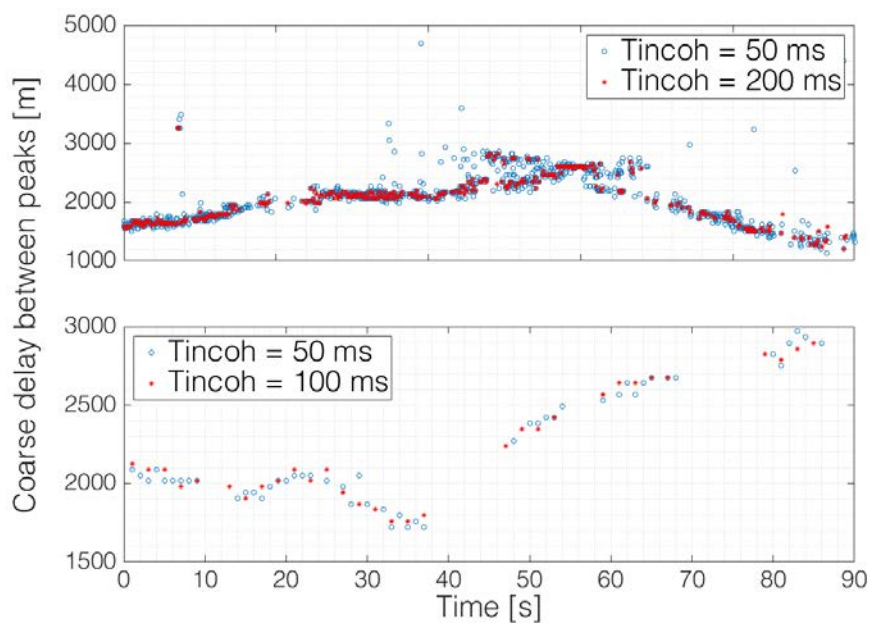


Figure 3.15: Delay difference between the correlation peaks of the direct and the reflected signals in L1 C/A (up), and L2CM (down).

Part II

Instrument Design, Implementation, Calibration, and Characterization

4

Chapter 4

Instrument Principles of Operation

4.1 Introduction

The MIR instrument was designed to track up to four different satellites, two at L1/E1, and two at L5/E5a frequency bands. In order to point these satellites, the instrument first needs to choose which satellites to point (section 4.2). Then, the instrument determines where the satellites and the approximate location of the specular reflection point are. These location are computed in the local coordinate reference system (section 4.3) taking into account the position of the satellites, and the position and attitude of the instrument, provided by a GNSS receiver, and by an Inertial Measurement Unit (IMU). Then, the system has to determine the required phase and gain at each antenna element (section 4.5) taking into account the calibration parameters. Setting these gains and phases in the beamformers takes a non-negligible amount of time. If it takes too long, the instrument might be pointing far from where the reflection is coming from due to the platform movement. In order to estimate the minimum beam refresh rate to keep tracking the satellites, section 4.6 analyzes three previous flights of the chosen airplane for the field campaign.

4.2 Satellite Selection Algorithm

In order to determine which satellites to point, the MIR instrument runs the algorithm described in Fig. 4.1 every 10 minutes separately for each frequency band. The system prioritizes the selection of one Galileo and one GPS satellites with the highest elevation angle if both elevation angles are over 65° . To do so, the GNSS receiver first provides to the algorithm all the satellites in view, and their elevation angle. Then, the algorithm first checks if there are satellites available. If just one is available, both beams of that frequency

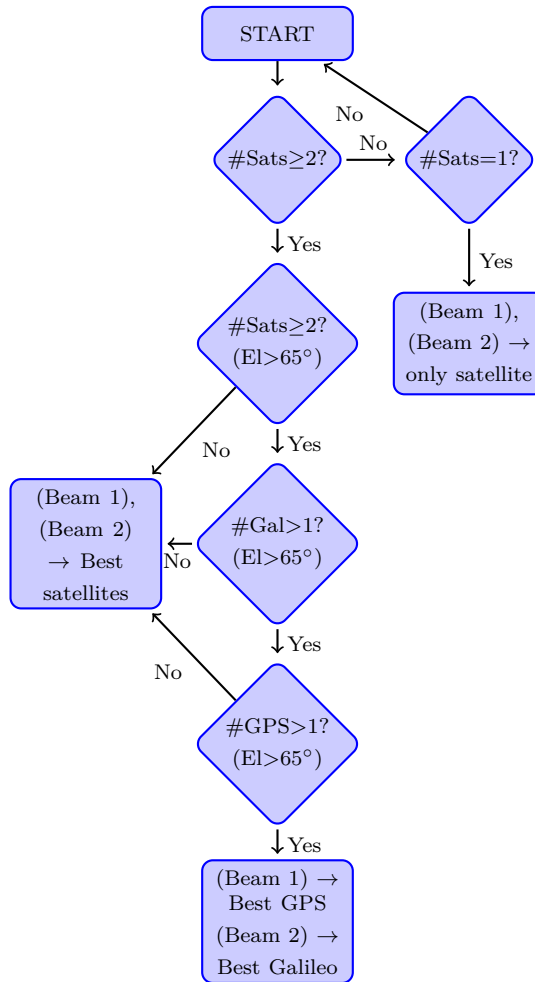


Figure 4.1: Algorithm developed to choose the best satellites available.

band point to it. If there are at least two satellites over 65° of elevation, at least one Galileo satellite over 65° of elevation, and at least one GPS satellites over 65° of elevation, the system points one beam to the GPS satellite with the highest elevation, and the other beam to the Galileo satellite with the highest elevation. If one of the previous conditions is not fulfilled, the system points to the two satellites with the highest elevation despite if they are GPS or Galileo. The system retrieves its position and the GNSS satellites in-view using a GNSS multi-constellation receiver Trimble BD982 [127], which is able to provide as well the satellite's Doppler frequency, but for that purpose it needs to be phase locked to the satellite. For this reason, all satellites whose phase has not been locked are discarded prior to the satellite selection.

Figure 4.2 shows a simulation of the selection algorithm run over satellite data obtained

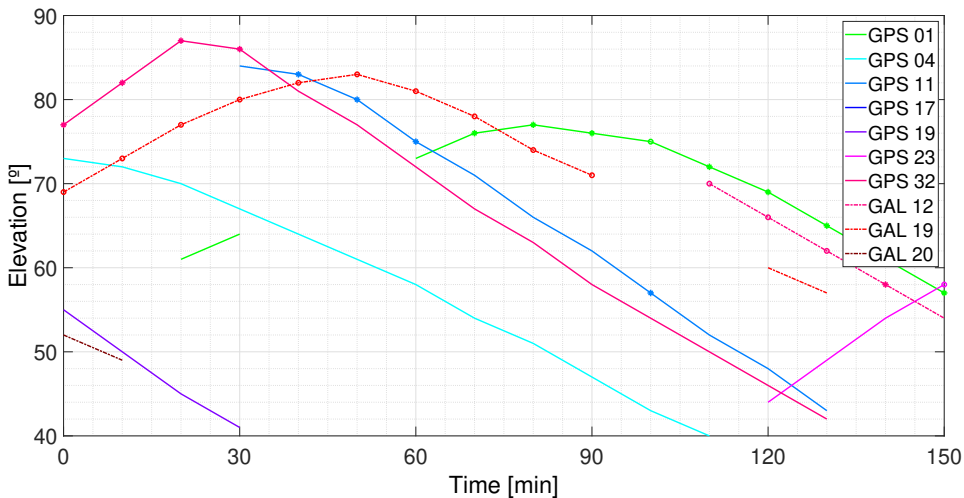


Figure 4.2: Selection algorithm simulation. The lines with dot markers correspond to the satellites that would be tracked.

from the GNSS receiver. The lines with markers correspond to the satellites that would be tracked.

The 10 minutes refresh rate and the 65° values are set in order to avoid the satellite's elevation dropping below 60° . Below this elevation angle, the side lobes of the array are worse than -7 dB to 0 dB at L1/E1 frequency band, and -24 dB to -15 dB at L5/E5a frequency band, depending on the array current distribution (see section 4.4). To obtain these the 10 minutes refresh rate and the 65° elevation mask, the elevation angle of all GPS and Galileo satellites for a random week and for an hypothetical receiver located in Melbourne were computed. Figure 4.3 shows how the satellite elevation would change after 10 minutes as a function of its elevation. The pink vertical line represents the 65° elevation mask, while the red line represents the 60° limit. The figure shows that if a satellite with an elevation of 65° is chosen, after 10 minutes its elevation will not drop more than 5° , so it will not drop below the desired limit. Note that the GPS satellites repeat their orbit twice a day [133], therefore many points in Fig. 4.3a are overlapped. On the contrary, the Galileo satellites repeat their orbit each 10 days [134], so the points in Fig. 4.3b are more dispersed.

The validation of the algorithm was conducted in the laboratory rooftop and the results are shown in subsection 6.3.2.

4.3 Satellite Position and Specular Reflection Point Determination

Once the satellites to be tracked are selected, their position with respect to the instrument have to be determined. To do so, it is first necessary to describe the different coordinate systems used. The transformations between coordinate systems are explained in Appendix E. Then, the relative position of the satellites is computed taking into ac-

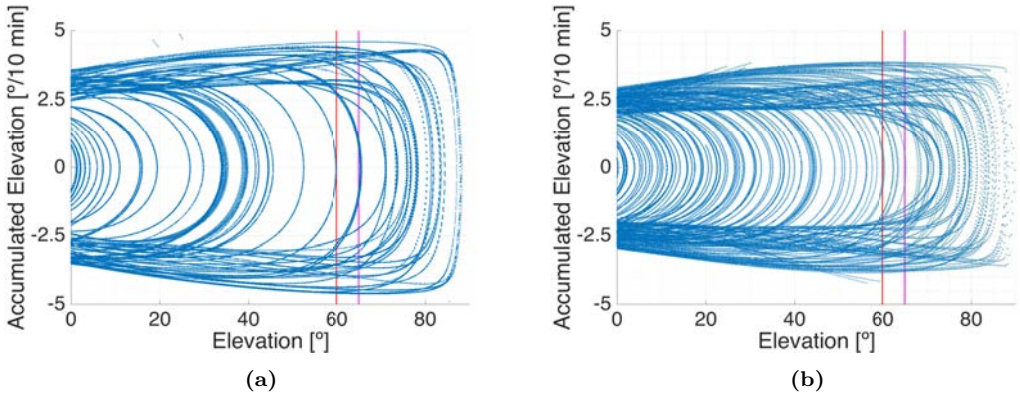


Figure 4.3: Satellite elevation difference after 10 minutes for a) GPS, and b) Galileo satellites. The pink vertical line represents the 65° elevation mask, while the red line represents the 60° limit

count the absolute position of both the satellites and the instrument, and the attitude of the latter.

4.3.1 Coordinate systems

This subsection summarizes the coordinate systems used to properly point to the desired satellites and their specular reflection points [135].

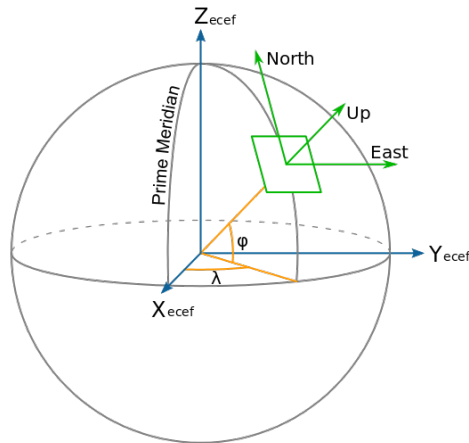


Figure 4.4: ECEF, ENU, and LLA coordinate systems over the WGS-84 reference ellipsoid surface (from [136]).

4.3.1.1 Geodetic coordinate system, or Latitude, Longitude, Altitude

Geodetic coordinate system, also known as Latitude, Longitude, Altitude (LLA), is a coordinate system widely used in navigation to locate a point over a reference ellipsoid's

surface. Three parameters are used to determine the position, two rotation angles and the height over the surface (see Fig. 4.4). The first angle is called latitude (φ) and measures the angle between the equatorial plane and the orthogonal vector to the ellipsoid surface that passes through the desired point. This angle is defined positive towards the North Pole and ranges from -90° to 90° . The second angle is called longitude (λ) and measures the rotational angle between the Prime Meridian and the point. It is defined positive towards the East, and ranges from -180° to 180° . Last, the height h is the distance in meters of the point with respect to the ellipsoid surface along the orthogonal vector to the ellipsoid surface that passes through the point. It is defined positive when the point is “outside” of the ellipsoid. When this coordinate system is used, the chosen reference ellipsoid must be specified, although GPS uses WGS-84 by default as the reference ellipsoid [137].

This reference system is used to locate the instrument and the specular reflection point on the Earth’s surface for mapping purposes.

4.3.1.2 Earth-Centered, Earth-Fixed Coordinate system

The Earth-Centered, Earth-Fixed (ECEF) system is a Cartesian coordinate system that rotates with the Earth and defines the Earth’s center as the origin. The X-axis of the system points towards the 0° latitude and 0° longitude. The Z-axis is aligned with the Earth’s rotation axis and points toward the North. Last, the Y-axis points to 0° latitude and 90° longitude (see Fig. 4.4).

This reference system is used to compute the satellite’s position from its orbital parameters and the given time.

4.3.1.3 Vehicle Carried Tangent Plane Coordinate systems

The Vehicle Carried Tangent Plane Coordinates systems define a Cartesian coordinate system in meters whose origin is located at the center of gravity of the flying vehicle. Two of its axes define a tangential plane to the Earth’s surface and the third one is orthogonal to it. There are two main right-handed systems: North-East-Down (NED), and East-North-Up (ENU) (see Fig. 4.4). The North vector is defined parallel to the meridians and points north. The East vector is defined parallel to the Parallels and points in the East direction. The Down and Up vectors are orthogonal to the reference ellipsoid, and point towards and against the Earth’s surface, respectively.

This reference system is used to compute the relative position of the satellite with respect to the airplane, and also to compute the specular reflection point location when using the flat Earth approximation, but it does not take into account the orientation of the airplane.

4.3.1.4 Body Coordinate system

The Body coordinate system (see Fig. 4.5) is a vehicle-carried Cartesian coordinate system defined on the airplane body and aligned with the flight direction. The X-axis is defined in airplane symmetric plane pointing towards the flight direction. The Y-axis points starboard, that is, the right side of the plane. Finally, the Z-axis is defined downwards. The body coordinate axes match the NED axes when the airplane flights

north parallel to the tangential plane to the reference ellipsoid. When they are not aligned, the rotation angles defined between them are called Euler angles: Yaw, Pitch, and Roll, noted respectively as $\{\psi, \theta, \phi\}$. They are defined as the rotations around the Z-axis, Y-axis, and X-axis, respectively. The rotations are defined positive in the direction shown in Fig. 4.5 and are applied using the rotation matrices $R_3(\psi)$, $R_2(\theta)$, and $R_1(\phi)$ as explained in Appendix F.

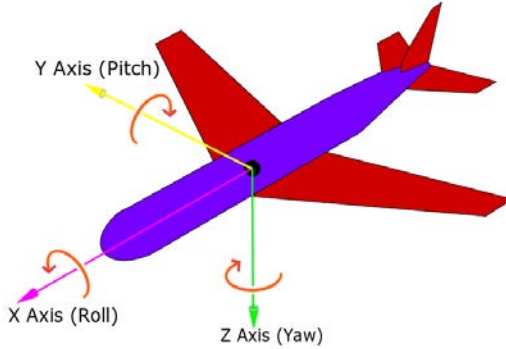


Figure 4.5: Body coordinate systems and rotation angles with respect to the NED coordinate system. Adapted from [138].

4.3.2 Satellite Position and Specular Reflection Point Determination

Once a satellite u to be tracked is selected, its ECEF positions $\{X_u, Y_u, Z_u\}$ are computed as explained in Appendix F. Then, the ECEF vector from the instrument to the satellite \vec{v}_{uECEF} is computed using the ECEF position of the instrument $\{X_r, Y_r, Z_r\}$ as

$$\vec{v}_{uECEF} = \{X_u, Y_u, Z_u\} - \{X_r, Y_r, Z_r\}. \quad (4.1)$$

Then, the ECEF vector to the satellite \vec{v}_{uECEF} is transformed to NED coordinates \vec{v}_{uNED} using the instrument latitude φ_0 and longitude λ_0 , and the rotation matrix $M_{ECEF}^{NED}(\varphi_0, \lambda_0)$:

$$\vec{v}_{uNED} = M_{ECEF}^{NED}(\varphi_0, \lambda_0) \cdot \vec{v}_{uECEF} = \begin{pmatrix} v_{x_uNED} \\ v_{y_uNED} \\ v_{z_uNED} \end{pmatrix}. \quad (4.2)$$

In the NED coordinate system the angle between the projection of a vector on the XY plane and the vector itself (the blue vector in Fig. 4.6) is called elevation angle, and is defined negative towards the Z axis. The angle between the projection of a vector on the XY plane and the X axis is called azimuthal angle and is defined positive from the X axis towards the vector projection. For ground-based experiments and low-altitude flights, the flat Earth approximation can be used to find the location of the specular reflection point d , approximating the azimuth angle of both vectors as equal, and the elevation angles as

the opposites. This approximation is used in the MIR instrument. Figure 4.6 shows the vector pointing to the satellite in blue, the vector pointing to the specular reflection point in red, and their elevation and azimuth angles in their respective colors.

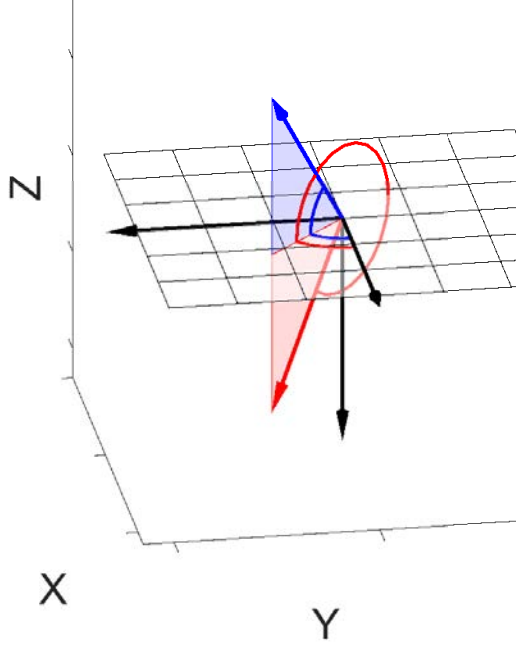


Figure 4.6: Vector pointing to a GNSS satellite in red, and pointing to its specular reflection point assuming flat Earth model in blue, both in NED coordinate system.

In order for the azimuthal angles to match, it can be easily seen in the figure that the x and y components of both vector must satisfy

$$Az_{up} = atan\left(\frac{\vec{v}_{yu}^{NED}}{\vec{v}_{xu}^{NED}}\right) = Az_{down} = atan\left(\frac{\vec{v}_{yd}^{NED}}{\vec{v}_{xd}^{NED}}\right), \quad (4.3)$$

that is, the ratio between the x and y of both vector must match:

$$\vec{v}_{yu}^{NED} = k \cdot \vec{v}_{yd}^{NED} \quad (4.4)$$

$$\vec{v}_{xu}^{NED} = k \cdot \vec{v}_{xd}^{NED}. \quad (4.5)$$

Furthermore, in order for the elevation angles to be the opposite, they must satisfy

$$El_{up} = atan\left(\frac{\vec{v}_{zu}^{NED}}{\sqrt{\vec{v}_{xu}^{NED}^2 + \vec{v}_{yu}^{NED}^2}}\right) = -El_{down} = -atan\left(\frac{\vec{v}_{zd}^{NED}}{\sqrt{\vec{v}_{xd}^{NED}^2 + \vec{v}_{yd}^{NED}^2}}\right), \quad (4.6)$$

which taking into account Eqns. (4.4-4.5) leads to

$$\vec{v}_{z_d^{NED}} = -k \cdot \vec{v}_{z_u^{NED}}. \quad (4.7)$$

The vector $\vec{v}_{u^{NED}}$, in blue, is pointed by the up-looking array, while the vector $\vec{v}_{d^{NED}}$, in red, is pointed by the down-looking one. Both vectors have been computed in the NED coordinate system, but since the down-looking array is pointing downwards, its axes do not match with the NED ones. In the MIR instrument, the down-looking array is oriented like the up-looking one, but rotated π radians around the X axis (roll angle). Figure 4.7a shows the two arrays, the up-looking one in red and the down-looking one in blue, with their corners numbered to ease the view of the array and vector rotations. The NED axes are shown in black, and the down-looking array rotated axes are shown in grey. Note that the X axis of both reference systems are overlapping. The vector pointing to the specular reflection point computed with respect to the NED reference axes is shown in red. The elevation and azimuth angles with respect to the same axes are represented in blue.

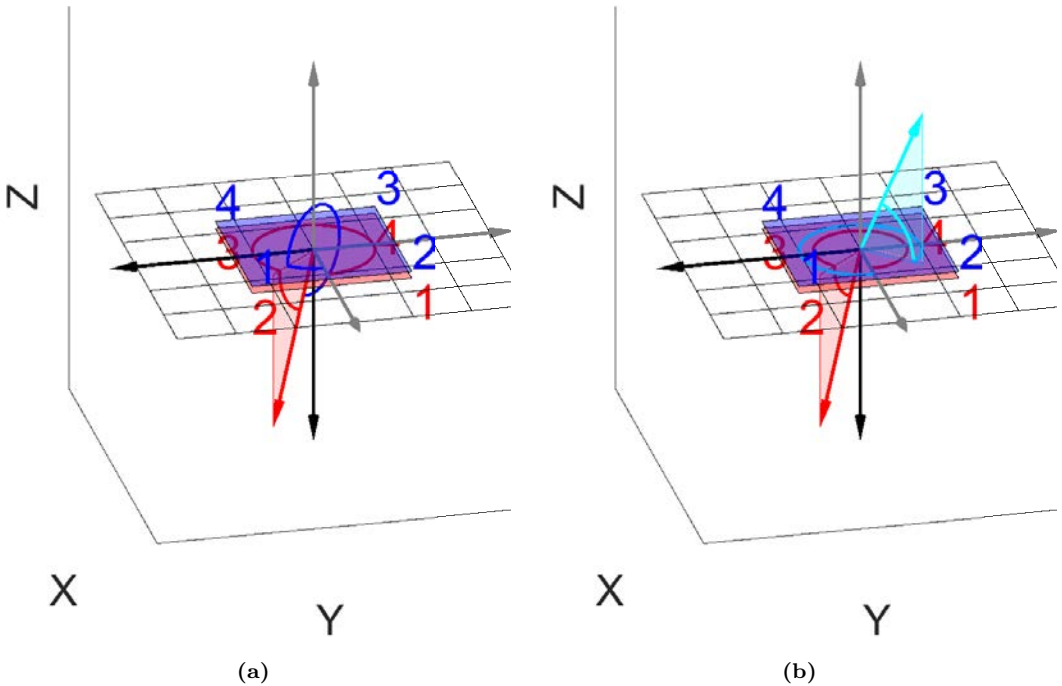


Figure 4.7: Vector pointing to a specular reflection point in red, azimuth and elevation angles with respect to the NED axes in dark blue, azimuth and elevation angles with respect to the down-looking array axes in red, equivalent pointing vector in bright blue, and azimuth and elevation angles of the equivalent pointing vector with respect to the NED axes in bright blue.

Nonetheless, these angles must be computed with respect to the down-looking reference axes, in red in the same figure. To do so, the equivalent pointing vector $\vec{v}_{d'^{NED}}$, shown in bright blue in Fig. 4.7b, is computed by applying a rotation matrix $R_1(\pi)$ to the $\vec{v}_{d^{NED}}$ vector:

$$\vec{v}_{d'NED} = R_1(\pi) \cdot \vec{v}_{dNED}. \quad (4.8)$$

As a result, the azimuths and elevations of the equivalent pointing vector are related to the vector pointing the specular reflection point as

$$Az'_d = 2\pi - Az_d \quad (4.9)$$

$$El'_d = El_d. \quad (4.10)$$

Last, the airplane attitude is taken into account by applying the rotation matrices to the vectors \vec{v}_{uNED} and $\vec{v}_{d'NED}$ to obtain the pointing directions \vec{p}_{uNED} and \vec{p}_{dNED} as shown in Fig. 4.8.

$$\vec{p}_{uNED} = R_1(\phi) \cdot R_2(\theta) \cdot R_3(\psi) \cdot \vec{v}_{uNED} \quad (4.11)$$

$$\vec{p}_{dNED} = R_1(\phi) \cdot R_2(\theta) \cdot R_3(\psi) \cdot \vec{v}_{d'NED} \quad (4.12)$$

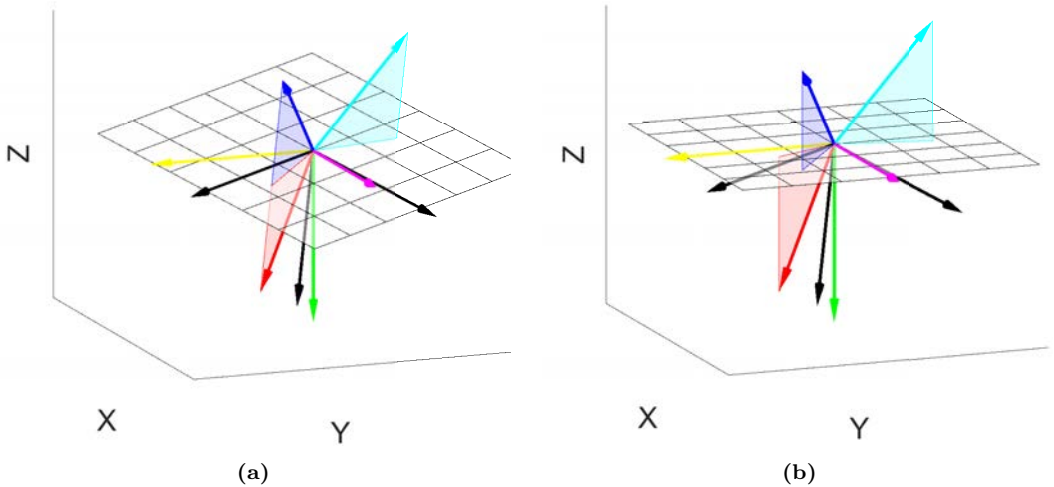


Figure 4.8: Vector pointing to a satellite in dark blue, vector pointing to a specular reflection point in red, and equivalent pointing vector in bright blue. The NED axes are shown in black, and are rotated $\{\psi, \theta, \phi\} = \{15^\circ, 15^\circ, 0^\circ\}$ with respect to the body axes. The body axes are represented in pink (X axis), yellow (Y axis), and green (Z axis). The vectors show its projections over the a) NED grid, and b) body grid.

4.4 Array Pointing

In order to point the antenna arrays to the previously calculated directions, the required amplitude and phase of each antenna element needs to be calculated for both frequency bands, which depends on the array topology, the separation between elements,

and the number of elements. The MIR instrument was designed to mimic the PARIS-IoD instrument [139], and therefore the arrays have 19-elements in a hexagonal distribution. Figure 4.9a shows the antenna element distribution, the baseline vectors \vec{m} and \vec{n} , and the element coordinates in the (m, n) format.

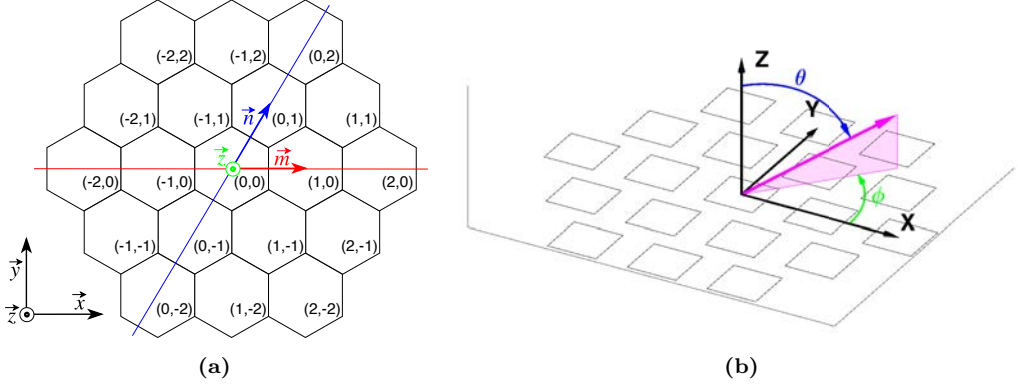


Figure 4.9: a) Array distribution with the element coordinates in (m, n) format, and b) definition of the propagation angles θ and ϕ . The director vectors \vec{m} , \vec{n} , \vec{x} and \vec{y} are shown. The \vec{x} and \vec{y} director vectors have their origin at the array center, but are shown apart in a) for clarity. The angle between \vec{m} and \vec{n} is 60° .

The array factor $AF(\theta, \phi)$ of a bidimensional phased array as function of the direction angles θ and ϕ is [140]

$$AF(\theta, \phi) = \sum_{m,n} I_{m,n} \cdot e^{j\beta_{m,n}} \cdot e^{j\xi_{m,n}}, \quad (4.13)$$

where θ and ϕ are the polar angles defined in Fig. 4.9b, $I_{m,n}$ and $\beta_{m,n}$ are the modulus and phase of each elements' complex weight introduced by the phase array, and $e^{j\xi_{m,n}}$ is the resultant excitation of each antenna caused by an induced electromagnetic field. $\beta_{m,n}$ and $\xi_{m,n}$ can be approximated by

$$\beta_{m,n} = -\frac{2\pi}{\lambda} \cdot (x_{m,n} \cdot \sin(\theta_0) \cdot \cos(\phi_0) + y_{m,n} \cdot \sin(\theta_0) \cdot \sin(\phi_0)) \quad (4.14)$$

$$\xi_{m,n} = \frac{2\pi}{\lambda} \cdot (x_{m,n} \cdot \sin(\theta) \cdot \cos(\phi) + y_{m,n} \cdot \sin(\theta) \cdot \sin(\phi)), \quad (4.15)$$

where θ_0 and ϕ_0 are the angles that define the main beam pointing direction. The $x_{m,n}$ and $y_{m,n}$ coordinates can be written as a function of $m_{m,n}$ and $n_{m,n}$ as

$$x_{m,n} = m_{m,n} + n_{m,n} \cdot \cos(60^\circ) = d \cdot (m + n \cdot \cos(60^\circ)) \quad (4.16)$$

$$y_{m,n} = n_{m,n} \cdot \sin(60^\circ) = d \cdot n \cdot \sin(60^\circ), \quad (4.17)$$

where m and n are the coordinates of each element in Fig. 4.9a. Then, the required phase to point to a desired direction θ_0 and ϕ_0 Eqn. (4.14) becomes

$$\beta_{m,n} = -2\pi \cdot \frac{d}{\lambda} \cdot ((m + n \cdot \cos(60^\circ)) \cdot \sin(\theta_0) \cdot \cos(\phi_0) + n \cdot \sin(60^\circ) \cdot \sin(\theta_0) \cdot \sin(\phi_0)). \quad (4.18)$$

The large separation between antennas of the PARIS-IoD could not be replicated in order to fit in the airplane where it had to be mounted (see Appendix C), and was finally set to 143.13 mm ($0.752\lambda_{L1}$ and $0.561\lambda_{L5}$). According to the current distribution $I_{m,n}$, the beam characteristics vary. Three analyzed current distributions are shown in Fig. 4.10: uniform, triangular, and binomial.

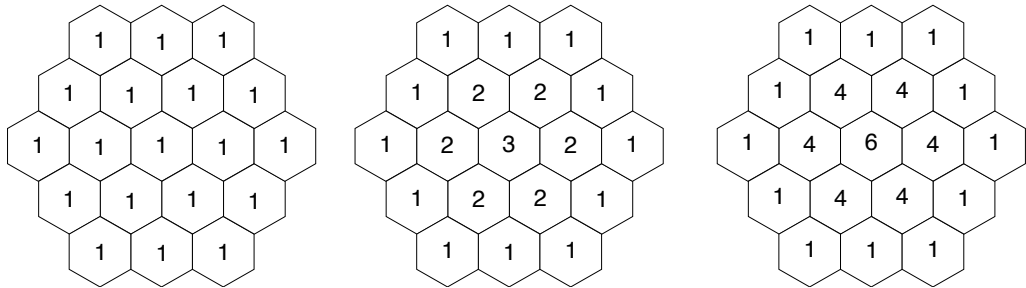


Figure 4.10: From left to right, simulated current distributions: uniform, triangular, and binomial.

Figure 4.11 shows the array factor for the three current distributions (from left to right, uniform, triangular and binomial), at L1/E1 frequency band on top, and at L5/E5a frequency band on bottom. The uniform current distribution is the most directive one ($D = 16.9$ dB at L1/E1, and $D = 14.6$ dB at L5/E5a), the binomial current distribution is the less directive one ($D = 15.5$ dB at L1/E1, and $D = 13$ dB at L5/E5a), and the triangular current distribution stands in between, but closer to the uniform one ($D = 16.7$ dB at L1/E1, and $D = 14.2$ dB at L5/E5a). The secondary lobes are 15 dB, 19 dB, and 24 dB below the main lobe in the uniform, triangular and binomial current distribution cases, respectively, and are equal at both frequency bands.

In order to simulate the φ planes where the side lobes appear, the array factor was simulated pointing far from the boresight, up to $\theta = 75^\circ$ for $\varphi = 0^\circ$, $\varphi = 15^\circ$, $\varphi = 30^\circ$, $\varphi = 45^\circ$, $\varphi = 60^\circ$, and $\varphi = 90^\circ$ angles. Figure 4.12 shows the results with uniform current distribution at L1/E1 and L5/E5a frequency band. Note that the number of side lobes and the φ plane where they are located depends on the pointing direction. For instance, when pointing in the $\varphi = 30^\circ$ or $\varphi = 90^\circ$ planes, only one side lobe appears and it is located in the same plane, however in the other cases two side lobes appear, and they are not necessarily symmetric with respect to the pointing φ plane. It must also be noted that the side lobe location changes from a frequency band to another one, such as for $\varphi = 60^\circ$, where one of the side lobes in L1/E1 is located in between the planes $\varphi = 135^\circ$ and $\varphi = 180^\circ$ (see Fig. 4.12e), while in the L5/E5a case it can be seen between the planes $\varphi = 180^\circ$ and $\varphi = 225^\circ$ (see Fig. 4.12k).

Figure 4.13 shows how the beamwidth increases as the off boresight angle increases. The pink vertical line represents the 30° maximum off-boresight angle according to section 4.2. Below this angle, the minimum achieved beamwidth is 20° at L1/E1 and 27.5° at L5/E5a frequency band. The sudden beamwidth increase between 40° and 60° is caused

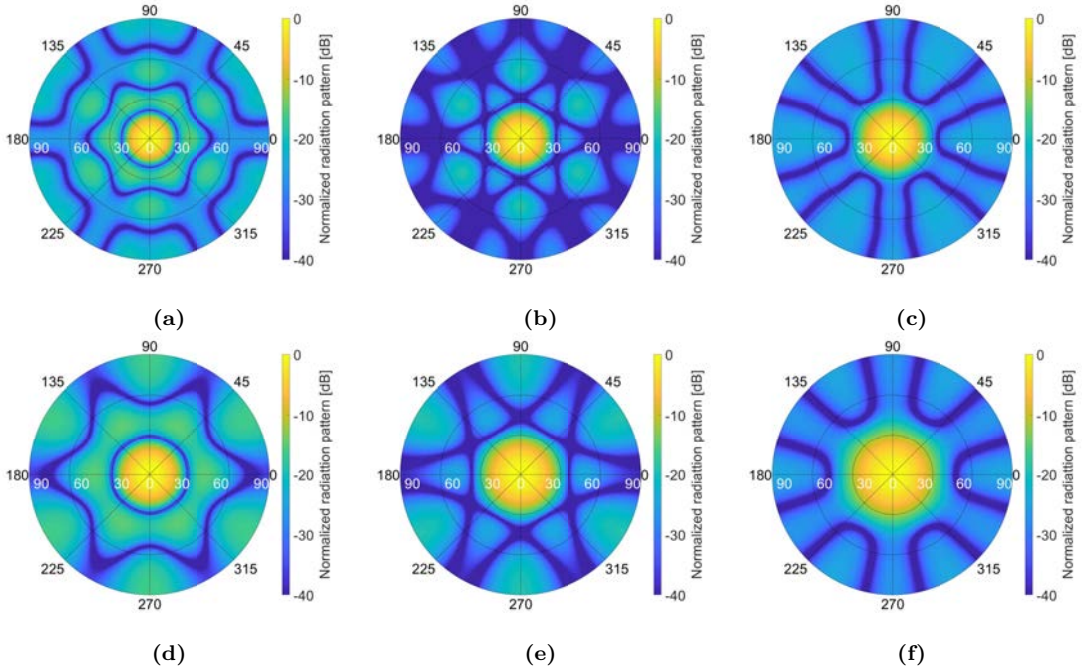


Figure 4.11: Array factor pointing to the boresight at L1/E1 frequency band with a) uniform current distribution and 16.9 dB directivity, b) triangular current distribution and 16.7 dB directivity, c) binomial current distribution and 15.5 dB directivity, and at L5/E5a frequency band with d) uniform current distribution and 14.6 dB directivity, e) triangular current distribution and 14.2 dB directivity, and f) binomial current distribution and 13 dB directivity.

by the back lobe of the array “touching” the main lobe. Figure 4.14 shows the Side Lobe Level (SLL) for the three current distributions and both frequency bands. The uniform current distribution has a lower SLL when pointing to the boresight, but as the off-boresight angle increases, the SLL of the other current distributions raise faster than in the uniform case. Finally, the uniform current distribution was chosen because of the narrowest beamwidth and the lowest side lobe levels for large off-boresight pointing angles.

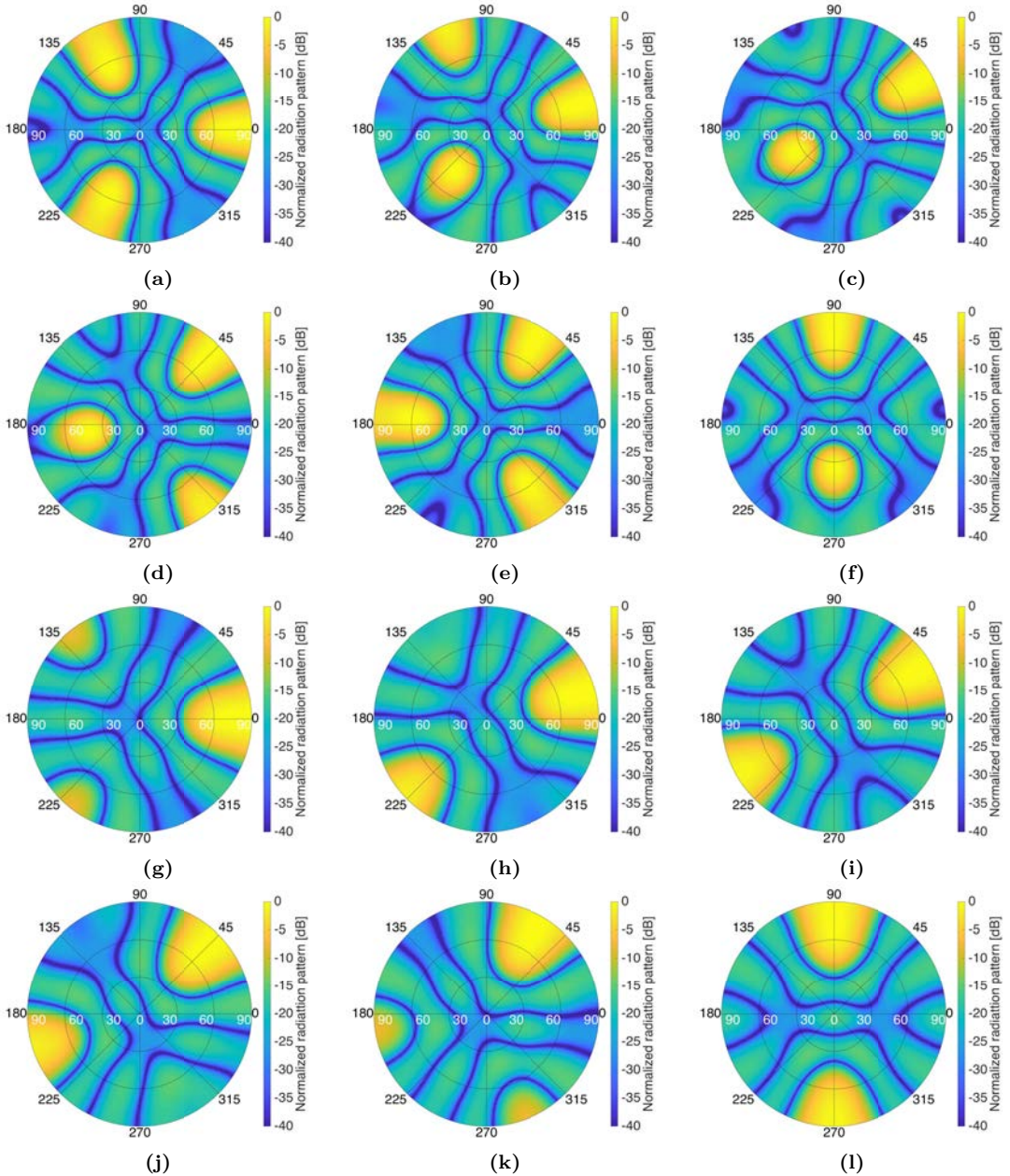


Figure 4.12: Simulated side lobes with uniform current distribution at a) to f) L1/E1, and g) to l) L5/E5a frequency band when pointing to $\theta = 75^\circ$ and a,g) $\varphi = 0^\circ$, b,h) $\varphi = 15^\circ$, c,i) $\varphi = 30^\circ$, d,j) $\varphi = 45^\circ$, e,k) $\varphi = 60^\circ$, and e,l) $\varphi = 90^\circ$.

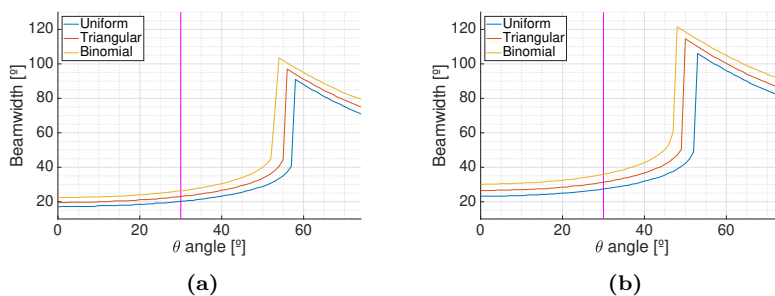


Figure 4.13: Beamwidth as function of the off-boresight pointing angle θ at a) L1/E1, and b) L5/E5a frequency bands.

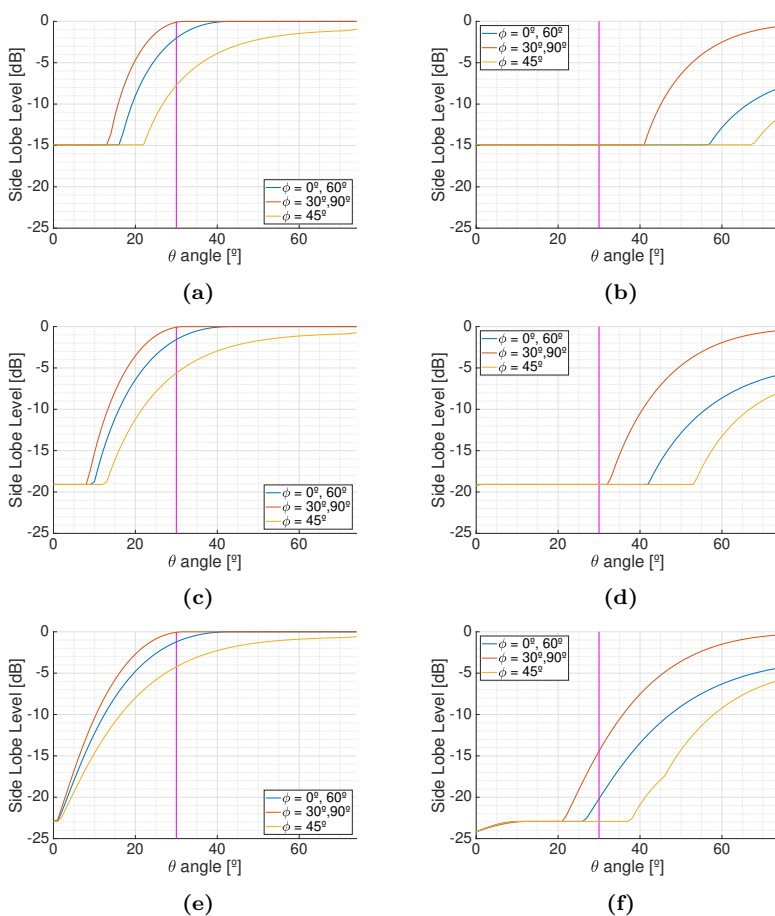


Figure 4.14: Side lobe level as a function of the off-boresight pointing angle θ for 5 different ϕ planes: 0° , 30° , 45° , 60° , and 90° with uniform distribution at a) L1/E1, b) L5/E5a, triangular distribution at c) L1/E1, d) L5/E5a, and binomial distribution at e) L1/E1, f) L5/E5a.

4.5 Phase and Amplitude Setting Using Vector Modulators

The beamforming process can be either analog or digital. For the former one, a hardware device consisting of a phase shifter and a variable gain amplifier or attenuator is required to change the amplitude and phase of the outgoing signal from each antenna. Both phase shifters and variable gain amplifiers or attenuators can be analog or digital as well, depending on whether the phase or amplitude changes are continuous or discrete. For instance, the 4-bit monolithic phase shifter MAPS-010143 [141] allows phase shifts in steps of 22.5° , which may not be accurate enough for certain applications, or the voltage controlled variable attenuator AVAGO AMMP-6640 [142], which allows attenuation ranging 0-25 dB. Forming multiple beams requires hardware replication, with a cost increase, and an increase in the beamforming control complexity. Furthermore, the target location has to be computed properly in real time and the beams have to be refreshed fast enough not to lose tracking. For multiband systems, different hardware is necessary for each frequency band. Once the beams have been formed, only one data sampling device is required per beam and band, and real time processing can be applied in smaller Field Programmable Gate Arrays (FPGAs) due to the reduced number of data streams.

On the contrary, digital beamforming requires sampling the outgoing data of each antenna element at each frequency band, and if stored, an infinite number of beams can be generated in post-processing. For large sampling rates and elevated number of antenna elements, this soon becomes unmanageable. For instance, for the MIR instrument, which has two arrays of 19 antennas each and a desired sampling rate of 32.736 Msps, digital beamforming at one frequency band would require

$$2 \text{ Arrays} \cdot \frac{19 \text{ Antennas}}{1 \text{ Array}} \cdot \frac{32.736 \text{ Msps}}{1 \text{ Antenna}} = 1.24 \text{ Gsps}. \quad (4.19)$$

Sampling I and Q components with 1 bit would require 296.6 Msps bandwidth, which represents 1.4 Tb of data to be stored per hour and per frequency band. Storing all that data, and post-processing it afterwards is very challenging, and doing it in real time inside an FPGA requires a really powerful one, or a bank of them. For this reason, analog beamforming was chosen.

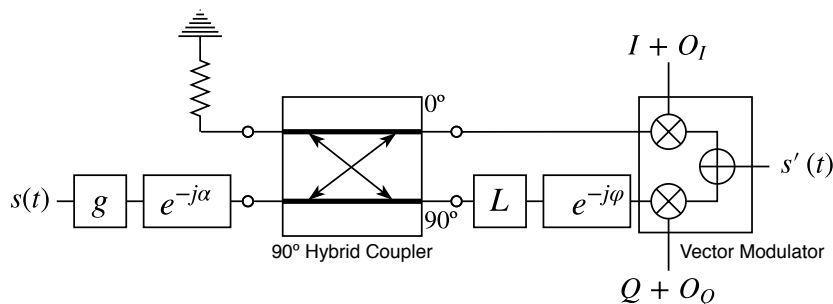


Figure 4.15: Used model for a whole MIR RF chain.

The devices in charge of the phase shifting and variable amplification are vector mod-

ulators. These devices (see Fig. 4.15) modify the amplitude of the signal's I and Q components according to the voltage applied to the gain control pins. In this way, the magnitude and phase of the input is changed. Figure 4.15 shows the model used for any RF chain of the MIR instrument, such as from the antennas or the calibration port to the sampling system. Each RF chain has a gain g and phase α . The vector modulator modifies separately the signal's I and Q components, but the separation of the I and Q components is not perfect, the signal paths of the I and Q components are not exactly equal, and therefore an attenuation L , also called amplitude unbalance, and a phase shift φ , also called phase unbalance, might be introduced. In an ideal case, the vector modulator and the later combiner, the output signal is

$$s'(I, Q, t) = s(t) \cdot (I + j \cdot Q) \cdot g \cdot e^{j\omega_c t - j\alpha} = s(t) \cdot g \cdot \sqrt{|I|^2 + |Q|^2} \cdot e^{j \cdot \text{atan2}(Q, I)} \cdot e^{j\omega_c t - j\alpha}, \quad (4.20)$$

where I and Q are the voltage gains in the I and Q channels, respectively (note that they can be negative), atan2 is the 2-argument arctangent function, $s(t)$ is the input signal, $s'(t)$ is the output signal, and ω_c is the carrier angular frequency.

If the unbalances and offsets are taken into account, the output signal becomes

$$s'(I, Q, t) = ((I + O_I) \cdot s(t) + j \cdot L \cdot (Q + O_Q) \cdot e^{-j\varphi} \cdot s(t)) \cdot g \cdot e^{j\omega_c t - j\alpha}, \quad (4.21)$$

where O_I and O_Q are the gain offsets in the I and Q channels, respectively. To simplify, the I and Q gains and the gain offsets will be written in complex notation as

$$\begin{aligned} k_I &= g \cdot e^{-j\alpha} \\ k_Q &= g \cdot L \cdot e^{-j\varphi} \cdot e^{-j\alpha} \\ O &= g \cdot (O_I + j \cdot O_Q \cdot L \cdot e^{-j\varphi}) \cdot e^{-j\alpha}. \end{aligned} \quad (4.22)$$

Then, Eqn. (4.21) becomes

$$s'(I, Q, t) = s(t) \cdot (I \cdot k_I + j \cdot Q \cdot k_Q + O) \cdot e^{j\omega_c t} = s(t) \cdot H_{VM}(I, Q) \cdot e^{j\omega_c t}. \quad (4.23)$$

The achieved gain can be represented in the I-Q plane (Fig. 4.16). Ideally, if the values $\{I, Q\} = \{\cos(\alpha), \sin(\alpha)\}$ are swept, the achieved gain will be represented as a constant radius circle, centered at the origin, starting at $\{I, Q\} = \{1, 0\}$ over the I axis, and k_I and k_Q will be orthogonal (blue vectors). Without calibration, the circle will not be centered (due to the gain offset O), the circle will become an ellipsoid (due to the gain unbalance L), the gain vectors will not be orthogonal (due to the phase unbalance φ , see red vectors), and the circle will be rotated around the origin (due to the phase α). Besides, if we plot the gain circles of all 19 vector modulators of a same beam, they will have a different radius (due to different gains g in each RF chain). These effects will induce an error in the gain and phase set to any signal that will require proper calibration.

Once the required gain $G_{m,n}$ and phase $\beta_{m,n}$ are determined for each antenna element in each frequency band and for each beam, the ideal voltage gains at the vector modulator inputs I_I and Q_I for that beam and band are computed from Eqn. (4.20) as

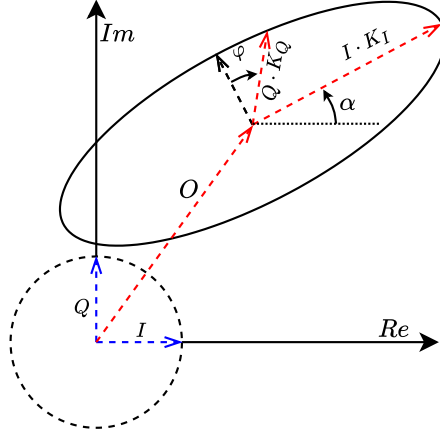


Figure 4.16: Ideal gain circle (dashed line), and modeled gain ellipsoid (solid line) in the IQ gain plane.

$$G_{m,n} = g \cdot \sqrt{|I_I|^2 + |Q_I|^2} \quad (4.24)$$

$$\beta_{m,n} = \text{atan2}(Q_I, I_I) - \alpha, \quad (4.25)$$

which can be written as

$$\left(\frac{G_{m,n}}{g} \right)^2 = |I_I|^2 + |Q_I|^2 \quad (4.26)$$

$$\tan(\beta_{m,n} + \alpha) = \frac{Q_I}{I_I}. \quad (4.27)$$

Equation (4.27) becomes

$$I_I \cdot \tan(\beta_{m,n} + \alpha) = Q_I, \quad (4.28)$$

which is used in Eqn. (4.26):

$$\left(\frac{G_{m,n}}{g} \right)^2 = |I_I|^2 + |I_I \cdot \tan(\beta_{m,n} + \alpha)|^2 = |I_I|^2 \cdot (1 + \tan^2(\beta_{m,n} + \alpha)) \quad (4.29)$$

to compute I_I as

$$I_I = \begin{cases} \frac{|G_{m,n}|}{g \sqrt{1 + \tan^2(\beta_{m,n} + \alpha)}}, & 270^\circ < \beta_{m,n} + \alpha < 90^\circ, \\ -\frac{|G_{m,n}|}{g \sqrt{1 + \tan^2(\beta_{m,n} + \alpha)}}, & 90^\circ < \beta_{m,n} + \alpha < 270^\circ. \end{cases} \quad (4.30)$$

Next, Q_I is obtained from eqn. (4.28):

$$Q_I = I_I \cdot \tan(\beta_{m,n} + \alpha). \quad (4.31)$$

The amplitude and phase unbalances have to be compensated by inverting the system of equations obtained from Eqn. (4.21):

$$\begin{pmatrix} I_I \\ Q_I \end{pmatrix} = \begin{pmatrix} 1 & L \cdot \sin(\varphi) \\ 0 & L \cdot \cos(\varphi) \end{pmatrix} \cdot \begin{pmatrix} I_C \\ Q_C \end{pmatrix}, \quad (4.32)$$

so the compensated values I_C and Q_C are obtained as:

$$\begin{pmatrix} I_C \\ Q_C \end{pmatrix} = \begin{pmatrix} 1 & -\tan(\varphi) \\ 0 & \frac{1}{L \cdot \cos(\varphi)} \end{pmatrix} \cdot \begin{pmatrix} I_I \\ Q_I \end{pmatrix}. \quad (4.33)$$

Last, if the complex offset O is known, the O_I and O_Q can be estimated with the same system of equations

$$\begin{pmatrix} O_I \\ O_Q \end{pmatrix} = \begin{pmatrix} 1 & -\tan(\varphi) \\ 0 & \frac{1}{L \cdot \cos(\varphi)} \end{pmatrix} \cdot \begin{pmatrix} \operatorname{Re}\left(\frac{O}{g \cdot e^{-j\alpha}}\right) \\ \operatorname{Im}\left(\frac{O}{g \cdot e^{-j\alpha}}\right) \end{pmatrix}, \quad (4.34)$$

and must be subtracted from I_C and Q_C .

4.6 Airplane Dynamics Analysis

Once the beams are steered to the desired directions, they need to be refreshed taking into account the new position and attitude of the platform, and the GNSS satellites new position. Ground-based instruments do not change their position or attitude, so the minimum beam refreshment rate is only determined by the GNSS satellites dynamics. Figure 4.3 shows that the GNSS satellite elevation difference is lower than $1^\circ/\text{min}$, which considering a beamwidth in the range $10\text{-}20^\circ$, leads to a required beam refreshment rate in the order of tens of minutes. In the case of airborne and spaceborne instruments, the speed and stability of the platform determines the minimum beam refreshment rate.

In the case of the MIR instrument, the chosen platform was an experimental Van's Aircraft RV-10. Figure 4.17 shows the flight height over the WGS-84 ellipsoid and the ground speed of three analyzed flights over Yanco (NSW), Australia, used to estimate the minimum beam refreshment rate. The first flight was on 4 December 2010, had an average flight height of 3300 meters and a flight speed varying between 240-310 km/h, and the average wind speed was 11-13 km/h. The second flight was on 6 July 2010, had an average flight height of 3100 meters and a ground speed oscillating between 250-320 km/h, and the average wind speed was 17-24 km/h. The last flight was on 6 December 2010, had an average flight height of 400 meters, and an average ground speed of 260 km/h, and the average wind speed was 13-17 km/h [143].

In order to analyze the minimum refreshment rate, the angular deviation that would occur with respect to the desired pointing direction caused by the airplane movement was computed. To do so, the angular deviation as function of time of all vectors in the range $\theta = 0^\circ \dots 30^\circ$ and $\varphi = 0^\circ \dots 360^\circ$ in steps of 1° was computed taking into account how the

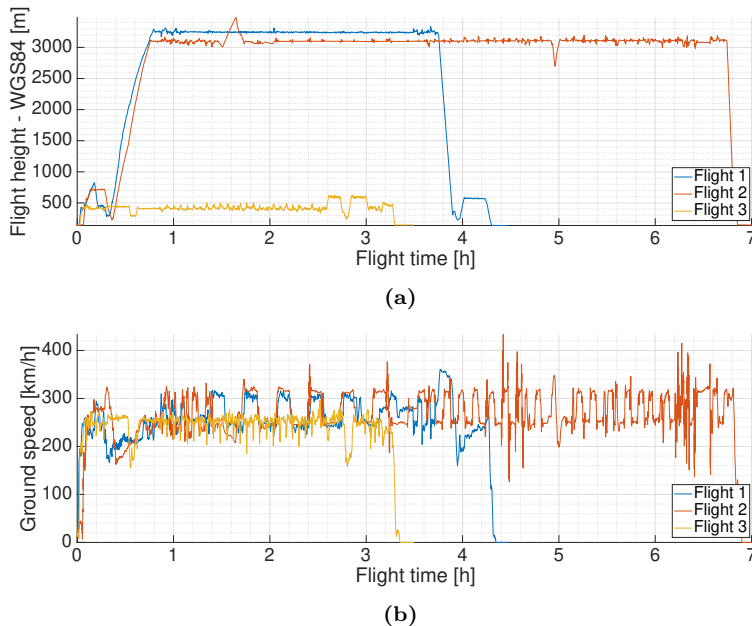


Figure 4.17: a) Flight height over the WGS-84 ellipsoid, and b) ground speed of the three analyzed flights.

platform attitude would have changed after three different beam refresh periods ($\Delta T = 500$ ms, $\Delta T = 1000$ ms, and $\Delta T = 1500$ ms) for the three flights as

$$\cos(\alpha)(t) = (M(t + \Delta T) \cdot \vec{v})^T \cdot (M(t) \cdot \vec{v}), \quad \vec{v} = \begin{pmatrix} \sin(\theta) \cdot \cos(\varphi) \\ \sin(\theta) \cdot \sin(\varphi) \\ \cos(\theta) \end{pmatrix} \quad (4.35)$$

where $M(t) = R_1(\phi(t)) \cdot R_2(\theta(t)) \cdot R_3(\psi(t))$, and $\phi(t)$, $\theta(t)$, $\psi(t)$ are the roll, pitch, and yaw angles as a function of time t , respectively. Figure 4.18 shows the computed mean and maximum angle deviation. The vertical pink line shows half the minimum beamwidth at -3 dB achieved by the studied current distributions in section 4.4. As can be seen, for beam refresh rates below 1 second it is expected that the specular reflection point will be within the antenna main beam at least 95 percent of time. Reducing the refresh rate down to 500 ms would ensure the specular reflection point to be in the main beam at least 98 percent of time. The MIR refreshment rate was finally reduced to approximately 333 ms as explained in Section 5.7.

4.7 Conclusions

This chapter has presented the sequence of calculations to be computed in order to point the beams to the “best” satellites in view. The satellite selection algorithm chooses the best satellites to be pointed, and once their position and the airplane position and

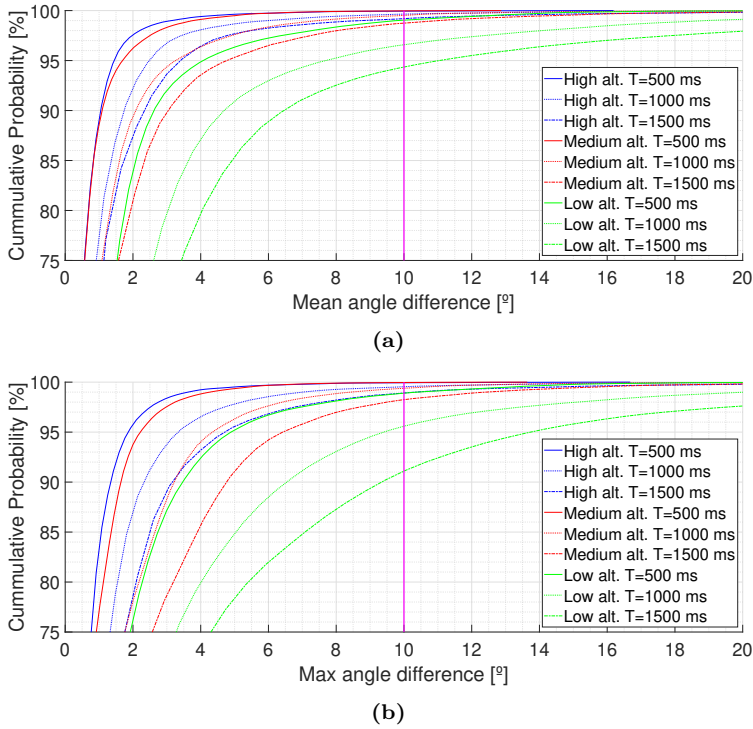


Figure 4.18: a) Mean, and b) maximum angle deviation for all possible pointing directions in the range $\theta = 0^\circ \dots 30^\circ$ and $\varphi = 0^\circ \dots 360^\circ$ caused by the airplane movement in three different flights. The pink line shows half the minimum beamwidth at -3 dB achieved by the studied current distributions. High altitude corresponds to 3300 meters, medium altitude corresponds to 3100 meters, and low altitude corresponds to 400 meters.

attitude are known, the pointing angles are computed. These angles are converted to voltages to be applied to the vector modulators, the elements in charge of changing the phase and amplitude of each antenna element. Last, the dynamics of previous flights have been analyzed in order to determine the minimum beam refresh rate to ensure that the satellites tracking is not lost.

5

Chapter 5

Instrument Description

5.1 Introduction

This chapter describes the MIR instrument, the main instrument developed during this Ph.D. thesis. It first describes in detail the hardware blocks, such as the antenna arrays of the beamformers, and how they are integrated; then the software that controls the instrument is described. Part of this chapter is adapted from the previously published work “The Global Navigation Satellite Systems Reflectometry (GNSS-R) Microwave Interferometric Reflectometer: Hardware, Calibration, and Validation Experiments” [144].

The MIR instrument is a GNSS reflectometer that has two steerable arrays. The up-looking one points directly to the GNSS satellites, while the down-looking one points to where the signals from these satellites are reflected on the Earth’s surface. Each of these arrays is connected to an analog beamformer that creates two beams at L1/E1 (1,575.42 MHz) and two beams at L5/E5A (1,176.45 MHz), therefore the instrument can track up to 4 different satellites, and their corresponding specular reflection points. The signals received from a satellite by the up-looking array are sampled synchronously by pairs with the signal from the same satellite received by the down-looking array after reflecting on the Earth’s surface. The signals coming from the down-looking array are amplified prior to be sampled in order to compensate the losses caused by the scattering in rough surfaces. The data is sampled using SDR, and then is stored for post-processing. All SDRs are time and frequency synchronized by a GPS-DO. The instrument is controlled by a Linux embedded computer that selects the best available satellites and points the instrument beams towards them, and to the expected specular reflection points taking into account the position of the satellites and the position and attitude of the plane given by a GNSS position + attitude receiver, an IMU and an inclinometer. Last, the instrument has an internal calibration system that generates PRN codes to calibrate the instrument both in

amplitude and phase. Figure 5.1 shows the instrument block diagram. The next sections explain all blocks in detail, and also the software that controls the instrument. Appendix H shows the procedure to set up the instrument and how to launch the MIR software.

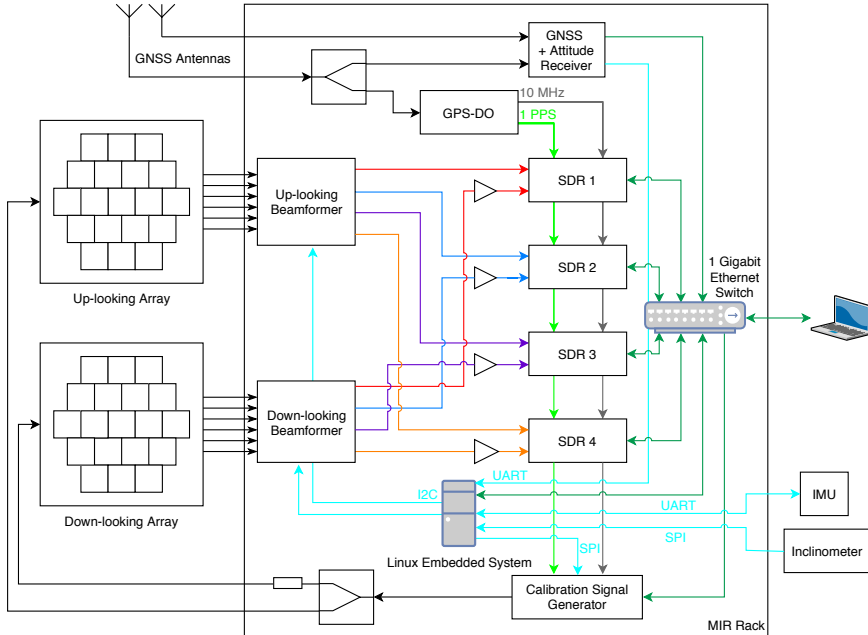


Figure 5.1: Block diagram of the MIR instrument.

5.2 Antenna Arrays

MIR has two antenna arrays, an up-looking RHCP one for the direct signal, and a down-looking LHCP one for the reflected signal. Each array consists of 19 dual-band patch antennas distributed in a hexagonal grid (see Fig. 5.2a). The antenna elements (see subsection 5.2.1) are separated 143.13 mm ($0.752\lambda_{L1}$ and $0.561\lambda_{L5}$). An RF Front-end is attached behind each antenna (see Figs. 5.11c and 5.11d). The Front-end forms the circular polarization, amplifies and band-pass filters the received signals. Each array has also attached a 1-to-19 power splitter that distributes a calibration signal to all RF Front-ends. The two arrays are built almost identically, just the mechanical part differs: the down-looking array has a larger ground plane, and the frame that holds it is also larger. The reason is that the down-looking array was designed to be hanging from a plane's belly, and the up-looking one had to fit inside the airplane cabin (see chapter 8).

5.2.1 Antenna Elements

The antenna elements are patented dual-band patch antennas of 95x95x8 mm specifically designed for the MIR instrument [145]. The antennas (Fig. 5.3) are made of two square conductive patches stacked between dielectric substrate layers (Rogers 4003c). The conductive patches are tuned to resonate at the L1/E1 central frequency (1,575.42 GHz),

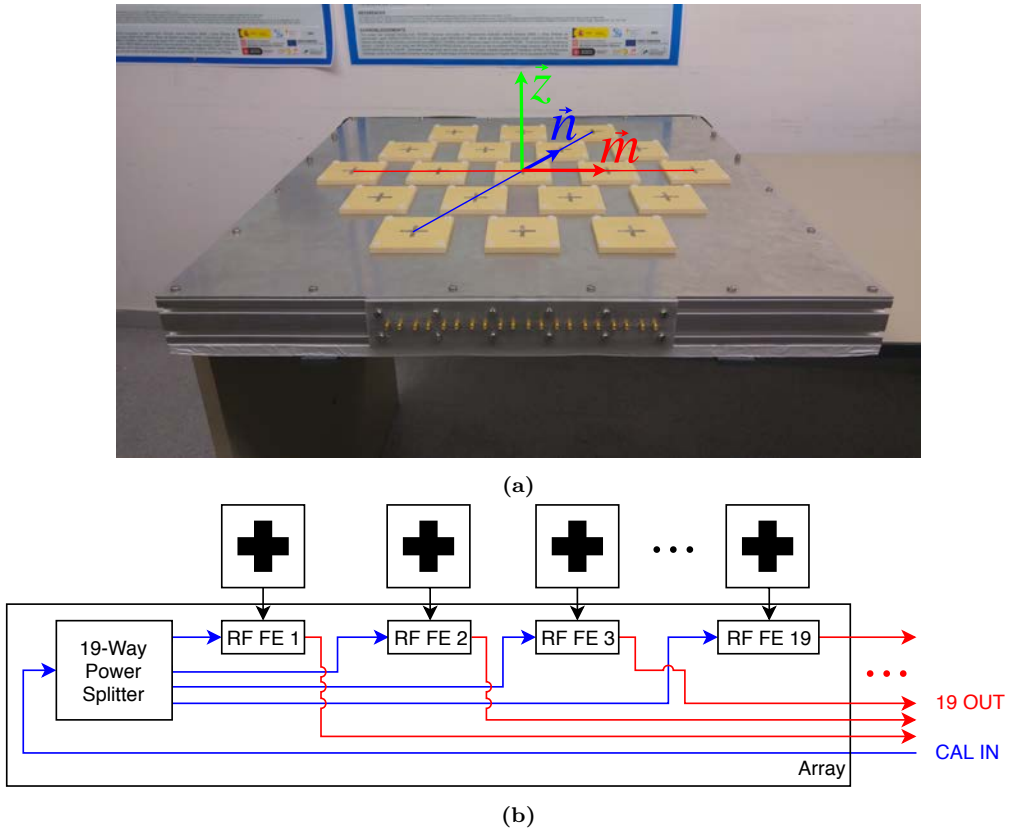


Figure 5.2: a) Front view of the up-looking array, and b) schematic of the components inside each array. The up-looking array includes the baseline used to define each antenna element by a $\{m_i, n_i\}$ pair of values. The azimuthal pointing angle φ is defined anti-clockwise from vector \hat{m} to \hat{n} . The off-boresight pointing angle θ is defined from vector \hat{z} to the antenna array ground plane.

and at the E5 central frequency (1,191.795 GHz), respectively. The antenna is fed by capacitive coupling using a cross-shaped feeding patch on the top of the antenna that is electrically fed by two coaxial connectors or probes. Each probe corresponds to an orthogonal linear polarization. The shape of the feeding patch was found to be useful to increase the bandwidth of the antenna, but at the expense of reducing the axial ratio of the antenna [145]. The size of the feeding patch and the position of the feeding probes were optimized to maximize the antenna matching and bandwidth at the desired frequency bands. The manufactured design can be seen in Appendix A.1.

Figure 5.4 shows the matching of the two linear polarizations of one of the manufactured antennas. The bandwidth at -10 dB was found to be 34 MHz at L5/E5A frequency band, and 21 MHz at L1/E1 frequency band.

Figure 5.5 shows the measured full radiation patterns of one of the manufactured antenna elements. The measured directivity was 7 and 7.8 dB at L1/E1 and L5/E5A

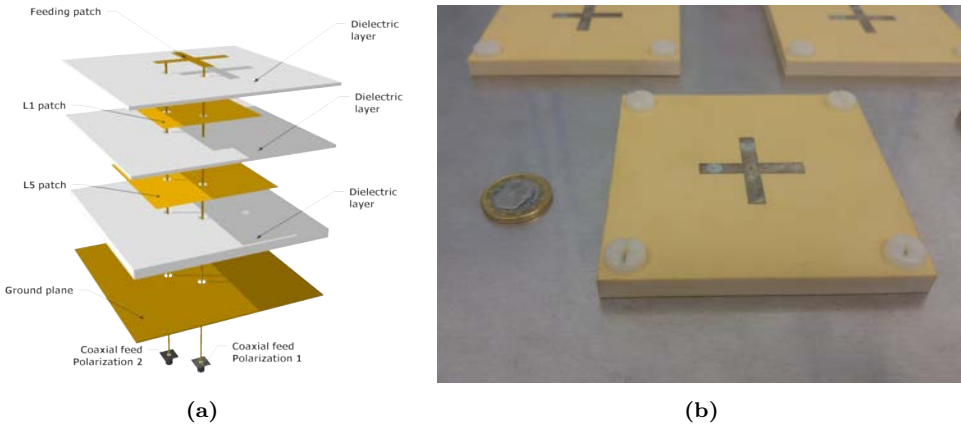


Figure 5.3: a) 3D model of the antenna elements, and b) photograph of one of the manufactured antennas.

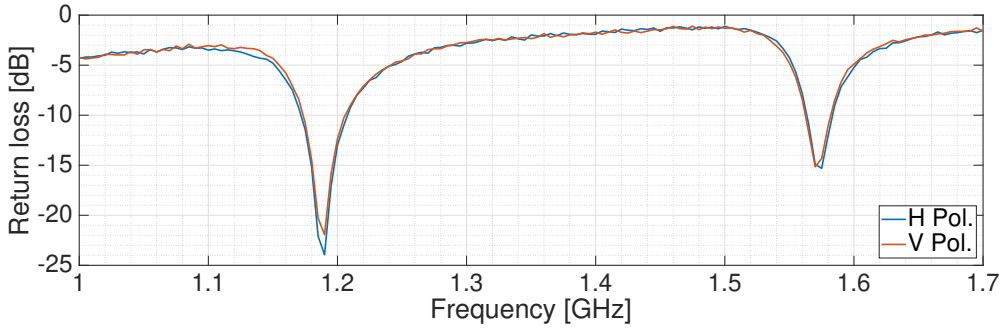


Figure 5.4: Antenna matching of one of the manufactured antennas.

respectively, and the radiation efficiency was estimated in 65% and 80%, respectively.

5.2.2 RF Front-ends

Figure 5.7 shows the block diagram of the RF Front-ends, a front view of a manufactured one, and how the front-ends are attached to the ground plane and connected to the

Table 5.1: Measured directivity (D), beamwidth, and the estimated radiation efficiency (Rad. η) of the antenna elements.

Freq. Band	Directivity	Beamwidth	Rad. η
L5/E5A	7.8 dB	75°	80% °
E5	8 dB	70°	70% °
L1/E1	7 dB	80°	65% °

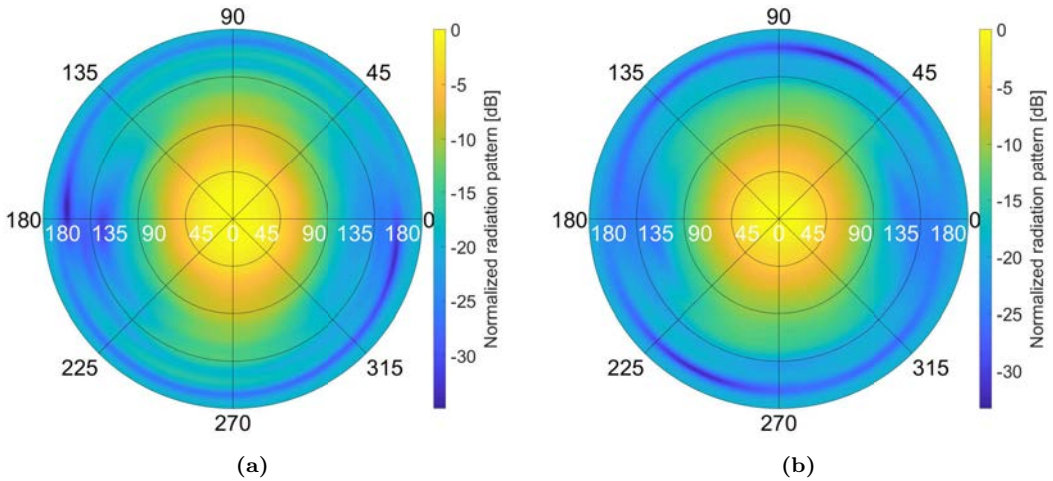


Figure 5.5: Measured full radiation patterns at a) L1/E1 and b) L5/E5A frequency bands.

antennas. A 90° hybrid combines the two linear polarizations of the antennas to generate a circular polarization: RHCP for the zenith looking antenna, and LHCP for the nadir looking one. The selection between circular polarizations is done mechanically with two resistors. The outgoing signal is then connected to one of the inputs of an RF switch. The other input is used to inject a calibration signal. The switch is always commuted to the antenna signal, thus behaving as a directional coupler. In this way, the signal from the antenna is connected to the “transmitted port”, and the calibration signal is connected to the “coupled port”. Fig. 5.6 shows the temperature effect in the path difference between the transmitted port and the coupled port both in a) amplitude, and b) phase. For a change of 60°C of temperature, the maximum amplitude change is lower than 0.2 dB and the maximum phase change is approximately 1° .

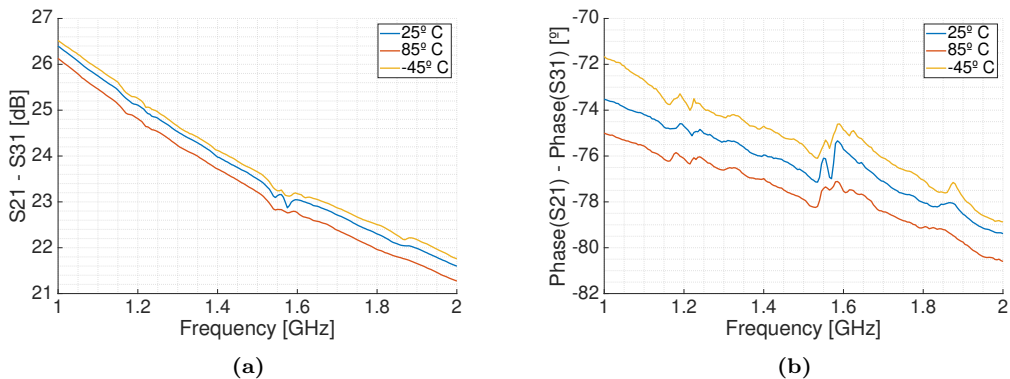


Figure 5.6: Temperature effect in the path difference between the coupled port and the transmitted port a) up-looking array, and b) down-looking array.

The combined signals after the calibration switch are amplified with a LNA ($G \approx 15$

dB, $NF \approx 0.8$ dB), high-pass filtered ($F_c = 880$ MHz) to attenuate broadcasted Frequency Modulation (FM) signals (80-100 MHz) and Global System for Mobile communications (GSM) signals (800-900 MHz), amplified again ($G \approx 22$ dB, $NF \approx 2.1$ dB), and low-pass filtered ($F_c = 1,825$ MHz) to attenuate broadcasted GSM signals (1,700-1,900 MHz) and Wi-Fi signals (2.4 GHz), and to avoid undesired high-frequency oscillations. Wi-Fi signals might not affect during flight operations, but are filtered to avoid any interference in laboratory tests. The Front-ends are fed through the output ports, which have a T-bias to distribute the power signal to the Low-DropOut regulator (LDO) regulators that feed the active components. The Front-ends originally had a second RF amplifier, the calibration switch was controlled from the calibration port, and the load in the calibration port was not in the design. However, all these elements had to be modified to avoid an oscillation that was not present in the prototypes, but that appeared in the final manufactured PCB. The schematics and PCBs can be seen in Appendix A.2.

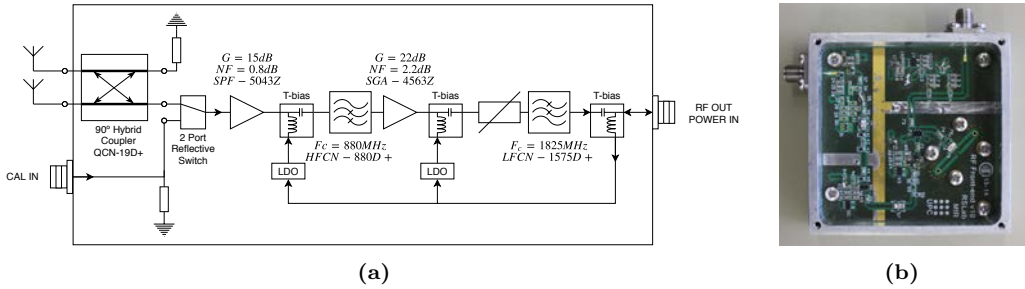


Figure 5.7: a) Block diagram of the RF Front-end, and b) front view of a manufactured RF Front-end.

Figure 5.8 shows the S_{21} parameter of the RF Front-ends of the up- and down-looking arrays. The rest of the S-parameters plots can be seen in Appendix B.1. The S-parameters statistics are shown in table 5.2. Note that the S_{22} parameters have a higher dispersion in the direct array, but also the average value is lower. Analogously, note that the S_{21} parameters have a higher but more disperse gain in the direct array as well.

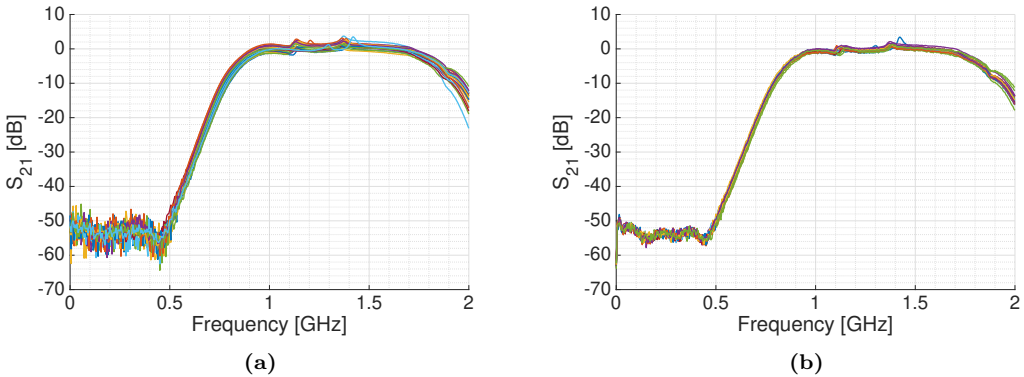


Figure 5.8: S_{21} Parameters of the 19 RF Front-ends of the a) up-looking array, and b) down-looking array.

Table 5.2: Gain and Phase statistics from the calibration port of all the RF Front-ends by array at L1/E1 and L5/E5A frequency bands. For the gain, the geometric mean and geometric standard deviation have been used.

	Direct Array		Reflected Array	
	L1/E1	L5/E5A	L1/E1	L5/E5A
$ S_{11} $	$\mu = -8.9$ dB $\sigma = 0.3$ dB	$\mu = -10.6$ dB $\sigma = 0.2$ dB	$\mu = -9.1$ dB $\sigma = 0.4$ dB	$\mu = -10.9$ dB $\sigma = 0.4$ dB
$ S_{21} $	$\mu = 0.4$ dB $\sigma = 0.7$ dB	$\mu = 0.3$ dB $\sigma = 0.8$ dB	$\mu = -0.1$ dB $\sigma = 0.4$ dB	$\mu = -0.3$ dB $\sigma = 0.4$ dB
$\angle(S_{21})$	$\sigma = 10.3^\circ$	$\sigma = 11.5^\circ$	$\sigma = 4.2^\circ$	$\sigma = 3.3^\circ$
$ S_{22} $	$\mu = -14.3$ dB $\sigma = 3.3$ dB	$\mu = -6.8$ dB $\sigma = 2$ dB	$\mu = -11.8$ dB $\sigma = 0.6$ dB	$\mu = -5.3$ dB $\sigma = 0.4$ dB

In order to study the linearity of the RF Front-ends and avoid any saturation, the gain response to a power sweep was measured at the central frequency of the L1/E1 and L5/E5A frequency bands to find the 1 dB compression point in both the calibration and the antenna ports. To simulate how the Front-end will react to a circularly polarized incident waves, first two coaxial cables were soldered to the ports where the antennas are soldered (see Fig. 5.9) and one port of the Vector Network Analyzer (VNA) was connected to each of them. Then, the electrical length of one of the antenna ports was adjusted to match the phase of the other antenna port at the desired frequency to simulate the two orthogonal components of the GNSS signal being summed constructively after the 90° hybrid coupler. Last, the gain response to a power sweep was measured for each port individually, the measured output power of both ports was summed, and the gain was obtained. Fig. 5.10 shows a P_{1dB} around -15 dBm for the antenna ports, and around 7 dBm for the calibration port.

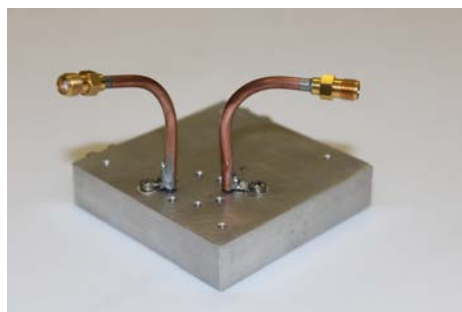


Figure 5.9: Semi-rigid cables soldered to antenna inputs of the RF Front-ends to measure the gain versus input power curve for a circularly polarized simulated incident wave.

The power consumption of each RF Front-end was measured to be 750 mW (100 mA at 7.5 V). The power supply was provided through the RF cable from the phase shifters.

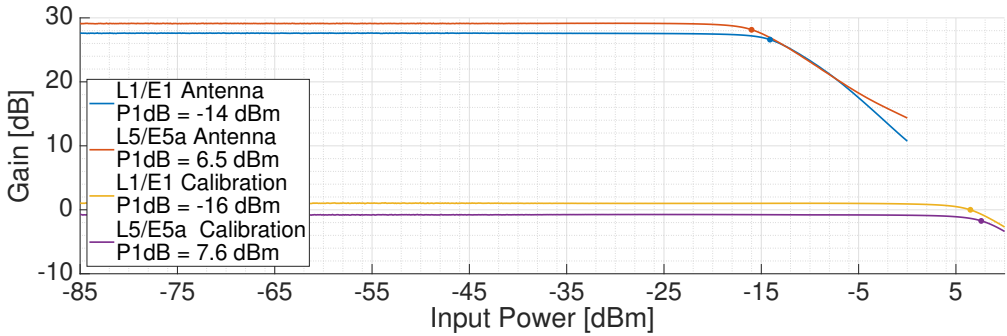


Figure 5.10: Gain response of the RF Front-end to a power sweep to find the P_{1dB} point.

5.2.3 Antenna Array Integration

The arrays were designed to fit in a Vans Aircraft RV-10 experimental airplane [146] that Monash University uses to operate the Polarimetric L-band Multibeam Radiometer (PLMR) [147]. The up-looking array and the instrument rack were required to fit inside the cabin of the airplane with the instrument rack below, whereas the down-looking array was designed to be hanging from the airplane fuselage, fitting in the same spot as the PLMR. The PLMR measurements, the cabin size, and a photo of the PLMR radome can be found in Appendix C.

The frames of both arrays are metallic squared structures made of 30x60 mm standard aluminum profile. The ground planes are 3 mm thick aluminum plates which were drilled using a laser cutting machine. The down-looking array needed a ground plane of 36.6x36.6 inches ($\sim 930 \times 930$ mm) and had to match with the PLMR mount bolt holes. To protect the array from the wind and the engine exhaust, a radome also had to be manufactured. Besides, since the down-looking antenna had to be hanging down from the airplane fuselage and to add more structural strength, several crossbars were added (see Fig. 5.11). Ideally, the up-looking array was expected to be as large as the down-looking one to minimize the differences in the radiation patterns and to reduce the differences and cost in the manufacturing process. The cabin is large enough to fit the up-looking array inside, but the door is smaller, so the up-looking array was reduced to 800x800x60 mm. A foam model of the antenna was manufactured in Australia to confirm that it could pass through the airplane doors.

Once both array structures were mounted, the RF Front-ends were screwed to the ground plane. Then, the antennas were mounted in the outer side of the array and soldered to the RF Front-end PCBs. The S-parameters of all RF Front-ends were measured again to ensure that nothing had been damaged during the mounting process. Then, a GNSS receiver was connected to each RF Front-end output to ensure that all the antennas were properly soldered to the RF Front-ends. The connectors of the arrays are located in an aluminum slide at the back side of each array. The required length for the cables and the type of connectors was determined at that time. The cables were then mounted, and finally the calibration power splitter was mounted. Figure 5.11 shows front and back views of both arrays. Figures 5.11c and 5.11d show the uncovered rear part of the down-looking array with the RF Front-ends and the calibration power splitter mounted in the back.

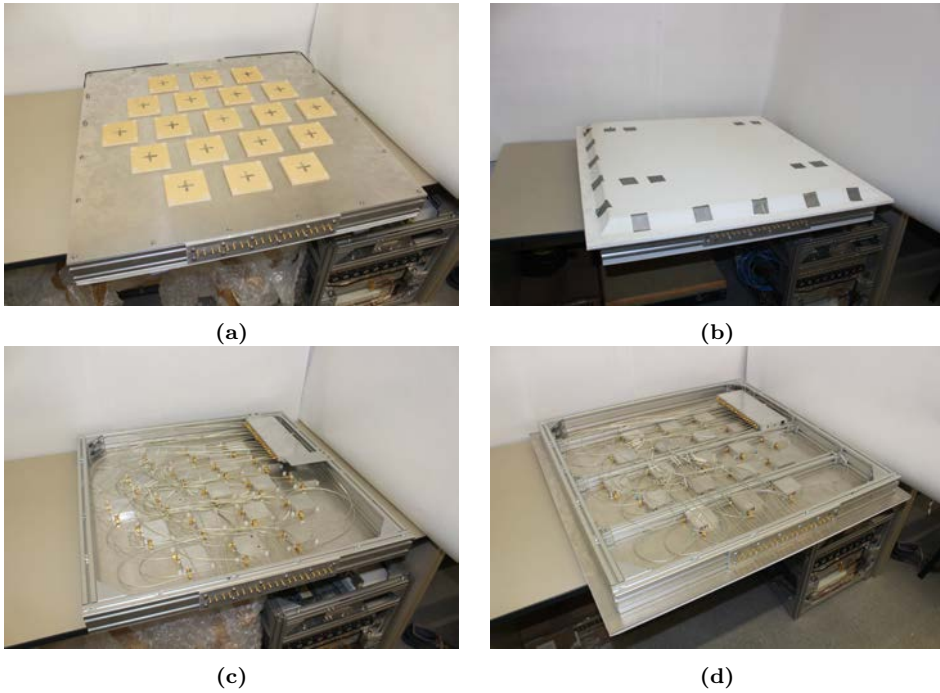


Figure 5.11: Front view of the a) up-looking and b) down-looking arrays, and back view of the c) up-looking and d) down-looking arrays.

The Computer-Aided Designs (CADs) of both arrays can be found in Appendix D.1. The down-looking array was screwed in the airplane fuselage using the parts shown in Fig. 5.12. Four pieces made of aluminum profile were screwed to the sides of the array (see Fig. 5.12a). The nuts for the upper holes of these pieces were easily placed, but the lower holes needed custom-made nuts carved into an aluminum piece that fitted inside the aluminum profile (see Fig. 5.12b).

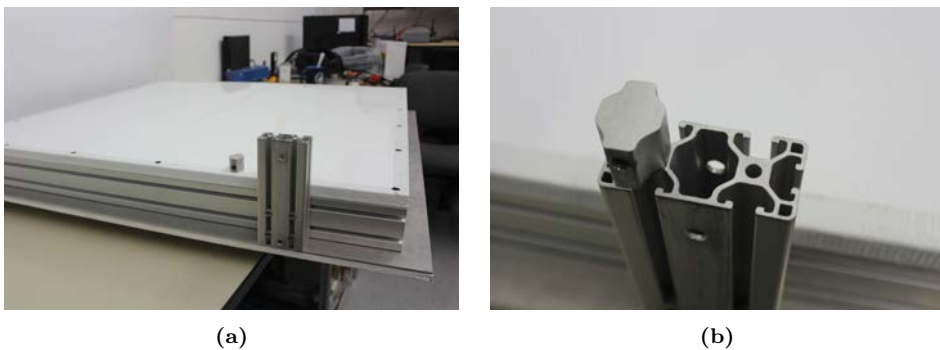


Figure 5.12: a) Structural elements used to hold the down-looking array to the airplane fuselage, and b) detail of the custom-made nuts used for the lower screws.

The back side of both arrays was covered with a stacked panel of 0.8 mm aluminum + 14 mm foam + 0.8 mm aluminum that can be seen in Fig. 5.12a. The front part of the down-looking array had to be covered to protect the antennas from the wind (the RV-10 can flight up to 150 knots \sim 280 km/h), water vapor in the atmosphere, and hot gases and particles coming from the engine exhaust, which is located below the airplane engine. The radome was made of a custom 3 layer panel made of a 1 mm aluminum plate (bottom), a 38.5 mm extruded polystyrene foam layer (mid), and a 2 mm fiberglass layer (top). Once the panel was stuck, it was carved using a drilling machine. Then it was covered with an adhesive vinyl sheet to avoid the side wind to strip off any of the material layers (see Fig. 5.13). Appendix D.1 shows the CAD design of the radome.

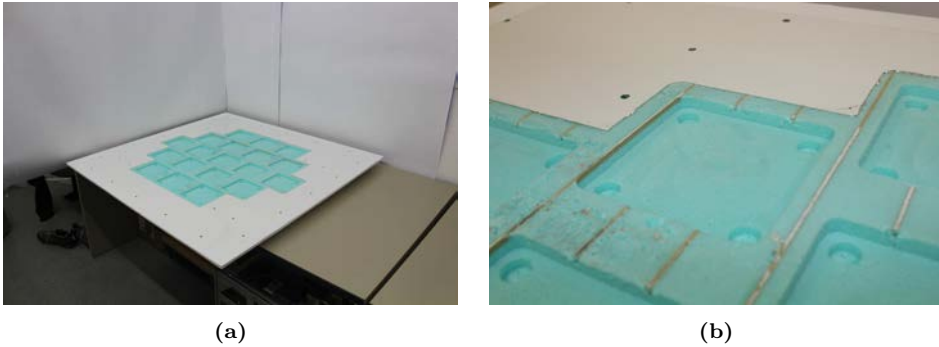


Figure 5.13: a) Photo of the back part of the spare radome, and b) detail of the holes that fit in the antennas and its bolts. In the used radome, the brown glue line along the extruded polystyrene foam layer were not present due to a different manufacturing process than the main one.

For each array it was necessary to use a cable from the panel connector to the 19-way calibration power combiner input, plus 19 cables that connected the 19-way calibration power splitter outputs to the RF Front-ends calibration inputs, plus 19 cables from the RF Front-end outputs to the panel connector. Table 5.3 summarizes the required cables for each array. The cable manufacture was outsourced requiring a minimum of -25 dB of return loss, and a maximum of 2° maximum phase error between types of cables at L1/E1 frequency band, that is, ± 0.39 mm. The input and output connectors are located in one of the sides of the array (see Fig. 5.14). The CAD designs of the holes and the slides that hold the connector can be found in Appendix D.

5.3 Beam-former

Each analog beamformer block (Fig. 5.15) consists of 19 phase shifters that change the amplitude and phase of the received signal from each antenna individually at each desired frequency band and for each beam. Then, the 19 outgoing signals of each beam and band are combined using 19-way power combiners that are located below the phase shifter boards and the motherboard (the 4 horizontal long boxes marked in blue in Fig. 5.15c). Thus 4 RF lines are obtained, one for each particular band and beam (2 beams

¹One of the spare “RF Front-end \rightarrow Array Panel” cables was used.

Table 5.3: Summary of the required cables per array. In parenthesis, the number of spare ones.

	Input Connector	Output Connector	Lenght	Number
Array Panel → Calibration PS	SMA Panel	SMA 90° aerial	860 mm	1 ¹
Calibration PS → RF Front-end	SMA straight aerial	SMA straight aerial	860 mm	19 (+2)
RF Front-end → Array Panel	SMA 90° aerial	SMA Panel	860 mm	19 (+2)
Array Panel → Beamformer	SMA straight aerial	SMA straight aerial	2000 mm	19 (+2)



(a)



(b)

Figure 5.14: Pictures of the a) connector panel in the up-looking array, and b) the holes in the structure where the sma cables pass through.

at L1/E1 and 2 beams at L5/E5A frequency bands). There is one of these beamformer blocks for each array.

5.3.1 Phase Shifters

Each phase shifter board (see Fig. 5.16) is connected to an RF Front-end and feeds it electrically. These boards first divide the incoming signal into two branches that are amplified ($G = 17$ dB), and band-pass filtered at L1, or L5 bands using Surface Acoustic Wave (SAW) filters. The L1 filter is centered at 1,583 MHz, and has a bandwidth at -3 dB of 58 MHz. The L5 filter is centered at 1,178.12 MHz and has a bandwidth at -3 dB of 55 MHz. Each of these branches is split again to generate two different beams for each band. The amplitude and phase of these signals is then modified to steer the beams electronically to the desired direction as explained in Section 4.4.

The component in charge of changing the amplitude and phase of each signal is an

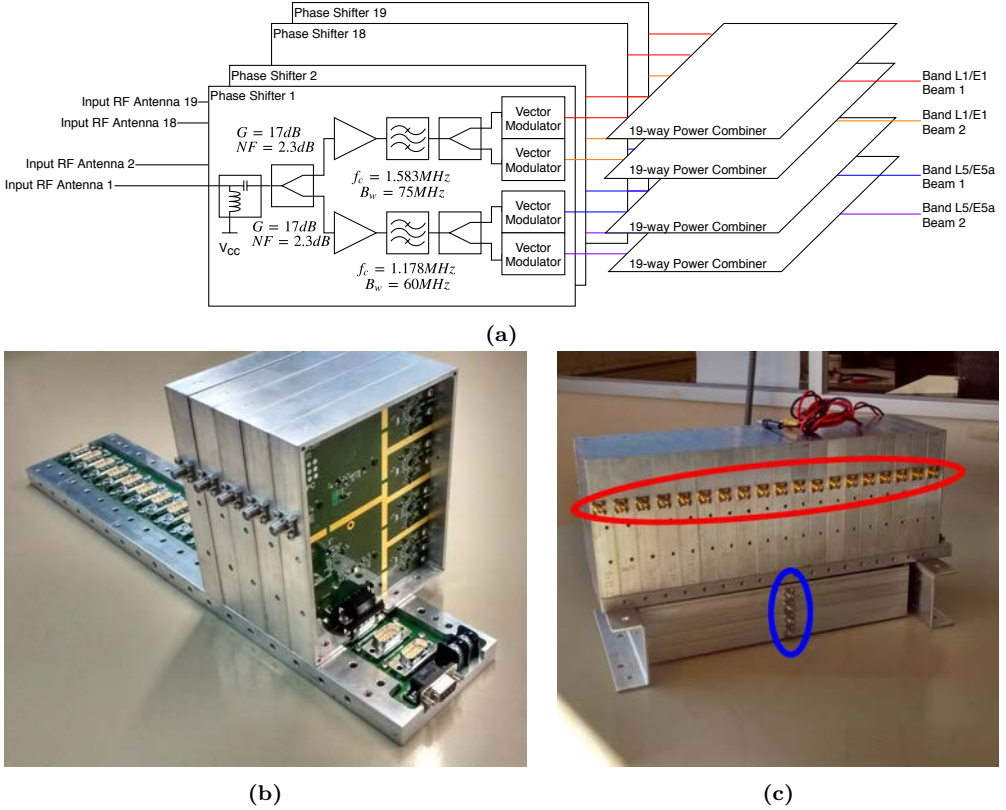


Figure 5.15: a) Block diagram of one of the beamformers, b) phase shifters stacked in the motherboard, and c) front picture of one of the assembled beamformers. Note the 19 inputs (red), and the 4 outputs (blue). The beamformer picture was taken before adding the forced ventilation.

ADL5390 Vector Modulator [148]. These devices multiply the I and Q components by different gains, thus changing the amplitude and phase of the signal (see section 4.5). The gain control of the I and Q channels of the Vector Modulator are differential inputs. The differential inputs should have a common-mode level of 0.5 V, and have “a nominal input swing of ± 0.5 V differential around the common-mode level” [148]. Therefore, the voltages that drive the differential inputs are

$$V_I^+ = 0.5 + \frac{I_C}{2} \quad (5.1)$$

$$V_I^- = 0.5 - \frac{I_C}{2} \quad (5.2)$$

$$V_Q^+ = 0.5 + \frac{Q_C}{2} \quad (5.3)$$

$$V_Q^- = 0.5 - \frac{Q_C}{2}, \quad (5.4)$$

where I_C and I_Q are voltages obtained in Eqn. (4.33) after subtracting the offsets from Eqn. (4.34). To set these desired voltages at the vector modulator inputs, differential Digital-to-Analog Converters (DACs) were used. The AD5627R 12 bits DAC with Inter-Integrated Circuit (I2C) protocol was chosen [149], with a 1.225 V reference voltage

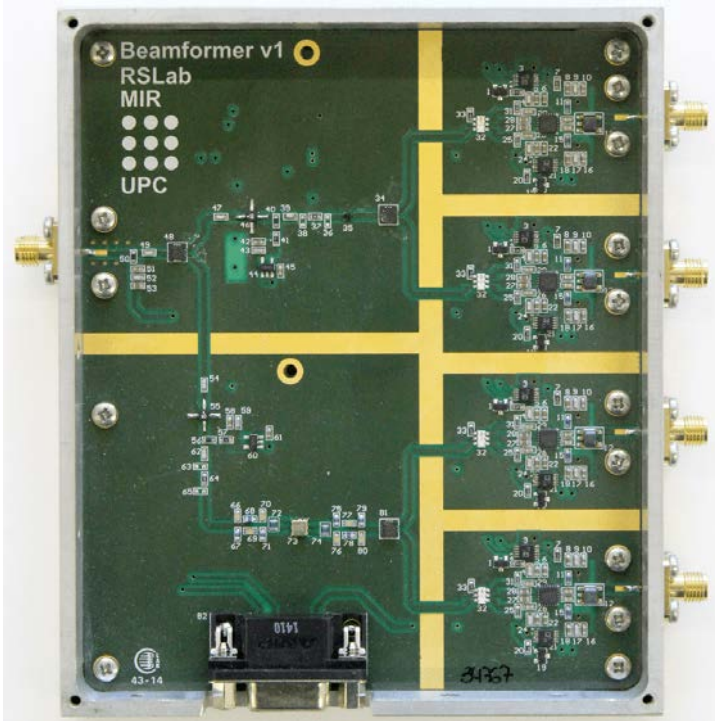


Figure 5.16: Manufactured phase shifter.

LM4041-N [150]. Therefore, the input digital value D required by the DACs to obtain an output voltage V is:

$$D = \frac{V}{1.225} \cdot (2^{12} - 1) \quad (5.5)$$

Each beamformer block has 152 DAC (19 boards x 4 Vector Modulators/board x 2 DAC/Vector modulators), so it is therefore required to use a serial protocol to control all these devices. I2C protocol instead of Serial Peripheral Interface (SPI) was chosen to avoid having a control line for each device, which would had been impractical. The chosen DACs only have three possible addresses, which are selected forcing a certain voltage to a pin, so it was required to have a 4-port I2C multiplexer in each beamformer board (see Fig. 5.17). The PCA9546A multiplexers have an address in the range 0x71 to 0x75 [151]. Five of these boards were connected to the same I2C line, which was in turn connected to one of the inputs of a multiplexer with address 0x70. The input of this multiplexer was connected to one of the I2C ports of the embedded system. The boards are stacked vertically in the “motherboard” (see Fig. 5.15c). The schematics and the PCB design can be seen in Appendix A.3.

In order to study the linearity of the phase shifters and avoid any saturation caused by the received or the calibration signals, the gain response to a power sweep was measured to find the 1 dB compression point at both frequency bands. Figure 5.18 shows a P_{1dB} of -9 dBm at L1/E1 and -13 dBm at L5/E5A. The calibration signal could reach this power level after the RF Front-end gain: Section 5.3.6 will analyze the gain response of an RF

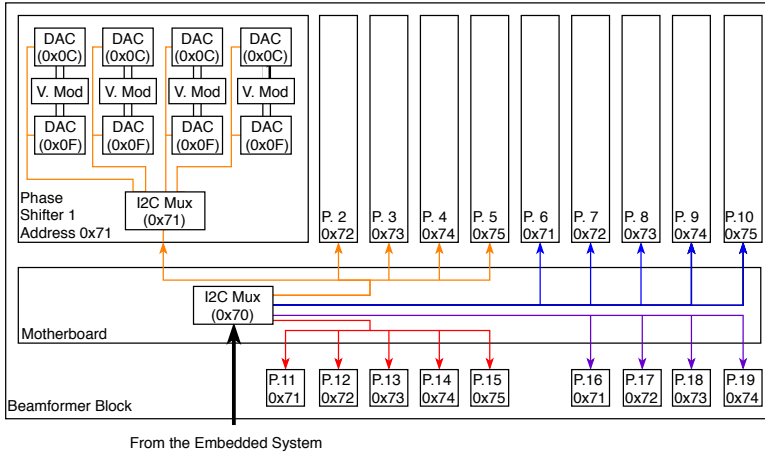


Figure 5.17: Block diagram of the I2C network.

Front-end connected to a phase shifter to find the 1 dB compression point of both the antenna and the calibration port.

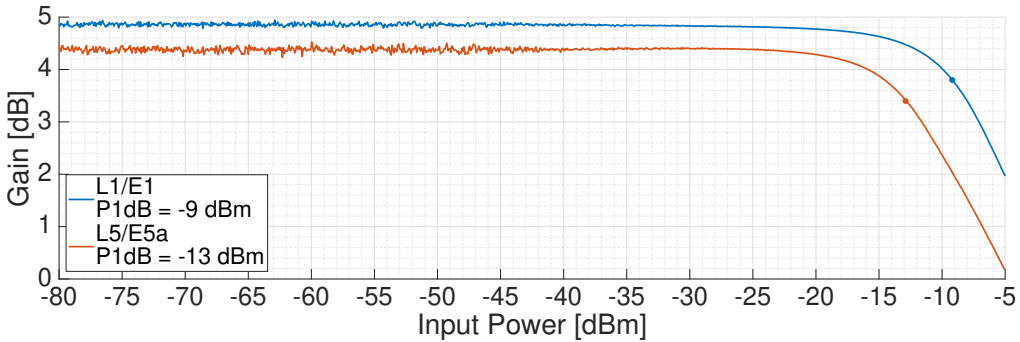


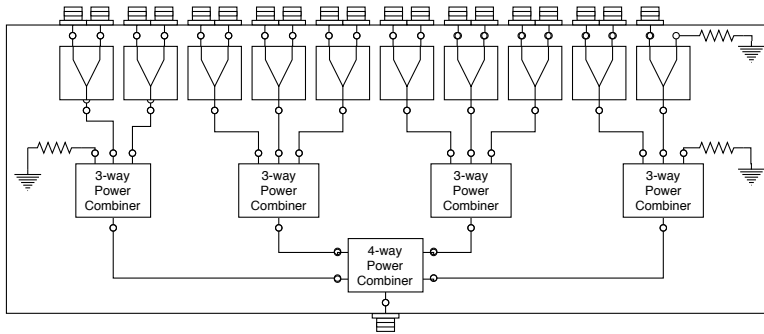
Figure 5.18: Gain response of the phase shifter as a function of the input power.

Each phase shifter board consumed an average of 4.65 W (620 mA at 7.5 V). The power supply is provided by the motherboard.

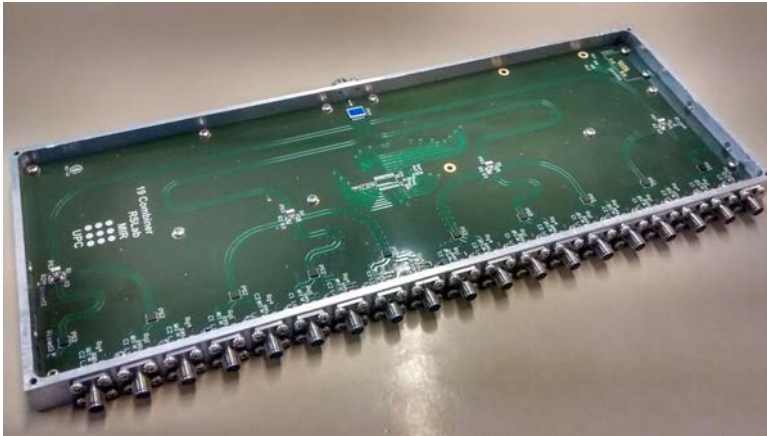
5.3.2 19-way Power Splitters/Combiners

The 19-way power combiners were designed using 4-to-1, 3-to-1, and 2-to-1 power splitters in cascade (see Fig. 5.19). The schematics, the PCB and the housing CAD design can be seen in Appendix A.4.

Due to the large number of measurements required, only one of the 19-way power combiners was fully characterized. To ensure the rest of them worked properly, just the transmission S-parameters were checked. Figure 5.20 shows the measured total transmission losses of one of the manufactured 19-way power combiners. The statistics about the transmission gain and phase are shown in table 5.4. Note again that S_{out} parameters have



(a)



(b)

Figure 5.19: a) Block diagram of the 19-way power combiners, and b) manufactured power combiner.

a higher dispersion at L1/E1 frequency band, but that also its average value is lower. The measured S-parameters plots of the measured power combiner can be found in Appendix B.2.

5.3.3 Motherboards

The Phase shifter boards of each beamformer were designed to be stacked in parallel in a single board, the so-called Motherboard, as can be seen in Fig. 5.15b. These two boards are not only in charge of mutiplexing the I2C signals, but also to feed the phase shifter boards, which in turn feed the RF Front-ends. Table 5.5 summarizes the power consumption of the RF Front-ends and the phase shifters, so each motherboard has to deliver a constant current of 13.7 A. The tracks were designed to support this current using the standard defined in the standard IPC-2221 [152]:

$$A = \frac{I}{(k \cdot \Delta T^b)^{\frac{1}{c}}}, \quad (5.6)$$

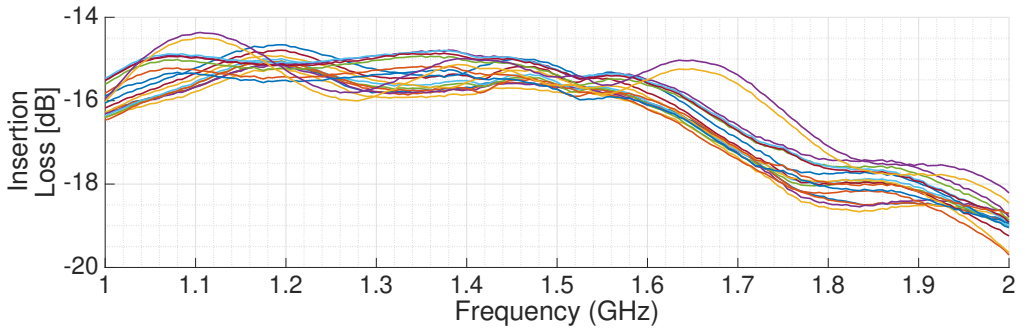


Figure 5.20: Measured total insertion losses of one of the manufactured 19-way power combiners.

Table 5.4: Insertion losses and Phase statistics of one of the 19-way power combiners at L1/E1 and L5/E5A frequency bands. For the insertion losses, the geometric mean and geometric standard deviation have been used. S_{SUM} stands for the sum port, and S_{ii} for the rest of the ports.

	L1/E1	L5/E5A
S_{SUM}	-15.1 dB	-14.6 dB
Insertion Losses	$\mu = 15.7$ dB $\sigma = 0.2$ dB	$\mu = 15.1$ dB $\sigma = 0.2$ dB
Phase	$\sigma = 2.7^\circ$	$\sigma = 1.1^\circ$
S_{ii}	$\mu = -37.5$ dB $\sigma = 4.5$ dB	$\mu = -27$ dB $\sigma = 2$ dB

where A is the cross-section of the track, I is the current, ΔT is the maximum temperature rise, and $k = 0.048$, $b = 0.44$, and $c = 0.725$ for external tracks. For a current of 13.7 A, a track thickness of $35 \mu m$, and a maximum temperature rise of $10^\circ C$, the required track width is approximately 10 mm.

The schematic, the PCB design, and the box design can be found in Appendix A.5.

Table 5.5: Summary of the power consumption of the RF Front-ends, the phase shifters, and the expected power consumed by each beamformer block.

	Measured Drained current	Estimated dissipated power
RF Front-end (x1)	100 mA @ 7.5V	0.75 W
Phase Shifter board (x1)	620 mA @ 7.5 V	4.65 W
Total (per beamformer)	13.7 A @ 7.5 V	102.8 W

Table 5.6: Summary of the required cables per beamformer from the phase shifter boards to the 19-way power combiners. All connectors were SMA straight aerial. In parenthesis, the number of spare ones.

Band and Beam	Length	Number
L1-1	248 mm	19 (+2)
L1-2	196 mm	19 (+2)
L5-1	146 mm	19 (+2)
L5-2	106 mm	19 (+2)

5.3.4 Beamformer Integration

Once all phase shifter boards, the 19-way power combiners, and the motherboards were tested, the two beamformer blocks were assembled using U-shaped aluminum profiles on their sides so they can slide along 30x60 mm standard aluminum profile (see Appendix D.2 for the detailed CAD of their assembly and Fig. 5.21 for a front and back view of the first version of one of the assembled beamformers). The phase shifters are screwed to the motherboard box, and both the motherboard and the power combiners are screwed to the U-shaped aluminum profiles. In this way, the weight of the phase shifters and the motherboard rests directly in the aluminum profiles where the U-shaped are fitted in, whereas the U-shaped profile only hold the weight of the power combiners. The required number of cables and their lengths for each beamformer are shown in Table 5.6.

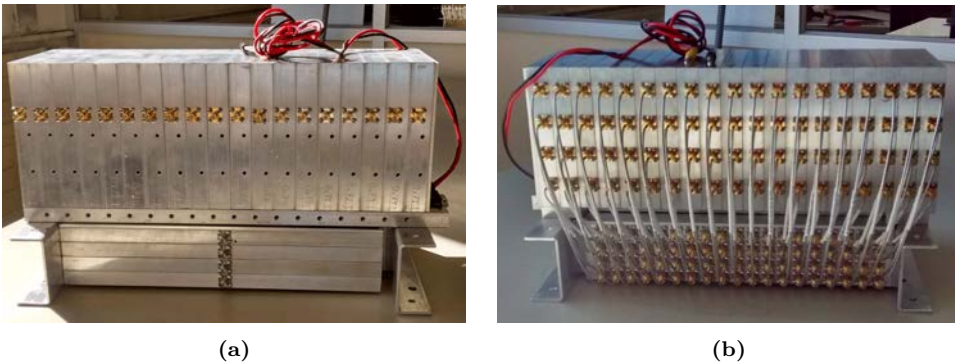


Figure 5.21: a) Front view, and b) back view of one of the assembled beamformers prior to add forced ventilation.

As soon as the first tests were conducted, high temperatures were reached in the sides of the boxes. First, 5 contiguous phase shifters were mounted in a motherboard, were fed, and a thermal camera [153] was used to measure the temperature of the central phase shifter less than an hour after they were turned on. Figure 5.22 shows the temperature at the center of the image of about 50 °C (white cross) and the point with the highest temperature (red cross). In this experiment only the central element was measured, but the farther to the center of the beamformer, the colder it is expected the phase shifter to be. In order to avoid the risk of overheating, ventilation was added.

A thermal simulation was carried out to determine whether non-forced ventilation

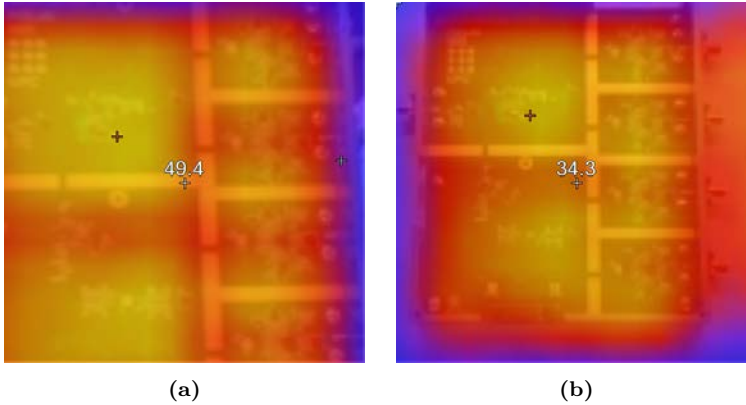


Figure 5.22: Two thermal images of one of the phase shifter boards after 15 minutes being turned on between 4 other phase shifter boards. The white cross shows the temperature at the center of the image. The red cross shows the maximum temperature in the image. The images were taken before adding the forced ventilation.

would be enough to keep a low temperature using the previously measured power consumption of each phase shifter board (see table 5.5). Then, the simulations in Fig. 5.23 were carried out using Ansys Icepak. Results in Fig. 5.23a show a maximum of 65 °C if only two slits were carved to allow ventilation, one on the left side and one in the top. Adding forced ventilation reduced the maximum temperature to 37 °C as seen in Fig. 5.23b. The CADs of the modified boxes and the pieces that hold the fans can be seen in Appendix A.3. Figure 5.24 shows a beamformer once it was modified to include forced ventilation.

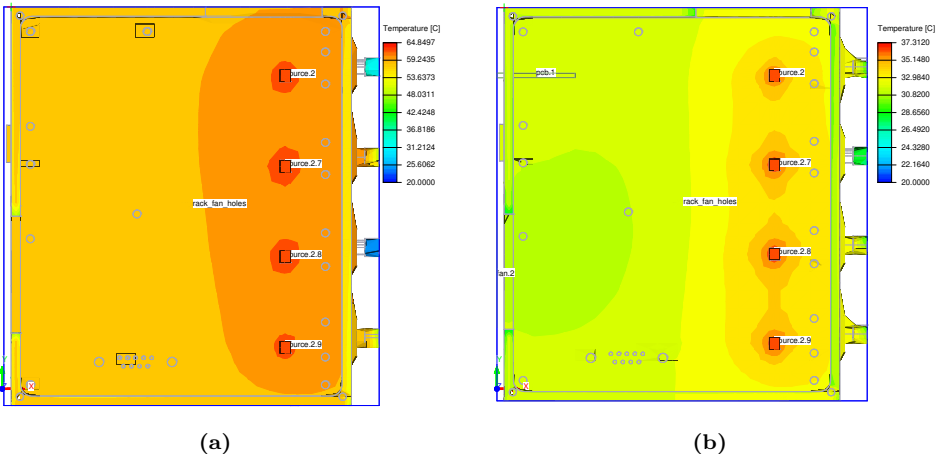


Figure 5.23: Ansys Icepak thermal simulation with a) no forced ventilation (maximum temperature: 65 °C), and b) forced ventilation (maximum temperature: 37 °C).

From this point it was considered safe to test the beamformers. First, the S-parameters of both beamformers were measured. Figures 5.25a shows the measured I ($G_I=1$, $G_Q=0$)

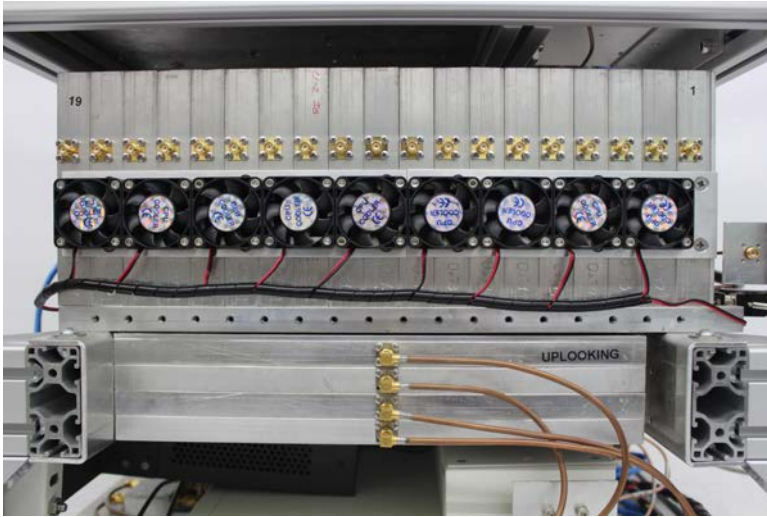


Figure 5.24: Modified beamformer including forced ventilation.

and Q ($G_I=0, G_Q=1$) gains of the 19 phase shifter boards of one beamformer. Figure 5.25a shows the gains of the two beams at L1/E1 frequency band (Beam L1-1 and beam L1-2), and Fig. 5.25b shows the gains of the two beams at L5/E5A frequency band (Beam L5-1 and beam L5-2). Ideally, the I and Q gains should be equal for all the phase shifters.

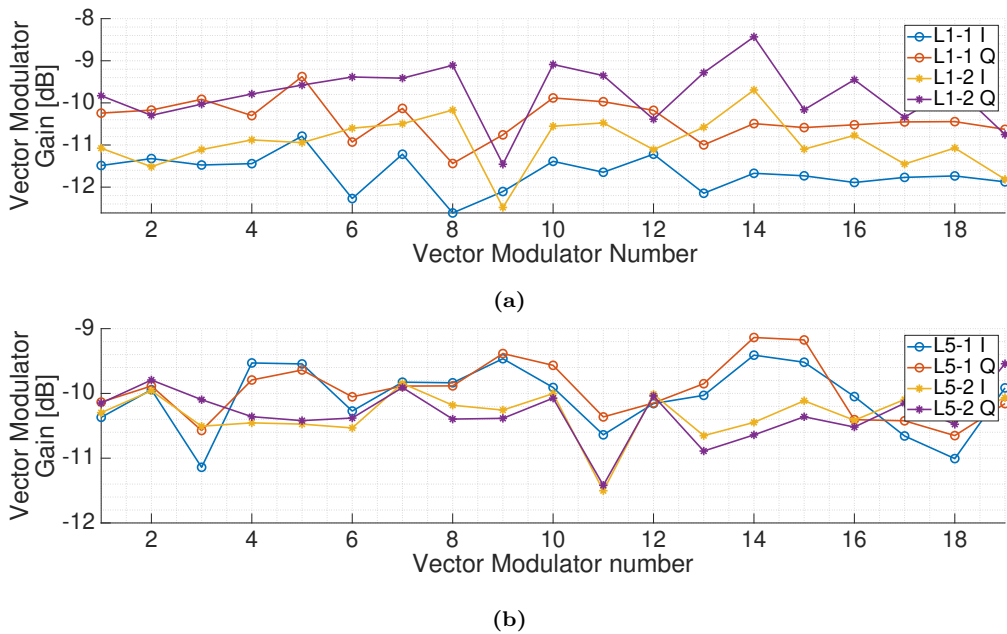


Figure 5.25: Measured I and Q gains of one of the beamformers at a) L1/E1, and b) L5/E5A frequency bands.

Figure 5.26a shows the measured phase difference between the I and Q gains of the 19 phase shifter boards of one beamformer. Figure 5.26a shows the phase difference of the two beams at L1/E1 frequency band, and Fig. 5.26b shows the phase difference of the two beams at L5/E5A frequency band. Ideally, they all should be 90° . The cause of the average IQ Phase difference being higher than 90° in all cases remains unknown.

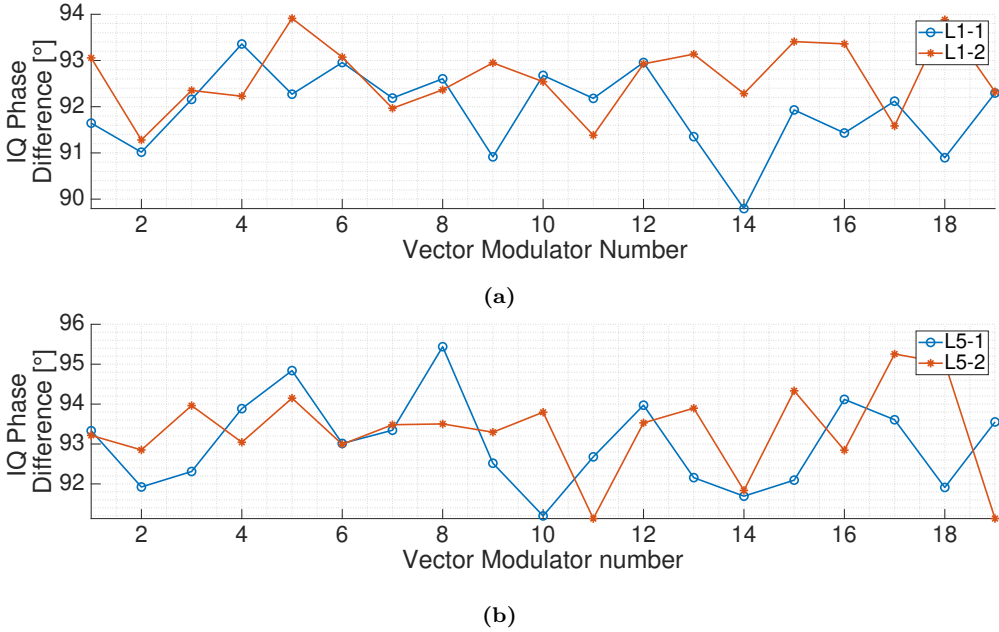


Figure 5.26: Measured I and Q phase differences of one of the beamformers at a) L1/E1, and b) L5/E5A frequency bands.

Table 5.7 shows a summary of the measured S-parameter of both manufactured beamformers. The complete set of measurements can be found in Appendix B.3. To obtain the calibration parameters g , α , L , and φ more than two measurements are needed, however for this set of measurements only two measurements per vector modulator were taken, just to check that the beamformer was working properly. However, the parameters $\angle(I/Q)$ and $\angle(S_{21}) - 90$ are approximations to the L and φ calibration parameters. Chapter 6 will show the calibration parameters of all beamformers, the impact of these parameters in the array directivity, and how the calibration process improves it.

5.3.5 Extra RF Amplifiers in the Down-looking RF Chains

After the scattering on the Earth's surface, the reflected signal power in an airborne case is expected to be 0-30 dB lower than the direct one [154]. This power loss has to be compensated in order to ensure that the received power at the input of the down-looking USRPs is at least as strong as at the input of the up-looking ones. To do so, two RF amplifiers with a total gain of ≈ 35 dB and noise figure ≈ 3 dB are placed between the down-looking beamformer and the USRPs in all RF chains. The schematics, the PCBs and the box design can be found in Appendix A.9. One of the manufactured amplifier

Table 5.7: S-parameters summary of the two manufactured beamformers.

	Direct Beamformer		Reflected Beamformer	
	L1/E1	L5/E5A	L1/E1	L5/E5A
$ S_{11} ^2$	$\mu = -10.3$ dB $\sigma = 0.5$ dB	$\mu = -24.9$ dB $\sigma = 2.95$ dB	$\mu = -10.1$ dB $\sigma = 0.5$ dB	$\mu = -24$ dB $\sigma = 2.7$ dB
$ S_{21} ^2$	$\mu = -10.6$ dB $\sigma = 0.9$ dB	$\mu = -9.9$ dB $\sigma = 0.7$ dB	$\mu = -10.7$ dB $\sigma = 0.9$ dB	$\mu = -10.2$ dB $\sigma = 0.5$ dB
$\angle(S_{21})$	$\sigma = 6.4^\circ$	$\sigma = 7.6^\circ$	$\sigma = 6^\circ$	$\sigma = 9.7^\circ$
$ I/Q ^2$	$\mu = 1.3$ dB $\sigma = 0.4$ dB	$\mu = -0.1$ dB $\sigma = 0.5$ dB	$\mu = 1.2$ dB $\sigma = 0.2$ dB	$\mu = 0.1$ dB $\sigma = 0.2$ dB
$\angle(I/Q)$	$\mu = 92.1^\circ$ $\sigma = 1.4^\circ$	$\mu = 93.4^\circ$ $\sigma = 1.4^\circ$	$\mu = 92.3^\circ$ $\sigma = 0.9^\circ$	$\mu = 93.2^\circ$ $\sigma = 1.1^\circ$
$ S_{22} ^2$	$\mu_{L1.1} = -9.8$ dB $\mu_{L1.2} = -19.3$ dB	$\mu_{L5.1} = -9.6$ dB $\mu_{L5.2} = -9.4$ dB	$\mu_{L1.1} = -8.6$ dB $\mu_{L1.2} = -19.2$ dB	$\mu_{L5.1} = -10.9$ dB $\mu_{L5.2} = -9.3$ dB

boxes can be seen in the bottom left corner of Fig. 5.30a.

5.3.6 RF Front-ends and Beamformer Connection Test

In order to study the linearity of the RF Front-ends combined with the phase shifters, the previous data of both measurements was mixed in Fig. 5.27. The expected P_{1dB} at the antenna ports are -37 dBm and -42 dBm at L1/E1 and L5/E5A frequency bands, respectively. The expected P_{1dB} at the calibration port are -10 dBm and -12 dBm at L1/E1 and L5/E5A frequency bands respectively.

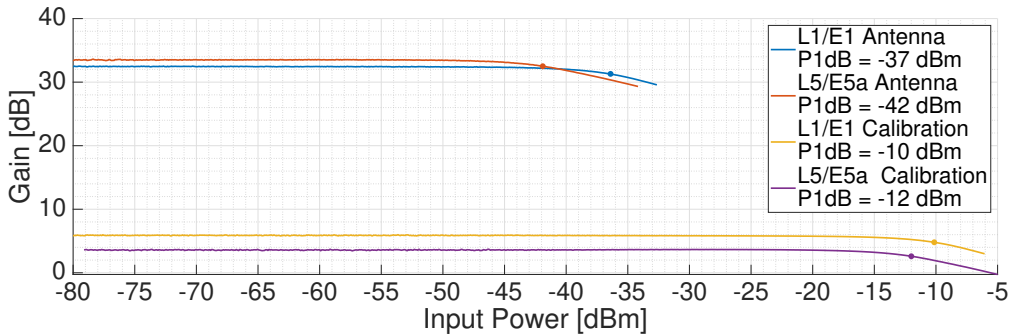


Figure 5.27: Gain response to a power sweep of the RF Front-end and the phase shifter combined.

5.4 Data Sampling and Processing

The outgoing data from the beamformers is sampled using 4 SDRs (see Fig. 5.28). Each pair of beams is sampled synchronously with a two-input SDR from Ettus Research model X310 [155]. The original firmware of the USRPs sample the data at base-band at

210 Msps and 28 bits (14 bits I + 14 bits Q). The data is received by a FPGA which encapsulates it into the User Datagram Protocol (UDP) streams to avoid unnecessary headers and sends them through 1 Gigabit Ethernet. The RF signals must be down-converted prior to be sampled, which is done by the daughterboards, interchangeable PCBs that cover different frequency ranges.

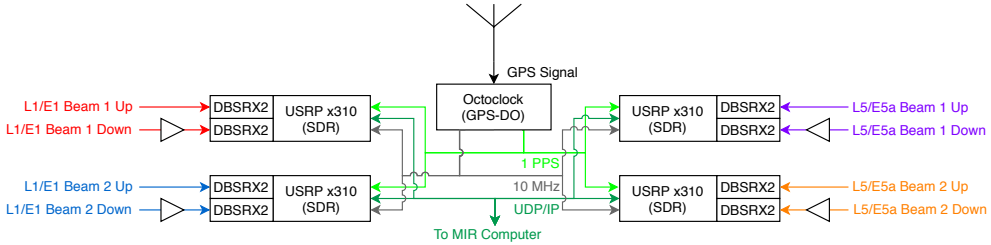


Figure 5.28: Block diagram of the data sampling system.

Each SDR has two DBSRX2 daughterboards [156] capable of doing a direct down-conversion in the range of frequency range 800-2300 MHz of the received signals. The FPGA configures the down-converter, which cannot synthesize perfectly the desired frequencies: $f_{L1} = 1575.42 \text{ MHz} - 2 \text{ Hz}$ and $f_{L5} = 1176.45 \text{ MHz} + 2 \text{ Hz}$. The firmware of the USRPs had to be modified to first make the X310 compatible with the DBSRX2, and then to include a digital down-conversion block that compensates the little error in the analog down-conversion.

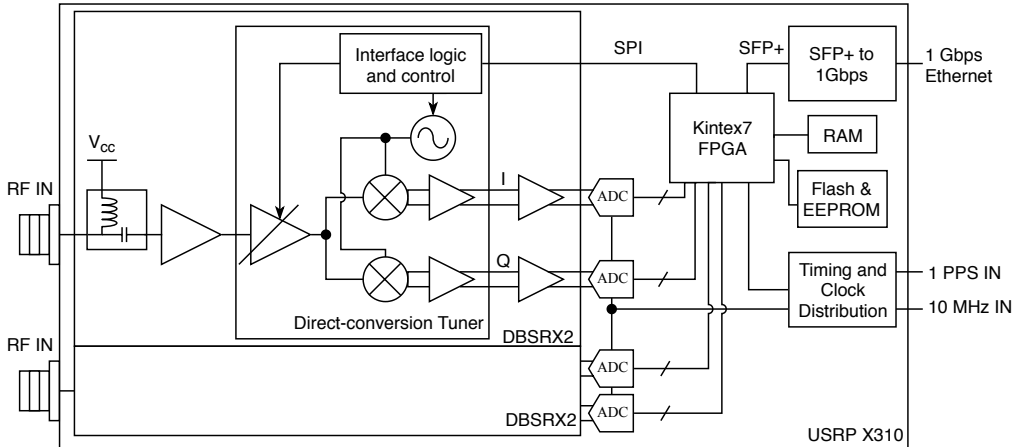


Figure 5.29: Simplified block diagram of the USRP x310 with two DBSRX2 daughterboards.

The two daughterboards inside each USRP must be synchronized, otherwise the relative measurements between the direct and the reflected signal will have errors. For instance, if the local oscillator of the daughterboards is not synchronized, the phase difference between them will be constantly rotating due to this residual frequency difference. Besides, the USRPs must be synchronized between them, for example for the calibration

process, and timestamping of the data is required for later geolocating it. For this purpose an Octoclock [157] was used, which is a device that uses a GPS-DO that generates a 10 MHz reference frequency signal and a 1 Pulses Per Second (PPS) signal for frequency and time synchronization respectively. The device also includes a distribution network to avoid any delay between signals. The Octoclock also provides the current date, which is timestamped to the data in the USRPs. Once the data is received by the computer, it is stored in a Solid State Disk (SSD) for later post-processing.

The 4 USRPs originally generated a data stream of

$$4 \text{ USRP} \cdot \frac{2 \text{ channels}}{1 \text{ USRP}} \cdot \frac{210 \text{ Msps}}{1 \text{ channel}} \cdot \frac{28 \text{ bits}}{1 \text{ sample}} = 47 \text{ Gbps}, \quad (5.7)$$

so the firmware had to be modified to sample using 1 bit I + 1 bit Q at a sampling frequency of $32 \cdot 1.023 \text{ Msps} = 32.736 \text{ Msps}$, which generates a data stream of 0.52 Gbps. Data streams over 0.8 Gbps can not be sustained even storing the data in a SSD. All of these modifications and the justification of all these decisions, such as choosing 1 bit or that particular bandwidth, are part of another Ph.D. thesis and are explained in depth in [29].

Figure 5.30 shows the data sampling system once it was mounted.

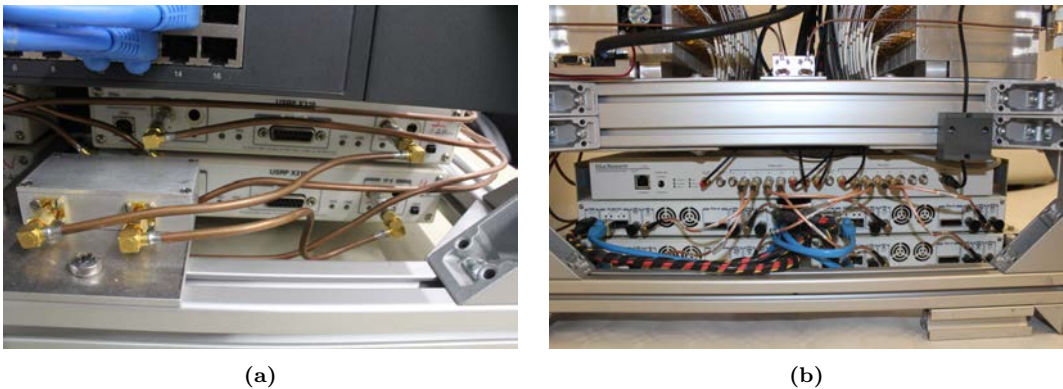


Figure 5.30: a) Front view, and b) back view of the data sampling subsystem. On the front view, the input connectors for the RF signals, and a box with the RF amplifiers for two of the USRPs can be seen. On the back view, the octoclock and the distribution of the time and frequency synchronization signals can be seen.

5.5 Calibration System

The instrument calibration is conducted in two steps, a first one in an anechoic chamber, and a second one with a calibration system embedded in the instrument. This calibration system (see Fig. 5.31) uses a periodic signal made of a concatenated sequence of 10 L5 PRN codes (10x10230 chips). The use of PRN codes to calibrate microwave radiometers was already proven useful in 2009 [158]. The codes are generated in a USRP N210 [159] which uses a 400 Msps DAC able to generate the PRN at intermediate frequency $f_{IF} = 100 \text{ MHz}$. The signal is generated at a 5 MHz chip rate (10 MHz bandwidth), with a

total sequence length of $T_c = 10$ ms (the last 2300 chips are removed), and a repetition period of T_c .

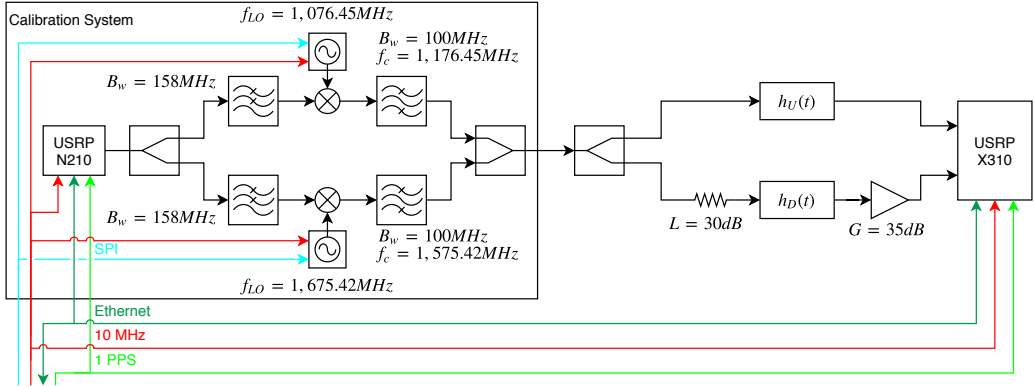


Figure 5.31: Calibration system block diagram.

The calibration signal is first split to be up-converted simultaneously at the two desired bands and then it is low-pass filtered to avoid odd harmonics of the PRN sequence to be up-converted. The filter is placed after the power splitter to avoid any leakage from one the mixers to propagate to the other mixer. The SPI controlled Local Oscillator (LO) [160] generate tones at $f_{LO-L1} = 1.67542$ GHz and $f_{LO-L5} = 1.07645$ GHz respectively. These devices use a fractional-N Frequency synthesizer [161] that generate tones at

$$F_{OUT} = F_{REF} \cdot \frac{1 + D}{R} \cdot \left(INT + \frac{FRAC}{MOD} \right), \quad (5.8)$$

where $F_{REF} = 10$ MHz is the reference frequency, and $0 \leq D \leq 1$, $1 \leq R \leq 15$, $31 \leq INT \leq 511$, $2 \leq MOD \leq 4095$, and $0 \leq FRAC \leq MOD - 1$ are configurable parameters chosen as shown in table 5.8.

Table 5.8: Chosen values for the configurable parameters of the frequency synthesizers.

F_{OUT}	D	R	INT	$FRAC$	MOD
1.67542 GHz	0	1	167	271	500
1.07645 GHz	0	1	107	129	200

The up-converted PRN codes are then located at $f_{LO-L1} - f_{IF} = 1.57542$ GHz and $f_{LO-L5} + f_{IF} = 1.17645$ GHz, and spectral replicas are expected at $f_{LO-L1} + f_{IF} = 1.77542$ GHz and $f_{LO-L5} - f_{IF} = 976.45$ MHz. In this way, the spectral replicas will be more attenuated by the high and low pass filters of the RF Front-ends. The up-converted PRN sequences pass through large bandwidth pass-band filters (90 MHz at L1/E1 [162], and 120 MHz at L5/E5A [163]), in order not to distort the spectrum of the calibration signal in the frequency band that has to be calibrated. After filtering, the up-converted signals are summed using a power combiner. Last, the calibration signal is

split to distribute the calibration signal to both arrays. Since the down-looking chain has 35 dB extra gain and the calibration signal is over the noise floor (see Fig. 5.35), a 30 dB attenuator is placed after the power splitter to avoid the saturation of the data sampling system during the calibration. Once the calibration process has finished, the synthesizers are digitally turned off.

Figures 5.32 and 5.33 show the expected transfer function after up-converting a baseband signal in L1/E1 and L5/E5A frequency bands respectively. The top x-axis shows the resulting frequency after up-converting a signal at the frequency shown in the lower x-axis. The yellow line represents a transmitted-like PRN code spectrum, which is split and then filtered by the red filter. The up-converted PRN signals, their aliases, and the local oscillator leakage (in pink) are band-pass filtered (in blue). The signals in the figures are representations of the expected one, and their power is merely representative.

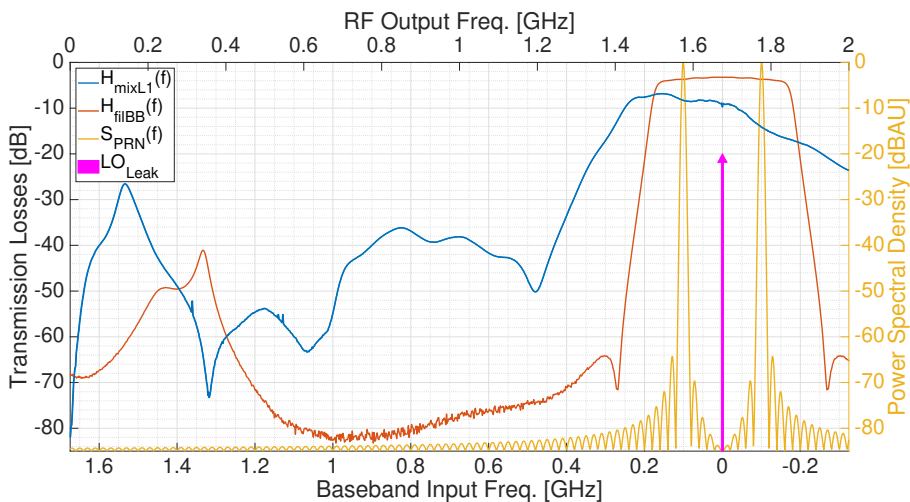


Figure 5.32: Measured transfer function after the L1/E1 up-conversion in blue. Measured baseband power splitter and low-pass filter transfer function in red. Transmitted PRN-like spectrum in yellow. Local Oscillator leakage representation in pink.

Appendix A.6 shows the schematics, PCBs, enclosures and the integration design of the calibration system hardware. Figures 5.34a and 5.34b show images of one of the synthesizers and the mixers respectively, and Fig. 5.34b shows the integrated system mounted over the transmitting USRP N210. Note that the two synthesizers and the two mixers are mounted one over the other, and that the power combiner and power splitter are mounted sideways.

The outgoing measured spectrum can be seen in Fig. 5.35. The bands to be calibrated are highlighted in green. In red the spectral replicas are shown, and in yellow the local oscillator leakages. The PRN codes were generated at the highest intermediate Frequency (IF) possible in order to separate as much as possible the up-conversion aliases and the LO leakage respect to the useful frequency band.

The transmitting SDR, the receiving SDR and the local oscillators used for the up-conversion all have a common 10 MHz reference. The transmitting and receiving devices

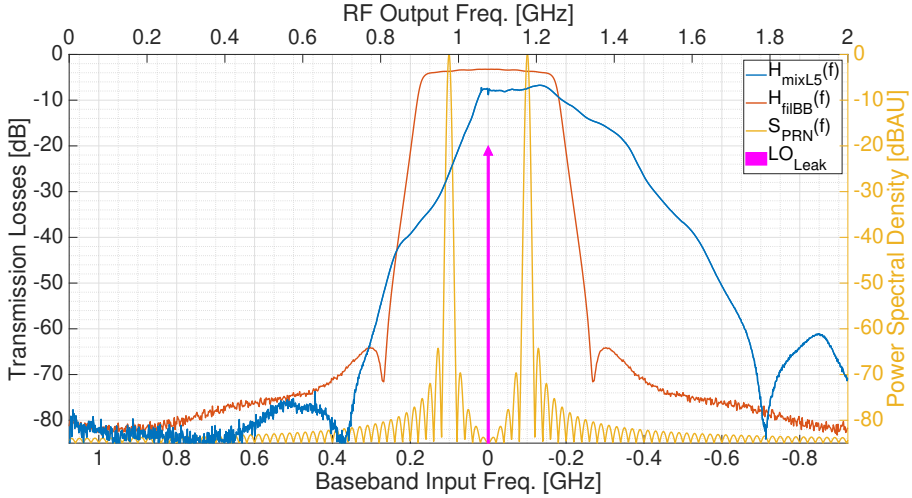


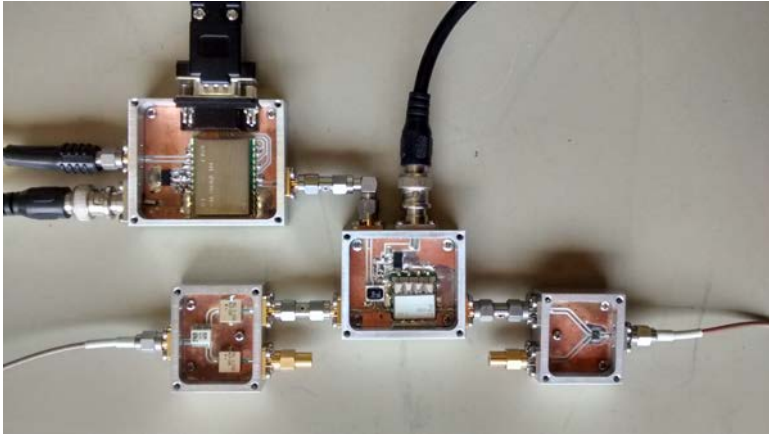
Figure 5.33: Measured transfer function after the L5/E5A up-conversion in blue. Measured baseband power splitter and low-pass filter transfer function in red. Transmitted PRN-like spectrum in yellow. Local Oscillator leakage representation in pink.

are also synchronized using a 1 PPS signal, in which the rising edge of the PPS signal is used to begin transmitting the PRN sequences in the N210 and the data sampling in the X310. The calibration signal is injected in the up-looking array $h_U(t)$ and in the down-looking array $h_D(t)$.

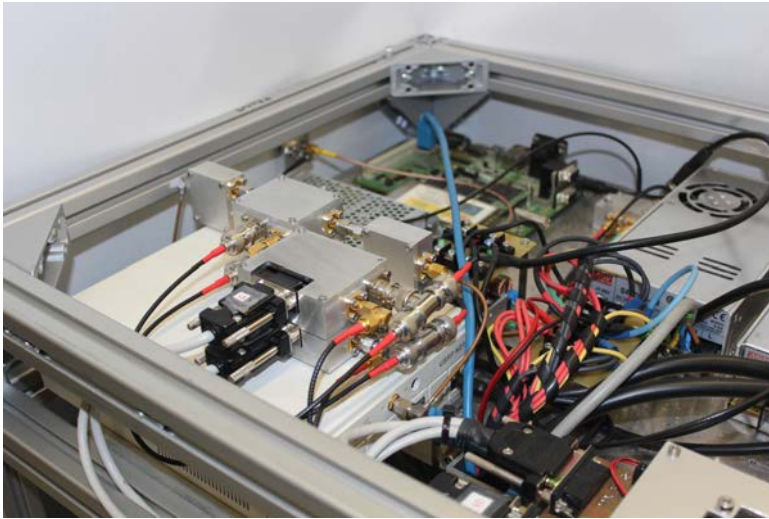
5.6 Position and Attitude Determination System

In order to properly point to the desired GNSS satellites, the MIR instrument requires a knowledge of the position and attitude of the instrument, and the position of the satellites. The position of the instrument is provided by a Trimble BD982 GNSS receiver with an accuracy at 1-sigma level below 1 meter using simultaneously for this purpose GPS, Galileo, GLONASS, and SBAS satellites [127]. Besides, the receiver has two antenna input connectors that can be used to determine two of the three Euler angles that determine the platform attitude with an accuracy below 1° . The two multiband and multisystem GNSS antennas [126] are placed at each side of the up-looking antenna, along the pitch rotating axis, thus determining the yaw and roll of the platform. The main antenna, the one used by the GNSS receiver to acquire the GNSS signals, is directly connected to the GNSS receiver, which feeds it. The auxiliary antenna, the one used to determine the attitude, is connected to a power splitter that feeds the auxiliary antenna and also distributes the GNSS signals to the GNSS receiver and to the Octoclock. The schematic, the PCB design, and the housing design can be seen in Appendix A.7.

In order to estimate the third Euler rotation angle, the pitch, an analog inclinometer Seika NG-4 [164] with better resolution than 0.01° is aligned with the pitch axis and screwed to one of the sides of the up-looking array. The inclinometer is held in an aluminum plate that also holds a PCB with the DAC that samples the analog output of the sensor. The schematic, PCB, and the design of the piece that holds both the



(a)



(b)

Figure 5.34: Photos of the a) uncovered boxes that contain the synthesizer (top left), the baseband power splitter (bottom left), the mixer (center), and RF power combiner, and b) the calibration system mounted over the transmitting USRP N210. Note in a) that only one of the mixers and synthesizers are mounted, and in b) the semi-rigid cable connecting the output of the USRP N210 to the calibration up-converter.

inclinometer and the PCB can also be found in Appendix A.7.

Rarely, if the visibility of the GNSS receiver suddenly changes and the receiver loses track of some satellites, the receiver can also temporarily lose the attitude determination capability, so a redundant Razor 9-DOF Inertial Measurement Unit [165] was added to avoid not knowing the attitude.

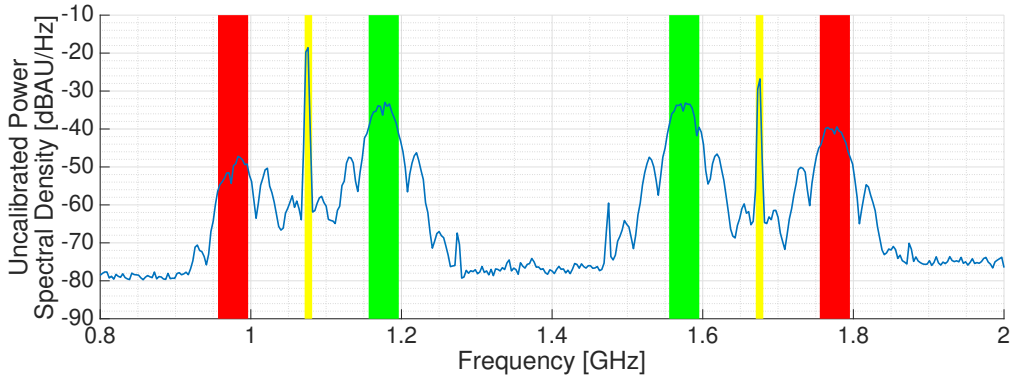


Figure 5.35: Measured spectra of the transmitted calibration signal at L1/E1 frequency band (left), and at L5/E5A frequency band (right). In green, the region of the spectrum that will be used for calibration. In red, the spectral replicas. In yellow, the local oscillator leakage.

5.7 Linux Embedded System

A Wandboard Quad revision C1 [166] Linux embedded is in charge of controlling the rest of the subsystems (see Fig. 5.36). This embedded system was chosen because it has 3 I2C ports (one for each beamformer, and a third one to control the switches in the RF Front-ends, even though this functionality was later dismissed), at least one SPI port for the calibration system, a Universal Serial Bus (USB) port for the redundant IMU, and General Purpose Input/Output (GPIO) pins. It also has four cores, which are used to run in parallel the threads that control each beamformer, thus speeding up the refresh rate of the beams up to approximately 333 ms, lower than the 500 ms desired in Section 4.6. The embedded system consists of two boards: the upper one, the CPU module, where the CPU, the RAM, and the SD card socket used to boot the system are placed, and the baseboard, where all the voltage regulators, external drivers, a secondary SD card socket, and connectors are located.

During the start-up, the embedded system enters into the calibration mode by turning on the calibration block using the SPI protocol and one of the phase shifter boards of each beamformer using the I2C protocol, and after finishing it turns off the calibration block to avoid any leakage in to the system. Once in the normal mode, it periodically retrieves the available GPS and Galileo satellites, the position of the platform, and two of the Euler angles of the platform attitude from the GNSS Receiver using Transmission Control Protocol/Internet Protocol (TCP/IP) and Universal Asynchronous Receiver-Transmitter (UART). The third Euler angle is sampled from the inclinometer using a SPI controlled Analog-to-Digital Converter (ADC). Then, the embedded system chooses the satellites to track and computes the required phases and gains for each element of the array taking into account the position of the selected GNSS satellites, the position and the attitude of the instrument, and the calibration parameters. These gains and phases are then converted to the required voltages at the vector modulator control pins, and are sent to the I2C controlled DAC. The whole process is explained in detail in Section 5.9. The SPI and I2C ports are accessible through an expansion port (see Fig. 5.37) that

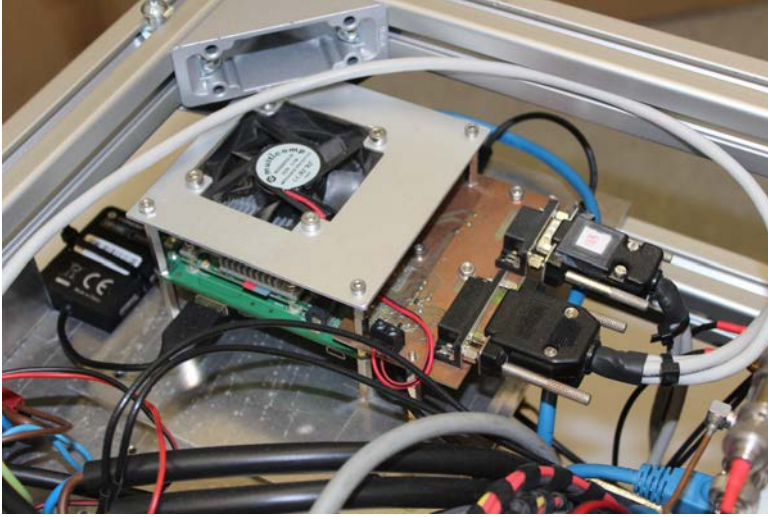


Figure 5.36: Embedded system with the expansion board to safely attach the cables that communicate with the beamformers, the calibration system, and the inclinometer.

require a PCB to attach safely the cables that communicate with the beamformers, the calibration system, and the inclinometer (see Fig. 5.36). Furthermore, the SPI port only had two Chip Select (CS) pins for three devices, so it was decided to use GPIO ports and OR gates to convert one of the CS pins to a three. The schematic and the PCB design of this expansion board can be seen in Appendix A.8.

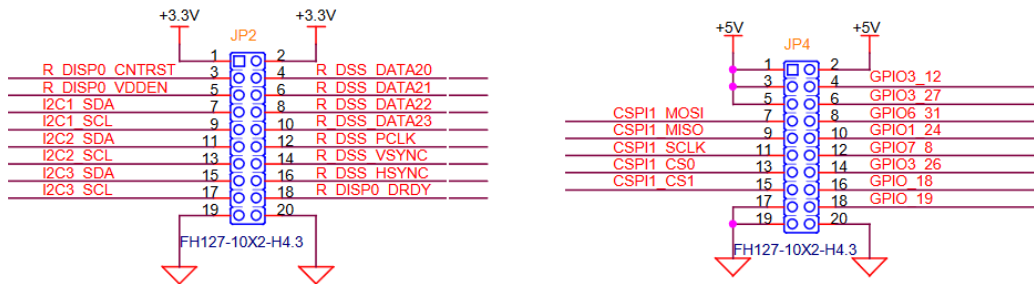


Figure 5.37: Part of the embedded system expansion port mapping. From [167].

The embedded system, as it was purchased, was not ready to be used, and some modifications had to be made:

- The available Linux images in the webpage included an old kernel which caused errors for high access rates to the I2C ports. The problem was solved by manually compiling the kernel and installing the last version of Ubuntu as explained in [168].
- The brochure of the product claimed to have 3 available I2C ports (I2C1 to I2C3 in the schematics, which correspond to the devices “/dev/i2c0” to “/dev/i2c2” inside the operating system), however only I2C2 was available. The first port I2C1 was

shared with the external HDMI hardware driver, which due to a bad design had a too low pull-up resistors that made the port unusable. The port I2C3 was internally shared in the CPU with the Ethernet pins, which was necessary for the operation of the instrument. It was then decided to hard disable the HDMI capability by removing the resistors R113 and R115 from the CPU board [169].

- The SPI ports were not enabled by default, so they had to be enabled by modifying the device tree [170] of the system and installing the “spidev” driver following the procedure described in [171].

5.8 Instrument Integration

Besides the two arrays, the instrument has a custom-made rack using 30x30 mm standard aluminum profile that holds all blocks except the arrays, the inclinometer, the GNSS antennas, and the IMU. The structure measures 500x540x530 mm and weights 70 kg approximately once all the subsystems are attached. Figure 5.38 shows the rack during the integration of the calibration subsystem when only the data sampling subsystem was attached on the bottom. Just over it, two 60x30mm aluminum profiles can be seen, which are used as rails to hold the beamformer blocks. The size and weight of each three parts of the MIR instrument (the two arrays and the rack) are provided in Table 5.9.

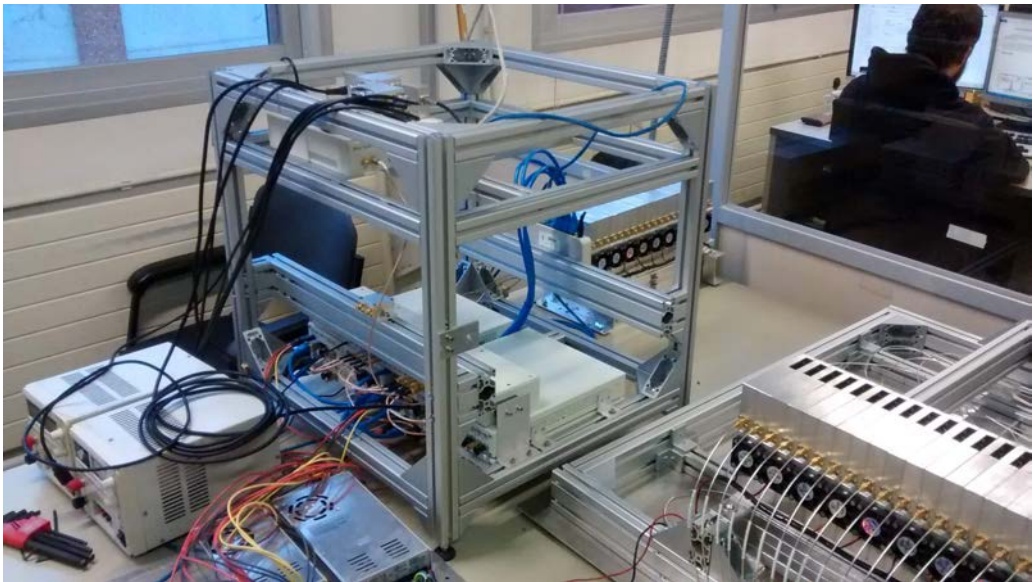


Figure 5.38: MIR rack with the data sampling subsystem attached during the integration of the calibration block.

The rack has three differentiated floors. The upper one (Fig. 5.39) has the GNSS receiver (circled in green), the calibration system (circled in blue), all power supplies (circled in white), and the Linux embedded system (circled in red). The beamformers (circled in orange) are attached in the middle level. There, the 19 cables coming from the arrays are connected to the beamformers. Additionally, there is an extra connector

Table 5.9: Total weight, size and power consumption of the three main MIR parts. The power consumption is shown as average and peak, such as during the turn on.

	Weight	Size	Power Consumption
Rack	~70 kg	500x540x530 mm	~450 W
Up-looking Array	~18 kg	800x800x60 mm	~10W
Down-looking array	~25 kg	960x960x60 mm	~10W
Total	~113 kg	-	~470 W

for the cable that connects the calibration system and the array (Fig. 5.39, bottom right). From each beamformer, the 4 output cables go to the lower floor. The cables from the up-looking beamformer are connected directly to the SDRs (circled in purple). The cables of the down-looking beamformers are first connected to RF amplifiers (circled in yellow). The bottom level has attached the gigabit Ethernet switch (circled in cyan), the Octoclock (circled in magenta), the extra RF amplifiers for the down-looking RF chain, and the SDRs. The CADs of the integration can be seen in Appendix D. The inclinometer is attached to one of the sides of the array, the GNSS antennas are attached one antenna at each side, and the IMU is attached at the front of the array. The RF systems are interconnected using coaxial cables with SMA connectors. All RF systems are fed using coaxial cables with, whenever possible, BNC connectors in order to avoid any interference being induced in the system that could potentially prevent the use of the interferometric technique. The CAD of the rack structure with the different subsystems attached to it can be found in Appendix D.3.

To carry on the calibration of the arrays and the beamformers in the anechoic chamber, they had to be attached together. Figure 5.40 shows how one of the beamformers, the power supplies, and the embedded were attached behind one of the antennas to calibrate them in the anechoic chamber. An adapting structure had to be designed to safely attach all that weight to the rotor of the anechoic chamber.

The different MIR subsystems require to be fed with different voltage levels and high current in some cases. The systems with a higher power consumption are the beamformers, and the USRPs X310. Each beamformer requires a current of 13.7 A, which is supplied by a 7.5 V, 40 A power supply. The inclinometer board, which samples and feeds the inclinometer, is also fed by the same power supply. The USRP X310 are fed by a 12 V, 20 A power supply that also feed the beamformers forced ventilation. The GNSS receiver, the calibration mixers and the calibration synthesizers are fed by a 18 V, 2.2 A power supply. The transmitting N210, the Octoclock, the GNSS power splitter, and the Linux embedded system, are fed by 5V, 12 A power supply. The remaining subsystems are fed through other subsystems: the arrays are fed from the beamformer blocks, and the IMU is fed through the USB port of the embedded system. Table 5.10 summarizes the power supplies used, and the system power consumption (average/peak) can be found in Table 5.9.

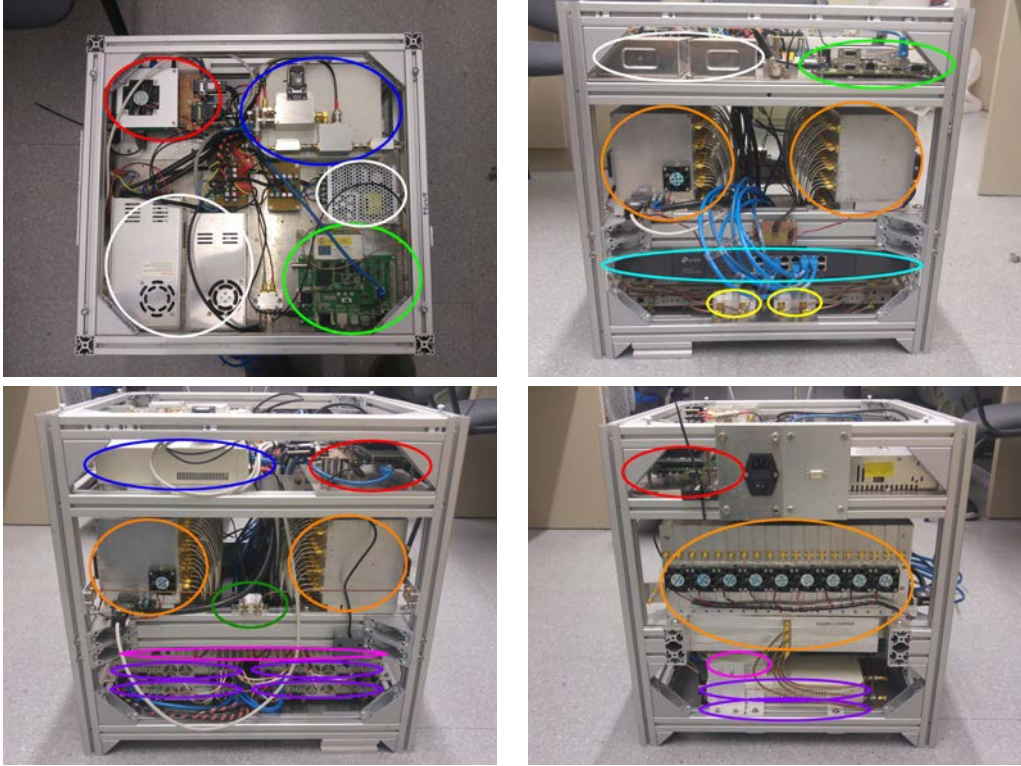


Figure 5.39: MIR rack. The top floor of the rack has the embedded system (red), the power supplies (white), the calibration system (blue), and the GNSS receiver (green). The middle floor has the beamformers (orange). The lower floor has the Octoclock (magenta), the SDR (purple), the gigabit Ethernet switch (cyan), and the extra amplifiers for the down-looking RF chain (yellow).

Table 5.10: Power supplies in the MIR instrument and subsystems fed by them.

Power supply:	18 V, 2.2 A	12 V, 20 A	7.5 V, 40 A	5 V, 12 A
Subsystem:	GNSS receiver Calibration	USRP X310 Ventilation	Beamformers Inclinometer	USRP N210 Octoclock GNSS power splitter Linux Embedded

5.9 Instrument Software

Two main programs must be run to use the MIR instrument: the controlling software, responsible of pointing the arrays to the best available satellites, and the data sampling software in charge of the USRPs, developed as part of the Ph.D. thesis [29]. This section describes the MIR controlling software.

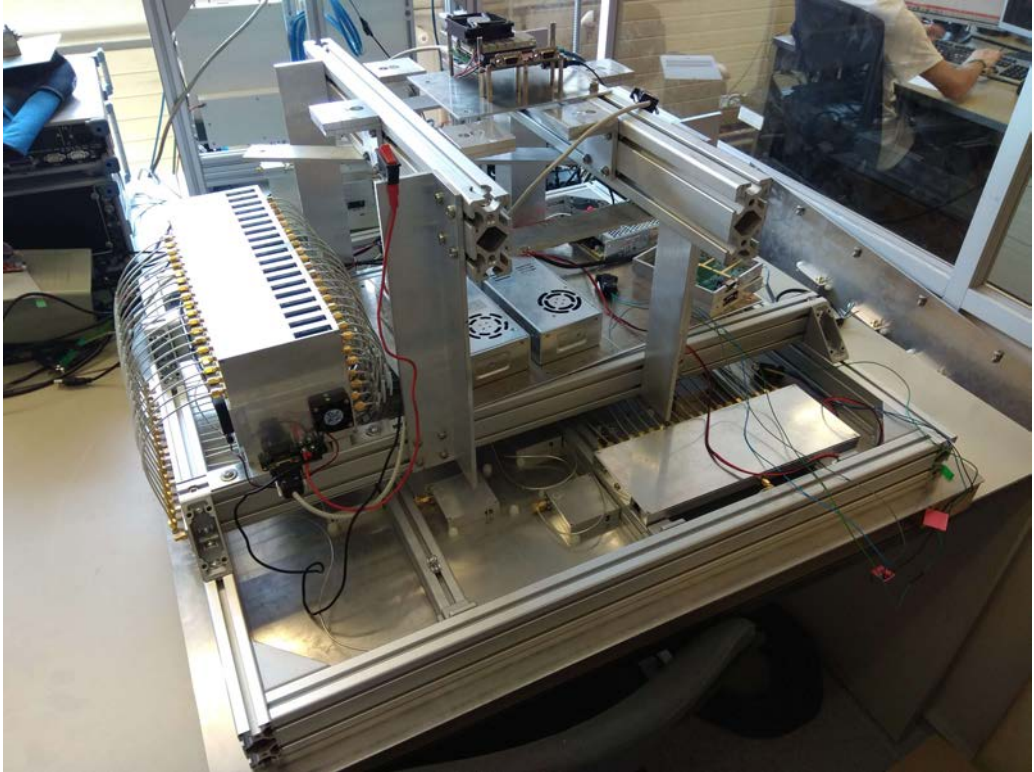


Figure 5.40: Beamformer, power supplies, and embedded system attached behind one of the arrays prior to the calibration in the anechoic chamber. An adapting structure had to be designed to safely attach all that weight to the rotor of the anechoic chamber.

The MIR controlling software has a main thread in charge of creating the rest of the threads that control the instrument. Originally, only two threads were planned: since programming the beamformers using I2C is slow, connecting the two beamformers to different I2C ports and having a thread for each one should have halved the programming time. However, as the program grew in complexity, multiple threads were created in order to simplify the code and to take advantage of the multiple embedded cores. The code currently consists of more than 11,000 code lines, and re-uses part of the GNSS Essential Project library codes [172].

The software has a main thread that initializes variables and configures the external devices to be used, creates the rest of the threads, waits until the user notifies the program to end, destroys the threads, and then releases the allocated memory. The created threads process the information sent from the GNSS receiver (GetDataFromDB982 and RT27 threads) or request some information to it (RequestSVData thread), then they read the IMU (IMU thread), compute the pointing angles (GetSVLookAngles thread), and store some log data for later post-processing and debugging.

These threads are created using pthreads instead of forks in order to have a single memory space to easily share information. The concurrent access to shared variables

has been regulated using mutex variables, and the synchronization between threads has been implemented with condition variables. Figure 5.41 shows how the different threads (rounded boxes) interact between them using shared variables (boxes with a locker), condition variables (boxes with bold text), and external devices (parallelograms).

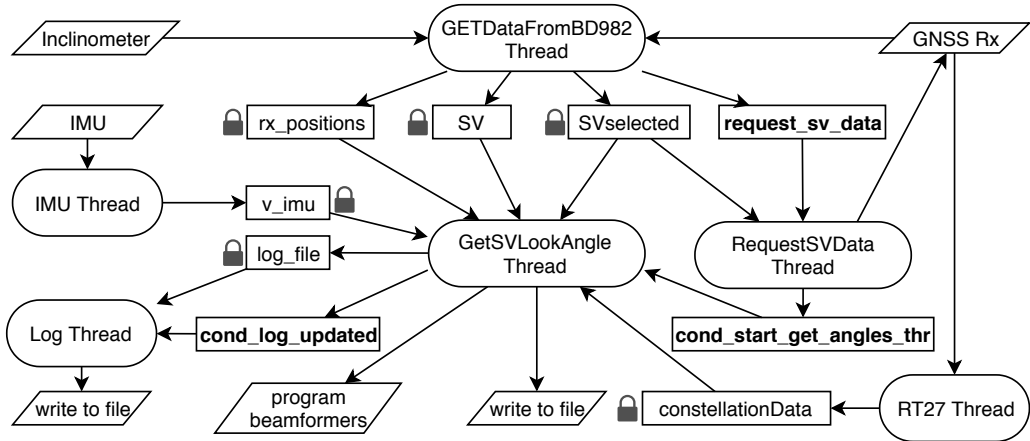


Figure 5.41: Interactions between threads. The parallelograms indicate external devices or the process to write a file. The rounded boxes indicate the threads. In bold, condition variables. The lock symbol indicates shared variables accessed using mutexes. The arrow indicate the destination of the information contained in a device, variable, or condition variable.

All the data shown in Tab. 5.11 is gathered by the threads and is used to determine the pointing angles using TCIP/IP, USB, or SPI protocols. Originally the RT27 packets were received through TCIP/IP, but when the packet was sent at rates of 1 Hz or higher, many packets were lost. The problem was solved by changing from TCIP/IP to a USB connection.

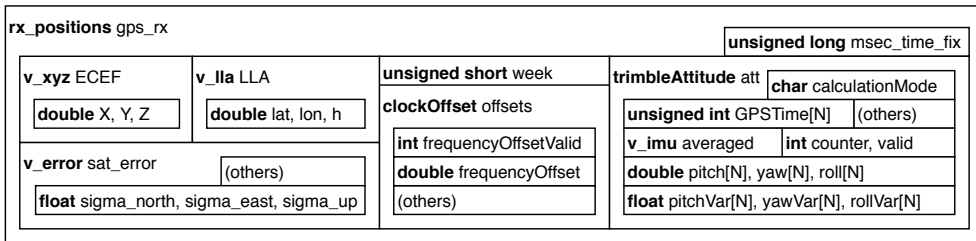
One of the main structure types in the MIR software is the *rx_positions* (see Fig. 5.42). It stores all the position and attitude information coming from the GNSS receiver. The variables *week* and *msec_time_fix* store the GPS week number and the GPS milliseconds of the week. In *ECEF* and *LLA* the position of the receiver is stored in the homonym formats, and the position error is stored in *sat_error*. The Doppler frequency given by the RT27 packets needs to be compensated with the frequency offset information contained in *offsets* prior to be used to cross-correlate the data sampled by the USRPs. Last, the heading angles estimated with the two GNSS antennas and the inclinometer is stored in *att*. The heading angles estimated from the IMU are instead stored in a *v_imu* variable (see Fig. 5.43).

All the information relative to the GNSS satellites coming from the GNSS receiver is stored in two arrays of *SV* structures (see Fig. 5.44). Each element contains the ECEF, LLA, elevation and azimuth of the satellite, and also its almanac and ephemeris.

Once the satellites to be pointed are chosen, the required data to process the sampled data is stored in a *SVselected* structure (see Fig. 5.45): the azimuth and elevation, the GPS time, the Doppler frequency, the PRN number, and an identifier for the system.

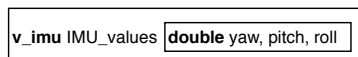
Table 5.11: Data sources used by the MIR instrument for the satellite tracking.

Source	Format/Protocol	Information	Rate
GNSS Receiver	GSOFF Packet (TCP/IP)	GPS Time	10 Hz
		Lat, Lon, Height	1 Hz
		ECEF Coordinates	1 Hz
		Clock Offset	1 Hz
		Sigma North, East, Up	1 Hz
		Yaw, Pitch, Roll	10 Hz
		Azimuth, Elevation, SNR	1 Hz
GNSS Receiver	RETSVDATA Packet (TCP/IP)	Ephemeris, Almanac	On demand
GNSS Receiver	RT27 Packet (USB)	SNR, Doppler Pseudorange	1 Hz
IMU	Serial (USB)	Yaw, Pitch, Roll	10 Hz
Inclinometer	SPI	Inclination	On demand

**Figure 5.42:** Data structure storing all position and attitude information coming from the GNSS receiver.

The Doppler frequency stored in the *SVselected* structure (see Fig. 5.46) is received from the RT27 packets, which are decoded and parsed in a structure type *constellationData*. It also contains the SNR of each satellite in multiple bands and sub-bands; for instance, the GNSS receiver provides the SNR in E5A, E5B, and E5A+B.

Last, the *log_file* structure (see Fig. 5.47) type contains all the information to be stored in a file in binary format for post processing and debugging purposes. Note the *SVangles* sub structure that contains the up-looking pointing angles, the down-looking pointing angles, and the elevation and azimuth of the satellites to be pointed. Besides storing this structure, some information for post-processing is also stored as plain text.

**Figure 5.43:** Data structure storing the attitude coming from the IMU.

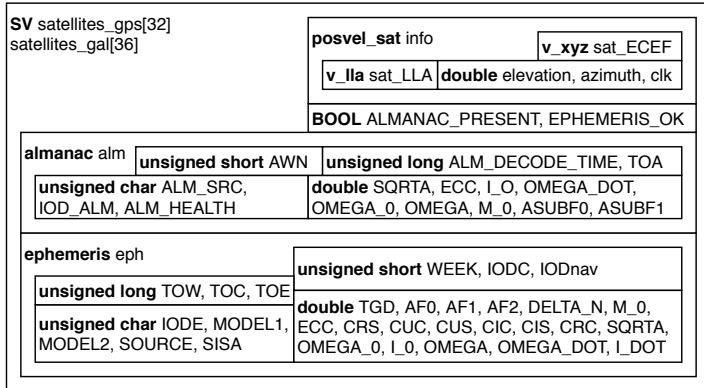


Figure 5.44: Data structure storing the satellite position and orbital information.

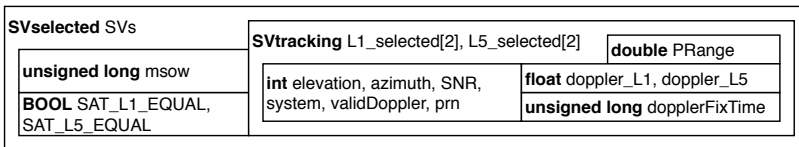


Figure 5.45: Data structure storing the selected satellites required information for the data processing.

5.9.1 Main Thread

The main thread of the MIR software (see Fig. 5.48) first initializes the system: initializes variables, opens the I2C and SPI ports, opens TCIP/IP sockets to the GNSS receiver, and opens the log files. Then, it loads the pre-calibration parameters and sets the MIR in the calibration mode waiting until the user presses any key. Next, the main thread creates the rest of the threads and waits until it receives the signal SIGINT, which happens when the user presses the ctrl+c key combination. In this idle state, the other threads are in charge of the instrument. Once the signal is received, the thread sends cancel signals to all threads and waits for them to finish. Last, it destroys all mutexes and conditions, releases all allocated memory, and closes all files, sockets, and devices.

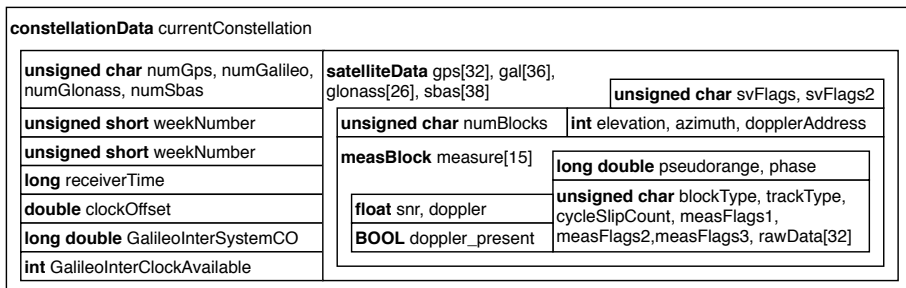


Figure 5.46: Data structure used to parse the RT27 packets.

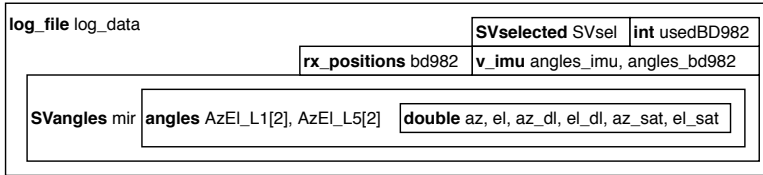


Figure 5.47: Data structure to be stored for post-processing and debugging purposes

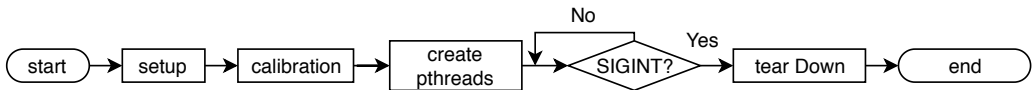


Figure 5.48: Main thread flow diagram.

5.9.2 Log Thread

The log thread (see Fig. 5.49) is in charge of storing all the log information in a file. It is a simple loop that starts waiting until new log information has to be stored using the condition variable `cond_log_updated`. Then, using a mutex it dumps the `log_file` structure to a file, and waits again.



Figure 5.49: Flow diagram of the thread in charge of writing the log information to a file.

5.9.3 IMU Thread

The IMU thread (see Fig. 5.50) is in charge of first configuring the IMU, and then continuously reading it, parsing the data, and saving it to a `v_imu` structure.

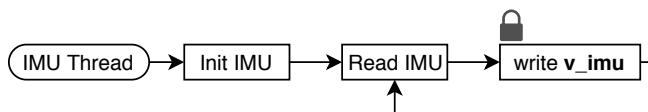


Figure 5.50: Flow diagram of the thread in charge of getting the attitude and heading information from the IMU.

5.9.4 GetDataFromBD982 Thread

The `GetDataFromBD982` thread (see Fig. 5.51) is in charge of processing every packet received from the GNSS receiver through TCIP/IP sockets. It concatenates the packets if necessary, checks their validity, and processes them. The received packets can be GSOF packets (see table 5.12), and almanac or ephemeris. The information from GSOF packets

is stored in the `rx_position` variable, while the ephemeris and almanac in the the SV arrays. If the GSOF packet contains the time (packet 0x01), it is also stored in the SVselected structures. In case it has valid attitude information (packet 0x1B), the inclinometer provides the third Euler angle that is not provided by the GNSS receiver¹.

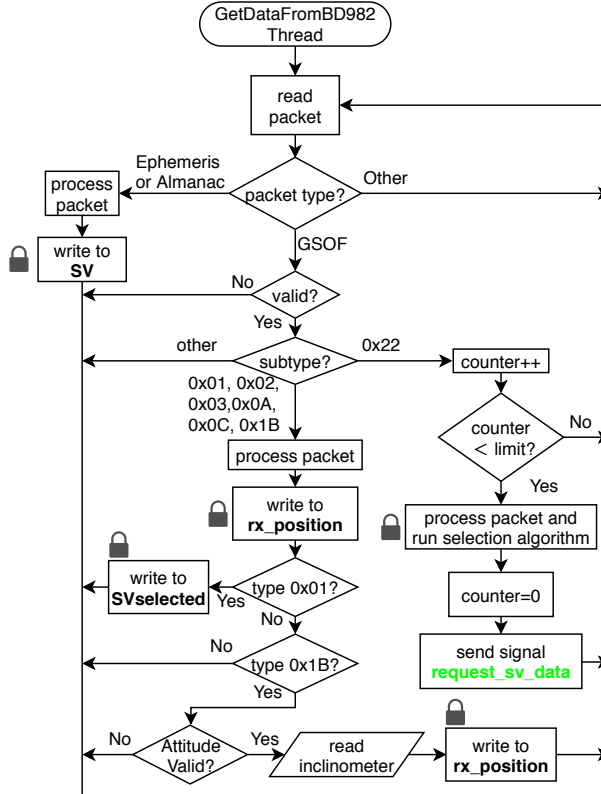


Figure 5.51: Flow diagram of the thread in charge of receiving the GSOF, ephemeris and almanac packets from the GNSS receiver.

5.9.5 RequestSVData Thread

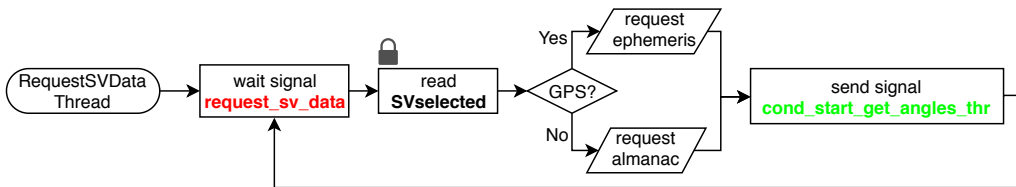
The RequestSVData thread (see Fig. 5.52) is in charge of requesting the orbital parameters of the satellites to be tracked. The thread waits for the condition variable `request_sv_data`, then checks which satellites require their orbital parameters to be updated, and requests the ephemeris parameters for the desired GPS satellites, and the almanac for the Galileo ones. When this part of the code was developed, the Galileo satellites still were not broadcasting their ephemeris, and therefore it was not possible to request them to the GNSS receiver, whereas the almanac was available. Since the position error using the almanac is estimated between 1 and 3 km [173], the angular error when pointing them is negligible, so it was decided not to implement the Galileo satellite position computation

¹The inclinometer is an inertial device, and therefore the system acceleration should be compensation.

Table 5.12: GOSF packets sent by the GNSS receiver, information that contain, and transmission rate.

GOSF packet type	Information	Rate
0x01 - Position Time	GPS Time	10 Hz
0x02 - LLH	Lat, Lon, Height	1 Hz
0x03 - ECEF	ECEF coordinates	1 Hz
0x0A - Clock Info	Clock offset	1 Hz
0x0C - SIGMA	Sigma north Sigma east Sigma up Position RMS	1 Hz
0x1B - Attitude Info	Yaw, Pitch, Roll, and variances	10 Hz

using the ephemeris. Nobody expects the Spanish Inquisition. Once the orbital information has been requested, the thread uses the condition variable `cond_start_get_angles_thr` to notify that the orbital parameters have been requested². Last, the thread will wait until new orbital information is required.

**Figure 5.52:** Flow diagram of the thread in charge of requesting the ephemeris or the almanac to the GNSS receiver.

5.9.6 GetSVLookAngles Thread

The GetSVLookAngles thread (see Fig. 5.53) is in charge of controlling the beamformers. At the startup, it points to the boresight and waits until it receives the `cond_start_get_angles_thr` signal, which notifies that all the required information to point to the satellites is available. Then, the thread reads all required information to compute the selected satellites position, computes the pointing angles taking into account the attitude of the platform and the calibration parameters, points the arrays to those angles, writes some log information to a file in plain text, fills the `log_file` structure, and sends the signal `cond_log_updated` to notify that the `log_file` structure can be stored to a file. In order to program the beamformers, the thread creates two threads, each one of them programs a single beamformer,

²This notification should be broadcasted once the orbital information has been received and processed, not once requested. However, since the position of the satellite is computed in each iteration of the thread, the packet will be eventually received, and therefore it will be computed with an old ephemeris or almanac just for a few seconds in the worst case scenario.

which are connected to different I2C ports. Programming the beamformers is the slowest part of the thread, and doing so simultaneously increases the beam refreshment rate.

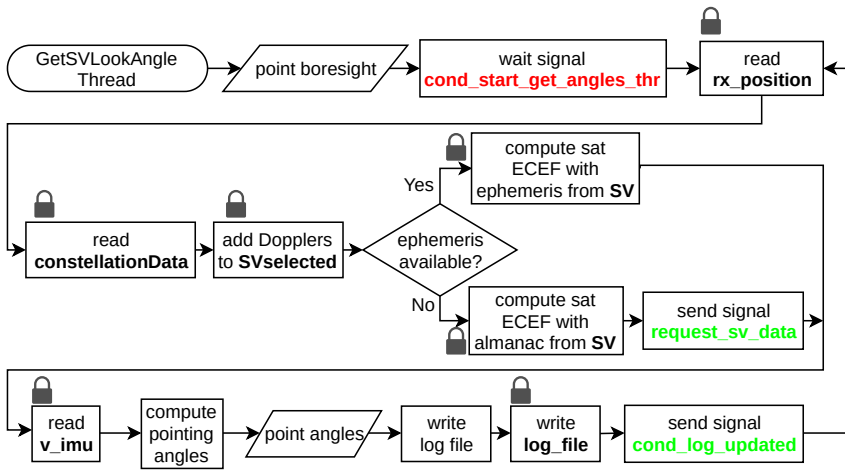


Figure 5.53: Flow diagram of the thread in charge of computing the pointing angles and to program the beamformers.

5.9.7 RT27 Thread

The RT27 thread (see Fig. 5.54) is in charge of receiving the RT27 packets from the GNSS receiver via USB. The thread opens the USB connection, receives packets, concatenates them if necessary, parses them, stores all the information in a constellationsData structure, and waits for more packets. If the packets are not correct, they are discarded.

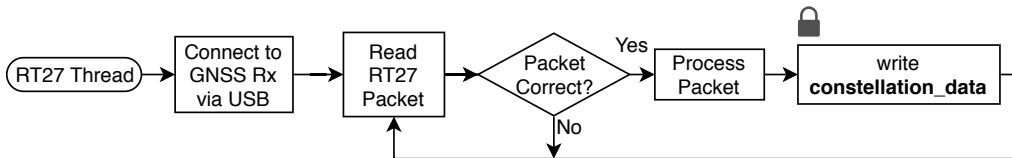


Figure 5.54: Flow diagram of the thread in charge of receiving the RT27 packets from the GNSS receiver.

5.10 Conclusions

This chapter has presented the hardware blocks that form the MIR instrument: the antenna arrays, the beamformers, the data sampling system, the calibration system, and the position and attitude determination system. The chapter also presents the tests carried on to validate these blocks, and how they are integrated together. Last, the software that controls the instrument is described in detail, explaining the threads that form the software, and the data structures involved.

6

Chapter 6

Instrument Calibration and Characterization

6.1 Introduction

The first section of this chapter shows an overview of the different calibration steps, and then they are explained in depth. The second part of this chapter shows some of the experiments carried out to validate the instrument, including the measured radiation patterns before and after calibration, how the calibration impacts the instrument performance, and an outdoor experiment aiming to prove that the instrument could track the satellites in view properly.

Part of this chapter is adapted from the previously published work “The Global Navigation Satellite Systems Reflectometry (GNSS-R) Microwave Interferometric Reflectometer: Hardware, Calibration, and Validation Experiments” [144].

6.2 Instrument Calibration

Despite the complexity of the scattering process of the GNSS signals on the Earth’s surface, in ground-based and airborne experiments the coherent reflectivity ρ can be approximated by [154]

$$\rho \approx \frac{P_r}{P_d} = |\Gamma|^2, \quad (6.1)$$

where P_d and P_r are the power of the direct $d(t)$ and reflected $r(t)$ signals received in the up- and down-looking arrays respectively shown in Fig. 6.1. For altimetric applications

the delay τ and the phase difference between $d(t)$ and $r(t)$ are the parameters to be estimated. However, the sampled signals in the USRPs $d'(t)$ and $r'(t)$ have passed through the different blocks that may have affected their amplitude, phase and delay, so it is necessary to characterize and calibrate these blocks in order to estimate properly the power or delay difference.

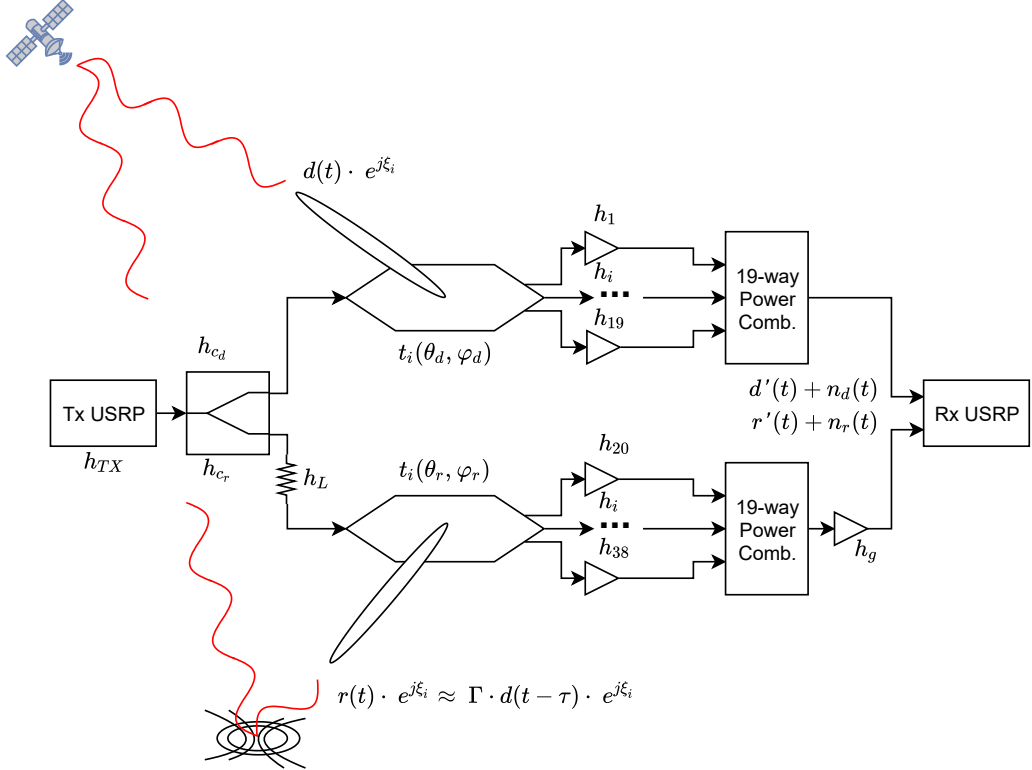


Figure 6.1: Simplified model of the blocks to be calibrated in the MIR instrument.

The sampled signals are related to the received ones as

$$d'(t) = \sum_{i=1}^{19} d(t) \cdot e^{j\xi_i} \cdot t_i(\theta_d, \varphi_d) * h_i(t) \quad (6.2)$$

$$r'(t) = \sum_{i=20}^{38} r(t) \cdot e^{j\xi_i} \cdot t_i(\theta_r, \varphi_r) * h_i(t) * h_g(t), \quad (6.3)$$

where the subscripts d and r stand for the direct and reflected signals, or the up- and down-looking arrays and RF chains, respectively; the subscript i stands for each of the 38 elements of both arrays, the first 19 belong to the up-looking array and RF chains, while the next 19 correspond to the down-looking ones; ξ is the propagation phase of the received signal; $t_i(\theta, \varphi)$ are the normalized complex voltage radiation patterns, that depend on the

angles of arrival θ , φ ; h_i are the impulse responses of each RF chain including the antennas; h_g is the impulse response of the extra RF amplifier in the down-looking RF chain; h_c is the impulse response of the calibration splitting network; h_L is the impulse response of the attenuator placed in the down-looking chain; and n is the noise at the input of the receiving USRPs. The vector modulators used to compensate the differences between RF chains only allow to set a single gain and phase for the whole frequency band, and the measurements at the anechoic chamber are carried out at a single frequency. Besides, the system can be considered narrow band because the bandwidth (20-30 MHz) is much smaller than the central frequencies (1.57542 GHz and 1.17645 GHz). It was therefore decided to calibrate the instrument at the center of each desired frequency band f_c and to model the impulse responses of the amplifier, the attenuator, the calibration splitting network, and the RF chains as:

$$h_g(t) = A_g \cdot \delta(t - \tau_g) \cdot e^{j\alpha_g} \quad (6.4)$$

$$h_c(t) = A_c \cdot \delta(t - \tau_c) \cdot e^{j\alpha_c} \quad (6.5)$$

$$h_i(t) = L \cdot \delta(t - \tau_L) \cdot e^{j\alpha_L} \quad (6.6)$$

$$h_i(t) = A_i \cdot \Delta A_i \cdot K_i \cdot \delta(t - \tau_i) \cdot e^{j(\alpha_i + \Delta\alpha_i + \beta_i)}, \quad (6.7)$$

$$(6.8)$$

where A_i and α_i are defined as

$$A_i = \begin{cases} A_d, & 1 \leq i \leq 19 \\ A_r, & 20 \leq i \leq 38 \end{cases} \quad (6.9)$$

$$\alpha_i = \begin{cases} \alpha_d, & 1 \leq i \leq 19 \\ \alpha_r, & 20 \leq i \leq 38, \end{cases} \quad (6.10)$$

and A_d and A_r are the average voltage gain of the direct and reflected array RF chains, respectively; α_d and α_r are the average phase of the direct and reflected array RF chains, respectively; ΔA_i and $\Delta\alpha_i$ are the voltage gain and phase difference of each element with respect to the average ones in their array; K_i and β_i are the voltage gain and phase introduced by each vector modulator; τ_i is the delay introduced by each RF chain; A_g , τ_g , and α_g are the voltage gain, delay and phase introduced by the extra amplifier in the RF chain; and A_c , τ_c , and α_c are the voltage gain, delay and phase introduced by calibration splitting network.

The delay τ_i can be modeled analogously to the amplitude and phase as $\tau_d + \Delta\tau_d$ and $\tau_r + \Delta\tau_r$. The mean group delays τ_d and τ_r can be characterized and compensated in post processing, but the terms $\Delta\tau_d$ and $\Delta\tau_r$ cannot, neither they can be compensated using vector modulators, and the consequence is a widening of the cross-correlation function [174]. The level of widening is unknown. Therefore they will be modeled as τ_d and τ_r for the direct and the reflected channels respectively, and the differences $\Delta\tau_d$ and $\Delta\tau_r$ will be omitted for simplicity and assumed as the aforementioned widening.

In order to properly estimate ρ or the delay between $d(t)$ and $r(t)$, several terms must be compensated for. First, for a proper beam steering, the received phase ξ_i has

to be compensated, and also the terms ΔA_i and $\Delta \alpha_i$ have to be “equalized”, all of them through the variable gain and phase of the vector modulators by setting $K_i = 1/\Delta A_i$ and $\beta_i = -\Delta \alpha_i - \xi_i$. This procedure is carried out in an anechoic chamber as explained in section 6.2.1. The received signals $d(t)$ and $r(t)$ are summed constructively, therefore Eqns. (6.2-6.3) become

$$d'(t) = A_d \cdot e^{j\alpha_d} \cdot d(t) * \delta(t - \tau_d) \cdot \sum_{i=1}^{19} t_i(\theta_d, \varphi_d) \quad (6.11)$$

$$r'(t) = A_r \cdot A_g \cdot e^{j(\alpha_r + \alpha_g)} \cdot r(t) * \delta(t - \tau_r - \tau_g) \cdot \sum_{i=20}^{38} t_i(\theta_r, \varphi_r). \quad (6.12)$$

The complex voltage radiation pattern of each antenna element t_i and the band-pass behavior of the RF chains could not be measured individually, but was measured in the anechoic chamber as the average of the whole array at any pointing direction at the proper circular polarization and central frequency of the desired frequency band as

$$\widehat{t}_d(\theta, \varphi) = \sum_{i=1}^{19} t_i(\theta, \varphi) \quad (6.13)$$

$$\widehat{t}_r(\theta, \varphi) = \sum_{i=20}^{38} t_i(\theta, \varphi). \quad (6.14)$$

which can be first measured and then compensated from both $d'(t)$ and $r'(t)$. Once compensated, Eqns. (6.11-6.12) become

$$d'(t) = A_d \cdot e^{j\alpha_d} \cdot d(t) * \delta(t - \tau_d) \quad (6.15)$$

$$r'(t) = A_r \cdot A_g \cdot e^{j(\alpha_r + \alpha_g)} \cdot r(t) * \delta(t - \tau_r - \tau_g). \quad (6.16)$$

Note that the gains A_d and $A_r \cdot A_g$, the phases α_d and $\alpha_r + \alpha_g$, and the delays τ_d and $\tau_r + \tau_g$ are unknown, but since all observables are based on the comparison it is only required to determine the difference between them. For instance, in order to estimate the reflectivity P_{Rx_d} is divided by P_{Rx_u} , and therefore only the ratio between A_d and $A_r \cdot A_g$ has to be known. In altimetry, both the delay and phase difference between the direct and reflected branches is required. Since the parameters of the different beams are different, this calibration step is also used to calibrate the results between beams and bands. This calibration has to be conducted every time the USRPs are powered up, since the phases of the local oscillators used to the down-conversion are random, and the gain of the whole RF chains might be affected by the temperature. For this purpose, the instrument has a calibration port to inject a calibration signal to the central element of each array as explained in section 6.2.2. The calibration signal does not follow the same path as the signals received from the antennas:

$$y_d(t) = x(t) * h_{c_d}(t) * h'_{10}(t) \quad (6.17)$$

$$y_r(t) = x(t) * h_{c_r}(t) * h_l(t) * h'_{29}(t) * h_g(t), \quad (6.18)$$

where $y'(t)$ are the calibration signals at the USRP inputs, h_{c_d} and h_{c_r} are the impulse responses of the calibration power splitter, respectively, h_l is the impulse response of the 30 dB attenuator in the down-looking channel, $h'_i = A'_i \cdot e^{j\alpha'_i} \cdot \delta(t - \tau_i)$ is the impulse response from the array calibration port to the output port of the beamformer passing through the phase shifter i , h_g is the impulse response of the extra RF amplifier in the down-looking channel, and $x(t)$ is the transmitted calibration signal. Note that h'_{10} and h'_{29} correspond to the RF chains connected to the central antenna elements of the array, the only one where the calibration signal is injected. The difference between the antenna path and the calibration port path, called ‘‘compensation parameters’’, does not change throughout time and can be measured in the anechoic chamber in the frequency domain as explained in section 6.2.3:

$$H_{comp_i}(f_c) = \frac{H_i(f_c)}{H'_i(f_c)}. \quad (6.19)$$

The compensation parameters were measured from the calibration port, and therefore the contributions from the calibration splitting network must also be characterized and compensated. In this way, the measured amplitude, phase, and group delay differences of the RF chains are obtained from the calibration signal as explained in section 6.2.5.

The signals $d'(t) + n_d(t)$ and $r'(t) + n_r(t)$ are sampled at one bit, which causes the cross-correlation peak value to depend on the signal’s SNR [29]. The SNR depends on the sampled noises $n_d(t)$ and $n_r(t)$, that can be measured, and on the noise generated inside the USRPs, which cannot be directly measured. Section 6.2.6 proposes the characterization of the curve that relates the input power with the peak value after correlation by injecting GNSS signals with the measured $n_d(t)$ and $n_r(t)$ and different SNR levels.

6.2.1 Pre-calibration Step 1: Calibration Through the Antenna

The received signals from the satellites follow the red path in Fig. 6.2. The signal $S_{sat}(f_c)$ is propagated from the satellite (or the transmitting antenna inside the anechoic chamber) to the phase center of the antenna ($H_{prop_i}(f_c)$), passes through the calibration switch ($H_{trans_i}(f_c)$), and through the vector modulator $H_{VM_i}(f_c, I, Q) = I \cdot k_{I_i}(f_c) + Q \cdot k_{Q_i}(f_c) + O_i(f_c)$. The contributions $H_{trans_i}(f_c)$ and $H_{VM_i}(f_c, I, Q)$ are the ones that must be calibrated. The total path covered To conduct these measurements, an external antenna is required. In the MIR case, it was mounted in an anechoic chamber. The transmitting antenna was a reference antenna connected to the transmitting port of a vector network analyzer, whereas the receiving port was connected to the output of the beamformer.

The outgoing signal $S'_{sat}(f_c)$ is

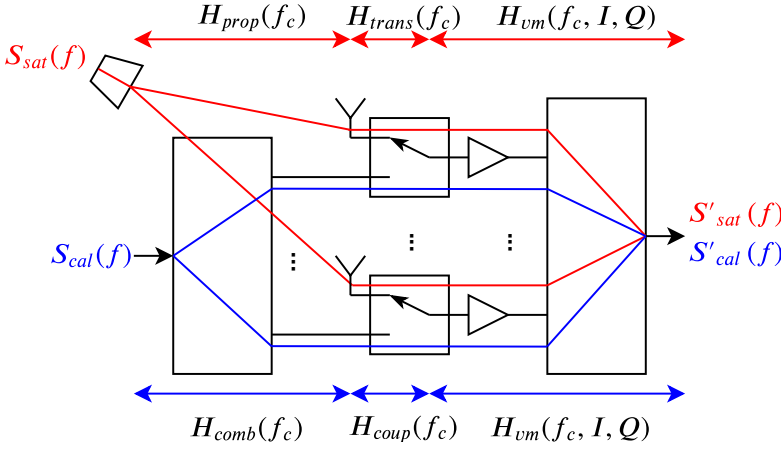


Figure 6.2: Received and calibration signals' paths to the receiver in one of the bands and beams.

$$\begin{aligned}
 S'_{sat}(f_c, I_1, Q_1, \dots, I_{19}, Q_{19}) &= \sum_{i=1}^{19} S_{sat}(f_c) \cdot H_{sat_i}(f_c, I_i, Q_i) \\
 &= \sum_{i=1}^{19} S_{sat}(f_c) \cdot H_{prop_i}(f_c) \cdot H_{trans_i}(f_c) \cdot H_{VM_i}(f_c, I_i, Q_i) \\
 &= \sum_{i=1}^{19} S_{sat}(f_c) \cdot H_{prop_i}(f_c) \cdot H_{trans_i}(f_c) \\
 &\quad \cdot (I_i \cdot k_{I_i}(f_c) + Q_i \cdot k_{Q_i}(f_c) + O_i(f_c)) \\
 &= S_{sat}(t) \cdot H_n(f_c), \tag{6.20}
 \end{aligned}$$

where $H_n(f_c)$ is the transfer function at the desired central frequency f_c measured by the VNA, and $H_{sat_i}(f_c, I_i, Q_i) = H_{prop_i}(f_c) \cdot H_{trans_i}(f_c) \cdot H_{VM_i}(f_c, I_i, Q_i)$. In case one single vector modulator i has to be characterized, the rest of gains can be set to zero in linear scale:

$$\begin{aligned}
 S'_{sat_i}(f_c, 0, 0, \dots, I_i, Q_i, \dots, 0, 0) &= S_{sat}(f_c) \cdot H_{prop_i}(f_c) \cdot H_{trans_i}(f_c) \\
 &\quad \cdot (I_i \cdot k_{I_i}(f_c) + Q_i \cdot k_{Q_i}(f_c)) \\
 &\quad + S_{sat}(f_c) \cdot \sum_{i=1}^{19} H_{prop_i}(f_c) \cdot H_{trans_i}(f_c) \cdot O_i(f_c) \\
 &= S_{sat}(f_c) \cdot H_{prop_i}(f_c) \cdot H_{trans_i}(f_c) \\
 &\quad \cdot (I_i \cdot k_{I_i}(f_c) + Q_i \cdot k_{Q_i}(f_c)) + S_{sat}(f_c) \cdot O_T(f_c). \tag{6.21}
 \end{aligned}$$

As it can be seen, the offset contribution does not depend on the i chosen vector modulator and is always present. In order to estimate the calibration parameters g_i , α_i ,

L_i , and φ_i , it is required to estimate the vectors $k_I(f_c)$, $k_Q(f_c)$, and $O(f_c)$ in Eqn. (4.23). For each vector modulator i , several transfer functions $H_n(f_c)$ are measured setting N different pairs of $\{I_n, Q_n\}$ values. The following linear system of equations is obtained:

$$\begin{aligned} A \cdot \vec{x} &= \begin{pmatrix} I_1 & Q_1 & 1 \\ \dots & \dots & \dots \\ I_n & Q_n & 1 \\ \dots & \dots & \dots \\ I_N & Q_N & 1 \end{pmatrix} \cdot \begin{pmatrix} H_{prop_i}(f_c) \cdot H_{trans_i}(f_c) \cdot k_{I_i}(f_c) \\ H_{prop_i}(f_c) \cdot H_{trans_i}(f_c) \cdot k_{Q_i}(f_c) \\ O_T(f_c) \end{pmatrix} \\ &= \begin{pmatrix} I_1 & Q_1 & 1 \\ \dots & \dots & \dots \\ I_n & Q_n & 1 \\ \dots & \dots & \dots \\ I_N & Q_N & 1 \end{pmatrix} \cdot \begin{pmatrix} k'_{I_i}(f_c) \\ k'_{Q_i}(f_c) \\ O_T(f_c) \end{pmatrix} = \begin{pmatrix} H_1(f_c) \\ \dots \\ H_n(f_c) \\ \dots \\ H_N(f_c) \end{pmatrix} = \vec{H}(f_c). \end{aligned} \quad (6.22)$$

If more than three independent measurements are used, the system can be solved using the linear least squared method [175]:

$$\hat{x} = (A^T \cdot A)^{-1} \cdot A^T \cdot \vec{H}(f_c). \quad (6.23)$$

This linear approximation requires a set of $\{I_n, Q_n\}$ values that maintain the RF devices in the linear region. The MIR instrument uses

$$\begin{aligned} \{I_n, Q_n\} &= \left\{ \cos \frac{n}{N} \cdot 360^\circ, \sin \frac{n}{N} \cdot 360^\circ \right\}, \quad \forall n \in \mathbb{N} : \{1..N\} \\ \{I_{N+1}, Q_{N+1}\} &= \{0, 0\}, \end{aligned} \quad (6.24)$$

with $N = 8$. Once the system is solved, the H_{prop_i} contribution can be removed

$$H_{prop_i}(f_c) = \frac{1}{|\vec{r}_i|} \cdot e^{-j \cdot 2\pi \cdot \frac{f_c}{c} \cdot |\vec{r}_i|}, \quad (6.25)$$

where \vec{r}_i is the vector between the phase centers of the transmitting and the i receiving antenna, and λ is the wavelength.

Then, the calibration parameters (g_i and α_i), and the unbalance parameters of the vector modulator (L_i and φ_i) of each RF chain are obtained from \vec{I}'_i and \vec{Q}'_i as:

$$g_i = |k'_i(f_c)|, \quad (6.26)$$

$$\alpha_i = -\angle\{k'_{I_i}(f_c)\}, \quad (6.27)$$

$$L_i = \frac{|k'_{Q_i}(f_c)|}{|k'_{I_i}(f_c)|}, \quad (6.28)$$

$$\varphi_i = \angle\{k'_{I_i}(f_c)\} - \angle\{k'_{Q_i}(f_c)\} + \frac{\pi}{2}. \quad (6.29)$$

Equation (6.21) shows that it is not possible to separate the contributions of the different offsets, but the aggregated offset can be compensated in a single vector modulator i . To do so, the offset $O_T(f_c)$ becomes the offset $O(f_c)$ from Eqn. (4.34), and the components O_I and O_Q are estimated and later subtracted to I_C and Q_C of that particular vector modulator.

6.2.2 Pre-calibration Step 2: Calibration Through the Calibration Port

Since it is unpractical to periodically calibrate the instrument with an external antenna, even more if the instrument is mounted in an airplane, the instrument has a calibration port in each array (blue path in Fig. 6.2). There, the calibration signal $S_{cal}(f_c)$ is split and distributed to the 19 RF Front-ends ($H_{comb_i}(f_c)$). The calibration signal is coupled to the RF main line due to the switch finite isolation ($H_{coup_i}(f_c)$), and then the signal follows the same route than the signal coming from the antennas through the rest of the RF chain ($H_{VM_i}(f_c, I, Q)$).

To conduct these measurements, the transmitting port of the anechoic chamber's VNA was connected to the calibration port, whereas the receiving port was connected to the output of the beamformer. In the MIR case it was done just after the first calibration step, connecting to the calibration port the cable that fed the transmitting antenna.

The outgoing signal $S'_{cal}(f_c)$ is in this case

$$\begin{aligned}
 S'_{cal}(f_c, I_1, Q_1, \dots, I_{19}, Q_{19}) &= \sum_{i=1}^{19} S_{cal}(f_c) \cdot H_{cal_i}(f_c, I_i, Q_i) \\
 &= \sum_{i=1}^{19} S_{cal}(f_c) \cdot H_{comb_i}(f_c) \cdot H_{coup_i}(f_c) \cdot H_{VM_i}(f_c, I_i, Q_i) \\
 &= \sum_{i=1}^{19} S_{cal}(f_c) \cdot H_{comb_i}(f_c) \cdot H_{coup_i}(f_c) \\
 &\quad \cdot (I_i \cdot k_{I_i}(f_c) + Q_i \cdot k_{Q_i}(f_c) + O_i(f_c)) = S_{cal}(f_c) \cdot H_n(f_c).
 \end{aligned} \tag{6.30}$$

where $H_{cal_i}(f_c, I_i, Q_i) = H_{comb_i}(f_c) \cdot H_{coup_i}(f_c) \cdot H_{VM_i}(f_c, I_i, Q_i)$. Again, the system of equations (6.22) has to be solved, but in this case the vector \vec{x} is

$$\vec{x} = \begin{pmatrix} H_{comb_i}(f_c) \cdot H_{coup_i}(f_c) \cdot k_{I_i}(f_c) \\ H_{comb_i}(f_c) \cdot H_{coup_i}(f_c) \cdot k_{Q_i}(f_c) \\ O_T(f_c) \end{pmatrix} = \begin{pmatrix} k''_{I_i}(f_c) \\ k''_{Q_i}(f_c) \\ O_T(f_c) \end{pmatrix}. \tag{6.31}$$

The calibration parameters in Eqns. (6.26-6.29) are then computed with $k''_{I_i}(f_c)$ and $k''_{Q_i}(f_c)$.

6.2.3 Pre-calibration Step 3: Obtaining the Compensation Parameters

As mentioned before, the calibration through the calibration port is more practical than the calibration with an external reference antenna, but the calibration signal does not follow the same path as the signals that come from the satellites. The path differences must be measured so they can be added to the calibration parameters obtained through the calibration port. From Fig. 6.2, they can be defined as

$$H_{comp_i}(f_c) = \frac{H_{sat_i}(f_c, I_i, Q_i)}{H_{cal_i}(f_c, I_i, Q_i) \cdot H_{prop_i}(f_c)} = \frac{H_{trans_i}(f_c)}{H_{comb_i}(f_c) \cdot H_{coup_i}(f_c)}. \quad (6.32)$$

Considering that they depend on a particular pair of $\{I_i, Q_i\}$ values, it is instead proposed to compute them as

$$\begin{aligned} H_{comp_i}(f_c) &= \frac{k'_{I_i}(f_c)}{H_{prop_i}(f_c) \cdot k''_{I_i}(f_c)} = \frac{(H_{prop_i}(f_c) \cdot H_{trans_i}(f_c) \cdot k_{I_i}(f_c))}{H_{prop_i}(f_c) \cdot (H_{comb_i}(f_c) \cdot H_{coup_i}(f_c) \cdot k_{I_i}(f_c))} \\ &= \frac{H_{trans_i}(f_c)}{H_{comb_i}(f_c) \cdot H_{coup_i}(f_c)}. \end{aligned} \quad (6.33)$$

Note that the compensation parameters do not depend on the vector modulators, and therefore will not change between beams of the same band.

6.2.4 Pre-calibration Step 4: Re-calibrating the Instrument

If any hardware after the calibration switch has changed or the instrument needs to be calibrated again, this can be done through the calibration port as explained in Section 6.2.2 to obtain a new pair of $\{\widehat{k''_i}, \widehat{k''_i}\}$ values, and then applying the “compensation parameters” H_{comp_i} :

$$\widehat{k''_{I_i}}(f_c) \cdot H_{comp_i}(f_c) = \widehat{k'_{I_i}}(f_c) \quad (6.34)$$

$$\widehat{k''_{Q_i}}(f_c) \cdot H_{comp_i}(f_c) = \widehat{k'_{Q_i}}(f_c), \quad (6.35)$$

where $\widehat{k'_{I_i}}$ and $\widehat{k'_{Q_i}}$ must be used to compute the calibration parameters as explained in Eqns. (6.26-6.29). After that, the offsets in Eqn. (4.34) should be recalculated.

6.2.5 In-flight Calibration

This step is required to compensate the random phase of the local oscillators when the system is turned on. Besides, the calibration parameters obtained in section 6.2.4 of both arrays were obtained in different experiments with different hardware, such as cables and adapters, so it is required to calibrate the gain between arrays. To do so, a known signal is injected in both arrays, the data is sampled, and in post-processing the amplitude

and phase difference between the up- and down-looking RF chains is first estimated and then compensated. The chosen signal is a PRN sequence, which has been proved useful to calibrate the Fringe Washing Function [176] in aperture synthesis interferometric radiometers [158]. Using these sequences instead of a single tone allows the estimation of the transfer function, as shown later in Fig. 6.5.

Ideally, if all antenna elements but one in each array are disabled and a known gain and phase are set to these elements, the phase and gain difference is the measured one. The elements can be disabled by disabling the corresponding vector modulators. However, the limited isolation of the switches of ≈ 30 dB will not prevent the contributions from the other 18 elements from affecting the estimation. This problem was solved by directly connecting the calibration port of the array to the central element of it. The gain and phase difference with respect to the previous cable configuration was measured with a VNA and later taken into account. As for the normal operation mode, the calibration signals are sampled by beam pairs, but one pair at a time and at 10 Msps with 16 bits for the I and Q components. The sampled signal $y(t)$ is

$$y(t) = \left\{ \left[\left(x_T(t) \cdot e^{-j(2\pi f_{TX}t + \phi_{TX})} \right) * \left(h_{TX}(t) \cdot e^{-j2\pi f_c t} \right) \right] * \left(h(t) \cdot e^{-j2\pi f_c t} \right) + n(t) \cdot e^{-j2\pi f_c t} \right\} \cdot e^{j(2\pi f_{RX}t + \phi_{RX})}, \quad (6.36)$$

where $x_T(t) = \sum_n x(t - n \cdot T_c)$ is the T_c periodic base-band transmitted calibration signal, f_{TX} is the up-conversion frequency, ϕ_{TX} is the random phase of the transmitting local oscillator, h_{TX} is the equivalent base-band impulse response of the transmitting USRP, $*$ is the convolution operator [177], h is the combined equivalent base-band impulse response of the Device Under Test (DUT), the splitting network after the calibration system, and the receiving USRP, f_c is the band central frequency, $n(t)$ is the base-band additive white Gaussian noise present in the channel, f_{RX} is the down-conversion frequency, and ϕ_{RX} is the random phase of the receiving local oscillator. If the transfer functions of $h_{TX}(t)$ and $h(t)$ are flat enough to state that $H(f_c) \approx H(f_{TX})$, $f_c = f_{TX}$ can be approximated to simplify Eqn. (6.36)

$$\begin{aligned} y(t) &= \left\{ \left[x_T(t) * h_{TX}(t) * h(t) + n(t) \right] \cdot e^{-j(2\pi f_{TX}t + \phi_{TX})} \right\} \cdot e^{j(2\pi f_{RX}t + \phi_{RX})} \\ &= \left[x_T(t) * h_{TX}(t) * h(t) + n(t) \right] \cdot e^{-j(2\pi \Delta f t + \Delta \phi)} \\ &= \left[x_T(t) * h'(t) \right] \cdot e^{-j(2\pi \Delta f t + \Delta \phi)} + n'(t), \end{aligned} \quad (6.37)$$

where $\Delta f = f_{RX} - f_{TX}$ and $\Delta \phi = \phi_{RX} - \phi_{TX}$ are the differences between the frequencies and the random phases of the local oscillators in the up and down conversion respectively, and $n'(t) = n(t) \cdot e^{-j(2\pi \Delta f t + \Delta \phi)}$, and $h'(t) = h_{TX}(t) * h(t)$ have been abbreviated for simplicity.

First, the residual frequency difference between oscillators has to be compensated, otherwise the phase will not remain constant over time. To do so, $y(t)$ is circularly cross-correlated with a T_c length clean replica of the calibration signal $x(t)$ as follows, and then

the phase in the cross-correlation peak is used to estimate the frequency error between oscillators:

$$\begin{aligned}
 R_{yx}(t, \tau, \Delta f) &= \left((x_T(t) * h'(t)) \cdot e^{-j(2\pi\Delta f t + \Delta\phi)} + n'(t) \right) * (x^*(-t)) \\
 &= \{\text{using Eqn. (6.39)}\} \\
 &= (h'(t) * x_T(t) * (x^*(-t) \cdot e^{j2\pi\Delta f t})) \cdot e^{-j(2\pi\Delta f t + \Delta\phi)} + n'(t) * x^*(-t) \\
 &= \{\text{using Eqn. (6.41)}\} \\
 &= \left(h'(t) * \left(\sum Y(t - n \cdot T_c, \Delta f) \cdot e^{j2\pi\Delta f n \cdot T_c} \right) \cdot e^{j2\pi\Delta f t} \right) \cdot e^{-j(2\pi\Delta f t + \Delta\phi)} \\
 &\quad + n'(t) * x_c^*(-t) \\
 &= \left((h'(t) \cdot e^{-j2\pi\Delta f t}) \overset{t}{*} \left(\sum Y(t - n \cdot T_c, \Delta f) \cdot e^{j2\pi\Delta f n \cdot T_c} \right) \right) (\tau, \Delta f) \cdot e^{-j\Delta\phi} \\
 &\quad + R_{n'x}(t, \tau), \tag{6.38}
 \end{aligned}$$

$$\begin{aligned}
 x(t) * (h(t) \cdot e^{-j2\pi f t}) &= (x(t) \cdot e^{-j2\pi f t} \cdot e^{j2\pi f t}) * (h(t) \cdot e^{-j2\pi f t}) \\
 &= \{\text{using Eqn. (6.40)}\} \\
 &= ((x(t) \cdot e^{j2\pi f t}) * (h(t))) \cdot e^{-j2\pi f t}, \tag{6.39}
 \end{aligned}$$

$$\begin{aligned}
 (x(t) \cdot e^{-j2\pi f t}) * (h(t) \cdot e^{-j2\pi f t}) &= \int x(t') \cdot e^{-j2\pi f t'} \cdot h(t - t') \cdot e^{-j2\pi f (t - t')} dt' \\
 &= \int x(t') \cdot e^{-j2\pi f t'} \cdot h(t - t') \cdot e^{-j2\pi f t} \cdot e^{j2\pi f t'} dt' \\
 &= e^{-j2\pi f t} \cdot \int x(t') \cdot h(t - t') dt' \\
 &= (x(t) * h(t)) \cdot e^{-j2\pi f t}, \tag{6.40}
 \end{aligned}$$

$$\begin{aligned}
 x_T(t) * (x^*(-t) \cdot e^{j2\pi\Delta f t}) &= \sum \delta(t - n \cdot T_c) * (x(t) * (x^*(-t) \cdot e^{j2\pi\Delta f t})) \\
 &= \sum \delta(t - n \cdot T_c) * \int_0^{T_{coh}} x(t') \cdot x(t' - t) \cdot e^{j2\pi\Delta f (t - t')} dt' \\
 &= \sum \delta(t - n \cdot T_c) * \left(e^{j2\pi\Delta f t} \cdot \int_0^{T_{coh}} x(t') \cdot x(t' - t) \cdot e^{-j2\pi\Delta f t'} dt' \right) \\
 &= \sum \delta(t - n \cdot T_c) \overset{t}{*} (Y(t, \Delta f) \cdot e^{j2\pi\Delta f t}) \\
 &= \sum Y(t - n \cdot T_c, \Delta f) \cdot e^{j2\pi\Delta f (t - n \cdot T_c)} \\
 &= \left(\sum Y(t - n \cdot T_c, \Delta f) \cdot e^{j2\pi\Delta f n T_c} \right) \cdot e^{j2\pi\Delta f t}, \tag{6.41}
 \end{aligned}$$

where T_c is the time length of the code, T_{chip} is the chip duration, $\overset{t}{*}$ is the convolution in the time domain, and $Y(\tau, \Delta f)$ is the WAF which for Binary Phase-Shift Keying (BPSK) codes can be approximated as [10]

$$Y(\tau, f) = \Lambda\left(\frac{\tau}{T_{chip}}\right) \cdot \text{sinc}(f \cdot T_{coh}), \quad (6.42)$$

where T_{coh} is the coherent integration time, and

$$\Lambda\left(\frac{\tau}{T_{chip}}\right) = \begin{cases} 1 - \frac{|\tau|}{T_{chip}}, & |\tau| < T_{chip}, \\ 0, & \text{elsewhere.} \end{cases} \quad (6.43)$$

If a simplified model of the transmitting impulse response $h_{TX}(t) = A_{TX} \cdot \delta(t - \tau_{TX}) \cdot e^{j\phi_{TX}}$ is assumed, so that the channel behaves as a simplified model $h(t) = A_h \cdot \delta(t - \tau_h) \cdot e^{j\phi_h}$, so $h'(t) = A_{TX} \cdot A_h \cdot \delta(t - \tau_{TX} - \tau_h) \cdot e^{j(\phi_{TX} + \phi_h)} = A_c \cdot \delta(t - \tau_c) \cdot e^{j\phi_c}$, Eqn. (6.38) becomes

$$\begin{aligned} R_{yx}(t, \tau, \Delta f) &= \\ &= \left((A_c \cdot \delta(t - \tau_c) \cdot e^{j\Phi_c} \cdot e^{-j2\pi\Delta f t}) \overset{t}{*} \left(\sum Y(t - n \cdot T_c, \Delta f) \cdot e^{j2\pi\Delta f n T_c} \right) \right)_{t=\tau} \cdot e^{-j\Delta\phi} \\ &\quad + R_{n'x}(t, \tau) \\ &= \left((A_c \cdot \delta(t - \tau_c) \cdot e^{-j(2\pi\Delta f \tau_c + \Phi_c)}) \overset{t}{*} \left(\sum Y(t - n \cdot T_c, \Delta f) \cdot e^{j2\pi\Delta f n T_c} \right) \right)_{t=\tau} \\ &\quad \cdot e^{-j\Delta\phi} + R_{n'x}(t, \tau) \\ &= A_c \cdot \left(\sum Y(\tau - n \cdot T_c - \tau_c, \Delta f) \cdot e^{j2\pi\Delta f n T_c} \right) \cdot e^{-j\Delta\phi} \cdot e^{-j(2\pi\Delta f \tau_c + \Phi_c)} \\ &\quad + R_{n'x}(t, \tau) \\ &= A_c \cdot \left(\sum \Lambda\left(\frac{\tau - \tau_c - n \cdot T_c}{T_{chip}}\right) \cdot \text{sinc}(\Delta f \cdot T_{chip}) \cdot e^{j2\pi\Delta f n T_c} \right) \\ &\quad \cdot e^{-j(2\pi\Delta f \tau_c + \Phi_c + \Delta\phi)} + R_{n'x}(t, \tau). \end{aligned} \quad (6.44)$$

The correlation peaks are located at $\tau = \tau_c + nT_c$, so that τ_c can be found by correlating the first T_{coh} of the sampled data. Then, the peak value is

$$\begin{aligned} R_{yx}(t, \tau = \tau_c + nT_c, \Delta f) &= A_c \cdot \text{sinc}(\Delta f \cdot T_{chip}) \cdot e^{j2\pi\Delta f n T_c} \cdot e^{-j(2\pi\Delta f \tau_c + \Phi_c + \Delta\phi)} \\ &\quad + R_{n'x}(t, \tau_c + n \cdot T_c). \end{aligned} \quad (6.45)$$

The phase rotates due to the term $e^{j2\pi\Delta f n T_{chip}}$. If the SNR is high enough, the phase can be used to estimate the term Δf , and then the frequency error can be compensated in a similar way [31, p. 196-200].

Figure 6.3 shows the cross-correlation peak phase of one of the USRPs during one of the calibration experiments before and after the frequency error compensation. After

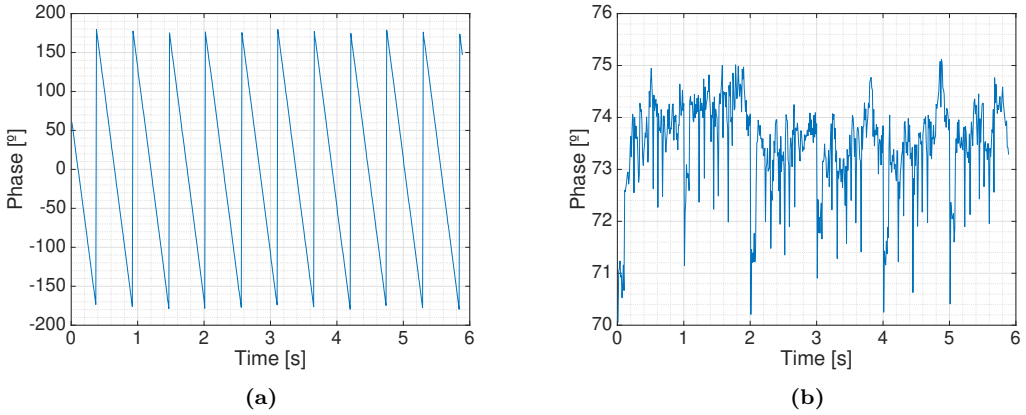


Figure 6.3: Cross-correlation peak phase a) before, and b) after frequency error compensation.

the compensation, the phase remains stable during the 6 seconds that the calibration lasts. Further experiments in this chapter will show if the phase really remains constant throughout time.

Once the frequency error is compensated, the sampled signal is correlated in intervals of T_{coh} with the clean replica of the code. The spectrum becomes

$$\begin{aligned}
 S_{yx}(f) &= (X(f) \cdot H_{TX}(f) \cdot H(f) + N(f)) \cdot e^{-j\Delta\phi} \cdot X^*(f) \\
 &= X(f) \cdot X^*(f) \cdot H_{TX}(f) \cdot H(f) \cdot e^{-j\Delta\phi} + N(f) \cdot X^*(f) \cdot e^{-j\Delta\phi} \\
 &= |X(f)|^2 \cdot H_{TX}(f) \cdot H(f) \cdot e^{-j\Delta\phi} + N(f) \cdot X^*(f) \cdot e^{-j\Delta\phi} \\
 &= |X(f)|^2 \cdot |H_{TX}(f)| \cdot e^{-j\angle H_{TX}(f)} \cdot |H(f)| \cdot e^{-j\angle H(f)} \cdot e^{-j\Delta\phi} + N(f) \cdot X^*(f) \cdot e^{-j\Delta\phi}.
 \end{aligned} \tag{6.46}$$

In order to retrieve the modulus of the combined transfer functions, the spectra contribution of the PRN codes $|X(f)|^2$ has to be removed. The Fourier transforms of the PRN codes are known and exhibit null values. Dividing S_{yx} by the code spectra $|X(f)|^2$ will therefore result in an inaccurate estimation of the transfer functions $H(f)$ and $H_{TX}(f)$. It is therefore recommended to estimate S_{yx} and $|X(f)|^2$ using the Barlett's method [177]. To do so, each T_c interval of the K intervals of the input signal $y(t)$ is divided into M sub-intervals. The optimum number of sub-intervals to reduce the variance of the estimation of all three parameters was found empirically to be $M = 500$ for the MIR instrument. Knowing the delay τ_c , these sub-intervals are cross-correlated with the corresponding part of the transmitted code. The M sub-intervals are then averaged to get a smoothed estimation of the spectra $|X_k(f)|^2$, which is used to estimate the transfer functions in Eqn. (6.47). Last, the K estimated transfer functions are averaged to reduce the impact of the noise $W(f)$.

From Fig. 6.4, the estimated transfer functions $H_{yx}(f)$ of the up-looking and down-looking channels are:

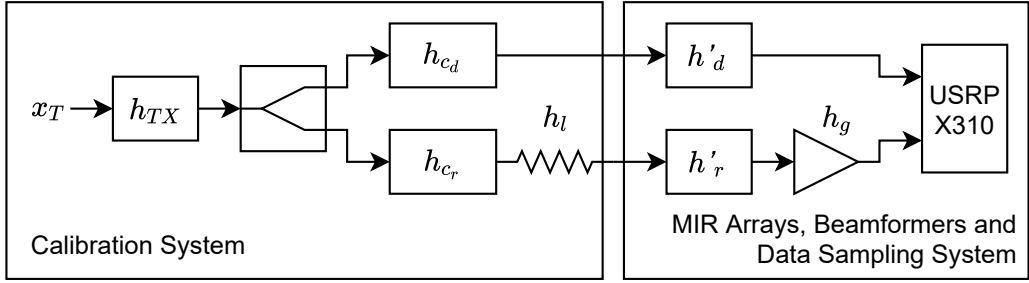


Figure 6.4: Detailed blocks of the in-flight calibration. Expanded from Fig. 5.31.

$$H_{y_{u,x}}(f) = H_{TX}(f) \cdot H_{c_d}(f) \cdot H'_d(f) \cdot e^{-j\Delta\phi_d} \quad (6.47)$$

$$H_{y_{d,x}}(f) = H_{TX}(f) \cdot H_{c_r}(f) \cdot H_l(f) \cdot H'_r(f) \cdot H_g(f) \cdot e^{-j\Delta\phi_r}, \quad (6.48)$$

where the subscripts d and r stand for the up- and down-looking channels, respectively, $H_c(f)$ stands for the transfer function of the calibration splitting network, which includes the power splitter, $H_l(f)$ is the transfer function of the attenuator placed at the output of the down-looking calibration path, and $H_g(f)$ is the transfer function of the extra amplifier in the down-looking chain. Note that $H_{TX}(f)$ cannot be measured since it includes the transfer function of the transmitting USRP, but $H_{c_u}(f)$ and $H_{c_D}(f) \cdot H_l(f)$ can be. By dividing both transfer functions it is obtained:

$$H_{dr}(f) = \frac{H_{c_d}(f) \cdot H'_d(f)}{H_{c_r}(f) \cdot H_l(f) \cdot H'_r(f) \cdot H_g(f)} \cdot e^{-j(\Delta\phi_d - \Delta\phi_r)}, \quad (6.49)$$

Then, the transfer function of the calibration splitting network can be measured and then removed as:

$$H'_{dr}(f) = H_{dr}(f) \cdot \frac{H_{c_r}(f) \cdot H_l(f)}{H_{c_d}(f)} = \frac{H'_d(f)}{H'_r(f) \cdot H_g(f)} \cdot e^{-j(\Delta\phi_d - \Delta\phi_r)}, \quad (6.50)$$

which is used for the relative calibration between channels.

Figure 6.5 shows the estimated $|H_{dr}(f)|$ and $\angle H_{dr}(f)$ for all T_c intervals of one of RF chains using $M = 500$ sub-intervals, and the estimated linearization. As it can be seen, the phase is linear, and the y-intercept points of the different T_c intervals are similar, proving that the frequency error between local oscillators is successfully compensated, otherwise the phase (y-intercept point) will be rotating. The estimated phase was 73.58° with a standard deviation of 0.89° . The estimated group delay was 12.53 ns with a standard deviation of 0.22 ns.

In order to determine if the calibration remains constant throughout time and the transient time, the direct and reflected channels of a single USRP were calibrated every 15 minutes for almost 12 hours. The experiment was carried out in a room without any

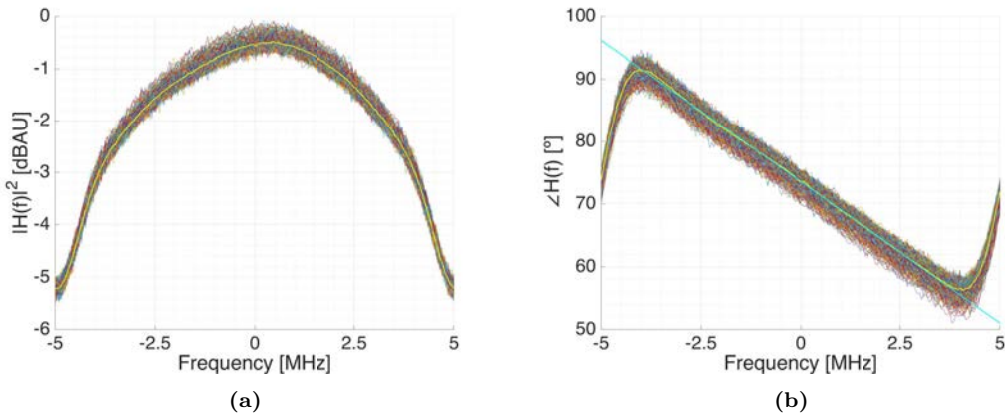


Figure 6.5: Estimated channel transfer function a) squared module, and b) phase for the different T_c intervals with $M = 500$. The time averaged estimations are plot in yellow. In the phase case, the linear approximation in shown cyan.

temperature control, which may have influenced the result. Figures 6.6 and 6.7 show the frequency error difference and the phase difference between the direct and the reflected channel throughout time. Both remain constant, which shows that the frequency error has been compensated properly. The gap between measurements around 200 minutes after power up may have been caused by the operating system in charge of periodically running the calibration measurements.

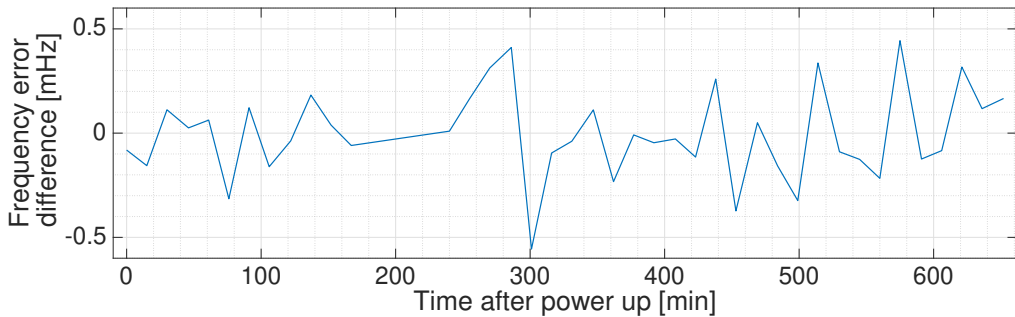


Figure 6.6: Estimated frequency error difference between the up-looking and down-looking RF channels throughout time for a single USRP.

Figure 6.8 shows the group delay difference, and Fig. 6.9 shows the gain between channels. The group delay difference takes up to $3\tau \approx 380$ minutes to converge. The gain difference, however, seems to slowly decrease linearly throughout time after $3\tau \approx 80$ minutes, which might be caused by the room temperature varying during the day.

A second experiment was set up to analyze the phase error of the four USRPs. Figure 6.10 shows the histograms of the phase noise after the frequency error compensation once the average estimated phase of each measurement has been removed. Each figure

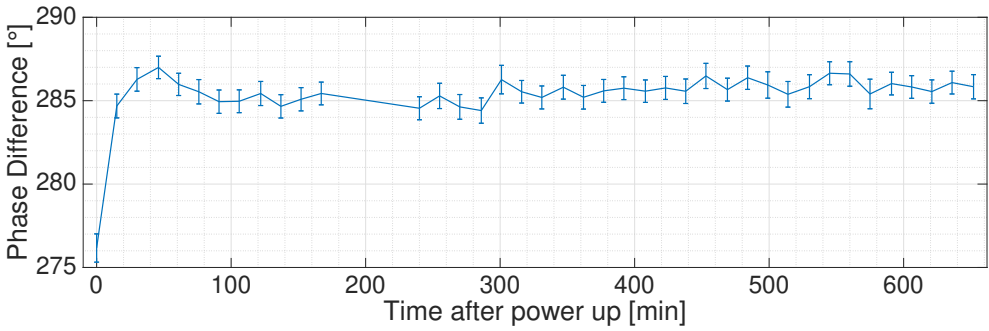


Figure 6.7: Estimated phase difference between the up-looking and down-looking RF channels throughout time for a single USRP. Markers show one standard deviation of uncertainty.

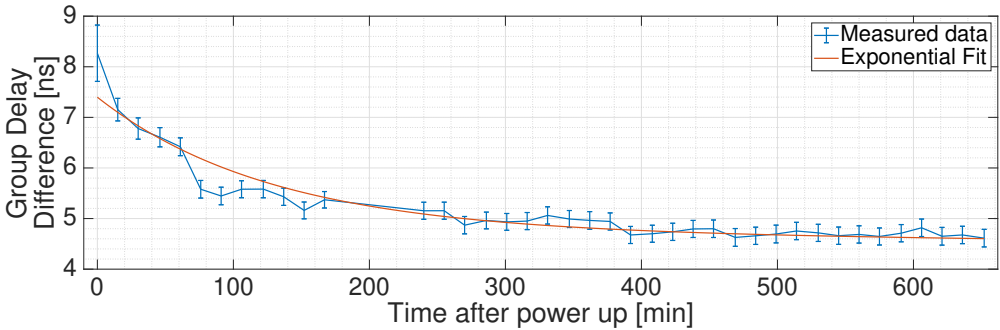


Figure 6.8: Estimated group delay difference between the up-looking and down-looking RF channels throughout time for a single USRP. Markers show one standard deviation of uncertainty.

corresponds to a different USRP, and displays the phase error of the up-looking channel, the down-looking channel, and the phase difference between them.

6.2.6 Noise Characterization of the USRPs and SNR Mapping

Once the signals $d'(t)$ and $r'(t)$ are sampled and cross-correlated with clean replicas of the code, it is required to convert the peak value in arbitrary units to power units. When sampling at 1 bit the peak value is proportional to the input SNR [29], which depends on the noises $n_d(t)$ and $n_r(t)$ generated in the RF chains, and on the noises generated inside the USRPs $n_{ud}(t)$ and $n_{ur}(t)$ that cannot be directly measured (see Fig. 6.11).

In order to estimate $n_{ud}(t)$ and $n_{ur}(t)$, first the noise powers P_{n_d} and P_{n_r} were measured over a 32.736 MHz bandwidth with a spectrum analyzer (see Table 6.1). Note that the noise power in the reflected channels is higher than in the direct channels because of the extra RF amplifier. Using a Vector Signal Generator Rohde & Schwarz SMU-200A [178], noises with these power levels were generated in conjunction with GNSS signals and were injected to the USRPs direct and reflected RF inputs. The GNSS signals injected to the USRPs tuned at L1/E1 were GPS L1 C/A and Galileo E1 B+C, while

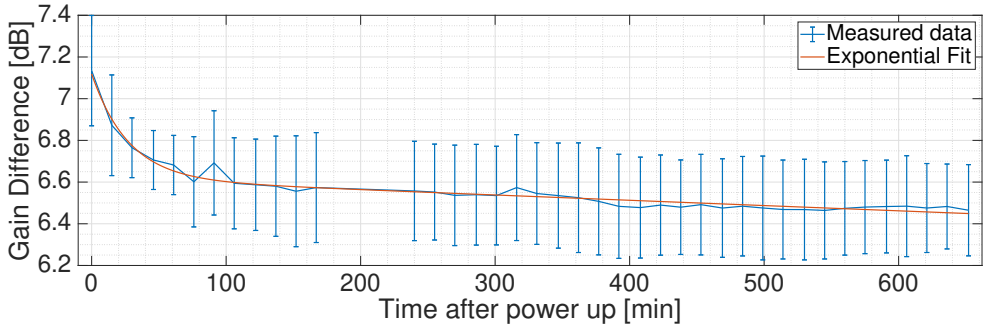


Figure 6.9: Estimated gain between the up-looking and down-looking RF channels throughout time for a single USRP. Markers show one standard deviation of uncertainty. The mean and the standard deviation have been computed as geometric mean and geometric standard deviation, respectively.

Table 6.1: Measured noise power at the USRP inputs.

	Beam	Up	Down
USRP1	L1-2	-72.7 dBm	-37.0 dBm
USRP2	L1-1	-70.5 dBm	-39.4 dBm
USRP3	L5-1	-69.2 dBm	-32.5 dBm
USRP4	L5-2	-69.6 dBm	-32.5 dBm

the signals injected to the USRPs tuned at L5/E5A were L5 I+Q and Galileo E5A I+Q. The power of the generated GNSS signals was swept to satisfy a SNR from 15 dB down to -50 dB. The sampled signal was cross-correlated with the appropriate code, and the resultant relationship between the peak value and the input power is shown in Fig. 6.12.

For high SNR, the cross-correlation peak value is up-limited by $\sqrt{2} \cdot N$, where N is the number of samples in the sequence to be cross-correlated. In the case of a real GNSS signal $c_r(t)$, such as GPS L1 C/A received with a phase γ in the presence of complex noise $n(t)$, the sampled signal $s(t)$ becomes:

$$s(t) = (c_r(t) \cdot \cos(\gamma) + \text{Re}(n(t))) + i \cdot (c_r(t) \cdot \sin(\gamma) + \text{Im}(n(t))). \quad (6.51)$$

If the phase γ is close enough to $n \cdot 90^\circ$, $n \in \mathbb{Z}$, the energy of the sampled signal will be concentrated mostly in the real or imaginary part of $s(t)$, and the other part could be dominated by the noise. In this uncommon case for high SNRs the cross-correlation peak value will not reach the maximum. In any other case, the real and imaginary parts of $s(t)$ will be dominated by the received code, and the cross-correlation peak value will saturate at $\sqrt{2} \cdot N$.

In the case of complex GNSS signals such as GPS L5, the sampled signal is:

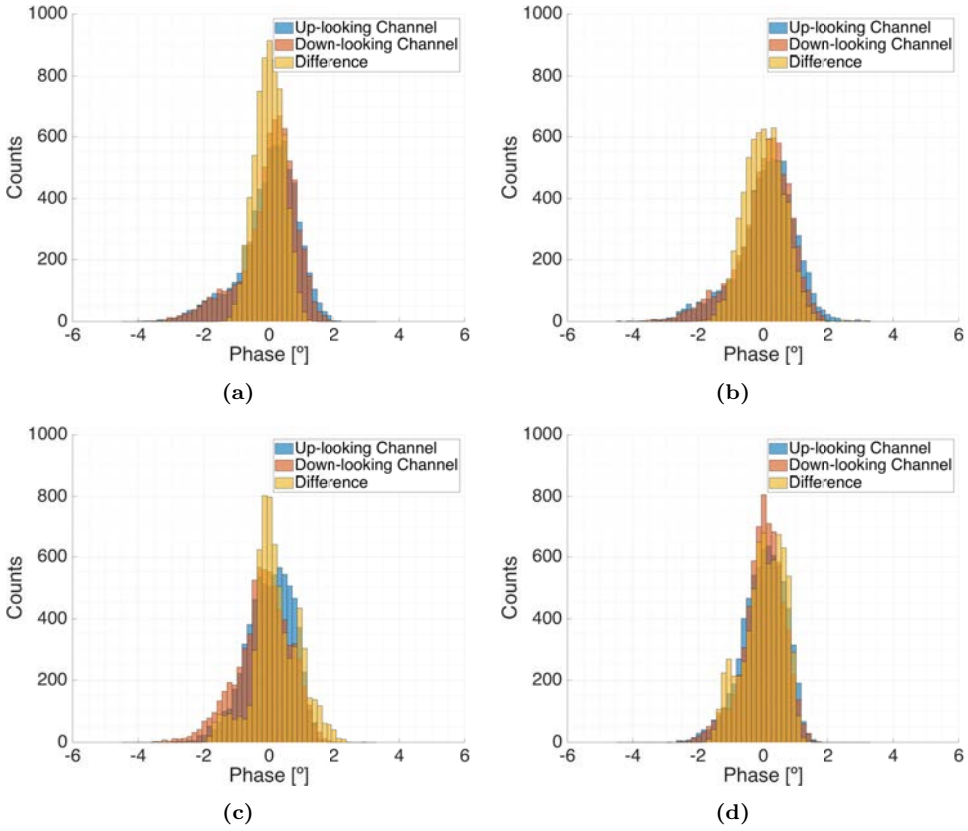


Figure 6.10: Phase noise histograms for the a) L1 Beam 1, b) L1 Beam 2, c) L5 Beam 1, and d) L5 Beam 2 USRPs after the frequency error compensation.

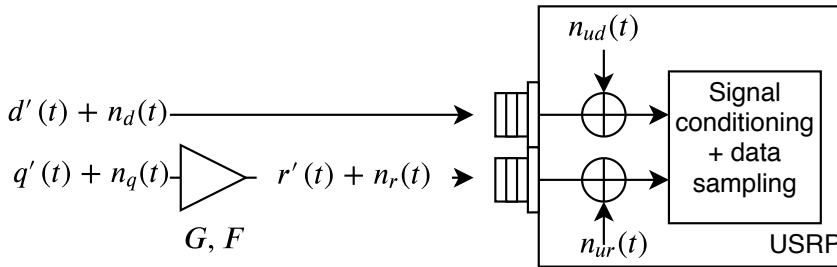


Figure 6.11: Used USRPs noise source model.

$$\begin{aligned}
 s(t) &= (c_r(t) \cdot \cos(\gamma) - c_i(t) \cdot \sin(\gamma) + \text{Re}(n(t))) \\
 &\quad + i(c_r(t) \cdot \sin(\gamma) + c_i(t) \cdot \cos(\gamma) + \text{Im}(n(t))), \quad (6.52)
 \end{aligned}$$

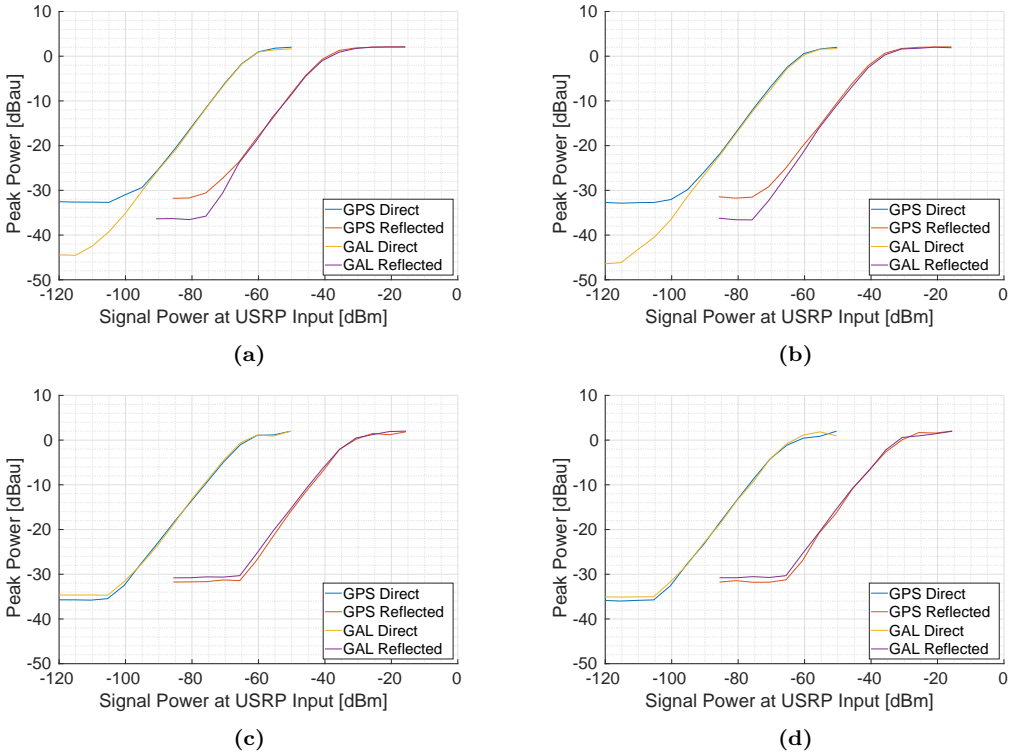


Figure 6.12: Measured peak power value as function of the signal input power for the expected noise power level in the a) L1 Beam 1, b) L1 Beam 2, c) L5 Beam 1, and d) L5 Beam 2 USRPs. The peak value has been normalized by the number of samples in the correlated sequence.

where $c_r(t)$ and $c_i(t)$ stand for the real and imaginary components of the GNSS signal. Analogously to the real case, when γ is close enough to $45^\circ + n \cdot 90^\circ$, $n \in \mathbb{Z}$,

$$\cos(\gamma) = \pm \sin(\gamma), \quad (6.53)$$

the codes c_r and c_i could cancel each other, so the real or the imaginary part of $s(t)$ could be dominated by the noise. Otherwise, for high SNRs the cross-correlation peak value will saturate at $\sqrt{2} \cdot N$.

As the SNR decreases, the number of bits that the noise affects increases. In the case of the up-looking channel, and assuming Additive White Gaussian Noise (AWGN) noise, the probability that the noise affects a bit is

$$P(X \leq 0) = \frac{1}{2} \cdot \left(1 + \operatorname{erf} \left(-\frac{1}{\sqrt{2}} \cdot \sqrt{\frac{\mu_{d'}^2}{\sigma_{n_d}^2 + \sigma_{n_{ud}}^2}} \right) \right), \quad (6.54)$$

where $\mu_{d'}^2$ is the power of the signal $d'(t)$, $\sigma_{n_d}^2$ is the noise power coming into the USRP,

and $\sigma_{n_{ud}}^2$ is the power of noise generated inside the USRP. Note that the probability decreases if the term $\frac{\mu_{d'}^2}{\sigma_{n_d}^2 + \sigma_{n_{ud}}^2}$ increases. In the case of the down-looking channel, if there is no extra amplifier; the received signal's power is $\rho \cdot \mu_{d'}^2 = \mu_{r'}^2$, where $|\rho| < 1$ is the reflectivity on ground; and assuming that the gain and noise were equal in the up- and down-looking RF chains, the probability of a bit's value being affected by the noise is

$$P(X \leq 0) = \frac{1}{2} \cdot \left(1 + \operatorname{erf} \left(-\frac{1}{\sqrt{2}} \cdot \sqrt{\frac{\rho \cdot \mu_{d'}^2}{\sigma_{n_d}^2 + \sigma_{n_{ud}}^2}} \right) \right). \quad (6.55)$$

If an extra amplifier with gain G and noise factor F is located before the USRP, then the probability becomes

$$\begin{aligned} P(X \leq 0) &= \frac{1}{2} \cdot \left(1 + \operatorname{erf} \left(-\frac{1}{\sqrt{2}} \cdot \sqrt{\frac{\mu_{r'}^2}{\sigma_{n_r}^2 + \sigma_{n_{ur}}^2}} \right) \right) \\ &= \frac{1}{2} \cdot \left(1 + \operatorname{erf} \left(-\frac{1}{\sqrt{2}} \cdot \sqrt{\frac{\rho \cdot G \cdot \mu_{d'}^2}{G \cdot F \cdot \sigma_{n_d}^2 + \sigma_{n_{ud}}^2}} \right) \right). \end{aligned} \quad (6.56)$$

After amplification, if the outcoming noise from the MIR instrument is larger than the noise generated in the USRP ($G \cdot F \cdot \sigma_{n_d}^2 \gg \sigma_{n_{ur}}^2$), then the probability becomes

$$P(X \leq 0) = \frac{1}{2} \cdot \left(1 + \operatorname{erf} \left(-\frac{1}{\sqrt{2}} \cdot \sqrt{\frac{\rho \cdot \mu_{d'}^2}{F \cdot \sigma_{n_d}^2}} \right) \right), \quad (6.57)$$

which implies a degradation with respect to the case without amplification, whereas if the USRP noise dominates then the probability becomes

$$P(X \leq 0) = \frac{1}{2} \cdot \left(1 + \operatorname{erf} \left(-\frac{1}{\sqrt{2}} \cdot \sqrt{\frac{\rho \cdot G \cdot \mu_{d'}^2}{\sigma_{n_{ud}}^2}} \right) \right), \quad (6.58)$$

which implies an improvement with respect to the non-amplified case.

The cross-correlation peak value decreases until it saturates when the sampled signal $s(t)$ is totally dominated by the noise. This saturation is caused by the non-null cross-correlation between the noise and the locally generated clean replica of the code.

In the case of the up-looking channels, the saturation point of the Galileo E1 B+C signals is much lower than for the GPS L1 C/A, which might be caused by the four times larger coherent integration time, and for having part of the code in the I and Q components (see Figs. 6.12a and 6.12b). In the GPS L5 I+Q and Galileo E5A, the slightly lower saturation point than for the to GPS L1 C/A might be caused only by having part of the code in the I and Q components. In the down-looking channels, where the noise level is much higher, the peak power saturates for a much higher input powers, displacing the curves towards the right. The saturation level increases in the case of the USRPs tuned at L5/E5A frequency bands, probably caused by the higher noise level at the input compared with respect to the USRPs tuned at L1/E1 (see table 6.1). Besides, Galileo E1 B+C shows an improvement with respect to GPS L1 C/A but not as large as in the up-looking case. These facts imply an excessive increase of the noise level in the down-looking channel, which might have degraded the instrument performance.

6.3 Validation Results

This section describes the main experiments carried out to check that the instrument works properly prior to start the field campaigns. First, during the pre-calibration in the anechoic chamber, some radiation patterns were measured, both with the instrument uncalibrated and calibrated, and the beam steering capabilities were tested. Later on, the instrument was placed in the laboratory rooftop tracking GPS and Galileo satellites to ensure that the instrument was able to receive properly all the desired GNSS signals with proper power levels.

6.3.1 Calibration impact and Measured Radiation Patterns

During the pre-calibration in the anechoic chamber (Fig. 6.13), the beam steering capabilities of the antenna arrays were also evaluated.



Figure 6.13: MIR down-looking array being calibrated and measured at the UPC anechoic chamber. The 19 elements MIR array is at the back left, while the transmitting reference horn antenna is at the front right. The transmitting antenna has linear polarization and can rotate around the boresight axis.

The beamformers and the arrays were calibrated following the procedure described in section 6.2.1. Figure 6.14 shows the IQ gain circles explained in section 4.5 of all vector modulators of an L1 beam before (left) and after calibrating (right). A red circle with the average gain has been drawn to ease the viewing of the improvement and the impact of the amplitude unbalance. The radii lines mark the α_i parameter, which is where the gain circle starts to “rotate”. Before calibration, when setting a desired angle in the vector modulators, the achieved angle had an RMS of 13° , at L1 and 16° at L5. After calibration, the RMS improves down to 4.9° and 4.2° , respectively. Similarly, amplitude errors were corrected from 0.55 dB and 0.11 dB to 0.02 dB and 0.03 dB at L1 and L5 respectively.

Table 6.2: Beamformer inaccuracy impact in the array directivity before and after calibration.

	Beamformer error		Array Directivity Loss	
	L1/E1	L5/E5A	L1/E1	L5/E5A
Amplitude (Uncalibrated)	0.55 dB	0.11 dB	0.061 dB	0.0027 dB
Amplitude (Calibrated)	0.02 dB	0.03 dB	<0.001 dB	<0.001 dB
Phase (Uncalibrated)	13°	16°	0.22 dB	0.34 dB
Phase (Calibrated)	4.9°	4.2°	0.03 dB	0.02 dB

The approximated impact of these errors in the array directivity are computed as in [179] and are shown in table 6.2.

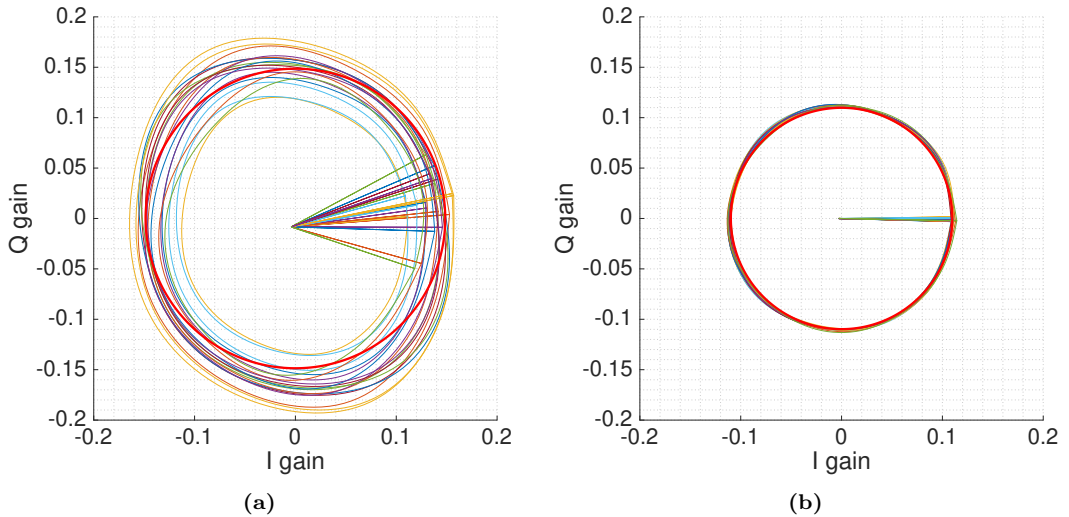


Figure 6.14: IQ gain circles a) before, and b) after calibration. The radii lines mark where the circle starts to “rotate”. A red circle with average radius has been added to ease the viewing the effect of the amplitude unbalance.

Figures 6.15a and 6.15b show the impact of the calibration in the radiation pattern when the LHCP down-looking array was pointing to the boresight of the antenna both at L1/E1, and L5/E5A frequency bands, respectively. The calibration improves the nulls of the radiation pattern in both bands. Besides, the uncalibrated beam in L1 is slightly tilted towards the right, which is corrected thanks to the calibration.

After the beamformer calibration, the beam steering capabilities were tested by tilting the beams from the boresight of the antenna to one of the sides, and some cuts of the antenna radiation pattern were measured. Figures 6.16a and 6.16b show the antenna radiation patterns measured in the same plane where the beams were tilted, at L1/E1, and at L5/E5A frequency bands, respectively. The experiment was carried out for Off-Boresight Angles (OBAs) from 0° to 50° in steps of 10° . As it can be seen, the maximum

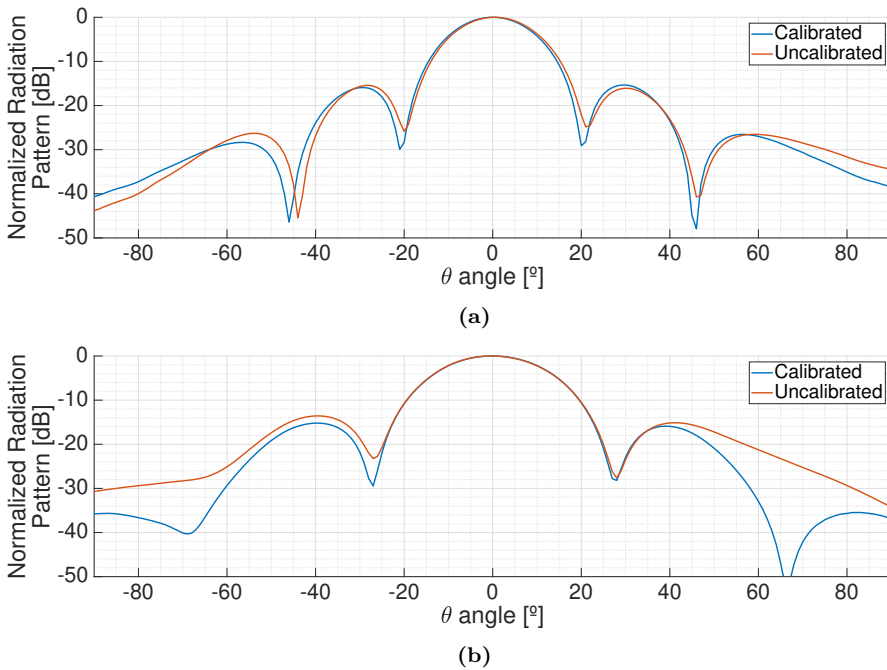


Figure 6.15: Effect of the calibration in the radiation patterns. Planar cuts in the $\varphi = 30^\circ$ plane at a) L1/E1, and b) L5/E5A.

Table 6.3: MIR arrays measured cross-polarization after calibration. The data from the up-looking was lost.

	L1/E1	L5/E5A
Up-looking Array	-	-
Down-looking Array	$\mu=-15.20$ dB $\sigma=2.38$ dB	$\mu=-20.43$ dB $\sigma=1.99$ dB

decreases as the beam is pointed far from the boresight due to the antenna radiation pattern of the individual elements, and due to the smaller projected area of the array. This loss of directivity was measured as well in order to be compensated while conducting scatterometric measurements, and it can be seen in Fig. 6.17. Similarly, the phase and cross-polarization dependence on the direction of arrival for altimetric measurements was also measured. The cross-polarization is shown in Fig. 6.18. Table 6.3 shows the mean and standard deviation of the cross-polarization inside the region limited by a maximum off-boresight angle of $\pm 35^\circ$ for the down-looking array. The data from the up-looking array was lost.

In order to power up any active antenna to be measured in the anechoic chamber, the rotor has a power connectors that are wired internally using a slip ring. Thus the rotor can spin freely without any cable being twisted and broken. However the slip ring was

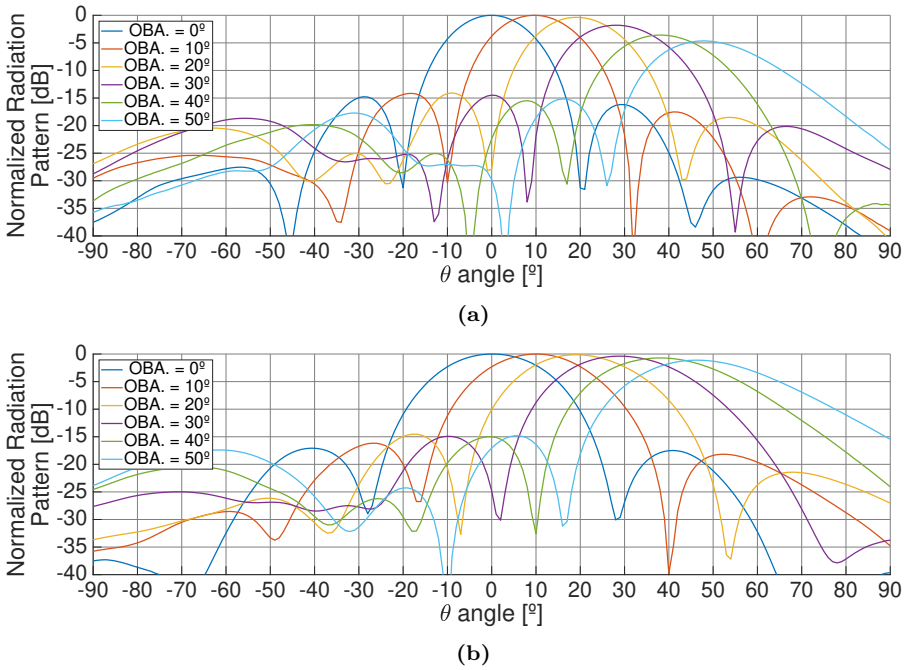


Figure 6.16: Planar cuts of the radiation pattern around the $\varphi = 0^\circ$ plane when tilting the beam in the same plane for different off-boresight pointing angles, at a) L1/E1, and b) L5/E5A frequency bands.

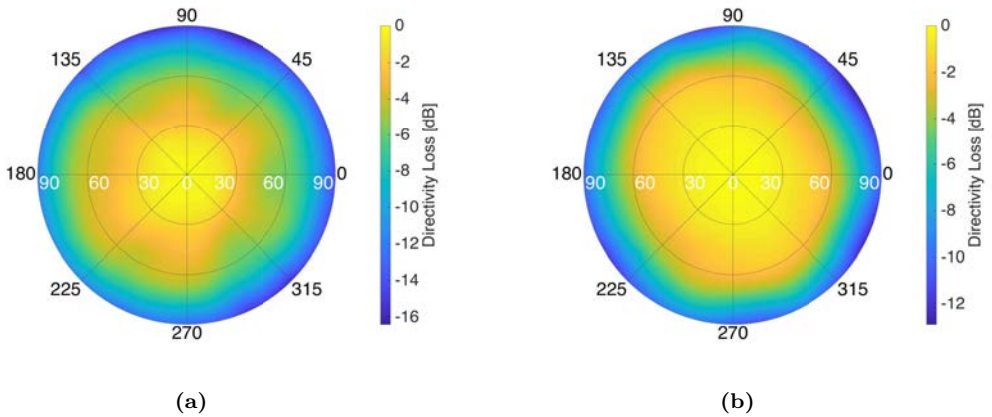


Figure 6.17: Directivity loss of the down-looking array as a function of the pointing direction at a) L1/E1, and b) L5/E5A frequency bands.

not rated for 220 V, the voltage required in the instrument, so it had to be powered using a power cord. Measuring the front part of the radiation patterns without supervision was possible by placing properly the cable, and ensuring that the rotors would not spin totally over the vertical axis. For the back part of the radiation patterns this was much

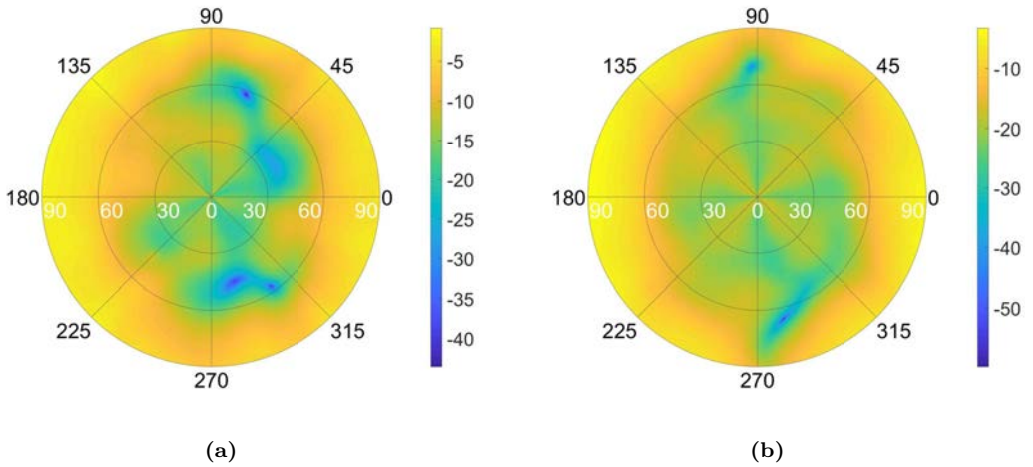


Figure 6.18: Fore hemisphere of the up-looking array cross-polarization, at a) L1/E1, and b) L5/E5A frequency bands.

Table 6.4: MIR arrays measured directivities after calibration pointing to the boresight.

	L1/E1	L5/E5a
Up-looking Array	20.30 dB	18.20 dB
Down-looking Array	20.46 dB	18.09 dB

more complicated, the measurements required constant supervision, and the process took much longer time. For this reason, the back lobes were measured only pointing to the boresight, and are shown in Fig. 6.19.

It was therefore complicated to accurately estimate the directivity of the array since only the fore hemisphere of the radiation pattern was measured (Fig 6.20). The estimated directivities for both arrays while pointing to the boresight can be seen in table 6.4.

Figure 6.21 shows different antenna radiation pattern cuts when pointing to an off-boresight angle of 35° . The side lobe levels are lower than 12 dB and 14 dB at L1/E1 and L1/E1 frequency bands, respectively.

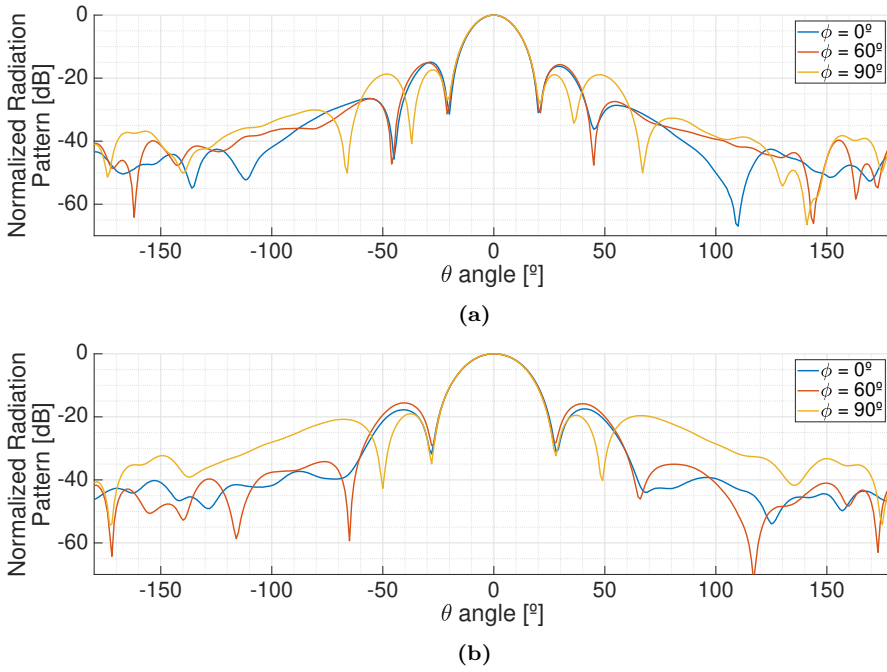


Figure 6.19: Azimuthal cuts of the full radiation pattern pointing to the boresight of the antenna, at a) L1/E1, and b) L5/E5A frequency bands.

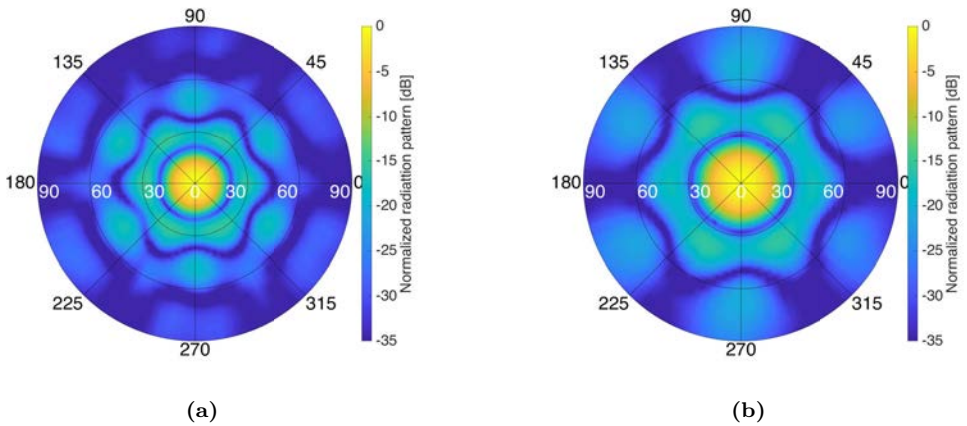


Figure 6.20: Fore hemisphere of the measured radiation pattern of the down-looking array, at a) L1/E1, and b) L5/E5A frequency bands.

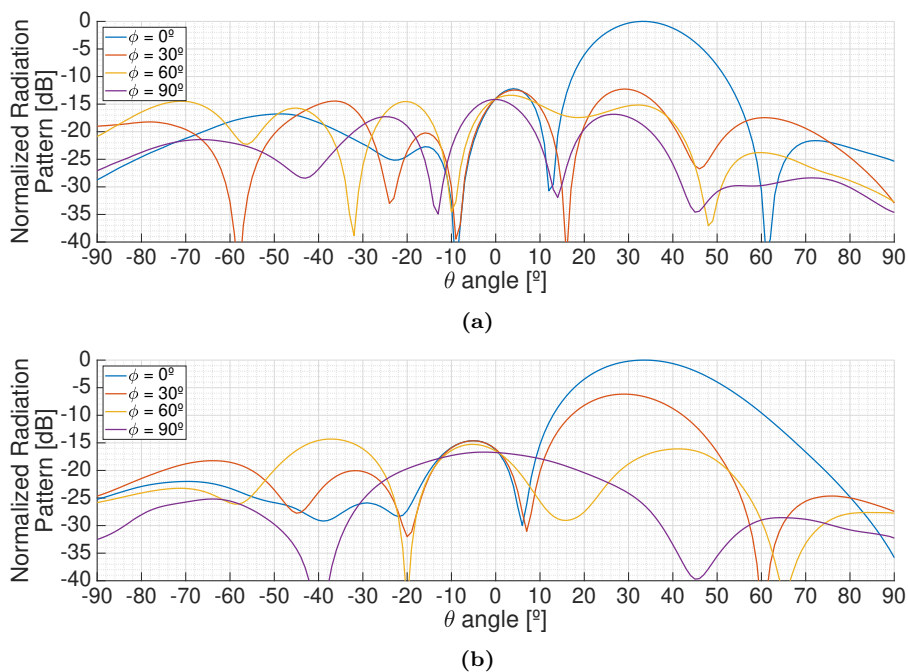


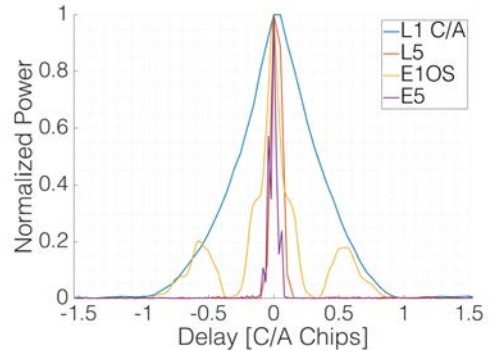
Figure 6.21: Side lobes for different azimuthal cuts of the antenna pattern when pointing to an off-boresight angle of 35° at a) L1/E1, and b) L5/E5A frequency bands.

6.3.2 Outdoor Experiments

Several experiments were carried out in the rooftop of the laboratory to ensure the proper working of the instrument. The first one aimed to check that the instrument was able to retrieve data from all systems and frequency bands with enough power. To do so, the up-looking array was placed with a random orientation with respect to the North (Fig. 6.22), pointing to GPS and Galileo satellites at both L1/E1 and at L5/E5A frequency bands. The received signals were sampled and stored at 16 bits and 20 Msps, and cross-correlated with clean replicas of the PRN codes. Figure 6.22 also shows four retrieved waveforms for GPS and Galileo in both frequency bands. The correlation peaks are displayed in the time origin of a single figure to for easier intercomparison. The experiment also aimed at checking if extra gain was required to reach the sensitivity of the SDR and to take advantage of the whole dynamic range of the ADCs, which was not. In order to check if more gain was required for the down-looking RF chain, attenuators were placed before the SDRs in order to determine the sensitivity level. Since the reflected signals are expected to be 0-30 dB weaker than those collected by the up-looking RF chain, two extra RF amplifiers with a total gain of ≈ 35 dB were added just before the SDRs in the down-looking chains.



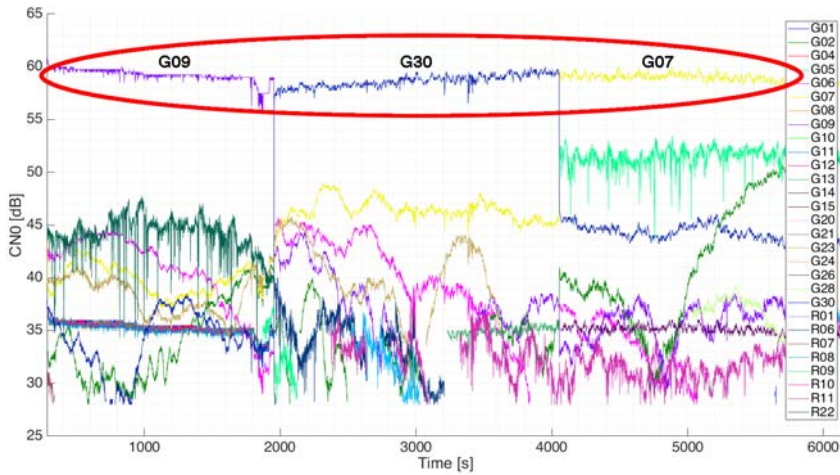
(a)



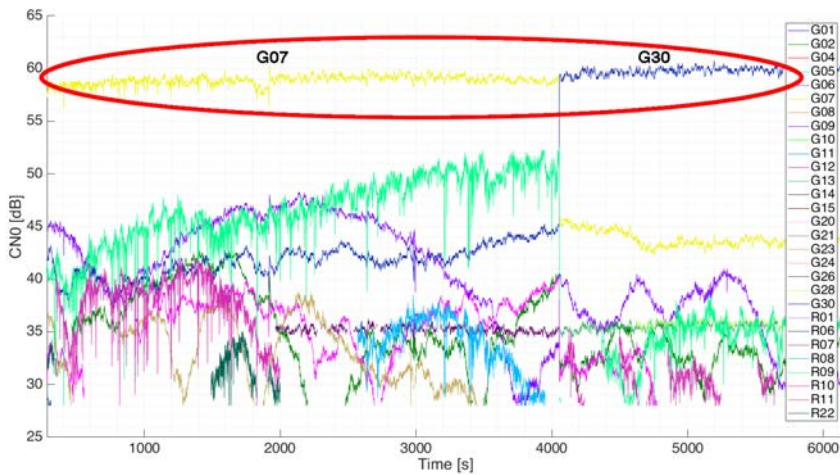
(b)

Figure 6.22: a) MIR up-looking array and rack during the rooftop experiments, and b) retrieved waveforms from GPS and Galileo satellites in both L1/E1 and L5/E5A frequency bands during the rooftop experiments [180].

Later on, the satellite selection algorithm was tested by leaving the instrument tracking the optimum satellites and monitoring the C/N0 at the output of the beamformers. To do so, the outputs of the L1-1 and L1-2 beams were connected to a dual-antenna GNSS receiver capable of tracking GPS and GLONASS satellites (the selection of Galileo satellites was deactivated in order to be able to track the pointed satellites). The C/N0 of all satellites was monitored for a long time. Figures 6.23a and 6.23b show the C/N0 tracked in the L1-1 beam, and the L1-2 beam, respectively. As it can be seen, the tracked satellite receives more power than the others. The satellite selection algorithm was set to choose the optimum satellites every 5 minutes. Two changes in the tracked satellites can be observed in the figure, where the C/N0 of the satellites drops or raises suddenly when the algorithm decided to track a different satellite.



(a)



(b)

Figure 6.23: Tracked C/N_0 of all satellites in the a) L1-1 beam, and b) L1-2 beam during the experiment in the laboratory rooftop [180]. The red circled C/N_0 corresponds to the tracked satellite.

6.4 Conclusions

This chapter has shown the different steps to calibrate the MIR instrument. The up- and down-looking arrays and beamformers are first characterized by separate prior to flight in the anechoic chamber in order to properly form the beams during the experiments. The cross-calibration between the arrays (or in-flight calibration) and the mapping between the cross-correlation peak value and the input power are applied in

post-processing. For the in-flight calibration, the use of PRN codes has been proposed and proved useful to estimate the amplitude, delay, and phase calibration of a channel. The USRP noise characterization suggests an excessive noise power in the down-looking chain, which might have degraded the instrument performance. The decision to add an extra amplifier was taken when the instrument was still supposed to sample at 16 bits, and it showed an improvement of the MIR performance at that time, while the noise characterization of the USRPs with 1 bit was suggested after the flights, when it was too late to change it.

Part III

Experimental Results

7

Chapter 7

DME/TACAN Impact Analysis in GNSS-R

7.1 Introduction

As soon as two prototypes of RF Front-ends were manufactured, some tests were carried out in order to validate them. The two front ends were connected to SDR, and were placed on the laboratory rooftop. Then, both SDRs sampled data synchronously at the different frequency bands (see Fig. 7.1). This experiment led to the conclusion that narrow band pass filters were required besides the digitally tunable band-pass filters included in the SDRs in order to increase the rejection to out of band signals.

The cross-correlation of the sampled data from both Front-ends at L5/E5A frequency band showed unexpected shapes both in the cross-correlation waveform and in the CAF as can be seen in Fig. 7.2. The cause was the presence of DME/TACAN signals coming from Barcelona airport that disrupted the cross-correlations.

This chapter studies the impact of DME/TACAN signals in GNSS-R, and then the particular case of Low Earth Orbit (LEO) orbit GNSS-R instrument like GNSS REflectometry, Radio Occultation and Scatterometry onboard ISS (GEROS-ISS) is analyzed. Last, a brief summary of RFI mitigation techniques is presented, and the impact of some techniques in the expected SNR is estimated.

This chapter is adapted from the previously published work “DME/TACAN Impact Analysis on GNSS Reflectometry” [46].



Figure 7.1: Experiment on the rooftop that lead to the discovery of the DME/TACAN interferences at L5/E5A frequency band.

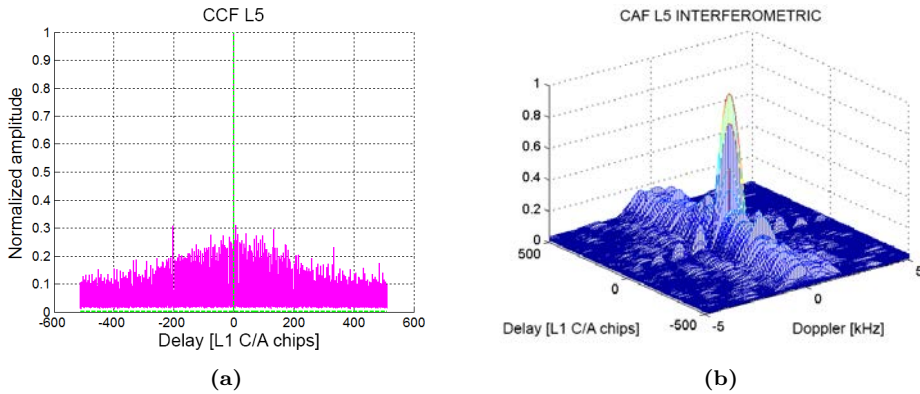


Figure 7.2: a) Cross-correlation waveform, and b) CAF of the sampled data at L5/E5A frequency band under presence of in-band DME/TACAN signals.

7.2 Radio Frequency Interference in GNSS/GNSS-R Systems

As GNSS signals are received below the noise floor, they are very vulnerable to any RFI. This might become an important problem in GNSS-R, and particularly in iGNSS-R, considering that some GNSS bands are shared with other services. In particular, the GPS L5 band (1,164 - 1,188 MHz), the Galileo E5 band (1,166 - 1,217 MHz), and the BeiDou B2 band (1,194 - 1,219 MHz) coexist with two radio navigation systems: a civilian one called DME, and a military one called TACAN. Both systems transmit in the band from 962 MHz to 1,213 MHz with powers reaching up to 3.5 kW [116].

The impact of radio navigation signals on GNSS navigation, and the evaluation of

several mitigation techniques have been widely studied. The impact of several airport equipment in a Galileo receiver has been studied in [181], and concluded that “DME signals are the most significant interference” and that a mitigation technique was needed to avoid the receiver to lose tracking. A degradation up to 12 dB over Europe at 12200 meters height in [182] was predicted, so a pulse blanking system to overcome this problem was proposed. Navigation systems cross-correlate the direct signal $y_d = d(t) + i_d(t) + n_d(t)$, and a clean replica of the code $c(t)$ [183]:

$$Y_{y_dc}(\tau, \nu) = Y_{dc}(\tau, \nu) + Y_{i_dc}(\tau, \nu) + Y_{n_dc}(\tau, \nu), \quad (7.1)$$

where d is the clean GNSS received signal, i is the interference signal, n is noise, c is the code used to despread the GNSS signal d , and Y_{xy} is the cross-correlation in the Delay-Doppler domain of the signals x and y as defined in Eqn. (2.2). The codes used in GNSS systems are robust against interferences and noise [184] because in the cross-correlation process the power spectrum of the interference signal is spread, and the spectral density of the interference over the GNSS resulting band decreases. Even with this spreading effect, if the interference is powerful enough, the terms Y_{i_c} and Y_{n_c} can reduce the signal quality, even to critical levels making impossible the use of GNSS [185]. Analogously, in the case of cGNSS-R the code $c(t)$ is correlated with the reflected signal $y_r = r(t) + i_r(t) + n_r(t)$:

$$Y_{y_rc}(\tau, \nu) = Y_{rc}(\tau, \nu) + Y_{i_rc}(\tau, \nu) + Y_{n_rc}(\tau, \nu). \quad (7.2)$$

Since the reflected signal is even weaker than the direct one, it is expected that for the degradation in GNSS-R to be more critical than in GNSS navigation. In navigation, the antenna is pointing towards the sky, so a receiver located in an airplane receives the DME signals attenuated from the back lobes of the antenna. However, in conventional reflectometry the antenna is pointing towards the ground, so the interference is stronger as it is received from the main beam of the antenna. Besides, the GNSS signal is received approximately 25 dB weaker due to the scattering process in the Earth surface [28].

In the iGNSS-R technique the direct signal y_d is cross-correlated against the reflected signal y_r :

$$Y_{y_dy_r}(\tau, \nu) = Y_{dr}(\tau, \nu) + Y_{di_r}(\tau, \nu) + Y_{dn_r}(\tau, \nu) + Y_{i_dr}(\tau, \nu) + Y_{i_d i_r}(\tau, \nu) + Y_{i_d n_r}(\tau, \nu) + Y_{n_d r}(\tau, \nu) + Y_{n_d i_r}(\tau, \nu) + Y_{n_d n_r}(\tau, \nu), \quad (7.3)$$

where r is the free of RFI reflected GNSS received signal, i_d and i_r are the interferences received by the direct and reflected antennas respectively, and n_d and n_r are the noise terms in the direct and reflected signals respectively. Y_{dr} is the useful part of the DDM. In the DME case, $Y_{i_d i_r}$ is expected to be the dominant term of the undesirable terms due to the high transmitted power. The other terms both for cGNSS-R and iGNSS-R were studied in [186], but not particularizing for any kind of interfering signal.

7.3 DME/TACAN Signal Properties

DME signals retransmitted from the transponder reach the up- and down-looking antennas of the reflectometer with a negligible time difference (as compared to the sampling

frequency), with the same Doppler frequency, but with different phase and amplitude due to the separation between antennas and their orientation. Therefore, in interferometric reflectometry, the correlation peak in the DDM is centered at the origin if the direct and the reflected signals are sampled simultaneously (“non-delayed cross-correlation”). Figure 7.3 shows the WAF [187] of a single DME pair of pulses, which is the auto-correlation function in the delay and Doppler domain $Y_{ss}(\tau, \nu)$. In the Doppler domain the main lobe is modulated by a $1/(12 \mu s) \approx 83$ kHz frequency, with a bandwidth of ≈ 40 kHz for the central peak.

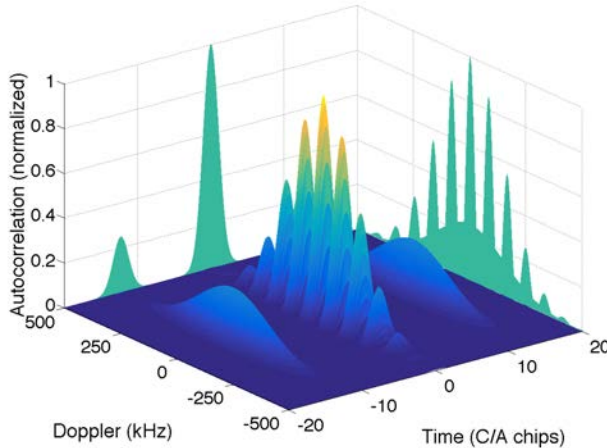


Figure 7.3: DME Woodward Ambiguity Function.

When N signals from different transceivers are received at the direct and reflected antennas, N cross-correlation peaks appear at the origin of the DDM. All these signals also correlate at 0-delay for multiple Doppler frequencies, but not as strongly. The signals received from two different stations have different delays and Doppler frequencies; and therefore, $N^2 - N$ cross-correlation peaks appear spread in the DDM plane. When several correlations are incoherently averaged, the contributions at 0-delay are always present, but the other ones spread along the DDM, and are not in the same position. Therefore, the energy of the DDM tends to concentrate along the 0-delay as well (Fig. 7.4b). If the number of DME signals present is small, the resulting DDM is almost constant for any Doppler frequency as it can be appreciated in Fig. 7.4a. However, as the number of DME pulses increases, the WAF changes and the energy of the DDM tends to concentrate also around the 0-Doppler. Figure 7.4 shows the resulting WAF after the incoherent averaging of 50,000 simulated WAFs with (a) 1 pair of pulses present in the coherent integration time, and (b) 10 pairs of pulses for the “non-delayed cross-correlation” considering uniformly distributed random Delay (as will be seen later in section 7.4) and Doppler between pulses.

The higher the altitude of the GNSS reflectometer, the longer the delay of the reflected signal as compared to the direct signal, so the latter has to be delayed prior to the correlation [179] (“delayed cross-correlation”). Therefore, the sequences of pulses in the direct and reflected signals are different, so they do not cross-correlate at the origin of

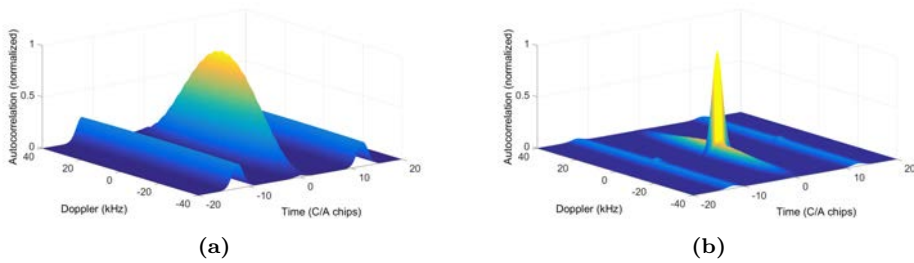


Figure 7.4: Resulting WAF for “non-delayed cross-correlation” after the incoherent averaging of 50,000 simulated WAFs considering uniformly distributed random Delay and Doppler between pulses with a) 1 pair of pulses present in the coherent integration time, and b) 10 pairs of pulses.

the DDM, but are uniformly distributed over the delay axis. The Doppler frequency difference between pulses from a same DME station is almost zero as it changes less than 1 Hz/ms [188], so the cross-correlation peaks between same stations are uniformly distributed along the 0 Hz Doppler line. Moreover, the Doppler frequency and delay between different stations is random, and so is the position of these cross-correlation peaks in the DDM plane. As a consequence, the WAF is uniform in delay, and it has a bit more energy for lower Doppler frequencies as it can be seen in Fig. 7.5. Increasing the number of pulses does not noticeably affect the shape of the DDM, except for its level that is increased, but it cannot be appreciated due to amplitude normalization. The figure shows the resulting WAF after the incoherent averaging of 50,000 simulated WAFs with (a) 1 pair of pulses present in the coherent integration time, and (b) 10 pairs of pulses for the “delayed cross-correlation” considering uniformly distributed Delay and Doppler frequency between pulses.

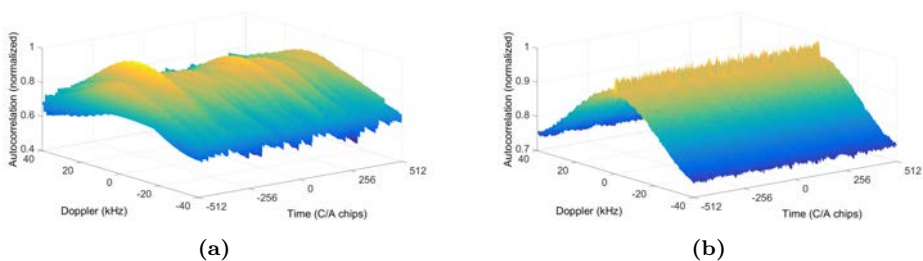


Figure 7.5: Resulting WAF for “delayed cross-correlation” after the incoherent averaging of 50,000 simulated WAFs considering uniformly distributed Delay and Doppler between pulses with a) 1 pair of pulses present in the coherent integration time, and b) 10 pairs of pulses.

The DME signals from different stations cross-correlate between them in the DDM plane only if they are allocated in the same frequency channel, i.e. the cross-correlation between signals in different channels will not be considered. The DME spectrum is 1 MHz wide, and the channels are separated by 1 MHz. The maximum Doppler of a received

DME signal was determined by simulation to be lower than ± 28 kHz in the spaceborne case. To do so, AGI STK was used to compute the received Doppler shift in a LEO orbit from several DME stations at different locations. The expected Doppler difference between the received GNSS signals in the up and down-looking antennas will not exceed ± 40 kHz [188], so the DDM does not have to be computed out of this range. As consequence, the part of the spectrum of two DME signals in adjacent channels that could overlap has a negligible amount of power.

From Eqn. (7.3), the average power in 1 ms after correlating two DME signals Y_{ii} in the “delayed cross-correlation” can be estimated as:

$$\left\langle |Y_{i_d i_r}(\nu)|^2 \right\rangle = \sum_k \sum_l \bar{P}_{i_{d_k}} \cdot \bar{P}_{i_{r_l}} \cdot \delta(f_k - f_l) \cdot \eta_{ACF} \cdot \Upsilon(\nu), \quad (7.4)$$

where $\bar{P}_{i_{d,r}}$ is the average power¹ of the DME signal in 1 ms, f is the frequency channel at which is transmitted, $\delta(f_k - f_l)$ is used to only compute the power of signals allocated in the same frequency channel, $\eta_{ACF} = -24.1$ dB is the average value along the delay axis of an ACF of an unitary mean power DME signal, and $\Upsilon(\nu)$ accounts for the effect of the spreading of the DME WAF in the DDM plane due to the relative Doppler between stations. $\Upsilon(\nu)$ is calculated statistically depending on the maximum Doppler between stations and its probability distribution. $\bar{P}_{i_{d,r}}$ is calculated with the DME peak power $P_{i_{d,r}}$, the average number of received pulses per ms \bar{N} , and the scaling factor between the DME peak power and the DME average power in 1 ms $\eta_{DME} = -24.3$ dB as:

$$\bar{P} = (P \cdot \eta_{DME} \cdot \bar{N}) \quad (7.5)$$

As mentioned before, in the “non-delayed cross-correlation” case the cross-correlation peaks between the same station are concentrated in the 0-Delay and 0-Doppler position. Therefore, to compute the term $Y_{i_d i_r}$ at 0 second Delay and 0 Hz Doppler, Eqn. (7.4) is evaluated with $\eta_{ACF} = 1$ for the terms that fulfill $k = l$, whereas the other points are computed evaluating the equation only for $k \neq l$.

The rest of the noise and interfering cross-terms $Y_{d_i r}$, $Y_{d n_r}$, $Y_{i_d r}$, $Y_{i_d n_r}$, $Y_{n_d r}$, $Y_{n_d i_r}$, and $Y_{n_d n_r}$ are estimated in a general form as:

$$\left\langle |Y_{s_1 s_2}|^2 \right\rangle = P_{s_1} \cdot P_{s_2} \cdot \gamma_{s_1 s_2} \quad (7.6)$$

where s_1 and s_2 are the direct GNSS clean signal d , the reflected GNSS clean signal r , the interference signal received in the up-looking and the down-looking antennas i_d and i_r respectively, or the noise signals in the direct and reflected antenna n_d and n_r respectively. P is the average power of the signal in 1 ms, which in the case of DME signals is calculated in Eqn. (7.5).

The Generalized Spectral Separation Coefficient (GSSC) $\gamma_{s_1 s_2}$ between signals s_1 and s_2 is defined in [186] as:

$$\gamma_{s_1 s_2}(\nu, \tau) = \overline{W_{s_1}}(t, f) * \overline{W_{s_2}}(t, f), \quad (7.7)$$

¹Recall that, following the definition in Eqn. (2.2), y_D is unitless and therefore, P_{i_d} is unitless as well, while P_{i_r} has units of Watts.

which depends on the normalized Wigner-Ville Spectrum (WVS) [189] $\overline{W}_{s_1}(\nu)$ and $\overline{W}_{s_2}(\nu)$ of signals s_1 and s_2 , respectively. The GSSC for Y_{dir} and Y_{idr} is obtained from [186]. The GSSC for Y_{dnr} is calculated as in [186]:

$$\gamma_{n_d n_r}(\nu, \tau) = \frac{1}{B \cdot T_c}, \quad (7.8)$$

where B is the system bandwidth, and T_c the coherent integration time.

The GSSC for $Y_{n_d r}$, $Y_{d n_r}$, $Y_{i_d n_r}$, and $Y_{n_d i_r}$ is derived from Fig. 7.6, which shows all possible cross-correlations between the separate components of two signals composed by a GNSS code (L5 or E5), a pair of DME pulses, and noise that have been simulated. Figure 7.6 shows the squared auto-correlation of the code (L5 or E5) in blue, the squared auto-correlation of a DME signal in red, the squared cross-correlation of the code against the noise in magenta, the squared cross-correlation of the DME against the code in black, and the squared cross-correlation of the DME signal against the noise in green. For the L5 case, all signals have 20 MHz bandwidth, while for the E5 case they have 50 MHz. All signals have been generated at 400 Msps, and have unit energy. The DME signals have been centered at 1,176.45 MHz. The figures are obtained as the incoherent averaging of 100 realizations of noise, and 32 different PRN codes.

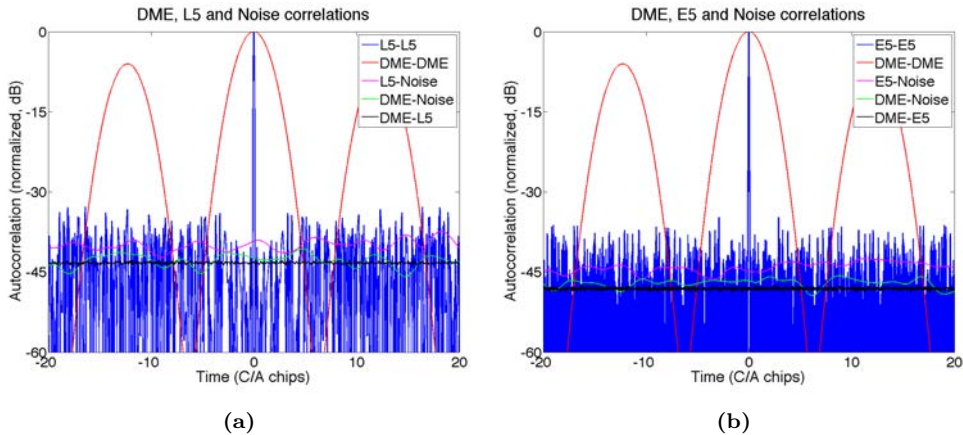


Figure 7.6: a) L5, DME and Noise auto- and cross-correlations and b) E5, DME and Noise auto and cross-correlations.

Figure 7.6 shows that the squared auto-correlation function of the DME signal has 3 lobes, a main one and two side lobes 6 dB below. Each lobe lasts $12 \mu s$, and are separated $12 \mu s$. As a consequence, and considering the high transmitted power, the correlation of GNSS signals might be easily masked. It can also be noticed that the DME-PRN, and DME-noise cross-correlations increase the noise floor, which further degrades the SNR. In both cases, the DME-code, and the DME-noise terms have a similar cross-energy to the code-noise term with unitary energy signals, but considering the high transmitted power of the DME system, the total impact is higher; which degrades the SNR even in navigation receivers. Figure 7.7 shows the impact of having a single pair of DME pulses inside the coherent integration time. To do so, real data was captured with a GNSS L1/E1

and L5/E5A dual-band antenna [145], and a SDR [190]. The data shows the presence of DME signals at the channel corresponding to the Barcelona airport (12 km far from the experiment location, out of the line-of-sight). One millisecond of data without DME pulses, and another one with a single pair of DME pulses were selected. The presence of a single pulse in the correlation window implied a SNR degradation of 5 dB.

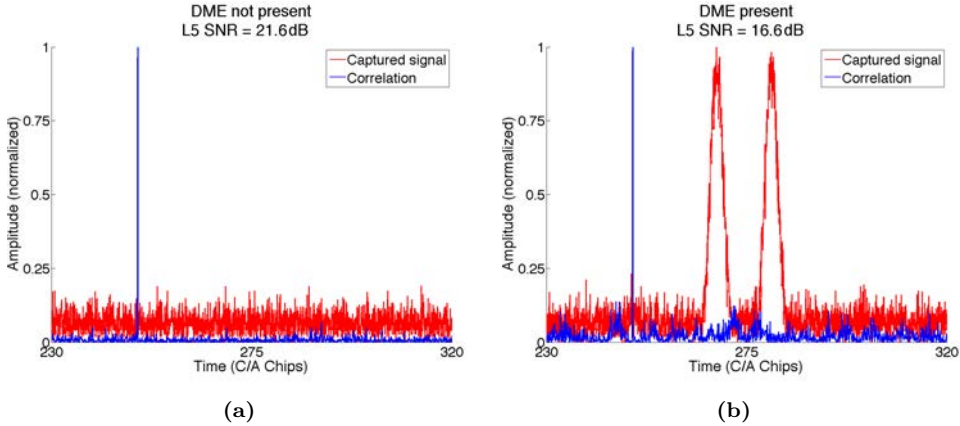


Figure 7.7: SNR degradation in the presence of a single DME pulse in the coherent integration time: a) 1 msec data without DME pulses, and b) 1 msec data with a single pair of DME.

7.4 DME/TACAN Traffic Properties

Figure 7.8 shows a sample of the recorded data. The analysis of this data shows that the time between pulses follows an exponential distribution, which means that the probability of having N pulses in T seconds with λ mean arrivals per second follows a Poisson distribution. In the MIR instrument, the data is correlated during $T_c = 1$ ms and then incoherently averaged in Eqn. (2.2). In order to estimate the random distribution of the pulses inside the correlation window with length T_c , the resulting Probability Density Function (PDF) is estimated by simulation. To do so, the pulse TOA is computed with an exponential random variable with parameter λ , and then the *modulo* T_c operator is applied TOA.

From Fig. 7.8a, an average of 935 DME pulses per second is estimated, which represents around 35 planes simultaneously. This is consistent with the fact that not even the busiest airports reach the DME stations capabilities (100 planes simultaneously). As a consequence of being a Poisson random variable, the traffic arriving from K transponders with $\lambda_1, \lambda_2, \dots, \lambda_K$ arrival rates, also follows a Poisson distribution with $\lambda = \sum \lambda_k$.

The PDF of the pulse position inside the correlation window of length $T_c = 1$ ms with $\lambda = 935$ resulted in a uniform random variable.

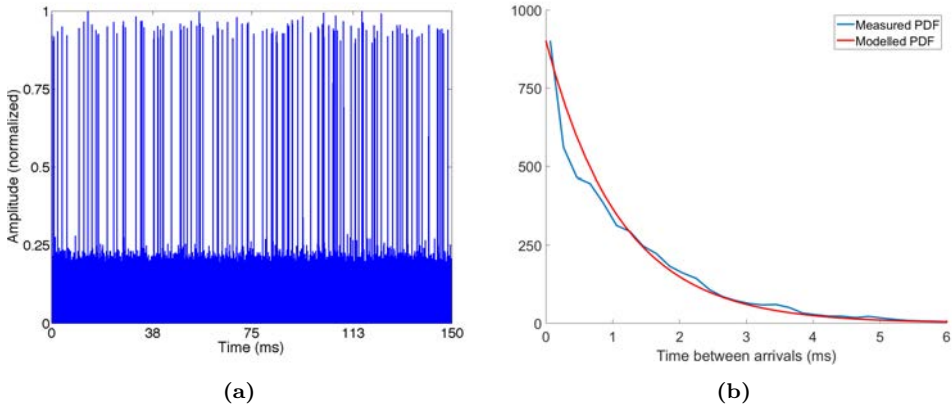


Figure 7.8: a) Sample of the captured data from the Barcelona Airport, and b) PDF of the measured time between arrivals and theoretical exponential PDF with $\lambda = 935$.

7.5 Application to GNSS-R from a LEO Orbit

In order to estimate the impact of these signals in upcoming iGNSS-R instruments in LEO, the Signal to Interference-plus-Noise Ratio (SINR) will be computed. The SINR is useful to estimate the impact for long incoherent averaging times. In this situation, the pulses are smoothed while averaging, resulting in an increase of the noise floor. First, the visibility and received power from all possible DME stations to an hypothetical receiver at 400 km height on-board the International Space Station (ISS) [191] must be estimated. It will be computed for latitudes between $\pm 52^\circ$, the maximum ones that reach the ISS.

First, the visibility of the receiver towards the stations, the arrival angle of the interference, and its expected Equivalent Isotropic Radiated Power (EIRP) has been computed. To do so, the Earth has been modeled using the WGS-84 ellipsoid with standard atmospheric refraction [192]. DME stations out of the Line-of-Sight (LoS) affect due to diffraction effects [193].

Free space transmission has been considered. The transmitted power for all DME stations in [117] has been considered 1 kW for DME stations and 3.5 kW for TACAN stations [194]. A commercial radiation pattern has been considered for the DME stations [195]. The radiation pattern is omnidirectional in azimuth with a directivity of 9.5 dBi, has its main beam pointing at 4° elevation, and transmitting at vertical polarization.

Then, the expected received power at the system has been calculated. To do so, the arrays proposed for the GNSS reflectometer of the GEROS-ISS experiment [191] are used (see Fig. 7.9) for the simulation. These arrays have 31 elements with a separation between elements of $0.93\lambda_{L1}$ and a directivity of 22 dBi [196]. The radiation pattern of each radiating element has been approximated as:

$$D(\theta) = D_{max} - 12 \cdot \left(\frac{\theta}{\theta_{-3dB}}\right)^2 \quad [dB] \quad (7.9)$$

where θ is the antenna off-boresight angle, D_{max} is the maximum directivity (8.4 dBi), and θ_{-3dB} is the antenna beamwidth at -3 dB (75°). This model is a good approximation

for the frontside of the antenna only. Since the reflectometer uses circular polarization, there are 3 dB of polarization losses in receiving the vertical polarized DME signals.

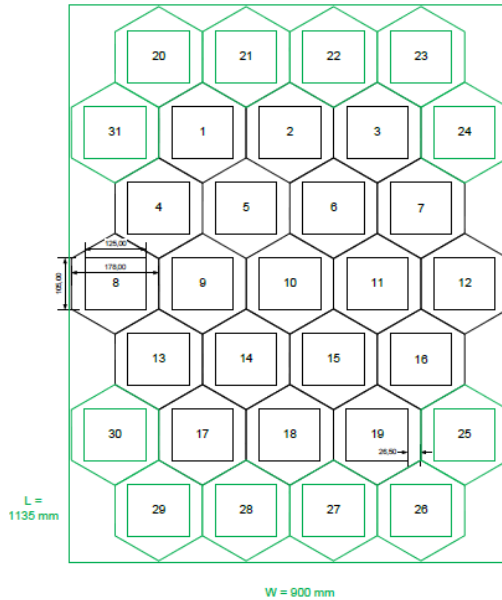


Figure 7.9: Array used for the interference power simulation [196].

In order to compute the expected received power before correlation in any possible position of the receiver (latitudes in the range of $\pm 52^\circ$, and longitudes in the range of $\pm 180^\circ$, both in steps of 1°), the arrays have been pointed to elevations from 90° to 50° in steps of 2.5° , and all azimuths in steps of 5° . Then, the coefficients in Eqns. (7.2-7.3) have been estimated.

The “delayed cross-correlation” has been considered. The DME and GNSS correlation peaks are assumed to be uniformly distributed in the delay axis. DME signals from different stations are received with uniformly distributed Doppler frequency in the ± 28 kHz range, while GNSS peaks are uniformly distributed with random Doppler frequency in the ± 40 kHz range. The Doppler frequency of the direct and the reflected signals from the same DME station are the same, and they change at a rate smaller than 1 Hz/ms [188]. In these conditions, the $\Upsilon(\nu)$ function from Eqn. (7.4) has been approximated empirically by:

$$\Upsilon(\nu) = -2 - \frac{|\nu|}{40 \text{ kHz}} \quad [dB]. \quad (7.10)$$

In order to estimate the average number of pulses per ms in Eqns. (7.4-7.5), the air traffic follows the density of DME stations has been considered. Areas with higher traffic, such as North America, Europe, and the East coast of China, have more density of DME transponders. As consequence, the traffic has been distributed uniformly between

all DME stations, and has been quantified as 13,000 aircraft flying simultaneously². This means an average of 3.17 planes per DME station. This consideration is not realistic for on-route areas between continents, such as the Azores, the Hawaii islands, the Canary Islands, Japan, South-East Asia, Qatar, or the Caribbean Sea. As mentioned above, aircrafts send an average of 27 PPS, but DME transceivers implement a 60 μs dead time after transmitting a pair of pulses to avoid retransmitting echoes which causes the loss of some pulses [197, p. 166-175]. Consequently, only an average of 26 PPS are retransmitted. In summary, each transponder sends an average of 82.52 PPS, with a mean time between arrivals of 12.12 ms.

In order to compute the useful term Y_{dr} from Eqns. (7.2-7.3), the expected power for the GPS direct signal is -157 dBW plus the antenna gain (22 dB) has been considered, and the expected power for GPS reflected signal is 25 dB below [28]. The expected power for the Galileo direct signal is -155 dBW plus the antenna gain (22 dB), and similarly the Galileo reflected signal is expected to be 25 dB below. To determine the noise power, the system has a bandwidth of 20.46 MHz for L5, and 51.15 MHz for E5, and the system temperature was assumed $T = 300$ K.

Finally, the SINR is computed for all pointing directions. For cGNSS-R it is computed as:

$$\text{SINR}_c = \frac{\langle |Y_{cr}|^2 \rangle}{\langle |Y_{ci_r} + Y_{cn_r}|^2 \rangle}, \quad (7.11)$$

and for iGNSS-R as:

$$\text{SINR}_i = \frac{\langle |Y_{dr}|^2 \rangle}{\langle |Y_{di_r} + Y_{dn_r} + Y_{i_{dr}} + Y_{i_{di_r}} + Y_{i_{dn_r}} + Y_{n_{dr}} + Y_{n_{di_r}} + Y_{n_{dn_r}}|^2 \rangle}. \quad (7.12)$$

In absence of interferences, the SINR becomes the SNR. For the previously assumed power levels, bandwidths, and system temperature, the top-boundaries of the SNR in cGNSS-R is 14 dB for L5, and 16 dB for E5. In the case of iGNSS-R, the boundaries are 8.4 dB for L5, and 8.9 dB for E5.

Besides, the degradation of the SINR caused by the interference terms for the conventional technique is computed as:

$$\Delta_{\text{SINR}_c} = \frac{\langle |Y_{ci} + Y_{cn}|^2 \rangle}{\langle |Y_{cn}|^2 \rangle}, \quad (7.13)$$

and for the interferometric one as:

$$\Delta_{\text{SINR}_i} = \frac{\langle |Y_{di_r} + Y_{i_{dr}} + Y_{i_{di_r}} + Y_{i_{dn_r}} + Y_{n_{di_r}} + Y_{dn_r} + Y_{n_{dr}} + Y_{n_{dn_r}}|^2 \rangle}{\langle |Y_{dn_r} + Y_{n_{dr}} + Y_{n_{dn_r}}|^2 \rangle}. \quad (7.14)$$

²Several websites provide in real time the position of all the planes in the world that use the Automatic Dependent Surveillance-Broadcast (ADS-B) system. However, not all commercial flights use this system. These websites show a peak of 15,000 planes during daylight in Europe and United States.

Last, to determine what the most relevant degradation terms are, each interfering term is compared to the total contribution from RFI as:

$$\Delta_I = \frac{\langle |Y_{di_r} + Y_{i_d r} + Y_{i_d i_r} + Y_{i_d n_r} + Y_{n_d i_r}|^2 \rangle}{\langle |Y_{s_1 s_2}|^2 \rangle}, \quad (7.15)$$

where $Y_{s_1 s_2}$ is the term to be studied. As higher and closer to 0 dB, the more relevance the term will have.

Figures 7.10a and 7.10b show the maximum expected degradation in conventional GNSS-R for L5 and E5, respectively. Figures 7.11a and 7.11b show the maximum expected degradation in interferometric GNSS-R for L5 and E5, respectively.

As expected, the highest degradation happens over the most populated areas in terms of DME stations: North America, Europe, and the East coast of China. In the case of North America, the degradation could have an effect even far from the coast. The maximum degradation in cGNSS-R is 2.45 dB at L5 (SNR = 14 dB), and 1.7 dB at E5 (SNR = 16 dB). For iGNSS-R, the maximum degradation is 2.77 dB at L5 (SNR = 8.4 dB), and 1.26 dB at E5 (SNR = 8.9 dB). These values can be used to study the impact on ocean altimetry using the equation (12) from [28]:

$$\sigma_h = \frac{c \overline{P_{Z,S}}}{2 \sin \theta_{elev,SP} \overline{P_{Z,S}'}} \cdot \frac{1}{\sqrt{N_{inc}}} \cdot \sqrt{\left(1 + \frac{1}{\text{SNR}}\right)^2 + \left(\frac{1}{\text{SNR}}\right)^2}, \quad (7.16)$$

where c is the speed of light, $\overline{P_{Z,S}}$ is the total received power waveform, $\overline{P_{Z,S}'}$ is the first derivative of the former, $\theta_{elev,SP}$ is the local elevation angle at the specular point, and N_{inc} is the number of incoherent averages. Taking into account the previously assumed SNRs, the relative degradation of the height precision caused by a degradation of the SINR at each point of the map can be computed as:

$$\Delta \sigma_h = \frac{\sigma_h (\text{SINR})}{\sigma_h (\text{SNR})}. \quad (7.17)$$

Figure 7.12 shows the the Cumulative Distribution Function (CDF) of the relative degradation for the worst pointing case. It can be seen that the conventional technique is more robust against DME/TACAN interferences than the interferometric one, and L5 is more sensitive to RFI than E5. Despite this, even in the worst pointing case, the precision height degradation will be lower than 4% with a probability higher than 90%. However, these results are extremely dependent on the antenna directivity which drives the SNR. Therefore, a lower directivity antenna will be more prone to suffer from RFI than a high one.

Finally, table 7.1 presents the most dominant terms in the degradation for L5 and E5 for worst pointing cases. The most powerful terms result from the interference coming from the down-looking antenna, where it is received with more power. In both cases, the largest contribution is due to the noise in the up-looking antenna and the interference in the down-looking one.

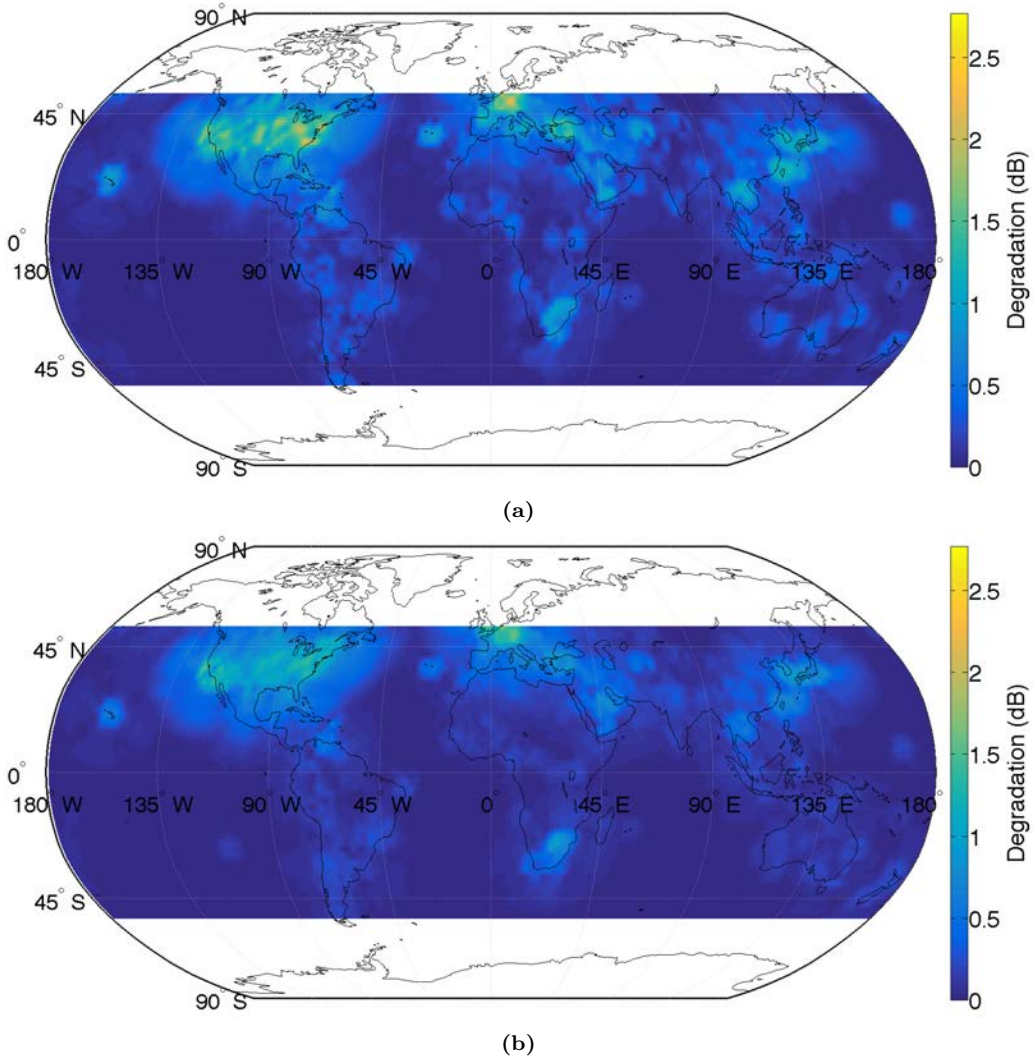


Figure 7.10: Maximum expected SINR degradation for cGNSS-R in a) L5 (maximum: 2.45 dB), and b) E5 (maximum: 1.7 dB).

7.6 Conclusions

This chapter has studied the DME/TACAN signals and how they affect conventional and interferometric GNSS-R. Then, a methodology to simulate scenarios to study the potential degradation in a L5/E5A reflectometer has been presented, and the geographic areas more prone to disturb the system analyzed. In particular, a GEROS-ISS like GNSS-R instrument has been simulated at LEO. The results show that for a 22 dBi directivity antenna a degradation of the height precision smaller than 4% can be expected 90% of the time. Even with such a small degradation, an iGNSS-R instrument should have a RFI

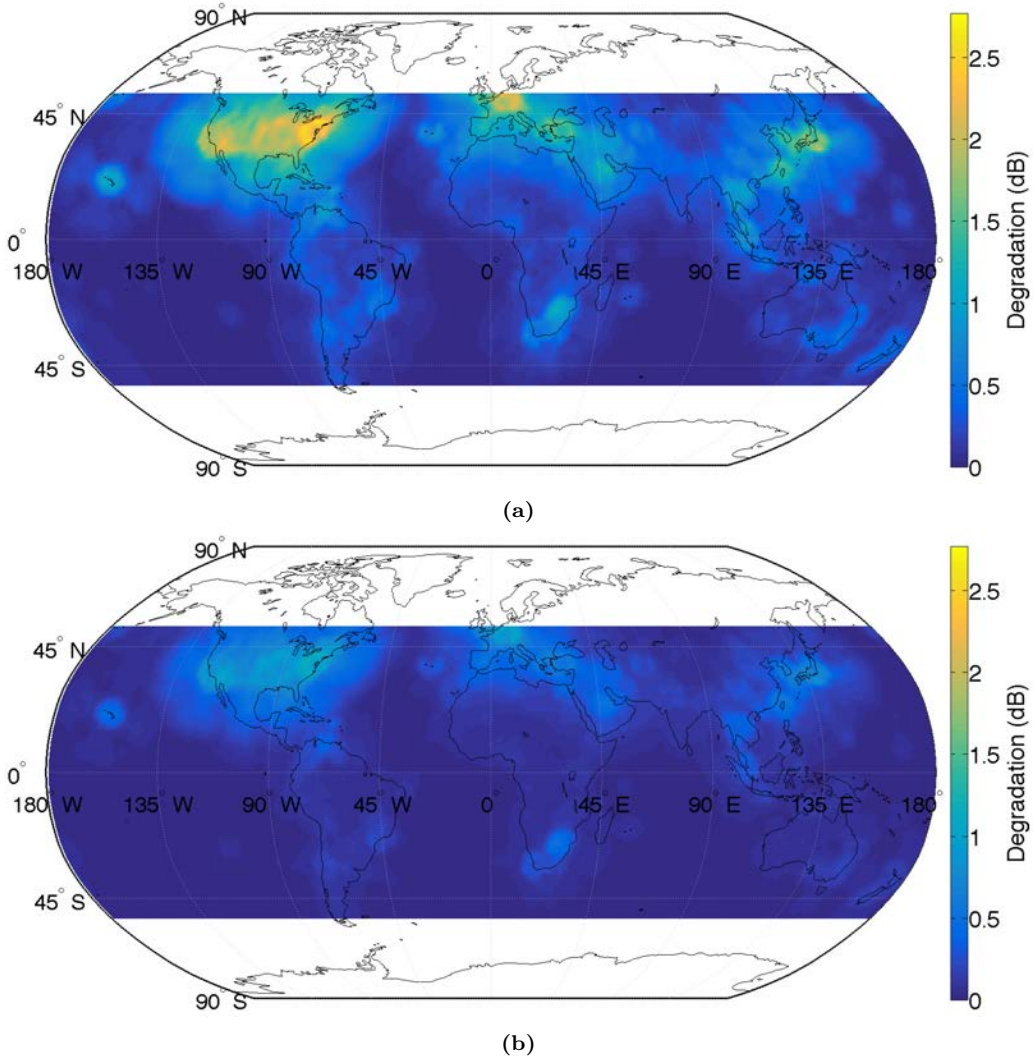


Figure 7.11: Maximum expected SINR degradation for iGNSS-R in a) L5 (maximum: 2.77 dB), and b) E5 (maximum: 1.26 dB).

mitigation system included such as a pulse blanking one [196]. This chapter has studied one particular kind of signal that shares the L5/E5A band, but other kind of interferences could severely degrade the system performance as well, such as out-of-band interferences or jamming as TDS-1 has experienced at L1.

The dominant degradation term of the cross-correlation in iGNSS-R is the result of cross-correlating the captured DME/TACAN signals in the down-looking antenna against the noise in the up-looking antenna (iGNSS-R), and not the cross-correlation of the interferences in both antennas as it could be expected a priori.

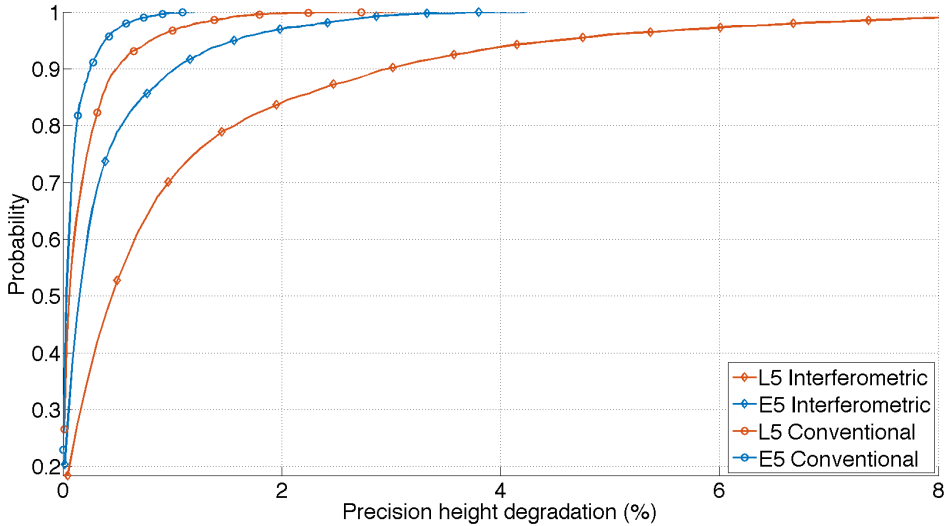


Figure 7.12: CDF of the relative degradation of the height precision in sea altimetry in the worst pointing case. Note that for ocean altimetry results will be significantly reduced since the worst degradation happens over land.

Table 7.1: Mean degradation in iGNSS-R caused by each interference cross-correlation term in L5 and E5, in the worst and best pointing cases.

	Y_{dir}	Y_{dr}	Y_{dir}	Y_{dr}	Y_{dir}
L5	-7.6 dB	-55.9 dB	-34.4 dB	-23.6 dB	-0.85 dB
E5	-6.07 dB	-54.2 dB	-29.5 dB	-24.1 dB	-1.3 dB

The impact on airborne instruments was not the object of this study, but it can be anticipated that it is even worse than in the spaceborne case. In GNSS, where the GNSS antenna is pointing to the sky (and therefore the DME signals are received from the back lobes), and where the received signal is cross-correlated with a clean replica of the code, at 12,000 meters height a 12 dB degradation was expected. In GNSS-R, the antenna is pointing to the ground, so the DME/TACAN signals are received from the front lobe of the antenna. Besides, the flying height is lower, and the scattered signals on ground have a lower power than the directly received from the satellites, so in cGNSS-R a larger degradation than 12 dB is expected. In iGNSS-R, where the clean replica of the code is substituted by a sampled signal that may contain RFI, an even higher degradation is expected.

8

Chapter 8

Field Campaign Description, Data Processing Considerations, and Preliminary Results

8.1 Introduction

This chapter describes the field campaign carried out in Australia between April 2018 and June 2018 consisting of four flights, two over land and two over sea, and presents some preliminary results to show the instrument possibilities. The chapter also shows the results of the calibration process in all four flights, some considerations on how the data should be processed, and how the location of the SRPs was computed.

Australia was chosen as the location for the field campaign for three different reasons. First, one of the main purposes of the MIR instrument was to measure sea altimetry, and the south coast of Australia has a large geoid gradient, which means that with relative short flights a large geoid difference can be measured (see Fig. 8.1). The second purpose of the MIR instrument was to measure soil moisture, and Australia has a soil moisture sensor network used as ground truth to calibrate the SMOS mission and several other National Aeronautics and Space Administration (NASA) and ESA missions. Last but not least, the European legislation is highly restrictive on flying custom devices, and they need to be approved by the air traffic authorities, which is a long and extremely expensive process. Australia, however, is open to flight experimental devices for research. The Passive Remote Sensing Lab had already worked in the past with the Civil Engineering group from Monash University, which has an experimental aircraft that had already been used for similar experiments with smaller sensors, and they were receptive to collaborate in this field campaign.

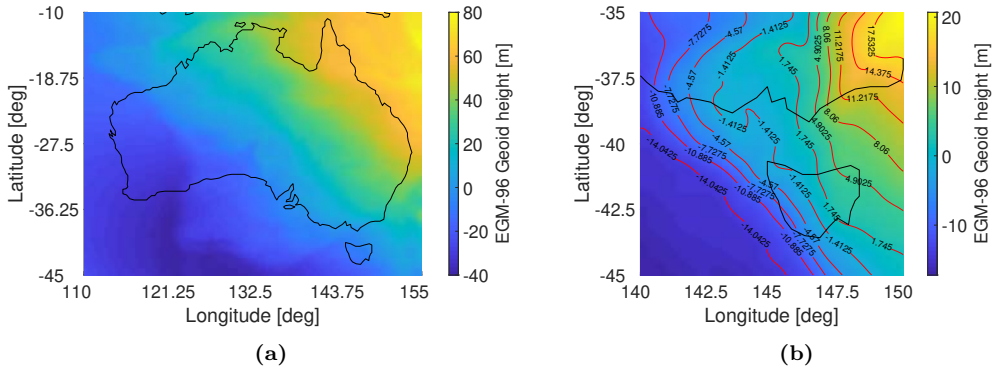


Figure 8.1: Geoid height of a) Australia, and b) Southern Australia.

Part of this chapter is an adapted from the previously published work “Satellite Cross-talk Impact Analysis in Airborne Interferometric Global Navigation Satellite System-Reflectometry with the Microwave Interferometric Reflectometer” [198].

8.2 Field Campaign Description

The first MIR field campaign was carried out in Victoria and New South Wales, Australia, between April 2018 and June 2018. Four flights were conducted, two flights over the sea, and two flights over land, and a total of 6 hours 30 minutes of data were collected.

8.2.1 Sea Flight in Port Phillip Bay

The first flight was conducted on 30 April 2018 over the entrance to Port Phillip Bay, Victoria (see Fig. 8.2), to test the instrument over open water. The airplane departed from the Tyabb airport, Victoria, and flew twice over the Point Lonsdale tide gauge and over the Point Nepean buoy, first at 800 and then at 1,500 meters above sea level (see Fig. 8.2a) to analyze the impact of the glistening zone size, and at an average ground speed of 65 m/s (see Fig. 8.2b), to analyze the impact of the pixel overlapping. The Point Lonsdale tide gauge provided the sea level, while the Point Nepean Buoy provided significant wave height, wave period, and wave direction. Nonetheless, the main goal of this flight was to check that the instrument worked properly.

8.2.2 Sea Flight in the Bass Strait

The second flight, over the Bass Strait, was conducted on 6 June 2018 departing from Mallacoota (Victoria) following a Cryosat-2 ground track to a distance of 125 km offshore, flying back, flying there again, and flying back again, always following the same track (see Fig. 8.3). The ground speed was 75-80 m/s when flying out and 60-70 m/s when flying back, and was flown at 1,400 meters above the sea level for the first half of the flight, and at 1,600 meters for the second half.

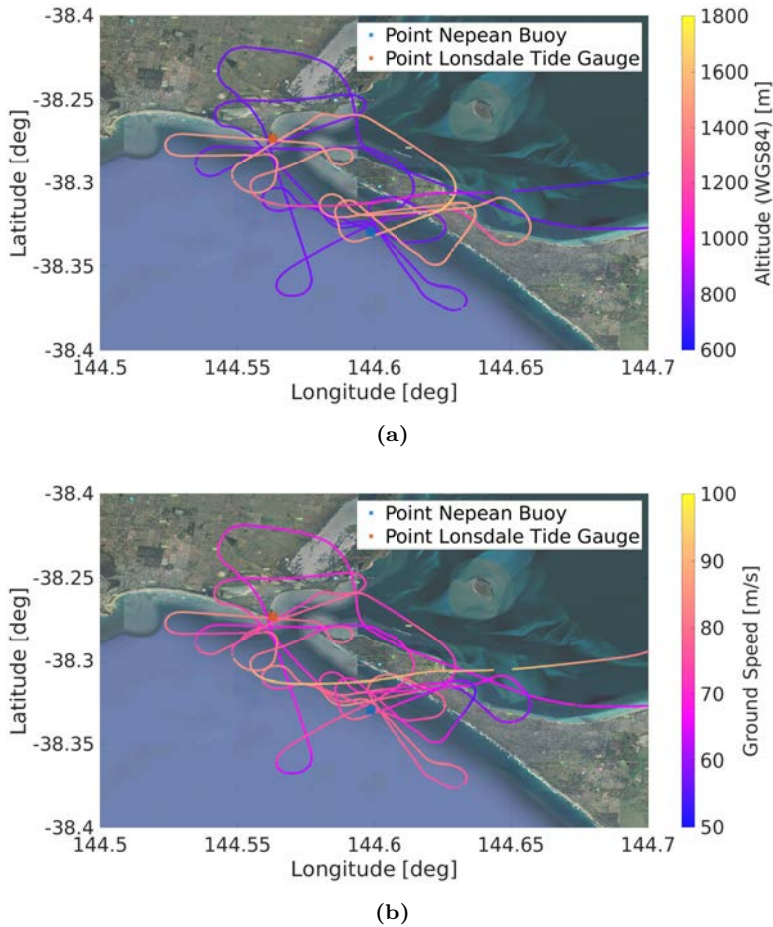


Figure 8.2: a) Flight altitude with respect to WGS84 ellipsoid, and b) ground speed during the Port Phillip Bay flight.

Several satellite passes of the Jason-2, Jason-3, Cryosat-2, and Sentinel-3, all of them with radar altimeters, were considered as candidates for the flight in both the east and west side of the Bass Strait. Figure 8.4 shows the accumulated geoid gradient, and the geoid gradient for the Cryosat-2 overpasses. The figure shows the chosen satellite overpass in green. The location and date of the flight was chosen prioritizing safety. First, daylight and good weather were mandatory. Second, the overpasses that maximized the geoid gradient were prioritized: in case of ditching, the farther the flight, the longer the rescue time, which was critical considering that the sea temperature was 0-10 °C during the winter. Third, the passes that flew closest to the coast and that started close to the departing aerodrome were considered safer. Also, the east overpasses were preferred considering that the weather in that region is more stable, and that the rescue team headquarter is located in that region [199]. Last, but not least, the availability of the pilot Mr. Jon Johanson had to be taken into account as well.

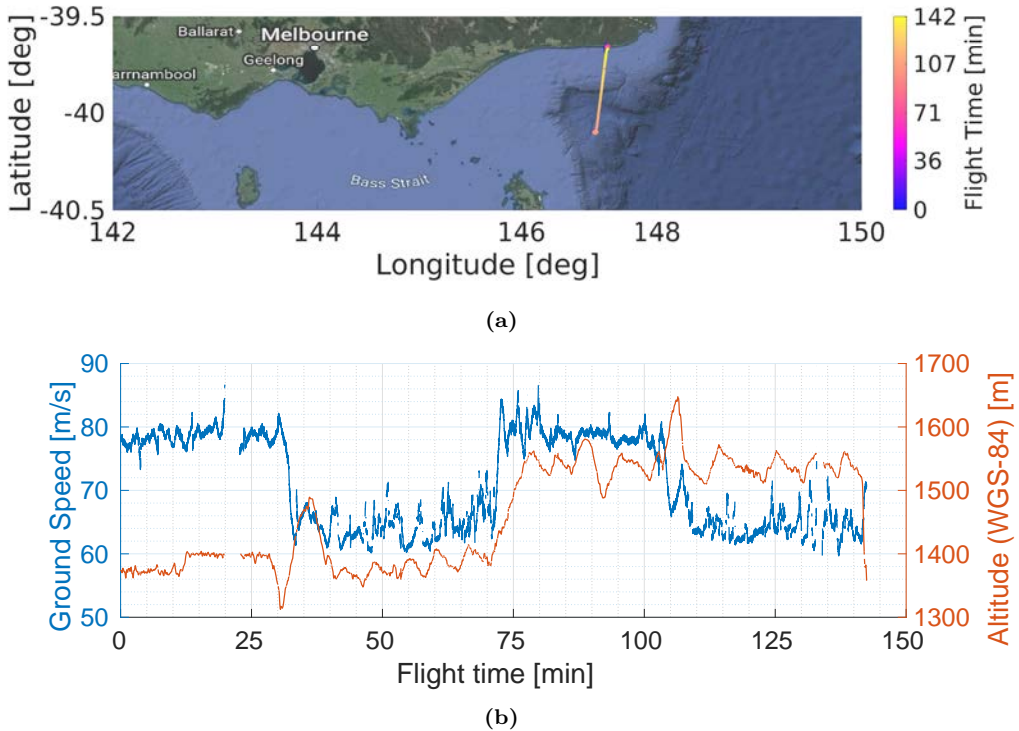


Figure 8.3: a) Flight path, and b) flight altitude with respect to the WGS-84 reference ellipsoid and ground speed during the Bass Strait flight.

8.2.3 Land Flights in Yanco

Two flights over land were conducted in Yanco (NSW), over grasslands and farmlands being monitored by the OzNet soil moisture sensor network, which provides soil moisture and soil temperature at several depths in intervals of 20 minutes, and some stations even provide rainfall [200]. The airplane flew over the Yanco area YB (see Fig. 8.5), consisting of 4x4 km of grasslands, and over the Yanco area YA (see Fig. 8.6), consisting of 2x6 km farmlands. The planned flight consisted of parallel tracks oriented from north to south separated by 500 meters.

The first flight, the “dry flight”, was conducted on 1 May 2018 (after 15 days without any rain event, and 9.2 mm accumulated rainfall in the previous 89 days, with an average soil moisture of 5.7% and a standard deviation of 3%), and the second one, the “wet flight”, on 18 June 2018 (after 8.2 mm accumulated rainfall the previous day, and 24.6 mm accumulated rainfall in the previous 9 days, with an average soil moisture of 19.1% and a standard deviation of 8.8%) [201]. Figure 8.7 shows the soil moisture ground truth provided by the OzNet stations three days before and after the flight, which is highlighted in red. Both flights were conducted at 250-350 meters above the sea level with an ground speed of 60-70 m/s (see Fig. 8.8).

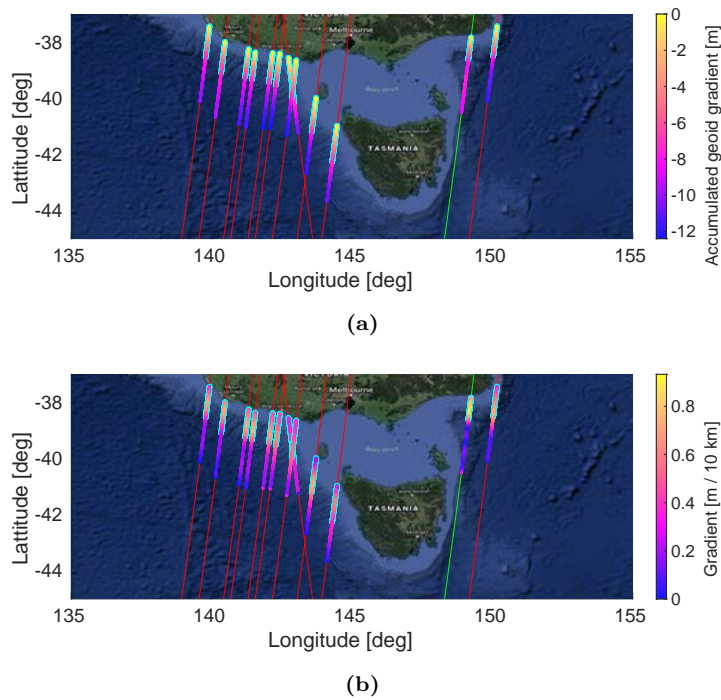
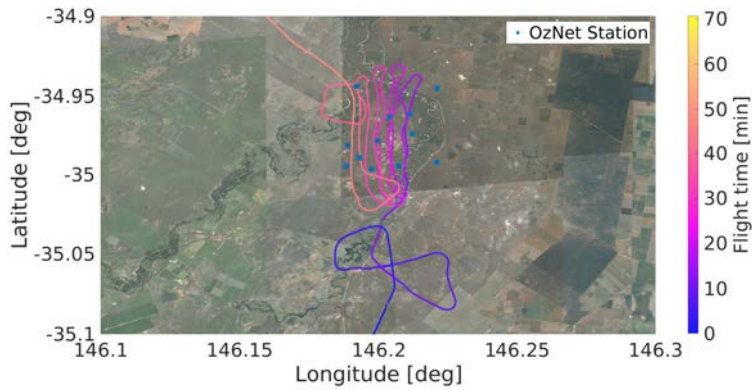
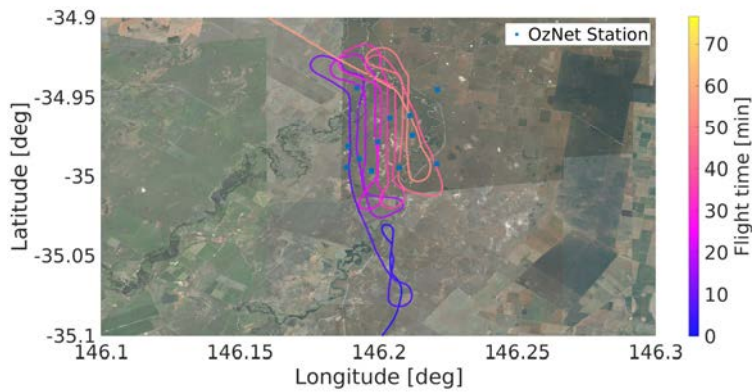


Figure 8.4: a) Accumulated geoid gradient, and b) geoid gradient in 2 minutes of the Cryosat-2 feasible overpasses during May 2018 and June 2018 in the Bass Strait flight. The red and green lines show the satellite path. The green line shows the chosen one. The required flight distance to reach 7 meters of accumulated geoid gradient is highlighted in bright blue.



(a)



(b)

Figure 8.5: Flight path over the Yanco area YB in the a) dry, and b) wet flights.

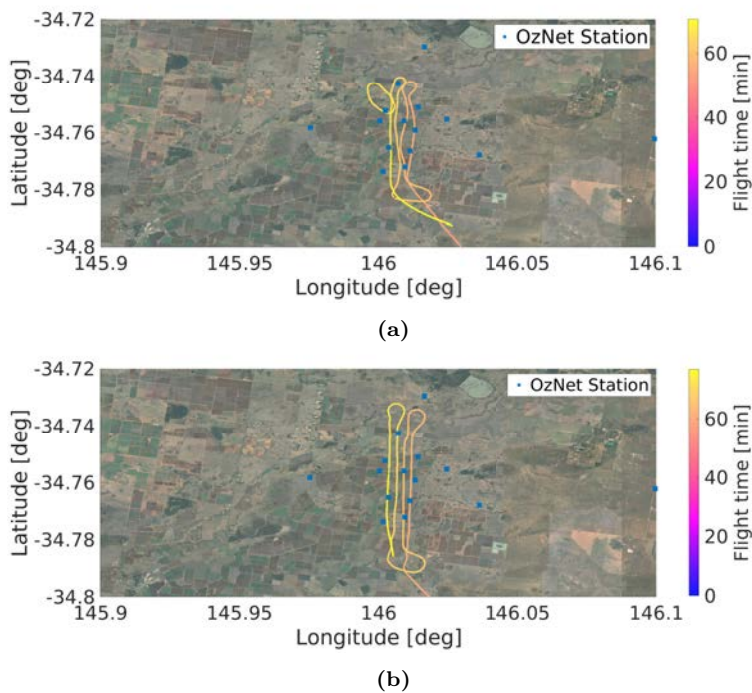


Figure 8.6: Flight path over the Yanco area YA in the a) dry, and b) wet flights.

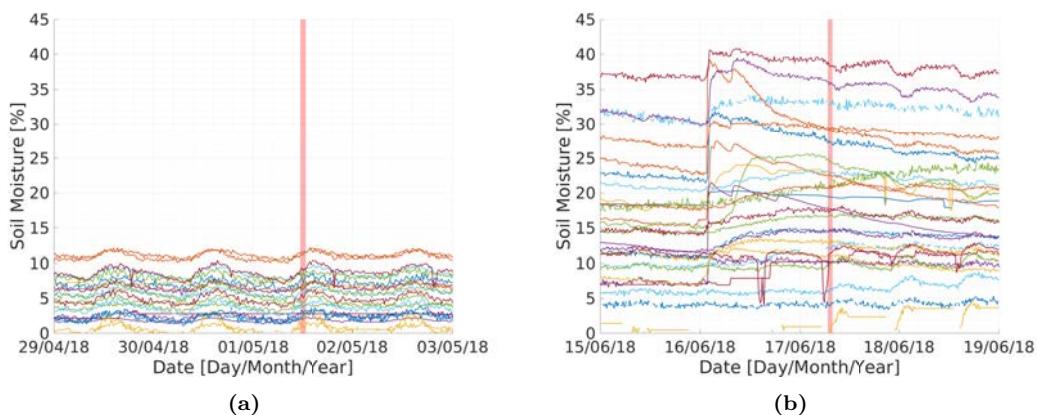


Figure 8.7: OzNet soil moisture measurements the days around the a) dry, and b) wet flights. The flight time is highlighted in red.

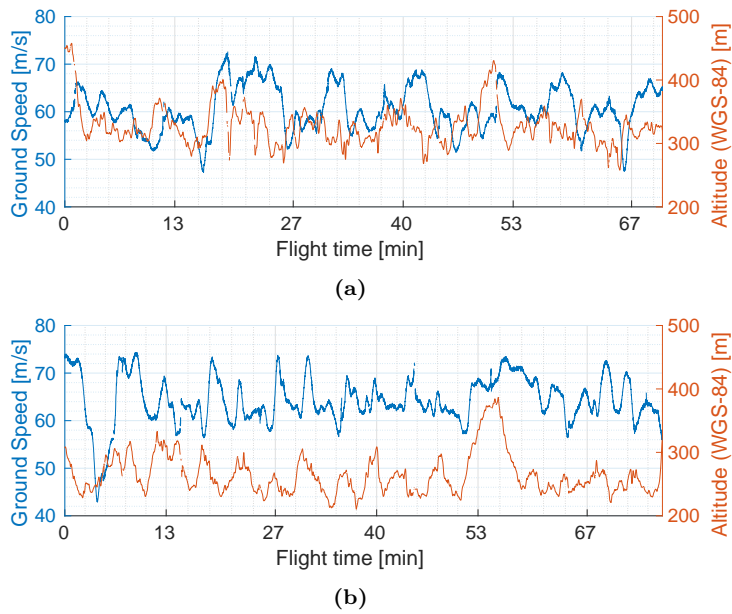


Figure 8.8: Flight altitude with respect to the WGS-84 reference ellipsoid and ground speed in the a) dry flight, and b) wet flight over Yanco, (NSW).

8.3 Calibration data

Figures 8.9, 8.10, and 8.11 show the calibrated group delay, phase and gain differences, respectively, once the contribution of the calibration splitting network had been compensated for the flight over the Bass Strait, the dry flight over Yanco, and the wet flight over Yanco. The calibration data from the Port Phillip Bay flight is not shown since it was found corrupted. In each flight several calibration measurements were carried out, one before taking off to ensure that the instrument was working properly, and multiple ones when the airplane was close to the area of interest, in order to calibrate the instrument as close as possible to the beginning of the GNSS-R measurements. Multiple calibrations were carried out in order to remove outliers and possible failed calibrations, such as some of the first set of measurements of the group delay difference in the flight over the Bass Strait (see Fig. 8.9).

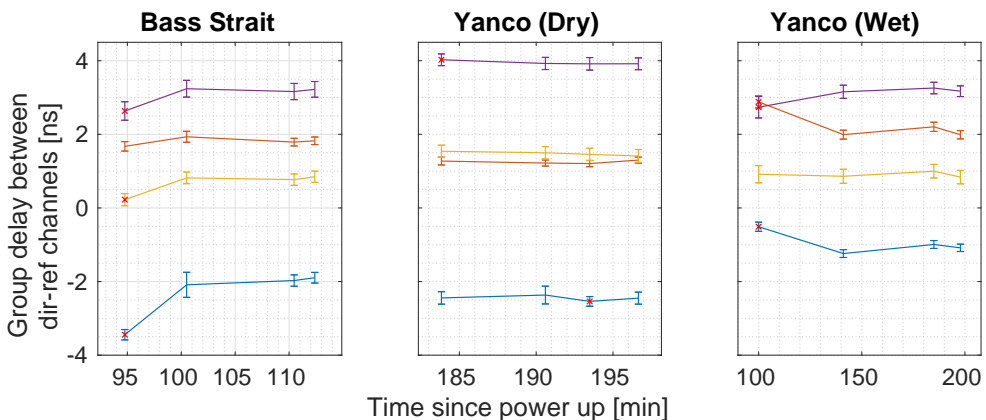


Figure 8.9: Estimated group delay difference for the flight over the Bass Strait, the dry flight over Yanco, and the wet flight over Yanco. The color line blue, red, yellow, and purple correspond to USRPs 1 to 4, respectively. The red crosses mark the discarded calibration datasets.

First, the calibration parameters are computed for each set of measurements individually. Then, the outlier sets, marked with red crosses in the figure, are removed. Last, the calibration parameters are computed from the aggregated data of the remaining calibration sets. Table 8.1 shows the average and standard deviation of the estimated group delay, phase and gain.

The reason why the group delay and gain slightly change between experiments remains unknown, for instance the case of the USRP 1 (blue), whose average gain varies up to 1 dB and the group delay up to 1.3 ns between experiments. Nevertheless, they are relatively similar between experiments, and consistent in order, that is, the USRP with the highest gain and group delay is the same between experiments, also the one with lowest parameters. Besides, the phase seems to slightly derive over time, which can be clearly seen in the USRPs 1 and 2 in the Yanco wet flight, which does not agree on the almost nonexistent phase stabilization time measured in Section 6.2.5. Further studies are required to determine if the phase difference between channels can be compensated or not.

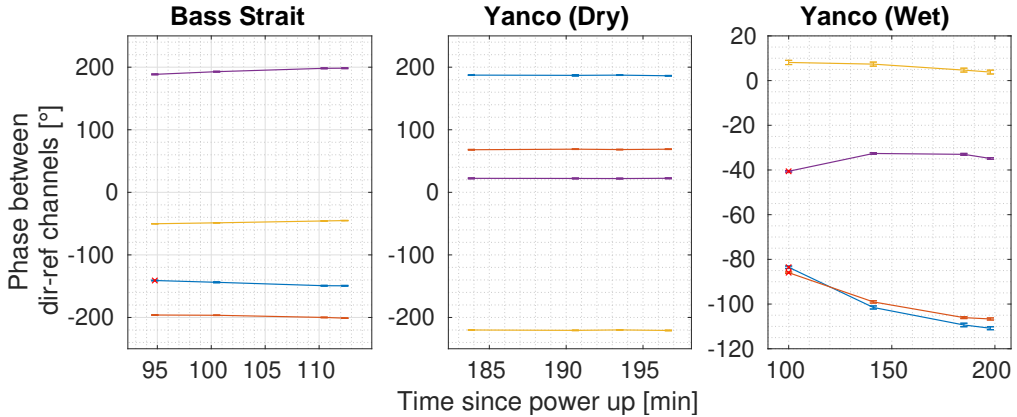


Figure 8.10: Estimated phase difference for the flight over the Bass Strait, the dry flight over Yanco, and the wet flight over Yanco. The color line blue, red, yellow, and purple correspond to USRPs 1 to 4, respectively. The red crosses mark the discarded calibration datasets.

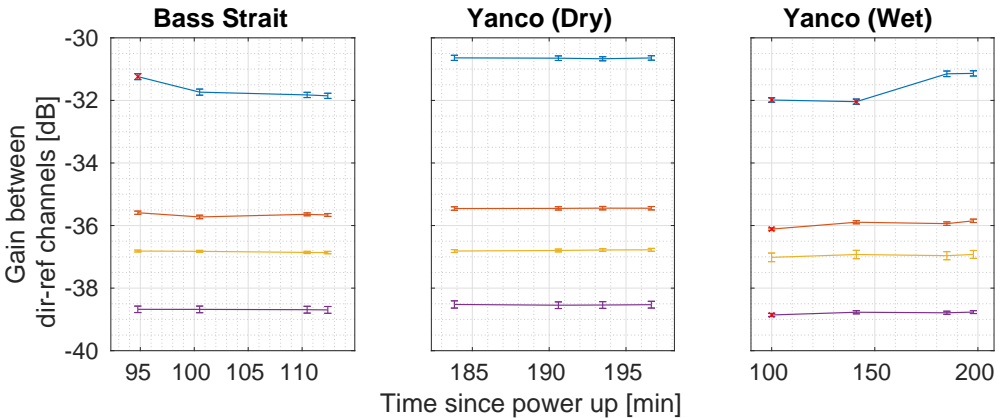


Figure 8.11: Estimated gain difference for the flight over the Bass Strait, the dry flight over Yanco, and the wet flight over Yanco. The color line blue, red, yellow, and purple correspond to USRPs 1 to 4, respectively. The red crosses mark the discarded calibration datasets.

8.4 Data Processing Considerations to Avoid the Effect of Secondary Codes

The validation experiment that led to study the impact of DME/TACAN signals in Chapter 7 aimed to test if the RF Front-ends were capable of properly receiving all of the desired GNSS signals in both frequency bands. The experiment consisted of a RF Front-end connected to an USRP sampling a few seconds of data to cross-correlate it with clean replicas of the code in post-processing and was carried out at the beginning of 2014, when the number of satellites transmitting the L5 codes was reduced [202] and their presence uncommon. During the experiment it was observed that more than one

Table 8.1: Mean and standard deviation of the computed calibration parameters. The geometric mean and geometric standard deviation have been used for the gain.

	Flight	USRP1	USRP2	USRP3	USRP4
Group Delay	Bass Strait	$\mu = -1.99$ ns $\sigma = 0.24$ ns	$\mu = 1.80$ ns $\sigma = 0.15$ ns	$\mu = 0.81$ ns $\sigma = 0.16$ ns	$\mu = 3.21$ ns $\sigma = 0.22$ ns
	Yanco Dry	$\mu = -2.42$ ns $\sigma = 0.20$ ns	$\mu = 1.25$ ns $\sigma = 0.10$ ns	$\mu = 1.47$ ns $\sigma = 0.18$ ns	$\mu = 3.92$ ns $\sigma = 0.17$ ns
	Yanco Wet	$\mu = -1.11$ ns $\sigma = 0.15$ ns	$\mu = 2.06$ ns $\sigma = 0.16$ ns	$\mu = 0.90$ ns $\sigma = 0.21$ ns	$\mu = 3.20$ ns $\sigma = 0.17$ ns
Phase	Bass Strait	$\mu = -147.5^\circ$ $\sigma = 2.7^\circ$	$\mu = -198.4^\circ$ $\sigma = 2.2^\circ$	$\mu = -47.5^\circ$ $\sigma = 2.1^\circ$	$\mu = 194.5^\circ$ $\sigma = 4.2^\circ$
	Yanco Dry	$\mu = 187.2^\circ$ $\sigma = 0.7^\circ$	$\mu = 68.6^\circ$ $\sigma = 0.6^\circ$	$\mu = -221^\circ$ $\sigma = 4.0^\circ$	$\mu = 22.4^\circ$ $\sigma = 0.7^\circ$
	Yanco Wet	$\mu = -107.2^\circ$ $\sigma = 4.1^\circ$	$\mu = -103.9^\circ$ $\sigma = 3.5^\circ$	$\mu = 6.0^\circ$ $\sigma = 2.0^\circ$	$\mu = -33.5^\circ$ $\sigma = 1.0^\circ$
Gain	Bass Strait	$\mu = -31.80$ dB $\sigma = 0.10$ dB	$\mu = -35.65$ dB $\sigma = 0.07$ dB	$\mu = -36.84$ dB $\sigma = 0.04$ dB	$\mu = -38.69$ dB $\sigma = 0.11$ dB
	Yanco Dry	$\mu = -30.78$ dB $\sigma = 0.07$ dB	$\mu = -35.45$ dB $\sigma = 0.05$ dB	$\mu = -36.52$ dB $\sigma = 0.05$ dB	$\mu = -38.53$ dB $\sigma = 0.11$ dB
	Yanco Wet	$\mu = -31.51$ dB $\sigma = 0.08$ dB	$\mu = -35.89$ dB $\sigma = 0.06$ dB	$\mu = -36.96$ dB $\sigma = 0.14$ dB	$\mu = -38.77$ dB $\sigma = 0.05$ dB

peak was present in coherent WAFs (see Fig. 8.12a). In the Doppler domain the WAF was expected to be a sinc of 1 kHz wide due to the 1 ms coherent integration time, but it was wider (see Fig. 8.12b). Last, if the waveform is only computed for the expected Doppler frequency, the peak amplitude varies largely over time (see Fig. 8.18).

When a secondary code bit change falls inside the correlation window, it acts as a square wave that modulates the PRN codes, whose harmonic frequencies depend on the location of the correlation window (see Fig. 8.13), thus modulating the WAF in the Doppler domain. Figure 8.14 shows the effect in the WAF of a secondary code bit change when it happens at different moments of the code sequence. The WAF amplitudes have been normalized to the maximum amplitude achievable when the sequences are aligned. The power loss as function of the misalignment for Galileo E1 OS, GPS L5 and Galileo E5A is shown in Fig. 8.15.

If only waveforms are computed, the non-alignment of the correlation window with the secondary codes might make the peak tracking more difficult. Besides, the peak amplitude is also affected, and this effect must be corrected for scatterometric applications. To do so, the correlation window must be aligned to the secondary code sequence [203]. The zero padding technique was chosen for its simplicity. It consists of the correlation of 2 ms of sampled data with 1 ms of code clean replica with 1 ms of zero padding. In this way, two cross-correlation peaks appear and one of them is never affected by a secondary code bit change (see Fig. 8.16). By doing so, the WAFs shown in Fig. 8.12 are not spread in the Doppler domain as shown in Fig. 8.17, and the cross-correlation peak variability

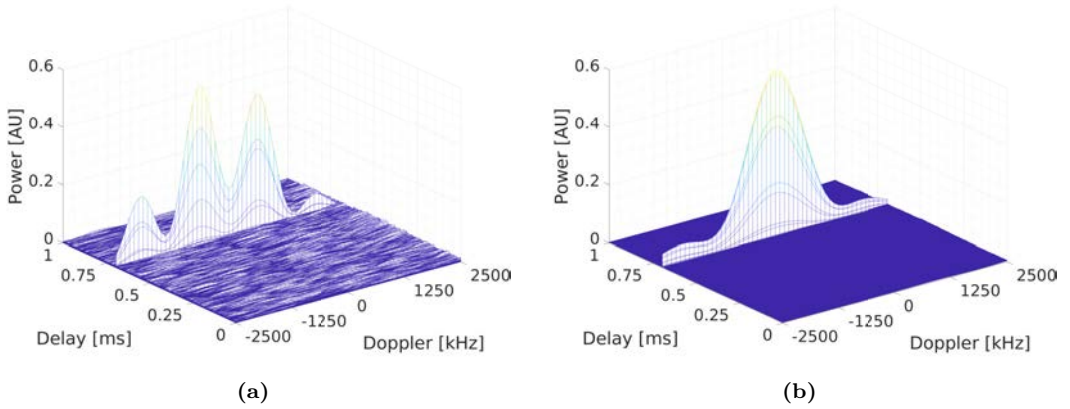


Figure 8.12: a) Coherent, and b) 1000 incoherent averaged waveforms when the secondary codes are not aligned with the coherent integration window. Real data from the up-looking array and from the Bass Strait flight was used.

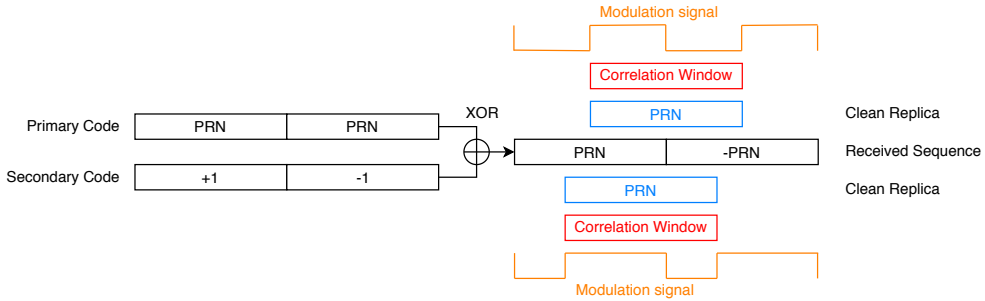


Figure 8.13: Modulation effect caused by the cross-correlation window misalignment.

when just correlating for the expected Doppler frequency is reduced drastically as shown in Fig. 8.18.

For the MIR data processing the use of the zero padding in the direct signal is proposed to determine the proper correlation window, to apply it to both the direct and the reflected signals, and then to interpolate the waveform around the peak in the reflected one. The reflected signal will still be slightly affected by the misalignment, but the effect will be minor. Considering that the instrument did not fly higher than 1,700 meters, the maximum delay between the direct and the reflected signals is 3,400 meters for satellites located on the local zenith. Consequently, the down-looking cross-correlation peaks will be in the first 380 samples. For such a small misalignment the peaks do not shift in the Doppler domain as shown in Fig. 8.15, and the peak amplitude losses can be compensated using the linear approximation

$$l = 1 - 997.45 \cdot \Delta\tau, \quad (8.1)$$

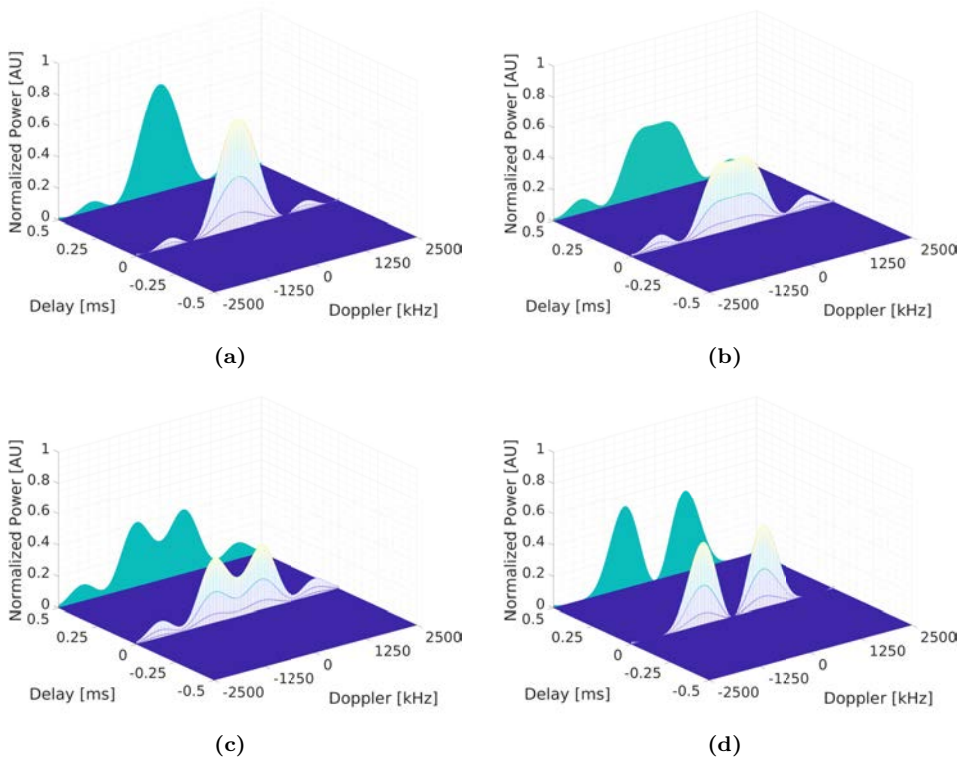


Figure 8.14: L5 I+Q WAF when a secondary code bit change happens at the a) 8%, b) 16%, c) 25%, and d) 50% of the GNSS sequence.

for Galileo E1 OS, being $\Delta\tau$ the delay difference between the direct and the reflected signals in seconds, and

$$l = 1 - 3953 \cdot \Delta\tau, \quad (8.2)$$

for GPS L5 and Galileo E5A.

8.5 Preliminary Results

This section presents some preliminary results from the field campaign as a qualitative proof that the instrument works and that it is sensitive to the applications it was designed for. The data shown here has been processed using CUDA and the correlation window alignment to the secondary codes proposed in Section 8.4 has not been applied yet. The post-processing calibration explained in Sections 6.2.5 and 6.2.6 has not been corrected. Only the peak value and position were stored, therefore no interpolation has been applied for altimetry. All results presented here are the result of a joint effort with Mr. Daniel Pascual, so they are also shown in his Ph.D. thesis [29].

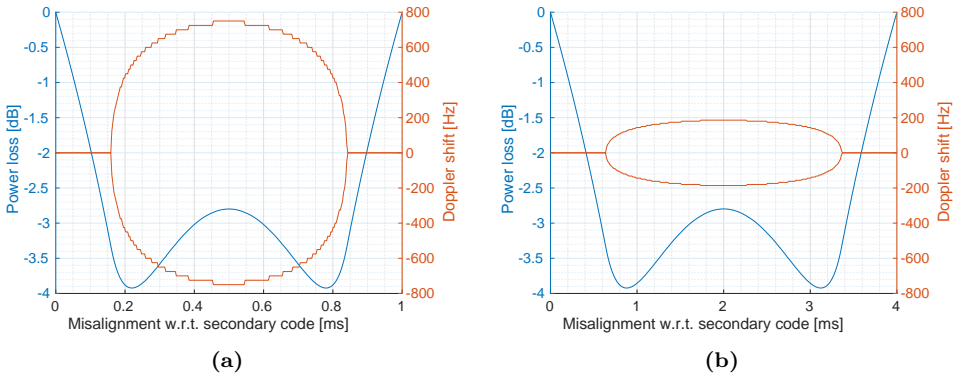


Figure 8.15: Power loss and Doppler shift as function of the correlation window misalignment with the secondary codes in a) GPS L5 and Galileo E5A, and b) Galileo E1 OS.

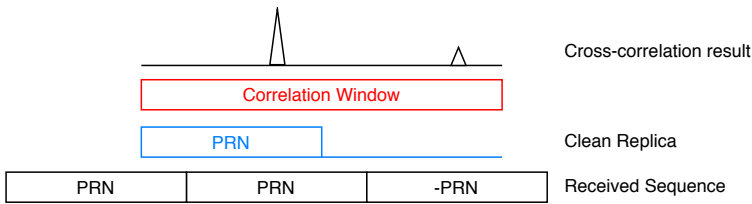


Figure 8.16: Zero padding strategy for cross-correlation window alignment.

The SRP locations have been computed using the EGM2008 geoid [204] for the sea experiments, and the EGM96 geoid combined with the SRTM3 version 2.1 Digital Elevation Model (DEM) [205] for the land experiments. The SRP has to fulfill the three

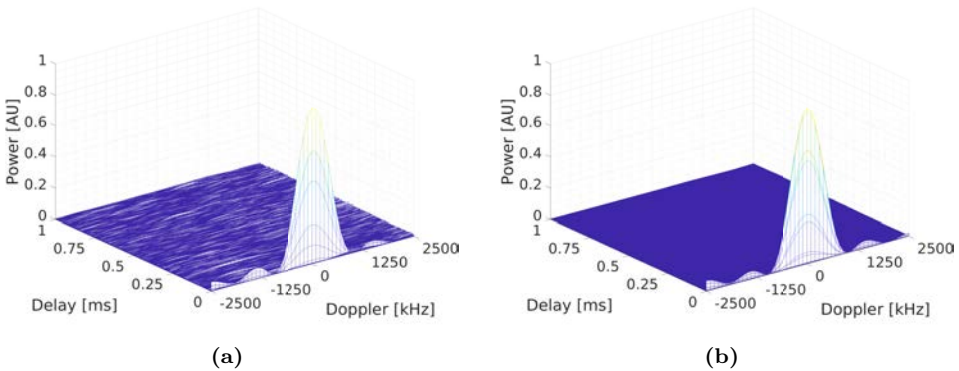


Figure 8.17: a) Coherent, and b) 1000 incoherent averaged waveforms when the secondary codes are aligned with the coherent integration window. Real data from the up-looking array and from the Bass Strait flight was used.

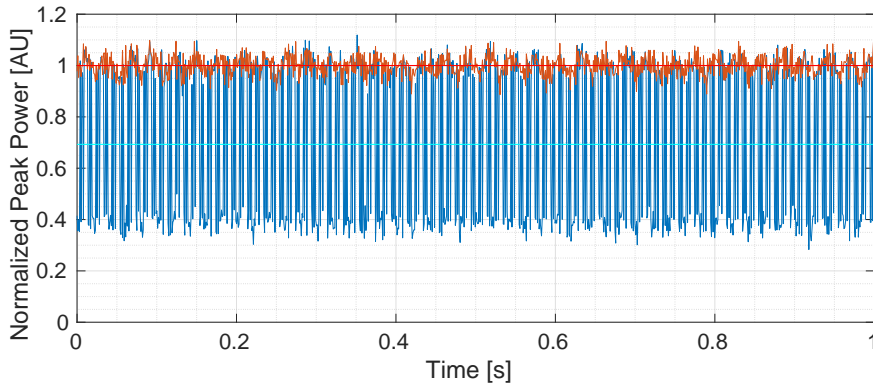


Figure 8.18: GPS L5 direct signal normalized coherent peak power along 1 second with 1 ms coherent integration time with no code alignment (blue), and code alignment (red).

following conditions [33]:

- The normal vector to the SRP has to be in the plane defined by the receiving antenna, the SRP, and the satellite. Mathematically, the point has to satisfy the condition

$$c_1 = (v_{sat \rightarrow SRP} \times v_{SRP \rightarrow RCV}) \cdot v_{norm} = 0, \quad (8.3)$$

where $v_{sat \rightarrow SRP}$ is the vector from the satellite to the SRP, $v_{SRP \rightarrow RCV}$ is the vector from the SRP to the down-looking antenna, v_{norm} is the normal vector to the SRP, \times is the cross product, and \cdot is the dot product. Figure 8.19 shows the absolute value of c_1 for an airplane at 1,000 meters height, located at latitude and longitude 0° , displayed at the center of the image as a red cross, and for a given satellite with an azimuth of 90° and 45° of elevation. The plane that contains the three vectors is projected on ground in the line with zero value.

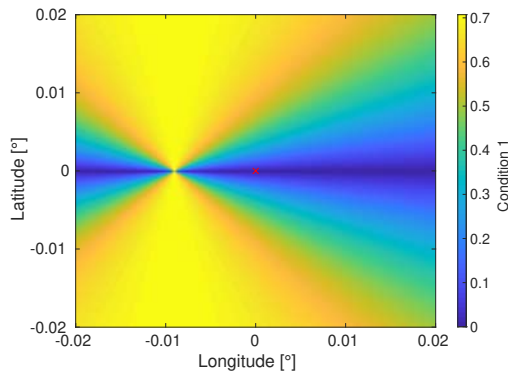


Figure 8.19: Representation of the specular reflection first condition's absolute value.

- The local incident angle and the local reflection angle are equal. Mathematically,

the point has to satisfy the condition

$$c_2 = (v_{SRP \rightarrow sat} \cdot v_{norm}) - (v_{SRP \rightarrow RCV} \cdot v_{norm}) = 0. \quad (8.4)$$

where \bar{v} is the unit vector of v .

Figure 8.20 shows the absolute value of c_2 for the same scenario.

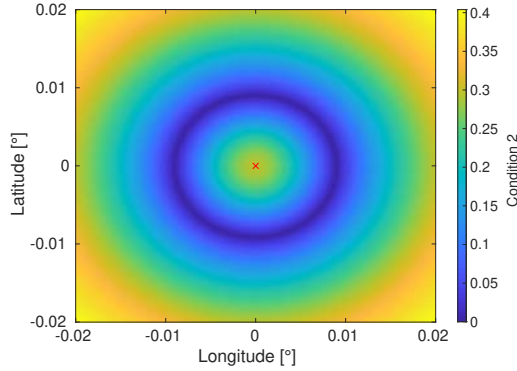


Figure 8.20: Representation of the specular reflection second condition's absolute value.

The two previous conditions need to be the closest possible to zero, so they can be unified as

$$c_{12} = 1 - ((1 - |c_1|) \cdot (1 - |c_2|)) = 0. \quad (8.5)$$

Figure 8.21 shows the absolute value of c_{12} for the same scenario. Still there is some ambiguity that needs to be removed.

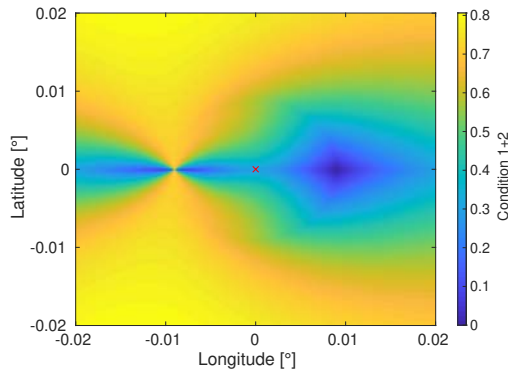


Figure 8.21: Representation of the specular reflection first and second conditions' absolute value.

- The distance from the satellite to the SRP, and from there to the airplane must be the shortest. Mathematically, it is computed as:

$$d = |v_{sat \rightarrow SRP}| + |v_{SRP \rightarrow RCV}|. \quad (8.6)$$

With no topography this condition would be sufficient, but if a DEM is used, this condition has to be combined with the previous two. To do so, it is suggested to normalize it as shown in Fig. 8.22 so in the analyzed scenario is ranged from 0 to 1 as

$$c_3 = \frac{d - \min(d)}{\max(d - \min(d))} = 0, \quad (8.7)$$

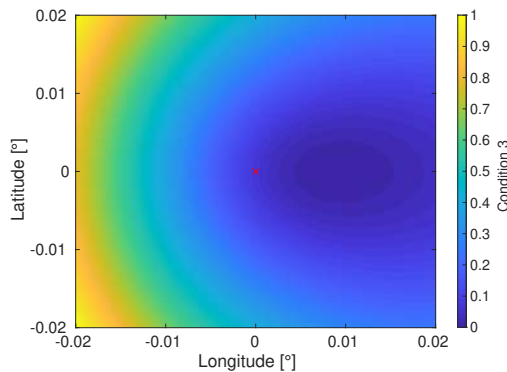


Figure 8.22: Representation of the specular reflection third condition's absolute value.

and then to combine with the two previous as

$$C_{123} = 1 - ((1 - |c_1|) \cdot (1 - |c_2|) \cdot (1 - |c_3|)) = 0. \quad (8.8)$$

Figure 8.23 shows the absolute value of c_{123} for the same scenario, where all ambiguity has been removed, and the computed SRP has been marked as a red circle.

8.5.1 Soil Moisture in the Yanco Flights

First, the direct and reflected signals were cross-correlated with the appropriate code with $T_{coh} = 1$ ms for GPS L1, GPS L5 and Galileo E5A, and $T_{coh} = 4$ ms for Galileo E1, and all with $T_{incoh} = 100$ ms and $T_{incoh} = 1000$ ms.

Figure 8.24 shows the uncalibrated reflectivity obtained from Eqn. 6.1 with $T_{incoh} = 100$ ms, of all frequency bands in the YA and YB regions during the dry and wet flights. It can clearly be seen that the wet flights have higher reflectivities, and also that the water content measured by the OzNet stations is higher in the wet flight.

The uncalibrated reflectivity histograms (see Fig. 8.25) show an increase of 4-5 dB from the dry flight to the wet one in both frequency bands for both $N = 100$, and $N = 1000$ incoherent averages. The mean reflectivity at L5/E5A is lower than in L1/E1, which might be caused by gain difference at L1/E1 and L5/E5A bands in the extra RF amplifier in the down-looking chain. The mean difference between bands should be solved by applying the in-flight calibration.

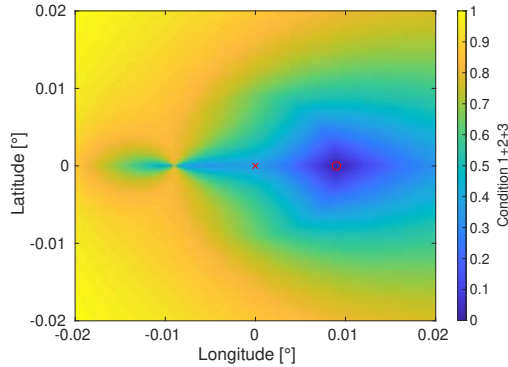


Figure 8.23: Representation of the specular reflection three conditions combined. The computed specular reflection point location is shown as a red circle.

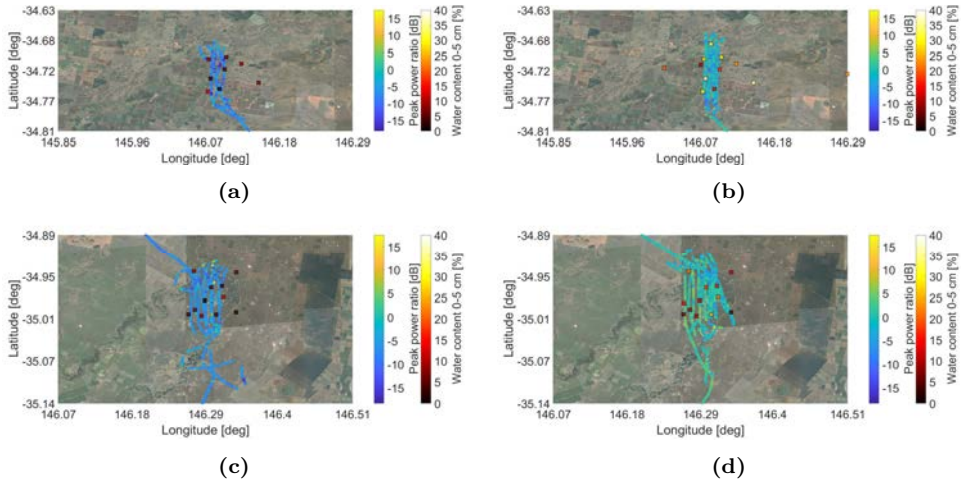


Figure 8.24: Uncalibrated reflectivity in the Yanco flights: a) area YA, dry flight, b) area YA, wet flight, c) area YB dry flight, and d) area YB, wet flight. $T_{incoh} = 100$ ms has been used for these plots. The squared markers show the reflectivity measured by an OzNet stations in that location.

8.5.2 Sea Altimetry

Since the MIR instrument was designed as a proof of concept of the PARIS IoD instrument, one of its main goals was sea altimetry. First, the direct and reflected signals were cross-correlated with the appropriate code with $T_{coh} = 1$ ms for GPS L1, and $T_{coh} = 4$ ms for Galileo E1, and both with $T_{incoh} = 100$ ms (as observed during the data processing of Chapter 9, longer integration times than 300 ms require waveform retracking, which has not been implemented yet in the CUDA processing code). The peak delay of the reflected τ_r and direct τ_d signals are then subtracted, the results are averaged for 50 seconds to reduce the noise as the result of a low incoherent averaging time, the airplane

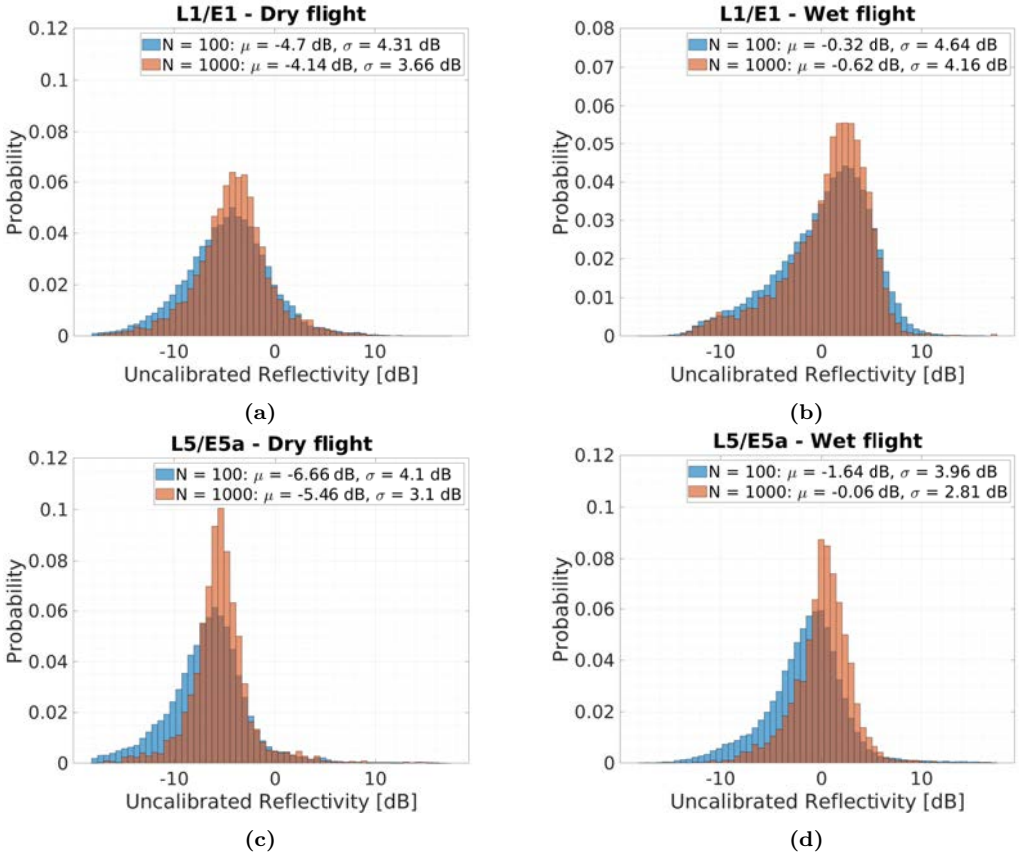


Figure 8.25: Uncalibrated soil moisture histograms in the Yanco flights: a) L1/E1 frequency band, dry flight, b) L1/E1 frequency band, wet flight, c) L5/E5A frequency band, dry flight, and d) L5/E5A frequency band, wet flight.

movement, and the sea state, then the satellite elevation θ is compensated, and the plane height over the ellipsoid h is then removed to obtain the SRP height over the ellipsoid h_{sea} (see Fig. 8.26):

$$h_{sea} = h - h' = h - \frac{c \cdot (\tau_r - \tau_d)}{2 \cdot \sin(\theta)}. \quad (8.9)$$

Figures 8.27a and 8.27b show the estimated sea height over the ellipsoid in blue, and the EGM2008 geoid height of the estimated SRP location in red, for the first (left) and second (right) beams, both at L1/E1 frequency bands. The data at L5/E5A was found to be too noisy, and further work is required.

The retrieved sea height has been compared to the EGM2008 geoid, and shows a systematic difference of 2-3 meters in the first beam, and 1-2 in the second one. This difference is caused by four factors that have not been yet compensated: tides (up to 1-2 meters in the Bass Strait region [206]), the different location between the direct and the

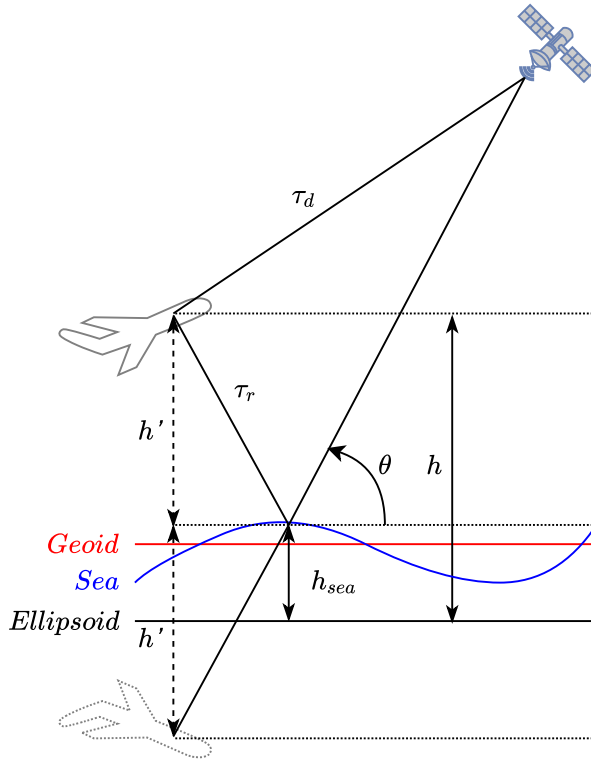


Figure 8.26: Delays of the direct and the reflected signals in altimetry.

reflected antenna (the reflected array is located 93 cm forward and 110 cm lower than the up-looking one), the path differences between beams, and the positioning error of the GNSS receiver.

8.5.3 Topography

When analyzing the results of sea altimetry, some correlation was found with topography in transects over land. Since the topography changes much faster than the sea slope, the retrieved height is averaged only for 1.5 seconds, but the coherent and incoherent averaging times remain equal to section 8.5.2: $T_{coh} = 1$ ms for GPS L1, and $T_{coh} = 4$ ms for Galileo E1, and both with $T_{incoh} = 100$ ms. Again, the L5/E5A beams were not used. Figure 8.28 shows the retrieved height at the beginning of the Bass Strait flight in beams L1-1 and L1-2, and the expected height of the computed SRPs, computed using the geoid EGM96 and the DEM SRTM3 v2.1. The retrieved measurements correlate with the expected topography, but not totally, maybe caused by an error in the location of the SRP.

The large picture of the Port Phillip Bay flight also shows correlation between the retrievals and the expected topography as can be seen in Fig. 8.29. A detailed zoom over Point Nepean National Park and over the Mornington Peninsula can be seen in Figs. 8.30

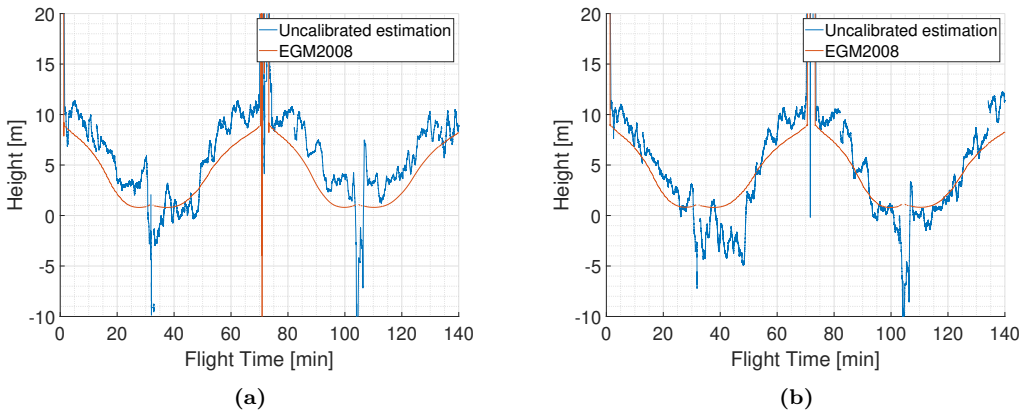


Figure 8.27: Uncalibrated sea height in the a) L1-1, and b) L1-2 beams in the Bass Strait flight.

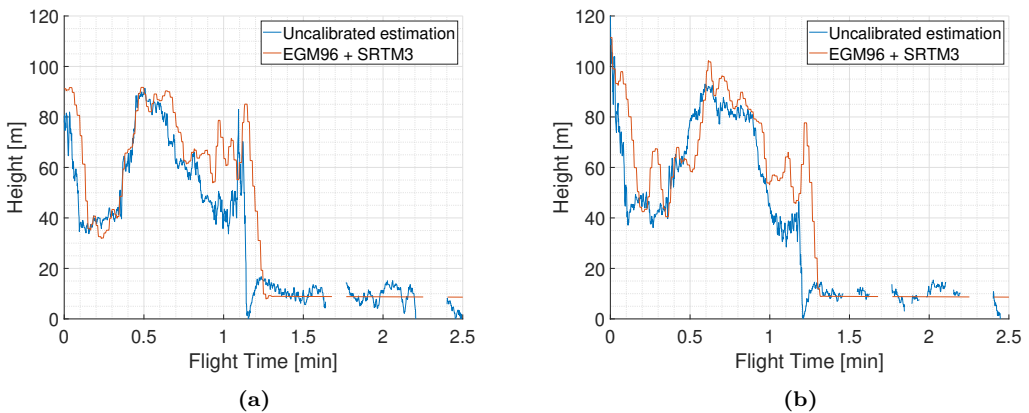


Figure 8.28: Uncalibrated topography in the a) L1-1, and b) L1-2 beams at the beginning of the Bass Strait flight.

and 8.31, respectively.

8.5.4 Land-Water Transitions

At the beginning of the Port Phillip Bay flight it was found that the reflectivity showed an interference pattern in the transition between land and water (see Fig. 8.32). This interference pattern could be the result of the different Fresnel zones passing from one medium to another when the coherent component dominates as predicted in [207]. At that moment the MIR instrument was tracking a satellite in both frequency bands. Figure 8.32 shows some vertical red lines highlighting when the interference patterns are aligned: in the L1/E1 case (blue line), 4 periods can be counted, while in the L5/E5A case (red

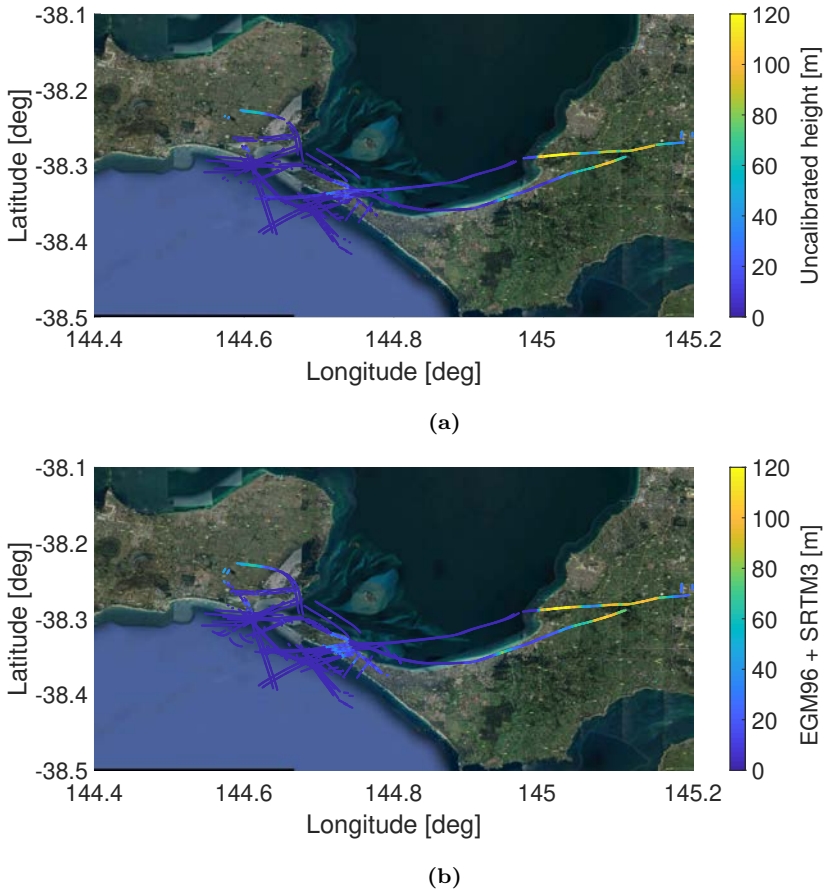


Figure 8.29: a) Uncalibrated retrieved height, and b) expected height computed from the geoid EGM96 and the SRTM3 digital elevation model in the Port Phillip Bay flight.

line), there are only 3. The interference pattern at L5/E5A is “slower” than at L1/E1A, and exactly it has a 3:4 ratio, the same ratio between the central wavelengths of both bands.

8.6 Conclusions

This chapter has summarized the field campaign carried out in Australia between May 2018 and June 2018, and some qualitative results are shown. The campaign consisted of 4 flights, 2 over land, and 2 over sea, to test the MIR instrument. The MIR instrument proved to be sensitive to the soil moisture change caused by rain events in the Yanco flights. Over sea, it not only proved to be useful for sea altimetry, but also to retrieve the terrain topography. The transitions between land and calmed water showed an interference pattern that could prove that the coherent component dominated the scattering

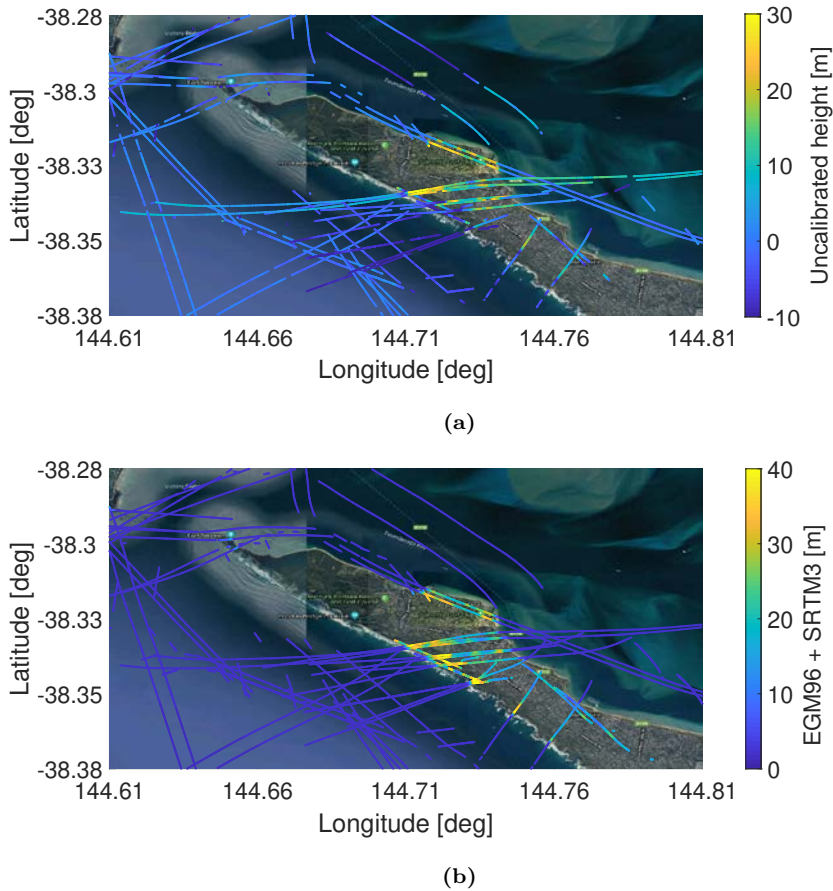
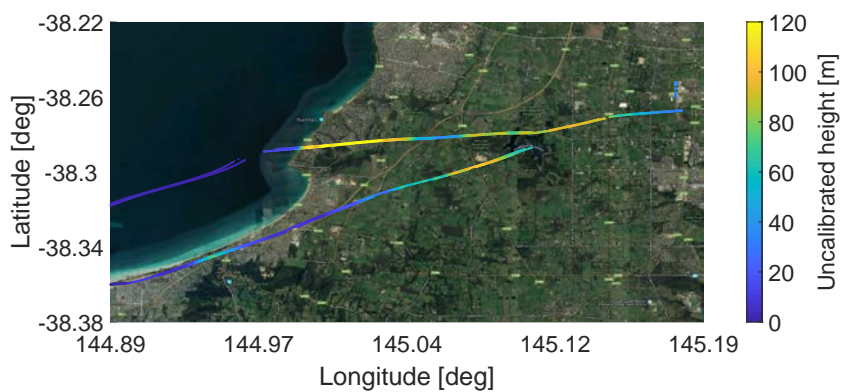
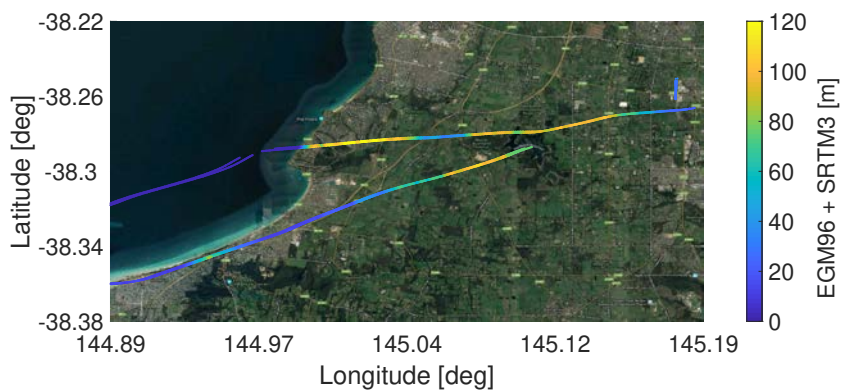


Figure 8.30: a) Uncalibrated retrieved height at L1 frequency band, and b) expected height computed from the geoid EGM96 and the SRTM3 digital elevation model in the Port Phillip Bay flight over Point Nepean National Park.

process. All these results can be improved by applying the in-flight calibration parameters, applying waveform peak retracking, and interpolating the waveforms around the peak, among others. After designing, building, testing and calibrating the instrument, there was not enough time to apply all of these improvements and to analyze the data: all this work, in fact, could be an entirely different thesis.



(a)



(b)

Figure 8.31: a) Uncalibrated retrieved height at L1 frequency band, and b) expected height computed from the geoid EGM96 and the SRTM3 digital elevation model in the Port Phillip Bay flight over Mornington Peninsula.

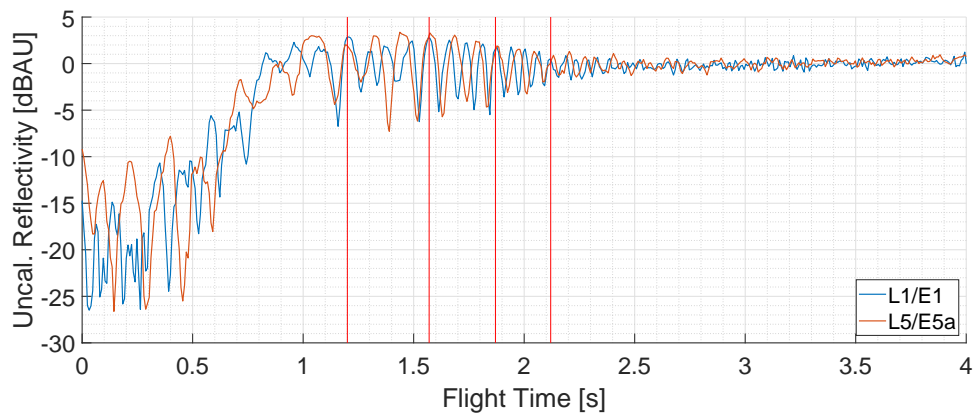


Figure 8.32: Retrieved reflectivity at GPS L1 (blue), and GPS L5 (red) in a land-sea transition. The vertical red lines mark where the oscillations at both frequency bands have the peaks aligned. Note that the oscillations have a 4:3 rate, the same between L1 and L5 central frequencies.

9

Chapter 9

Satellite Cross-talk

Satellite Cross-talk is the result of several cross-correlation peaks corresponding to different satellites appearing in the cross-correlation between the direct and the reflected signals in iGNSS-R [208, p. 161-179]. Avoiding satellite cross-talk in iGNSS-R was one of the reasons to design an instrument with high directive antennas with beam steering. According to [45], the MIR arrays (~ 19 dB) should be able to avoid most of the satellite cross-talk. However, when the Bass Strait flight data was analyzed, more than half of the data was found contaminated in the L5/E5A frequency band, which prompted an analysis to determine the instance when this occurred and its impact on the GNSS-R observables.

This chapter is adapted from the previously published work “Satellite Cross-talk Impact Analysis in Airborne Interferometric Global Navigation Satellite System-Reflectometry with the Microwave Interferometric Reflectometer” [198].

9.1 Methodology

In order to analyze how cross-talk contaminated the interferometric waveforms, it was first required to classify the flight intervals potentially contaminated. To do so, the angular distance between the tracked satellites and the closest ones was first computed using the position of the GPS and Galileo satellites derived from the satellite ephemeris [209]. A really low angular distance is an indicator of satellite cross-talk coming from the main beam, but the interfering signal can also be received from the secondary lobes of the array. Therefore it was decided to simulate the expected received power from both the direct and reflected signals from all satellites using the measured radiation pattern of one of the antenna elements, the array factor according to the array dimensions, and the attitude of the plane. In order to simplify the processing, a flat Earth, and a constant reflectivity were considered for all reflected signals. Still, if the interfering cross-correlation peak is

located in the delay domain far from the desired cross-correlation peak, it will not affect the interferometric waveform, so it was last decided to compute the delay $\Delta\tau$ between the direct and the reflected signals for each satellite using the approximation

$$\Delta\tau = \frac{2 \cdot h \cdot \sin(\theta)}{c}, \quad (9.1)$$

where h is the height of the plane over the ellipsoid, θ is the elevation angle of the satellite with respect to the receiver, and c is the speed of light. This delay determines where the center of the cross-correlation peak should be in the delay domain. The cross-correlation waveforms can be approximated by a two code chips wide triangle in the delay domain in specular reflections [10], one in the leading edge and one in the trailing edge. When the signal is scattered on a rough surface, the trailing edge is elongated. For instance, wind speeds from 6-22 m/s can enlarge the trailing edge of reflections over sea from two to three code chips in airborne GNSS-R [110]. For simplicity, all cross-talk cross-correlation peaks farther than two code chips and weaker than -10 dB compared to the tracked one are considered non-interfering.

Figure 9.1 shows an example of an interferometric contaminated waveform in blue retrieved during the Bass Strait flight, the conventional waveform of the tracked satellite in red, and the waveform of the interfering satellite in yellow. A large number of interferometric waveforms were found to be corrupted due to RFI as well, so they had to be discarded for the study of the cross-talk impact assessment. Besides, the interferometric waveform is more affected by noise than the conventional ones, which is used as reference for the comparison because they are not affected by satellite cross-talk. For this reason, it is proposed below how to reconstruct the interferometric waveform using the conventional ones as can be seen in purple in Fig. 9.1.

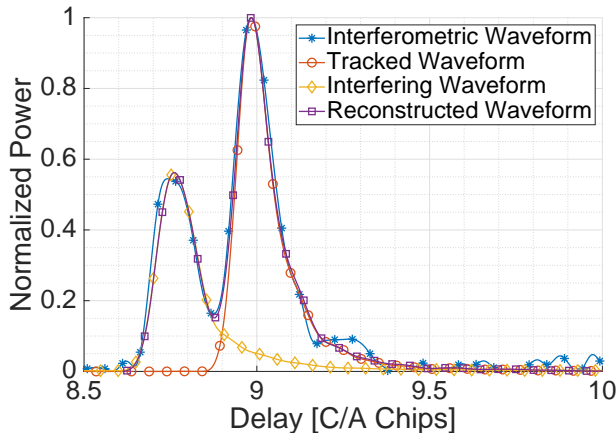


Figure 9.1: Retrieved L5/E5A interferometric GNSS-R waveform (blue), Galileo E5A tracked conventional GNSS-R waveform (red), GPS L5 interfering cGNSS-R waveform (yellow), and reconstructed contaminated waveform (purple). The data was collected during the flight over the Bass Strait.

The coherent waveform between the signals x and y as function of the delay τ and

Doppler frequency f_d between them is defined in [49] as

$$Y_{x,y}(t_0, \tau, f_d) = \int_{t_0}^{t_0+T_c} x(t_0 + t') \cdot y(t_0 + t' + \tau) \cdot \exp(j2\pi f_d t') dt', \quad (9.2)$$

where t_0 is the time at the origin, and T_c is the coherent integration time. Then, the incoherent average of M coherent waveforms is defined as

$$\langle |Y(\tau, f_d)|^2 \rangle = \frac{1}{M} \cdot \sum_{m=0}^{M-1} |Y(m \cdot T_c, \tau, f_d)|^2. \quad (9.3)$$

For GNSS signals, the cross-correlation peak is located at a Doppler frequency f_d that compensates the Doppler frequency difference between x and y , and is located at a delay τ that compensates the time difference between x and y . In the conventional case, when a signal s transmitted from a GNSS satellite with a noise n is cross-correlated with the code c corresponding to the transmitting satellite, the incoherent waveform becomes

$$\langle |Y(\tau, f_d)|^2 \rangle = \langle |Y_{s,c}(\tau, f_d) + Y_{n,c}(\tau, f_d)|^2 \rangle, \quad (9.4)$$

where $Y_{s,c}$ stands for the waveform resulting from cross-correlating the received signal s with the code c , and $Y_{n,c}$ is the noise term resulting from cross-correlating the noise n with the code c . In the interferometric case, if the signal s transmitted from the tracked satellite with noise n is received in conjunction with a signal z transmitted from a satellite which causes cross-talk, the incoherent waveform becomes

$$\begin{aligned} \langle |Y(\tau, f_d)|^2 \rangle = & \langle |Y_{s_D, s_R}(\tau, f_d) + Y_{s_D, z_R}(\tau, f_d) + Y_{s_D, n_R}(\tau, f_d) \\ & + Y_{z_D, s_R}(\tau, f_d) + Y_{z_D, z_R}(\tau, f_d) + Y_{z_D, n_R}(\tau, f_d) \\ & + Y_{n_D, s_R}(\tau, f_d) + Y_{n_D, z_R}(\tau, f_d) + Y_{n_D, n_R}(\tau, f_d)|^2 \rangle, \end{aligned} \quad (9.5)$$

where the subscripts D and R indicate if the signal has been received through the direct or the reflected antenna arrays, respectively, Y_{s_D, s_R} is the desired satellite term, Y_{z_D, z_R} is the cross-talk term, Y_{s_D, z_R} and Y_{z_D, s_R} are the so called cross-satellite terms, and Y_{s_D, n_R} , Y_{z_D, n_R} , Y_{n_D, s_R} , Y_{n_D, z_R} , and Y_{n_D, n_R} are the noise terms. For ground-based and airborne GNSS reflectometry, the Doppler difference between the direct and the reflected GNSS signals can be neglected, so the peak of Y_{s_D, s_R} and Y_{z_D, z_R} is located at $f_d = 0$. Due to the low power of the GNSS signals, the term Y_{n_D, n_R} dominates the other noise terms [186]. If an interference signal i is present, several cross terms appear and might dominate over the desired Y_{s_D, s_R} and Y_{z_D, z_R} terms, which happened during most of the flight over the Bass Strait. The interference terms must be avoided, so the contaminated waveform is reconstructed as

$$\begin{aligned} \langle |Y_{REC}(\tau)|^2 \rangle = & \langle |Y_{u_R, c_s}(\tau, f_s) + Y_{u_R, c_z}(\tau, f_z)|^2 \rangle \\ = & \langle |Y_{s_R, c_s}(\tau, f_s) + Y_{z_R, c_s}(\tau, f_s) + Y_{i_R, c_s}(\tau, f_s) + Y_{n_R, c_s}(\tau, f_s) \\ & + Y_{s_R, c_z}(\tau, f_z) + Y_{z_R, c_z}(\tau, f_z) + Y_{i_R, c_z}(\tau, f_z) + Y_{n_R, c_z}(\tau, f_z)|^2 \rangle, \end{aligned} \quad (9.6)$$

where $u_R = s_R + z_R + i_R + n_R$ is the signal received from the down-looking array, s_R is the received signal from the tracked satellite, z_R is the received signal from the satellite

causing cross-talk, i_R is an interfering signal, and n_R is noise; c_s and c_z are the codes of the desired satellite and the satellite causing cross-talk respectively, and f_s and f_z are the Doppler frequencies of the satellite being tracked and the satellite causing cross-talk. The transmitted GNSS codes are robust against RFI and noise, which implies that Y_{s_R, c_s} and Y_{z_R, c_z} dominate over the other terms, thus contributing as a much lower noise floor compared to the interferometric case, where several other noise terms are present. An example of a reconstructed contaminated waveform is shown in Fig. 9.1. The cross-correlation peaks are not symmetrical with respect to their maximum, that is, the trailing edge is longer than the leading one. This effect is caused by the scattering of the reflected signal in a rough surface, in this case the sea surface roughness caused by the wind [49]. For this reason, the “second” cross-correlation peak (the contribution of the satellite that is received later) is more affected by the “first” one (the contribution of the satellite that is received sooner) than vice versa.

Two datasets are created from the Bass Strait flight data: the XT (cross-talk) dataset with 670 s, and the NOXT (no cross-talk) data set with 470 s. The flights over land were not suitable for this analysis because the soil permittivity would have attenuated some of the tracked and interfering waveforms, affecting the impact analysis statistics. The Port Phillip Bay flight was not suitable because the aeroplane was repeatedly flying over two points of interest, therefore maneuvering constantly and abruptly, which caused the apparition of even larger side lobes that would have also affected the analysis statistics. In the XT dataset, the two beams of the instrument were pointing at two different satellites that were close enough in the sky to be received by the main lobe of both beams. The signals of both satellites were received in both beams and close enough in time to be overlapped. In one of the beams, the interfering cross-correlation peak was received before the tracked cross-correlation peak, and in the other beam it was received afterwards. In the NOXT dataset, both beams were tracking two different satellites that again were received in both beams, but the cross-correlation peaks were separated enough to not be overlapped, thus not being affected by the cross-talk. In the case of XT dataset, the interfering cross-correlation peak and the noise distort the tracked cross-correlation peak, thus introducing an error in any retrieved parameter such as the peak position or amplitude. In order to assess the impact of the cross-talk alone, the impact of the noise has also to be characterized, using for that purpose the NOXT data set.

In the altimetric case, the analysis focused on the three main delay estimators: the position of the maximum derivative (DER) [210], the position of the maximum amplitude (MAX) [210, 211], and the position when the leading edge reached the 75% of the maximum amplitude as proposed by [212], which is called half-power position (HALF) due to its similarity to the homonym estimator used by the radar community. The delay positions using MAX, DER, and HALF are estimated for the reconstructed and the tracked conventional waveforms. For each estimator, the error between the estimated positions was computed between both waveforms. Then, the results for the XT and NOXT data sets were compared in terms of their PDF. In the NOXT dataset, the tracked and the interfering cross-correlation peaks are not overlapping each other. For a given delay estimator, the estimated delay difference between the conventional and the reconstructed waveforms might only be caused by the different noise terms. The PDF of the NOXT term was used as reference. In the XT dataset, the tracked and the interfering cross-correlation peaks were overlapping each other, therefore the PDFs might be different to the NOXT ones. These PDFs were then compared to assess the impact of the cross-talk.

To evaluate the impact in scatterometry, the same analysis is applied to the peak amplitude difference between the reconstructed and the conventional waveforms.

The reconstructed contaminated waveform $\langle |Y_{REC}|^2 \rangle$ and the conventional waveforms of both the interfering $\langle |Y_{z_R, c_z}|^2 \rangle$ and the tracked satellites $\langle |Y_{s_R, c_s}|^2 \rangle$ were computed with $T_c = 1$ ms coherent averaging and $M = 1000$ incoherent averages, and then interpolated to reach 1 cm resolution around the peaks and in the leading edges. The waveforms were computed aligning the correlation window to the secondary codes as explained in Section 8.4.

While the cross-talk occurrence has been analyzed in both frequency bands, the cross-talk impact in altimetry and scatterometry has been analyzed only at the L5/E5A frequency band. This is because the L5/E5A beam is wider than the L1/E1 one, which allows the simultaneous reception of signals from more than one satellite that were not overlapping in time, so it was possible to have both XT and NOXT datasets. Furthermore, GPS L5 signals and Galileo E5A signals were similar in modulation, bandwidth, and chip length, so their correlation peaks are similar. This fact simplified the analysis, since just two cases have to be analyzed: the tracked satellite cross-correlation peak being located before or after the interfering satellite cross-correlation peak.

9.2 Results

Figure 9.2 shows skyplots of the satellites in view (black traces). The tracked satellites are represented with colored dots, where the color represents the angular distance to the closest satellite. In case the tracked satellite was affected by cross-talk it is also highlighted in red. Note that the four beams are represented in the same plot, and if the same satellite was tracked in both bands their representations are overlapped, which may under-represent the visual cross-talk occurrence.

Figure 9.3 shows the cumulative histogram of the cross-talk probability for a given signal-to-interference ratio (SIR), which is the relationship between the expected power of the tracked satellite over the expected power of the other satellites. The histogram was computed taking into account the lowest SIR from all visible satellites, since satellite cross-talk did not occur from more than one satellite simultaneously. The cross-talk occurrence of the two beams at each frequency band was aggregated if the beams were not pointing to the same satellite, that is, the data from the second beam was considered as if the flight was longer.

Several factors determine the likelihood to be affected by satellite cross-talk. First, the number of GNSS satellites transmitting in-band: L1/E1 may seem more likely to be affected because these signals were transmitted by the full GPS constellation (32 satellites) and Galileo constellation (16 satellites at the time of the experiment), while the signals allocated in L5/E5A were only transmitted by the GPS block IIF satellites (12 of the 32 current GPS satellites), plus the Galileo ones (16 satellites). Secondly, the L1/E1 transmitted signals were more susceptible to cross-talk because the chip length was 10 times longer than in L5/E5, which means that the range of elevation angles that might interfere according to Equation (9.1) was larger. Finally, the array factor at L1/E1 had a narrower beam as compared to the one at L5/E5A, which was more selective against the undesired signals, but the long separation between antenna elements ($0.75\lambda_{L1}$, where $\lambda_{L1} = 19.04$ cm) caused diffraction lobes as the instrument pointed far away from the

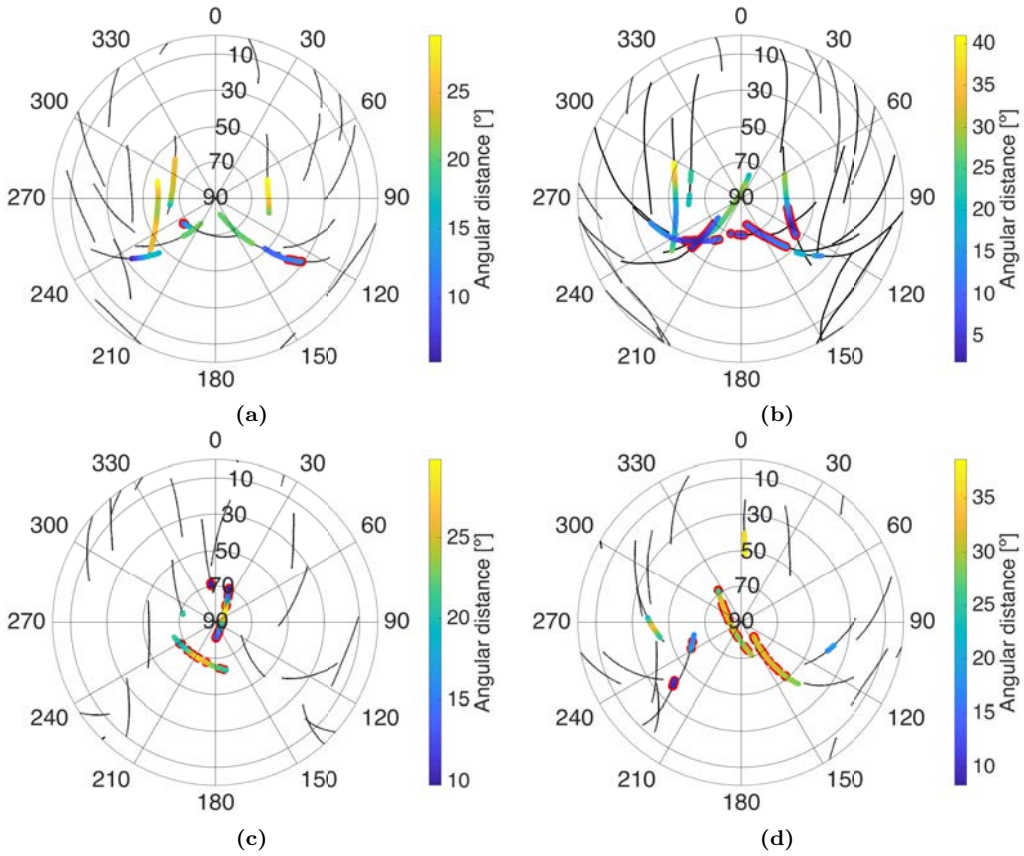


Figure 9.2: Skyplot of the tracked satellites in the a) flight over the entrance to Port Philip Bay, b) sea flight over the Bass Strait, and flights over Yanco under c) dry and d) wet soil conditions. The color scale indicates the angular distance to the closest satellite. Red lines highlight cross-talk from other satellites.

boresight, which happened often when the airplane rotated heavily about the pitch and roll axes. This effect can be clearly seen in the flights over land. In the skyplots in Figure 9.2 the cross-talk is intermittent, which was caused by the diffraction lobes generated when the airplane had to maneuver abruptly at the end of each transect over the farm fields.

The position of the satellites in the sky during the flights had a strong impact in the probability of having cross-talk because of their short duration. Counterintuitively, L1/E1 signals show much lower likelihood of being affected by cross-talk than the L5/E5A one, except during the second sea flight, which was contaminated almost half of the flight time. In the other flights, the probability of cross-talk was reduced to less than 2%. L5/E5A signals were instead more likely to be affected by cross-talk (5-10%). Since there are fewer satellites transmitting L5/E5A signals, there is a lower chance of finding one of them with a high elevation angle. The MIR instrument was therefore forced to track satellites with lower elevation angles, and therefore the cross-talk probability increases [45]. It was

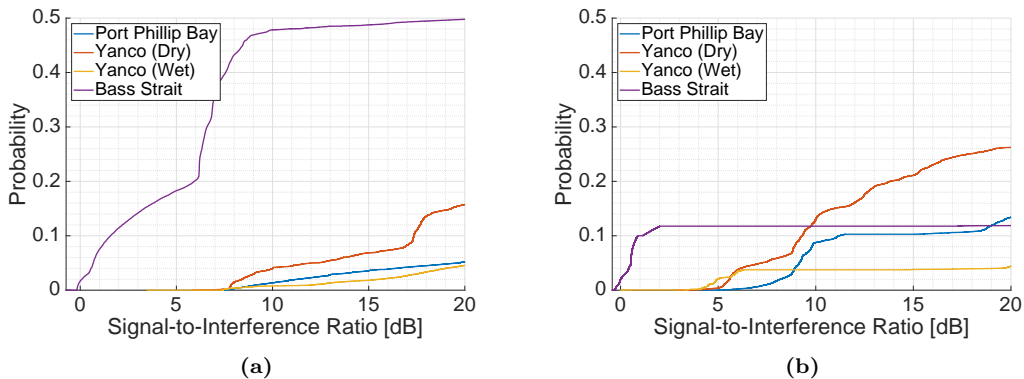


Figure 9.3: Cumulative histogram of the probability of having cross-talk in the (a) L1/E1 and, (b) L5/E5A frequency bands for the different MIR flights.

noteworthy that not even a 19-element array antenna with 18-20 dB directivity has been able to avoid a cross-talk contamination during half of one of the flights, and that it could not reduce the cross-talk at L5/E5A below 10%.

Figure 9.4 shows the error PDF when estimating a) the maximum derivative point, b) the half power point, c) the peak position, and d) the peak amplitude. The “NOXT” PDFs show the error estimation caused only by the noise. The “XT” PDFs show the error estimation caused by satellite cross-talk and the noise. The analysis distinguishes between the interfering cross-correlation peak arriving after the tracked satellite cross-correlation peak (“first peak”), and arriving before (“second peak”). The mean and standard deviation of each PDF is shown in Table 9.1. In the case of the amplitude, the mean and standard deviation are first estimated as the geometric mean and geometric standard deviation, and then are converted into decibels. The position error is considered positive if the point position is delayed, and the amplitude error is considered positive if the amplitude increases.

When the interfering cross-correlation peak was received after the tracked satellite one (“first peak”), the standard deviation of the estimations slightly increased with respect to the NOXT case, but the bias was not affected significantly. Since the delay estimators were applied to the leading edge of the first peak, the interfering one has to be really close to affect these estimators, that is, being almost totally overlapped. Furthermore, the symmetry of the PDF and the unchanged bias suggests that the PDF has changed only because the reconstructed waveform (see Eqn. (9.6)) has more noise terms than the conventional one (see Eqn. (9.4)).

On the contrary, when the interfering cross-correlation peak was received before the tracked satellite one (“second peak”), the PDF lost its symmetry, became biased, and the standard deviation was increased up to 40 cm with respect to the previous case. The PDFs show the DER point moving in the opposite direction than the HALF and the MAX points, as expected. The trailing edge of the interfering cross-correlation peak advanced in time with the MAX and the HALF positions because the trailing edge can be approximated by a decreasing exponential function $f(\tau) = e^{-k \cdot \tau}$, which is a monotonic decreasing function. On the other hand, the DER point was delayed because the derivative

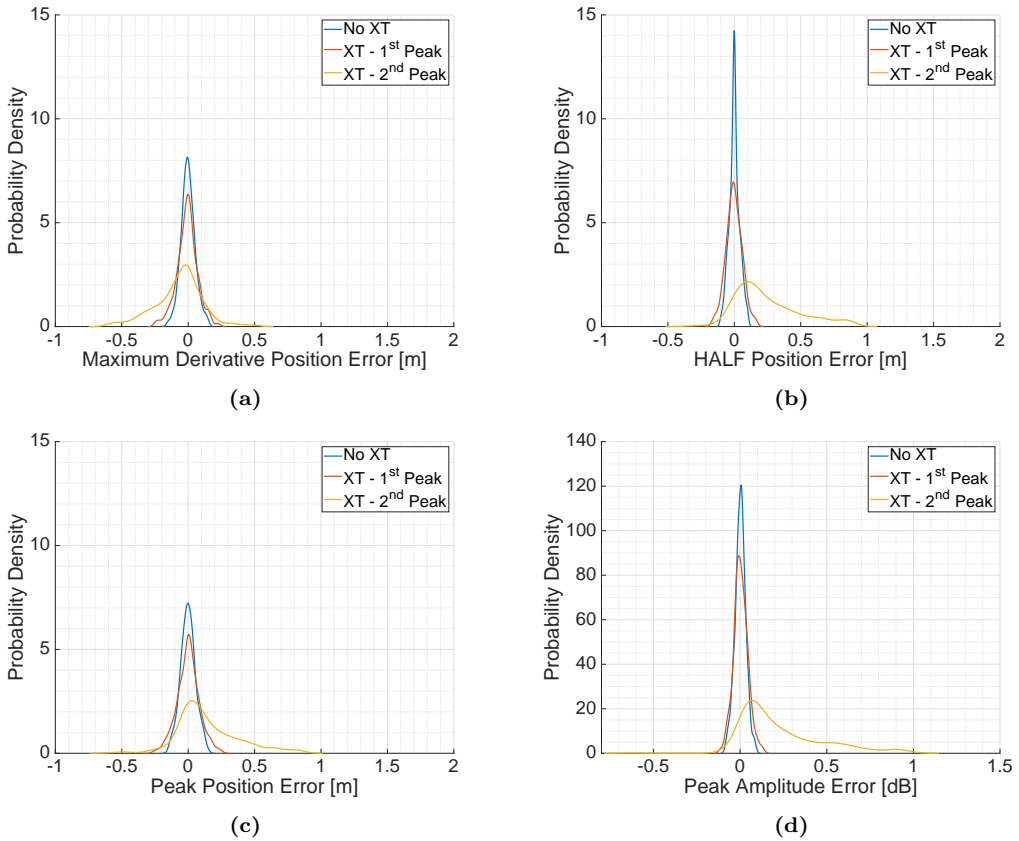


Figure 9.4: PDF of the estimation error of the (a) maximum derivative position (DER), (b) half-power position (HALF), (c) peak position (MAX), and (d) peak amplitude. The “XT” PDFs show the error estimation when the cross-correlation peaks are close enough to interfere with each other, while the “NOXT” show the error estimation when the cross-correlation peaks are far enough to not interfere. The analysis distinguishes between the interfering cross-correlation peak arriving later than the tracked satellite cross-correlation peak (“first peak”), or arriving sooner (“second peak”).

of the trailing edge $f'(\tau) = -k \cdot e^{-k \cdot \tau}$ is a monotonic increasing function. The maximum derivative delay estimator seemed to be the more robust one, whereas the half estimator was the most affected by cross-talk. All the estimators showed an increase of the standard deviation up to tenths of cm, which prevents the desired centimetric precision in altimetric applications [12]. The peak value estimation seems to be affected in the same way as the delay estimators; if the interfering cross-correlation peak was received after the tracked satellite cross-correlation peak, the amplitude estimation was not affected, whereas in the opposite case, the PDF was biased, and the standard deviation increased up to 0.24 dB, which would affect the accuracy of retrieved geophysical parameters, such as soil moisture.

Table 9.1: Effect of cross-talk in three different delay estimators and in the peak amplitude in the flight over the Bass Strait.

	No XT	XT	
		1st Peak	2nd Peak
MAX [cm]	$\mu = -0.14$ $\sigma = 5.6$	$\mu = 0$ $\sigma = 8.4$	$\mu = 14.4$ $\sigma = 23.5$
DER [cm]	$\mu = -0.1$ $\sigma = 5.3$	$\mu = -0.8$ $\sigma = 7.8$	$\mu = -6.9$ $\sigma = 18.1$
HALF [cm]	$\mu = -0.1$ $\sigma = 4.2$	$\mu = -0.4$ $\sigma = 6.4$	$\mu = 40.1$ $\sigma = 45$
Peak value [dB]	$\mu = 0$ $\sigma = 0.03$	$\mu = 0$ $\sigma = 0.04$	$\mu = -0.2$ $\sigma = 0.24$

9.3 Conclusions

This chapter shows evidence of satellite cross-talk in iGNSS-R even using highly directive antennas, and analyzes its impact on three different delay estimators and a peak value estimation. While this effect should be less important for spaceborne receivers [45], its effects are still not negligible and must be accounted for. The cross-talk probabilities for different signal-to-interference ratios have been computed and contaminated waveforms have been presented. The cross-talk occurrence below 10% of the total time in three of the four flights are in accordance with the predictions in [45], but longer flights are recommended to validate it.

The effect of cross-talk in the main three delay estimators (MAX, DER, and HALF) and in the peak amplitude estimation has also been assessed for this particular flight and sea surface roughness. The standard deviation of the error estimation increased from 18 cm up to 40 cm, which exceeds the centimetric precision of the altimetric accuracy requirements. Analogously, the standard deviation of the amplitude estimation increased up to 0.24 dB, which also might affect the retrievals of soil parameters such as surface roughness and soil moisture. Even using highly directive arrays, the degradation of the waveforms caused by satellite cross-talk could not be avoided, which should be taken into account for future ground-based and airborne interferometric GNSS-R missions. Results may differ for other sea conditions, and further studies are required both over sea and land.

Part IV

Conclusions and Future Work

10

Chapter 10

Conclusions and Future Work

10.1 Conclusions

Alongside this Ph.D. thesis a new airborne GNSS-R instrument with state of the art capabilities has been developed. The instrument successfully mimicked the PARIS IoD with two frequency bands, multiple beams, GPS and Galileo compatibility, and by being able to constantly track the chosen satellites taking into account the satellites' position and the aircraft position and attitude. The only notable difference was the use of analog beamformers, instead of digital ones. Besides the interferometric technique, the instrument can also apply the conventional one, thus allowing the performance comparison in “fair conditions” of different signals, and systems.

During the early development of the instrument it was found that the DME/TACAN radio navigation system was interfering the L5/E5A frequency band, which in the case of the interferometric technique could totally disrupt its use. The impact study of these signals in a future space mission lead to the conclusion that the use of an RFI detection and mitigation system was advised.

This thesis also proposed a method to calibrate the instrument in different steps. First, each array and beamformer was characterized individually in an anechoic chamber to pre-calibrate the imbalances of the vector modulators used as phase shifters for the beamformers, and the differences between RF chains in each element of the beamformer. Then, during the flight the average gain and phase difference between arrays was measured. To do so, internally generated PRN codes were successfully used as calibration signals.

Once the instrument was finalized, a field campaign was carried out in Australia to evaluate the instrument capabilities. A total of four flights were conducted: a test flight over sea, a second flight over sea to measure sea height, and two flights over land,

one before and one right after rain events, to estimate soil moisture. Even though at the time of writing this Ph.D. thesis the data has not been completely processed, the preliminary results are promising. The test flight not only proved that the instrument was operational, but also showed a power interference pattern in the land/water transitions caused by the different Fresnel zones of the reflection area passing from one medium to the other, with ringing patterns that depend on the frequency band. The instrument also proved its sensitivity to topography in both sea flights. The second sea flight shows a clear correlation between the estimated height and the expected sea height, but still many corrections have to be applied, such as the position difference between the up- and down-looking antennas. Besides, the second sea flight was used to study the impact of satellite cross-talk, which despite using highly directive and steerable arrays could not be avoided. In addition, the trailing edge of the retrieved waveforms in the cross-talk study also shows sensitivity to sea surface roughness. Last, the two flights over land showed that the instrument was sensitive to soil moisture changes on ground.

10.2 Future work

The MIR instrument has been finished, and a huge amount of data has been gathered. This section suggests future lines of work to consider. First, the field campaign sampled data must be totally processed, which includes, but is not restricted to:

- Properly processing L5/E5A data, which includes applying code alignment. Also applying peak retracking at both frequency bands to be able to use incoherent averaging times larger than 300 ms.
- Applying the in-flight calibration, by compensating the antenna position difference for altimetry, and by applying the noise characterization of the USRPs.
- Comparing the performance of cGNSS-R, and iGNSS-R. Comparing also results between frequency bands when a satellite is pointed simultaneously by one beam of each frequency band.
- Evaluate the soil moisture sensitivity over land, and the altimetric performance over land and sea once the calibration has been successfully applied.
- Study the instrument spatial resolution as function as the coherent and incoherent times.
- Analyze the ratio between the coherent and incoherent part of the reflected signals over different kinds of targets.

In case more field campaigns are carried out, the following hardware improvements are suggested to increase the instrument performance:

- Fabricating new RF Front-ends with higher gain and lower noise figure.
- Removing the airplane inertia effect on the inclinometer to properly retrieve the pitch angle; or ideally by upgrading the actual attitude determination system to an Attitude and Heading Determination System with Fiber Optic Gyros (FOG) and a GPS receiver to improve the performance and reliability of the current attitude determination system.

- Examining a removal of the extra RF amplifiers in the down-looking RF chains, which in Chapter 6 were suggested unnecessary.
- Enhancing the data processing subsystem by:
 - Modifying the FPGA to include real-time processing as it was originally planned to overcome the limitation of sampling at 1-bit, or at least to remove the offset present before 1-bit quantization.
 - Embedding a RFI mitigator system in the FPGA.

In the same way, the software can be improved by:

- Providing a user interface to show in real time the instrument status, and to be able to control it.
- Liberating one of the two mutexes involved in the call to the `processAllDetailedSVInfo()` function. This function is called inside the mutex `mutex_SVs` in `processGsofData()`, and calls to another mutex. One of the mutexes should be liberated or removed to avoid a concurrence blockage.
- Updating the condition variable `cond_start_get_angles_thr` once the ephemeris or the almanac have been received, not when they have been requested. When a ephemeris or almanac is required by `GetSVLookAngle` thread, a packet is sent to the GNSS receiver. The thread should wait until the ephemeris or almanac is received, but in the current state the thread wait until the request packet is sent.
- Reducing the number of variables that `GetSVLookAngles` accesses, which is a consequence of the lack of planning when the code was developed. For example, `GET-DataFromBD982` and `GetSVLookAngles` threads share three different data structures, which could be easily reduced to one.

Part V

Appendices

A

Appendix A

Subsystem Schematics, PCBs, and Housing CADs

A.1 Antennas

The antennas in Fig. A.2 were manufactured in Rogers 4003c and stacked as shown in Fig. A.1. The long side of the cross in fig. A.2a measures 35.7 mm, while the short one measures 5.5 mm. The L1/E1 resonator in layer mid 1 measures 48.1x48.1 mm. The L5/E5A resonator in layer mid 2 measures 61x61 mm.

TOP T2 COPPER (GERBER FILE PCB.GTL)	-0.035mm
1.50mm ROGERS 4003C	-1.500mm
1 X PRE-PREG ROGERS 4450B	-0.101mm
COPPER (GERBER FILE PCB.G2)	-0.035mm
1.50mm ROGERS 4003C	-1.500mm
1 X PRE-PREG ROGERS 4450B	-0.101mm
COPPER (GERBER FILE PCB.G4)	-0.035mm
1.50mm ROGERS 4003C	-1.500mm
1 X PRE-PREG ROGERS 4450B	-0.101mm
1.50mm ROGERS 4003C	-1.500mm
1 X PRE-PREG ROGERS 4450B	-0.101mm
1.50mm ROGERS 4003C	-1.500mm
BOTTOM T1 COPPER (GERBER FILE PCB.GBL)	-0.035mm

Figure A.1: Representation on how the layers of the antenna were stacked, following the order top, mid 1, mid 2, and bottom.

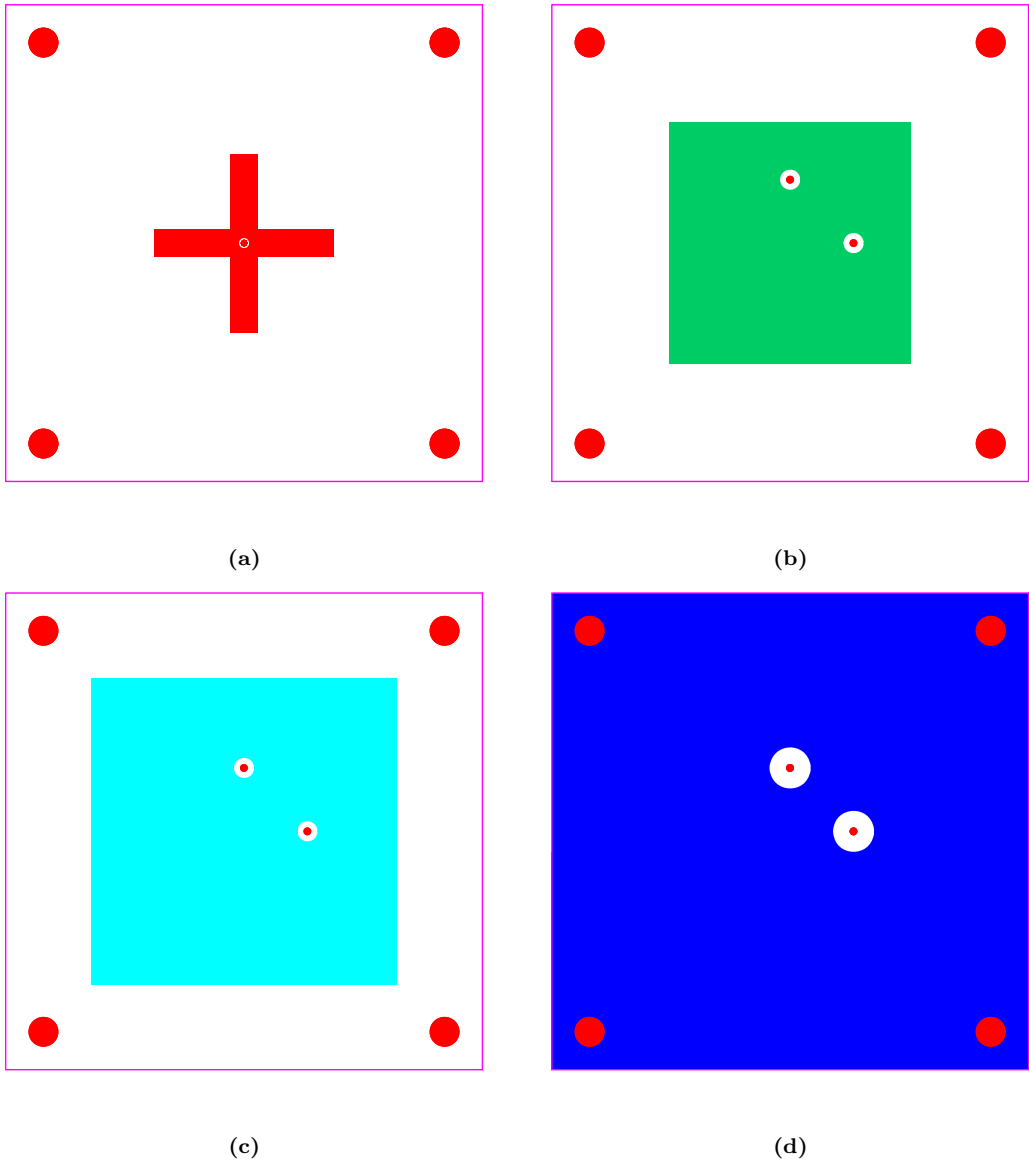


Figure A.2: a) Top layer, b) Mid 1 layer, c) Mid 2 layer, and d) Bottom layer of the antenna PCB.

A.2 RF Front-ends

Figure A.3 shows the original schematic of the RF Front-ends, and Fig. A.2 shows the PCBs when they were sent to be manufactured. The PCBs were manufactured using Rogers 4003c 0.5 mm thick between the Top layer and the Mid-1 layer, a prepreg between Mid-1 layer and Mid-2 layer, and FR-4 0.5 mm thick between Mid-2 layer and

Bottom layer. After testing, some parts of the circuit were modified to avoid an unwanted oscillation:

- To select the LHCP polarization, Rload1 and Rsc2 were mounted, but Rload2 and Rsc1 were not. To select RHCP polarization, Rload2 and Rsc1 were mounted, but Rload1 and Rsc2 were not.
- The amplifier AMP2 was bypassed with a 0 ohm resistor to reduce the total gain. Its voltage regulator REG3 and the associated components required (L6, C24-26, C10, C12, C15, R3, L3) were not mounted.
- The logic circuit that controlled the switch was removed because the oscillation that appeared in the calibration mode. The components XOR00, XOR01, L8, KL9, C30-35 were not installed. The voltage regulator REG4 and the components it required L10, C36-41 were not mounted either.
- The first variable attenuator made of Ratt1-3 was set to 0 dB, that is, Ratt2 is a 0 ohm resistor, and Ratt1 and Ratt3 were not mounted.
- The second variable attenuator made of Ratt4-6 was set to 7.75 dB, that is, Ratt5 is a 51 ohm resistor, and Ratt4 and Ratt6 are 120 ohm resistors.
- A 62 ohm resistor was mounted in the calibration line to ground to reduce the return loss of the calibration port of the reflective switch. This component is not shown in the schematics neither the PCB as it was added at the end.

All 38 RF Front-ends were mounted manually using a stencil to apply soldering paste and a soldering oven.

Figure A.5 shows the CAD of the boxes where the PCB are mounted. In blue, the SMA connectors, in green the PCB, in red M2,5 threaded holes, in orange 1 mm deep 3 mm diameter rabbet, in pink 1,5 mm diameter holes, and in cyan 2.5 mm diameter holes with small conic drill to hide the head of the bolts.

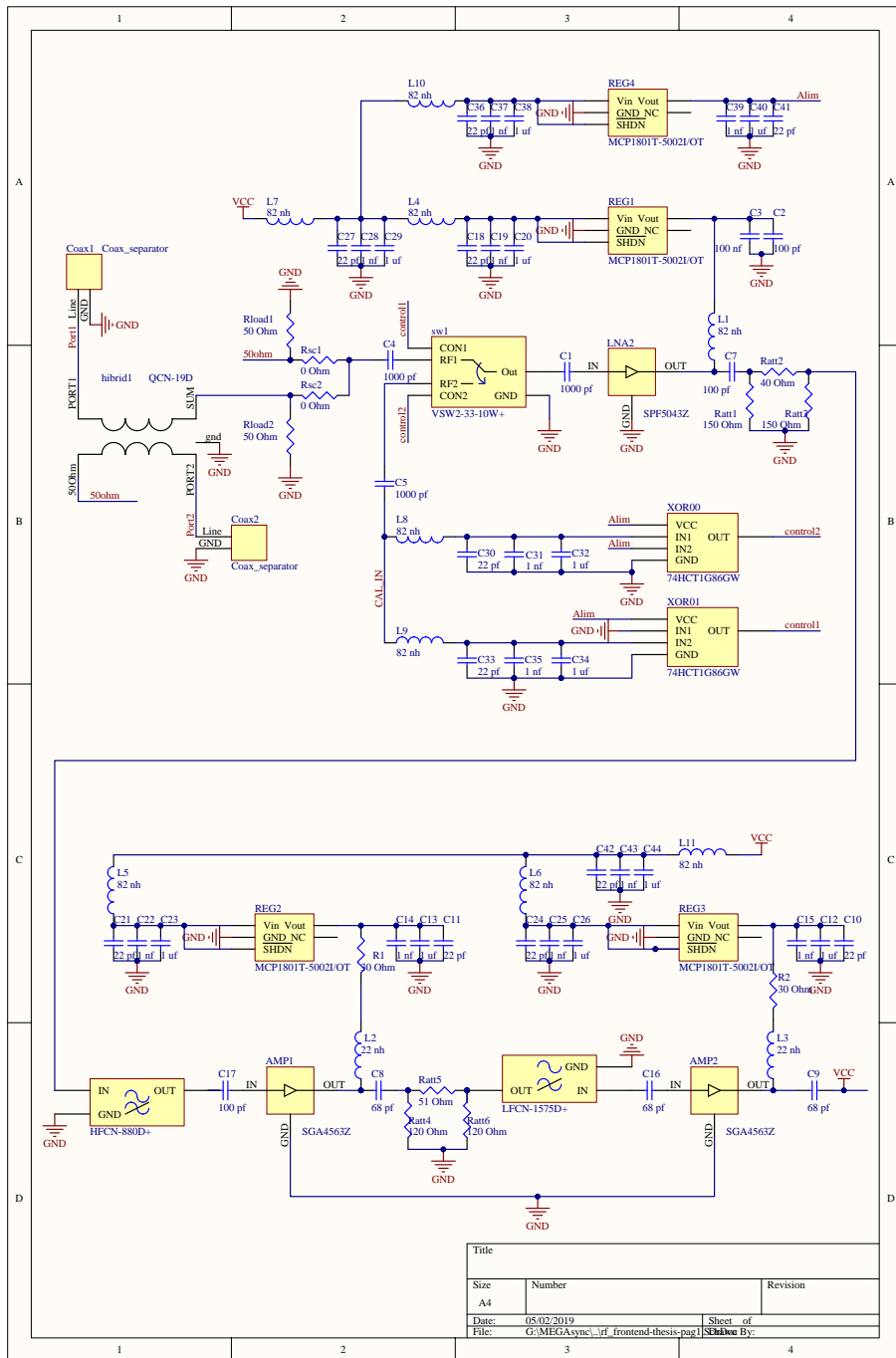


Figure A.3: Original schematic of the RF Front-ends.

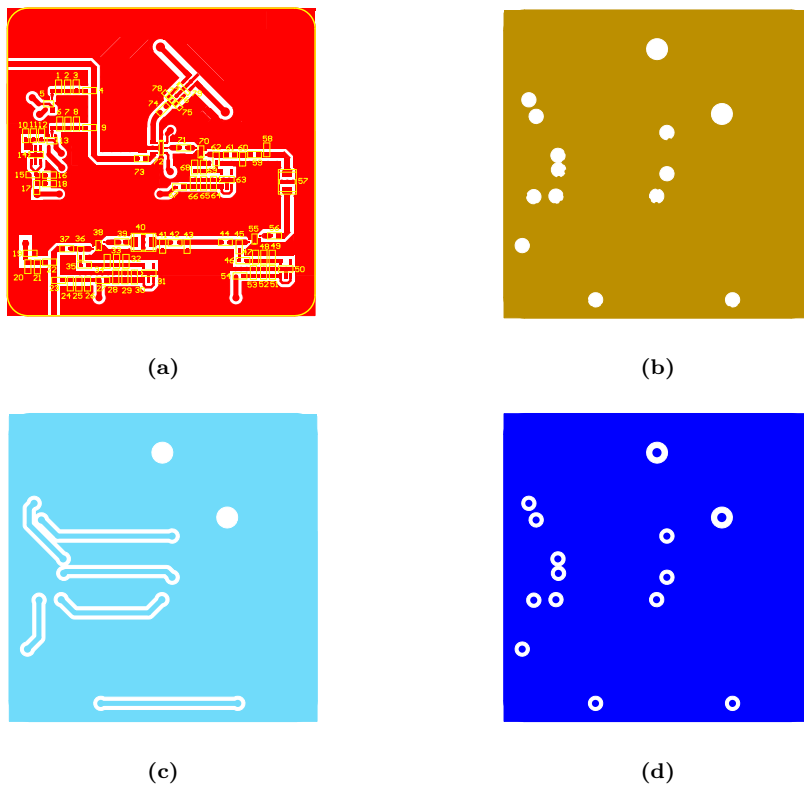


Figure A.4: a) Top layer, b) Mid 1 layer, c) Mid 2 layer, and d) Bottom layer of the RF Front-end PCB. The PCB measures 60x60 mm.

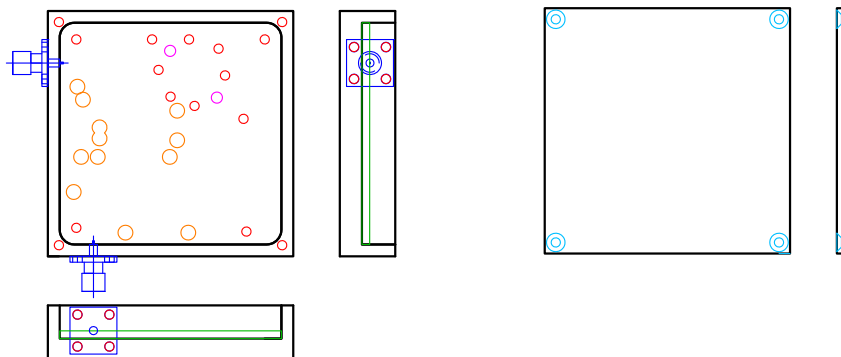


Figure A.5: CAD of the RF Front-ends box (left), and box cover (right). The box measures 66.4x66.4x15 mm, and the cover 66.4x66.4x3 mm.

A.3 Phase shifters

Figure A.6 shows the schematics of the phase shifter board. Inside it, there is a repeated block (green box) whose schematic can be seen in Fig. A.7. The different layers of the PCB can be seen in Fig. A.8. The PCB was manufactured using Rogers 4003c 0.5 mm thick between the Top layer and the Mid-1 layer, a prepreg between Mid-1 layer and Mid-2 layer, and FR-4 0.5 mm thick between Mid-2 layer and Bottom layer. The π attenuators made by the components Ratt1_1, Ratt2_1, Ratt3_1, Ratt1_2, Ratt2_2, Ratt3_2 were placed in case it was necessary to match the amplifiers, but they were not. Ratt1_1 and Ratt1_2 are 0 ohm resistors, and Ratt2_1, Ratt3_1, Ratt2_2, and Ratt3_2 were not mounted. The resistors Raddress1-6 are mounted according to the desired address as specified in Table A.1.

Due to the large number of components and the complexity to solder some of them, the soldering of the phase shifters was the only one that was outsourced using a Pick and Place machine.

Figure A.9 shows the CAD of the boxes where the Phase shifter PCBs are mounted. In blue the SMA and the DE-9 connectors, in green M2.5 threaded holes, and in purple M4 threaded holes. Figure A.10 shows the CAD of the pieces that hold the fans and how are they mounted together. Each box covers the previous one, so only the last box needs a cover. The first 18 phase shifters are cooled down from the same side where the input connector is located. The last board has a fan on the aluminum plate that covers the box. In red are represented the fans, on purple the pieces designed to hold the fans, and in orange the holes to hold the last fan.

Table A.1: Phase shifter address setting as function of the 0Ω resistors mounted. (X) stands for mounted, and (-) for not mounted.

	Raddress1	Raddress2	Raddress3	Raddress4	Raddress5	Raddress6
0x71	-	X	X	-	X	-
0x72	X	-	-	X	X	-
0x73	-	X	-	X	X	-
0x74	X	-	X	-	-	X
0x75	-	X	X	-	-	X

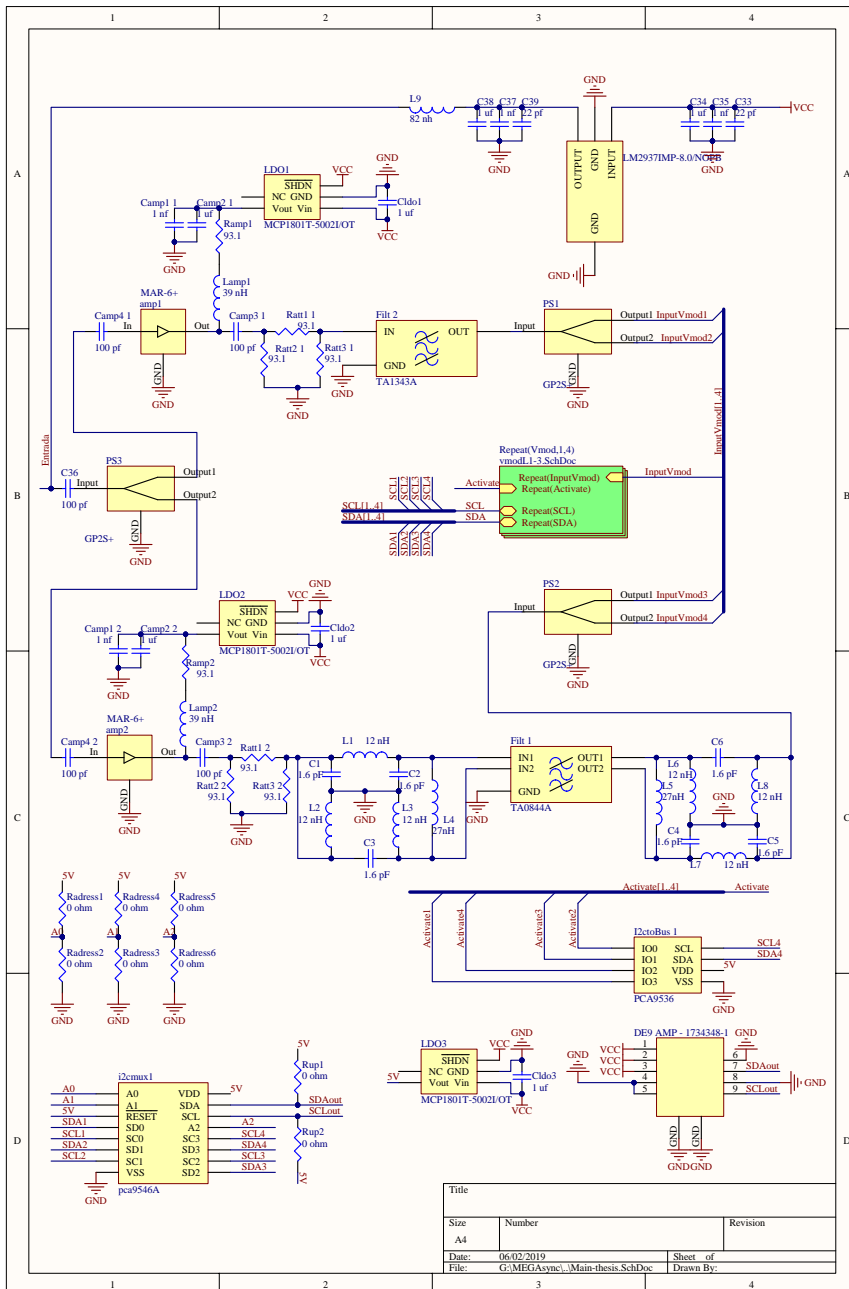


Figure A.6: Phase shifter schematic.

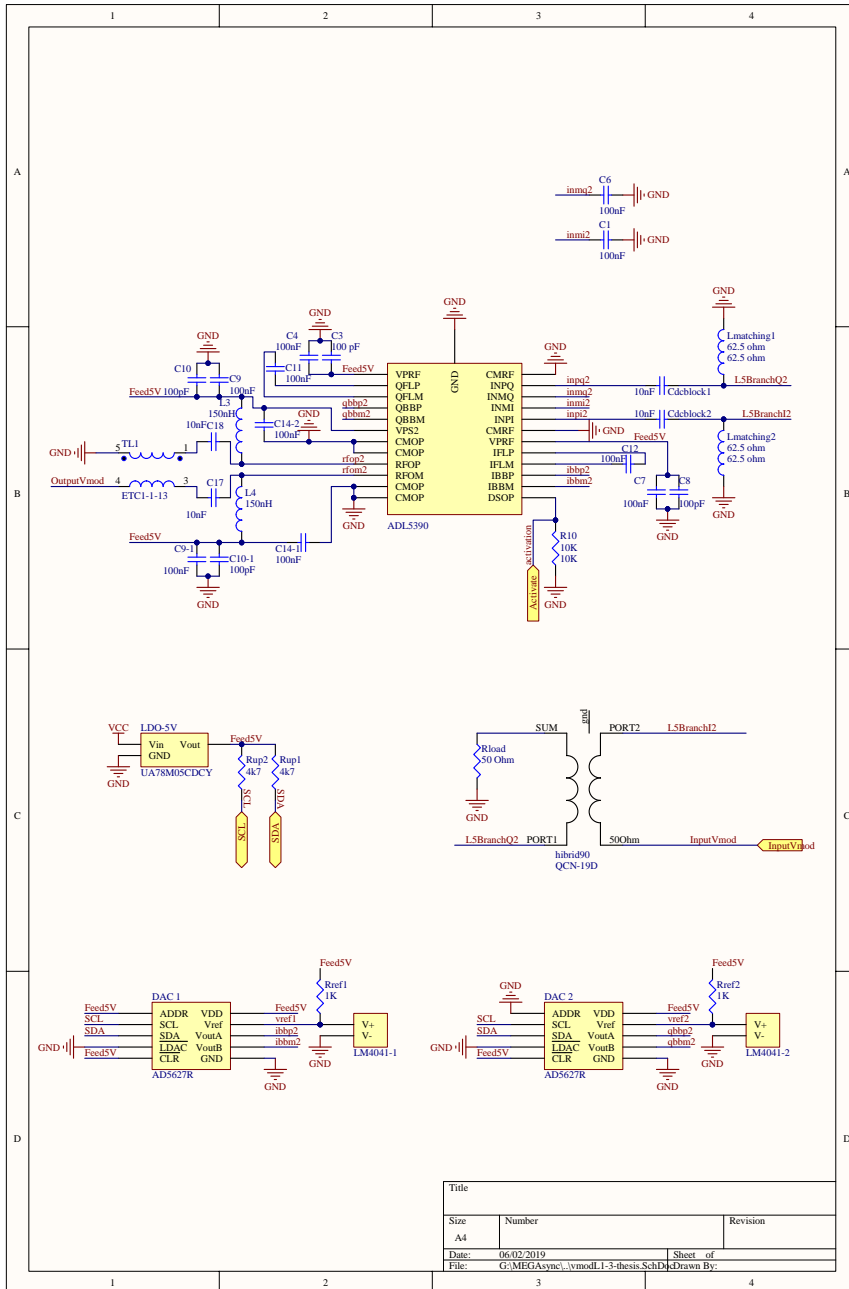


Figure A.7: Schematic of the Vmod Block inside Fig. A.6.

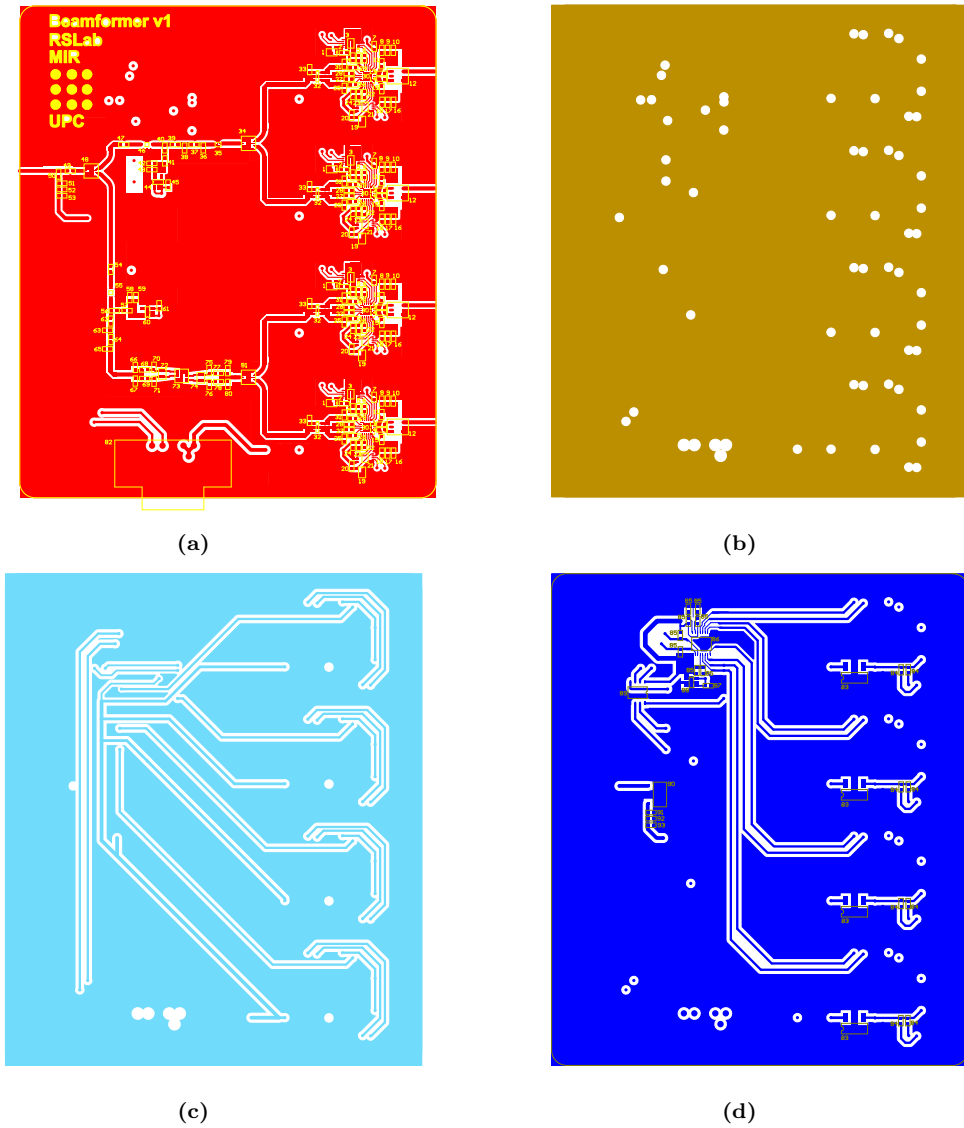


Figure A.8: a) Top layer, b) Mid 1 layer, c) Mid 2 layer, and d) Bottom layer of the Phase Shifter PCB. The PCB measures 110x130 mm.

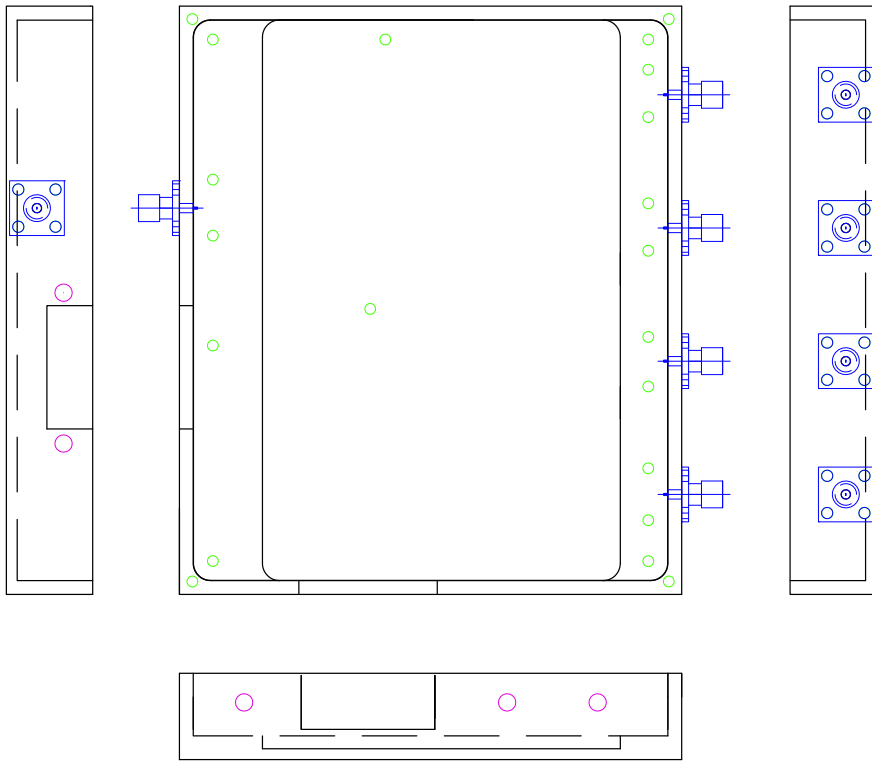


Figure A.9: Phase shifter box CAD design. The box measures 116.5x136.5x20 mm.

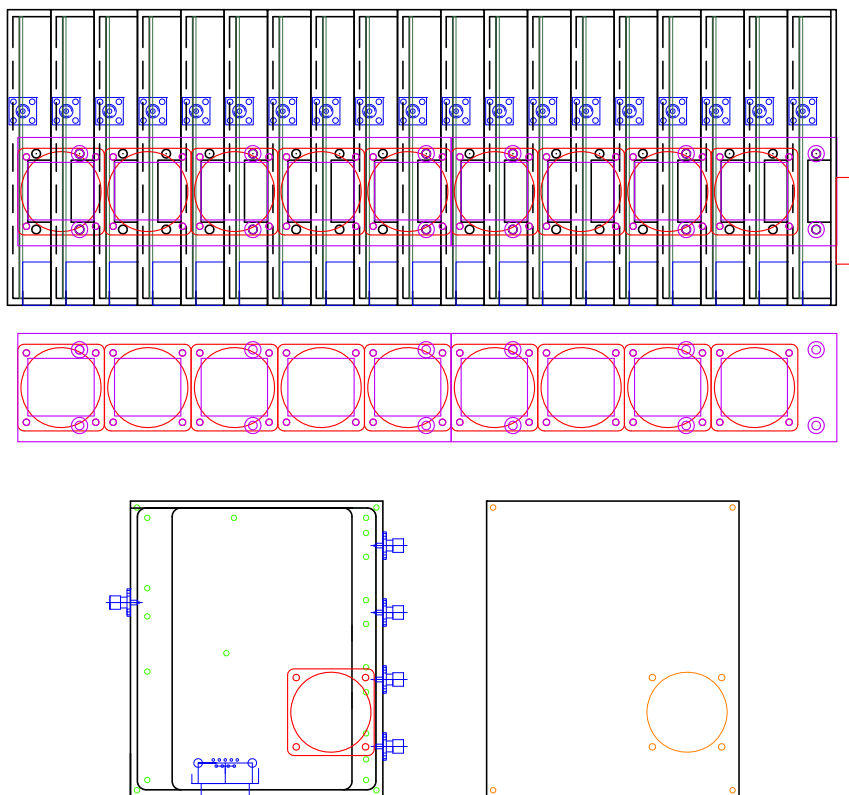


Figure A.10: Fan holding pieces CAD design.

A.4 19-Way Combiners

Figure A.6 shows the schematics of the 19-way power combiner/splitter board. Inside it there are two repeated block (green boxes) whose schematics can be seen in Fig. A.12. The different layers of the PCB can be seen in Figs. A.13 and A.14. The PCB was manufactured using Rogers 4003c 0.5 mm thick between the Top layer and the Mid-1 layer, a prepreg between Mid-1 layer and Mid-2 layer, and FR-4 0.5 mm thick between Mid-2 layer and Bottom layer. The PCB was designed to be able to set a logic value in the 19 inputs/outputs controlled by SPI serial protocol in order to control the calibration switches of the RF Front-ends. The components MAX7300, Ra1-4, R1, C1, XOR01, Rp1, Rp2, L1, L2, and RJE71 were planned to be mounted on the two power splitters located inside the arrays, while only the resistors Rgnd1-2 were planned to be mounted in the 8 power combiners for the beamformers. The calibration switches are finally set to a fixed position, and therefore all of the 2 power splitters for the arrays were mounted as the other power combiners.

All power combiners were mounted manually using a stencil to apply soldering paste and a soldering oven.

Figure A.15 shows the CAD of the box used for the 19-way power splitter/combiner. In blue the SMA and ethernet connectors, in green M2.5 threaded holes, and in orange M4 threaded holes. The CAD of the cover is not shown, it is a 2.5 mm thick aluminum plate with holes on the corners

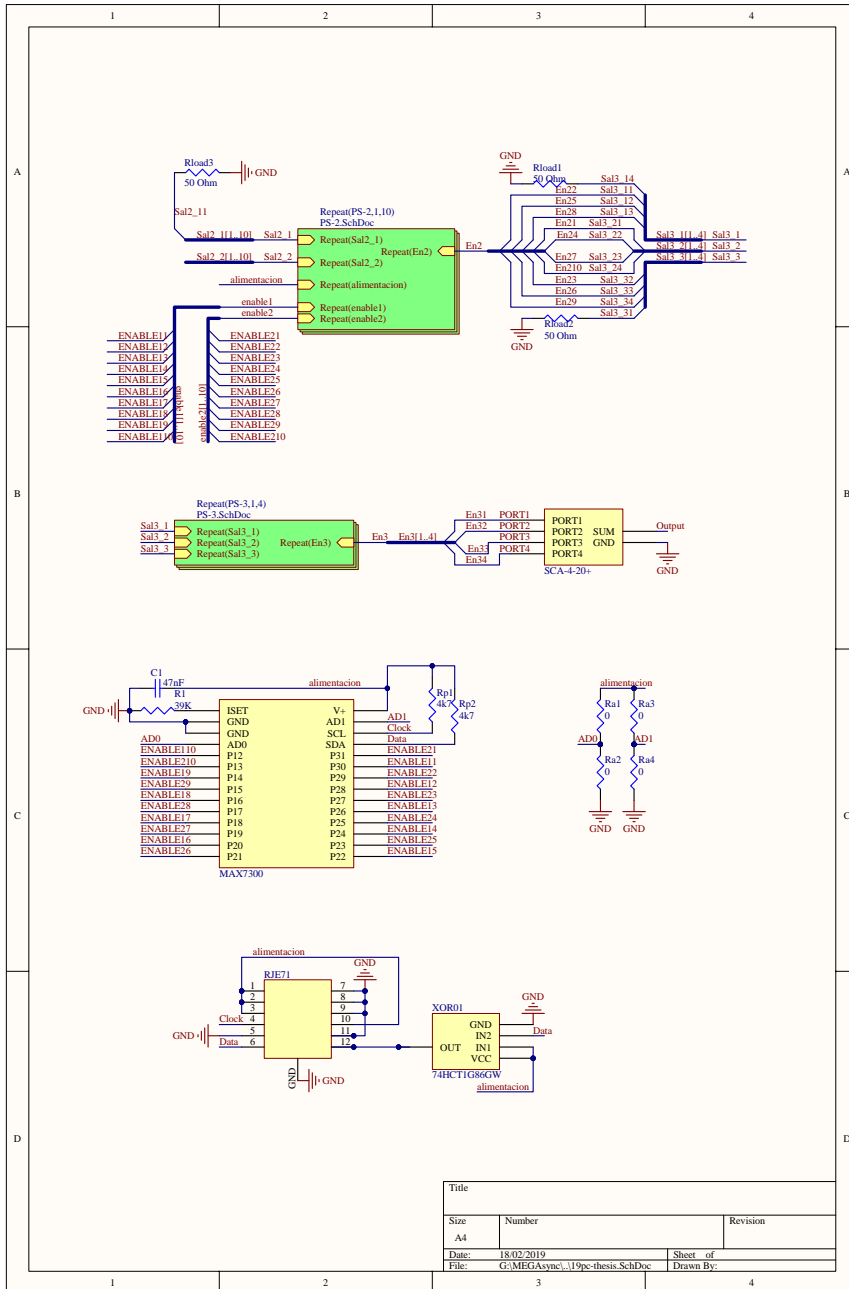
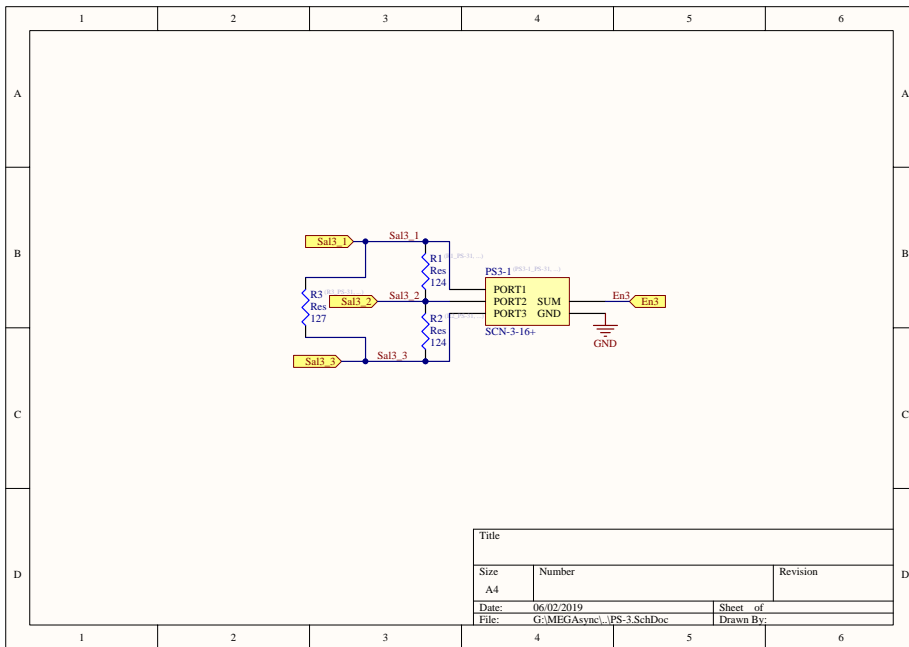
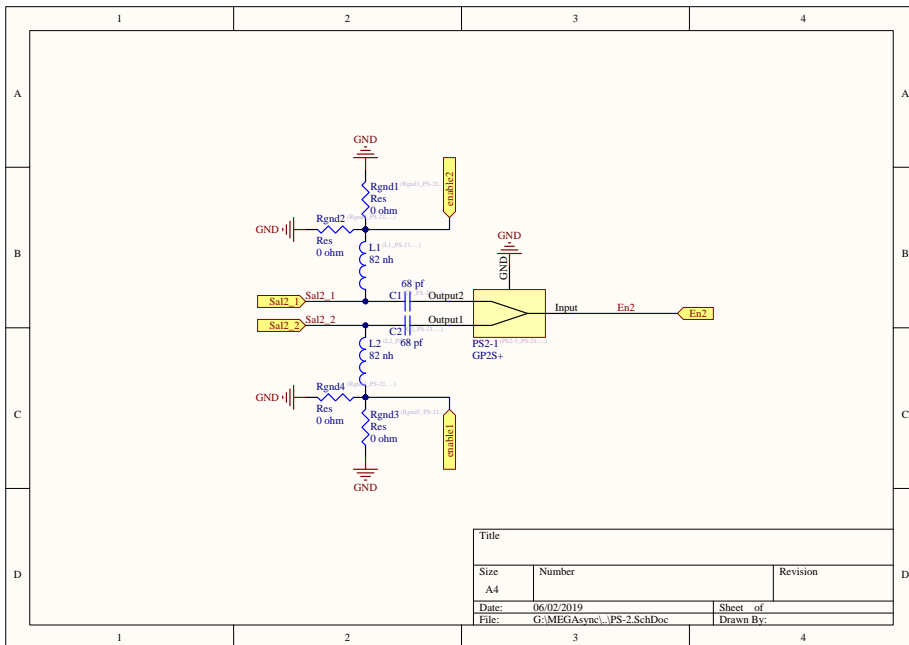


Figure A.11: 19-way power splitter/combiner schematic.

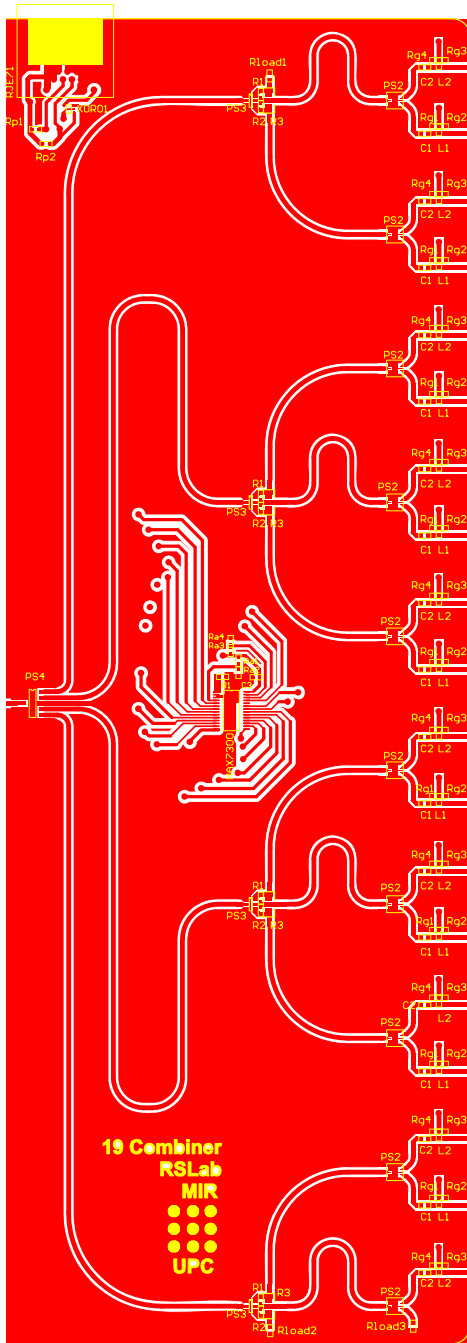


(a)

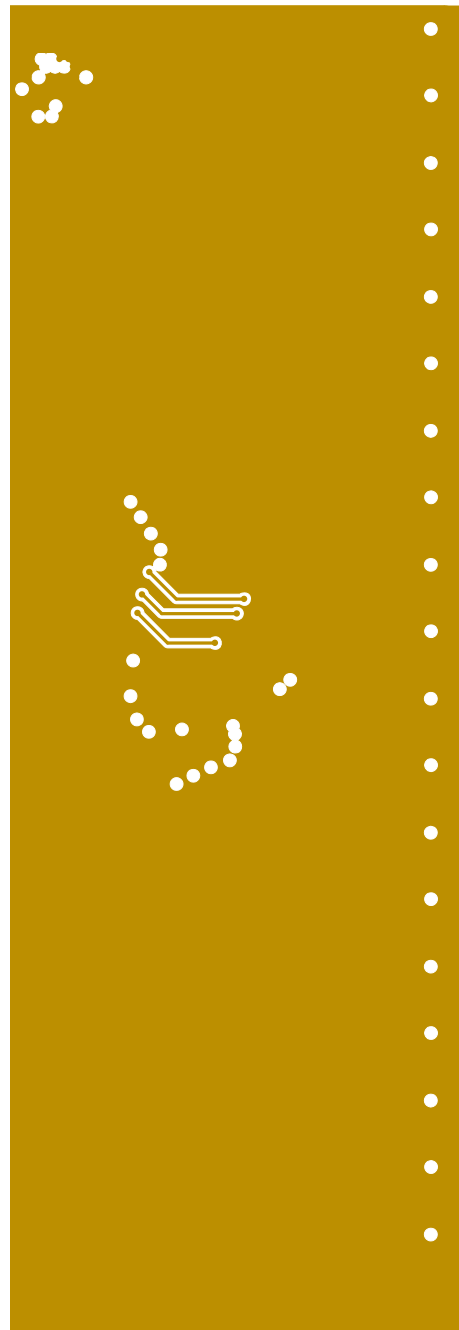


(b)

Figure A.12: Schematic of the a) 3-way, and b) 2-way power splitters/combiner blocks inside Fig. A.11.

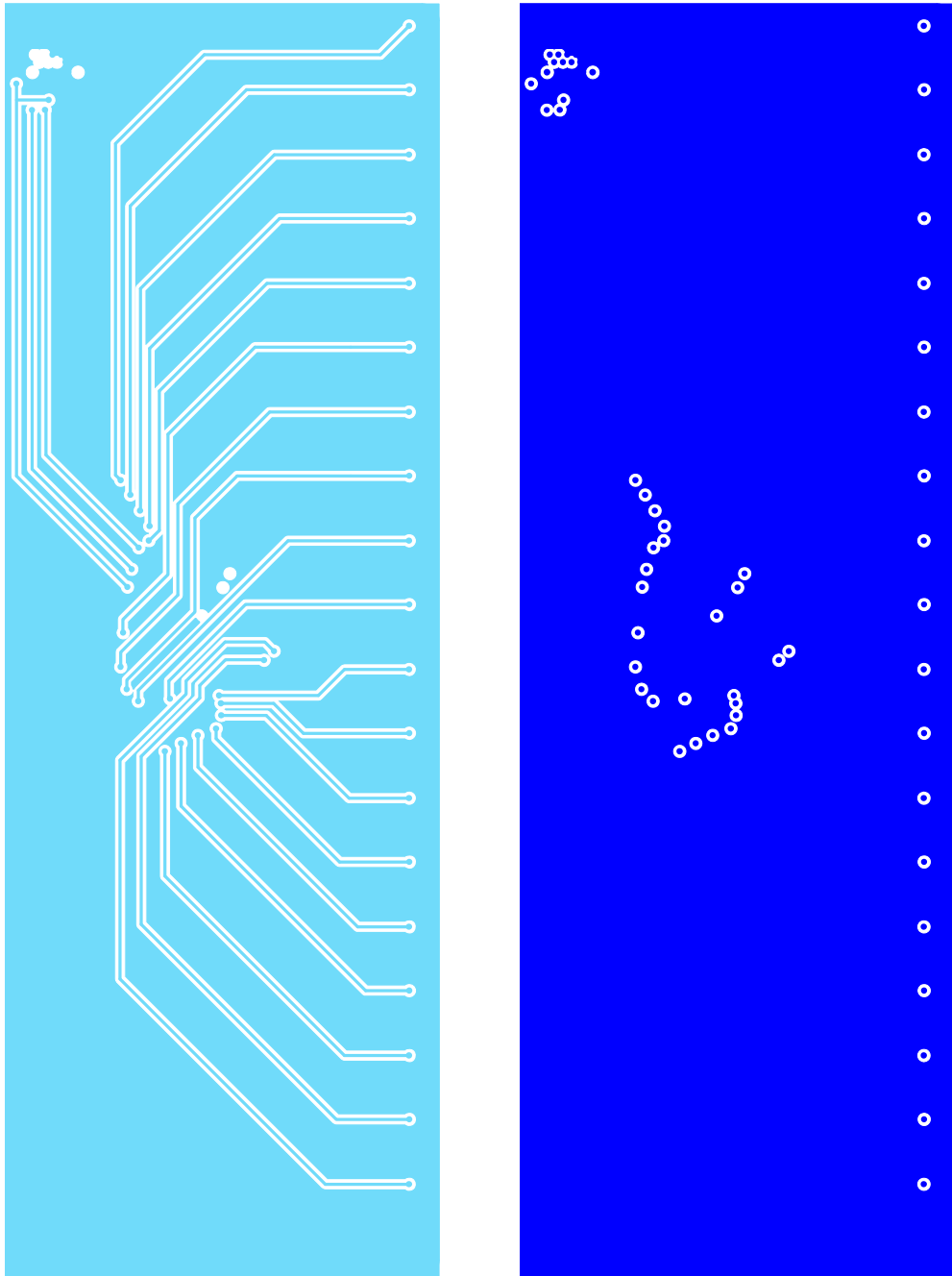


(a)



(b)

Figure A.13: a) Top layer, and b) Mid 1 layer of the 19-way power splitter/combiner PCB. The PCB measures 110x300 mm.



(a)

(b)

Figure A.14: a) Mid 2 layer, and b) Bottom layer of the 19-way power splitter/combiner PCB. The PCB measures 110x300 mm.

A.5 Motherboard

Figure A.16 shows the 3D model of the box that contains the motherboards and that holds the 19 phase shifters and the 4 19-way power combiners. It was designed in 3D because it was used in a Computer Numerical Control (CNC) drilling machine at Universitat Politècnica de Catalunya (UPC) Facilities to manufacture the required parts.

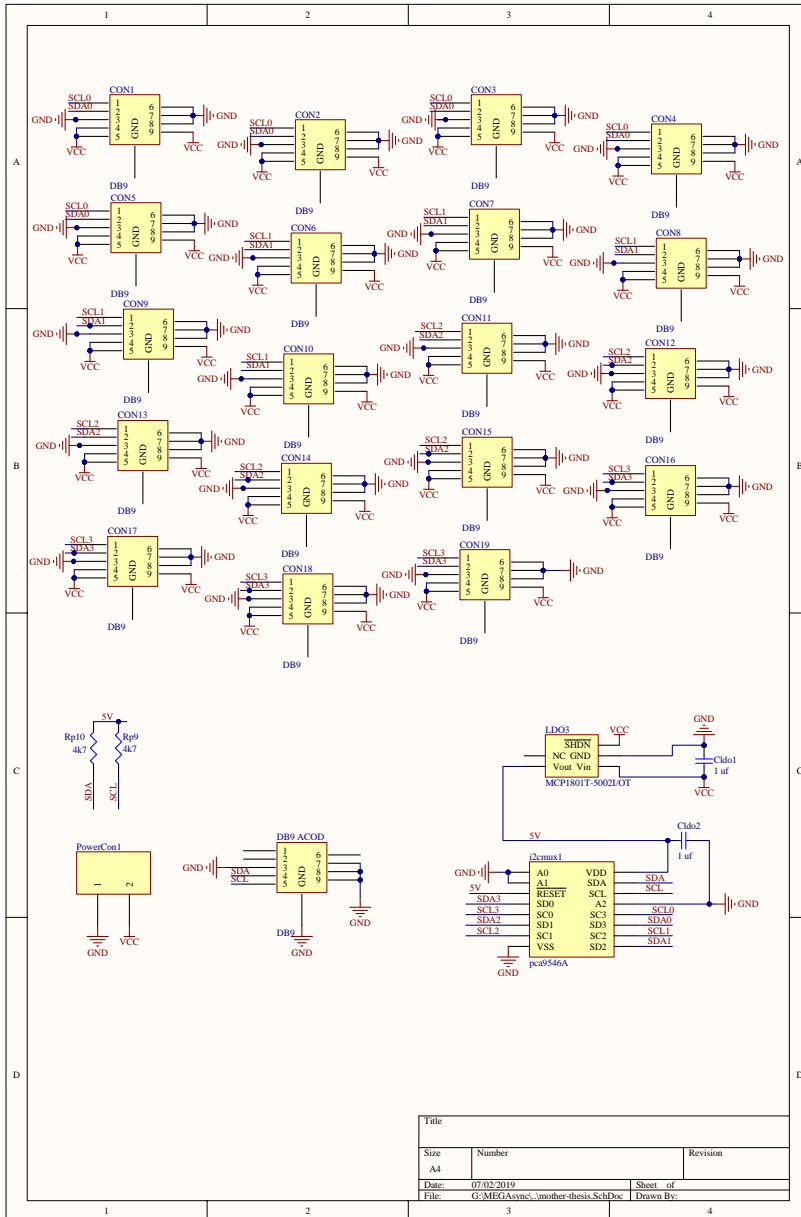


Figure A.16: Motherboard schematic.

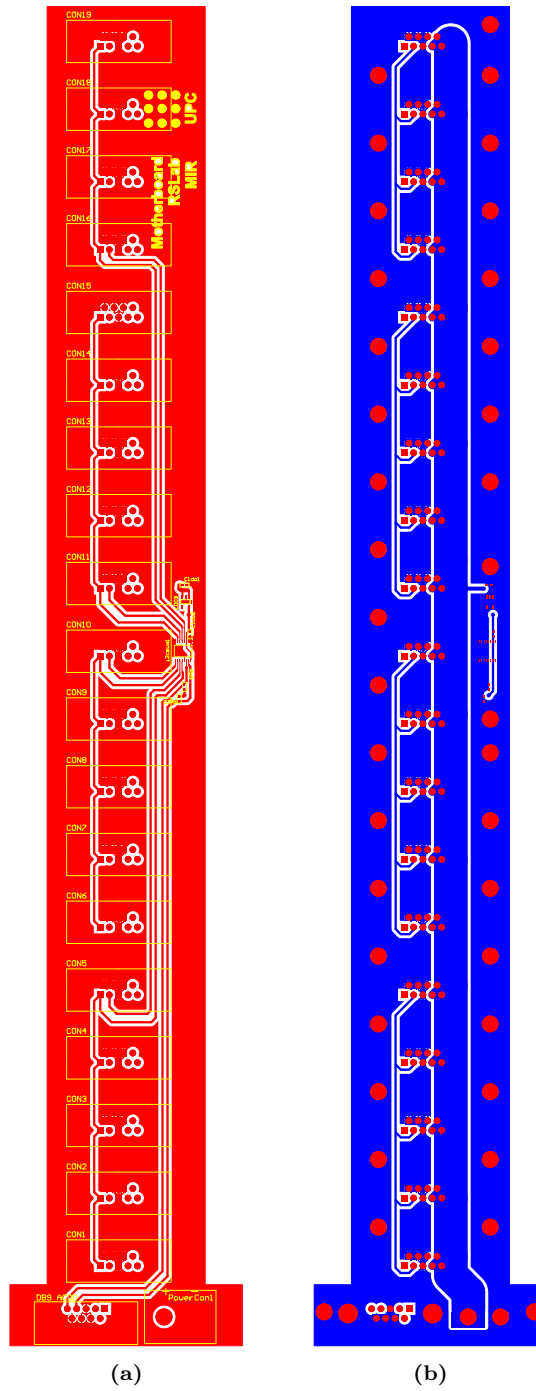


Figure A.17: a) Top layer, and b) Bottom layer of the Motherboard PCBs. The long side measures 395.3 mm. The widest side measures 68.6 mm, while the narrowest one measures 46.6 mm.

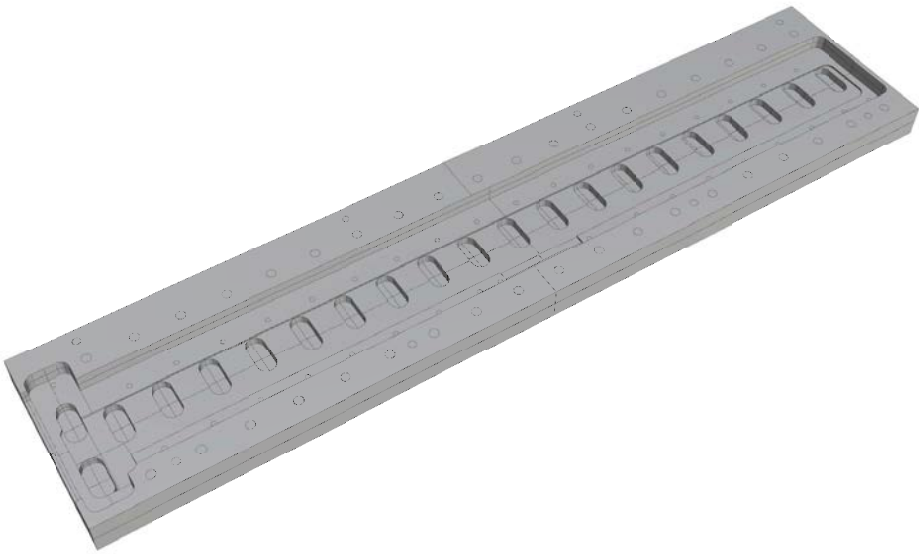


Figure A.18: Motherboard box 3D model. The box measures 400x85x15 mm.

A.6 Calibration System

Figure A.19 shows the schematics of the different parts of the calibration system. The first prototype had all parts in the same PCB, but there was coupling between the different oscillators and mixers, and therefore it was decided to have them in separated enclosures, which also simplified the characterization.

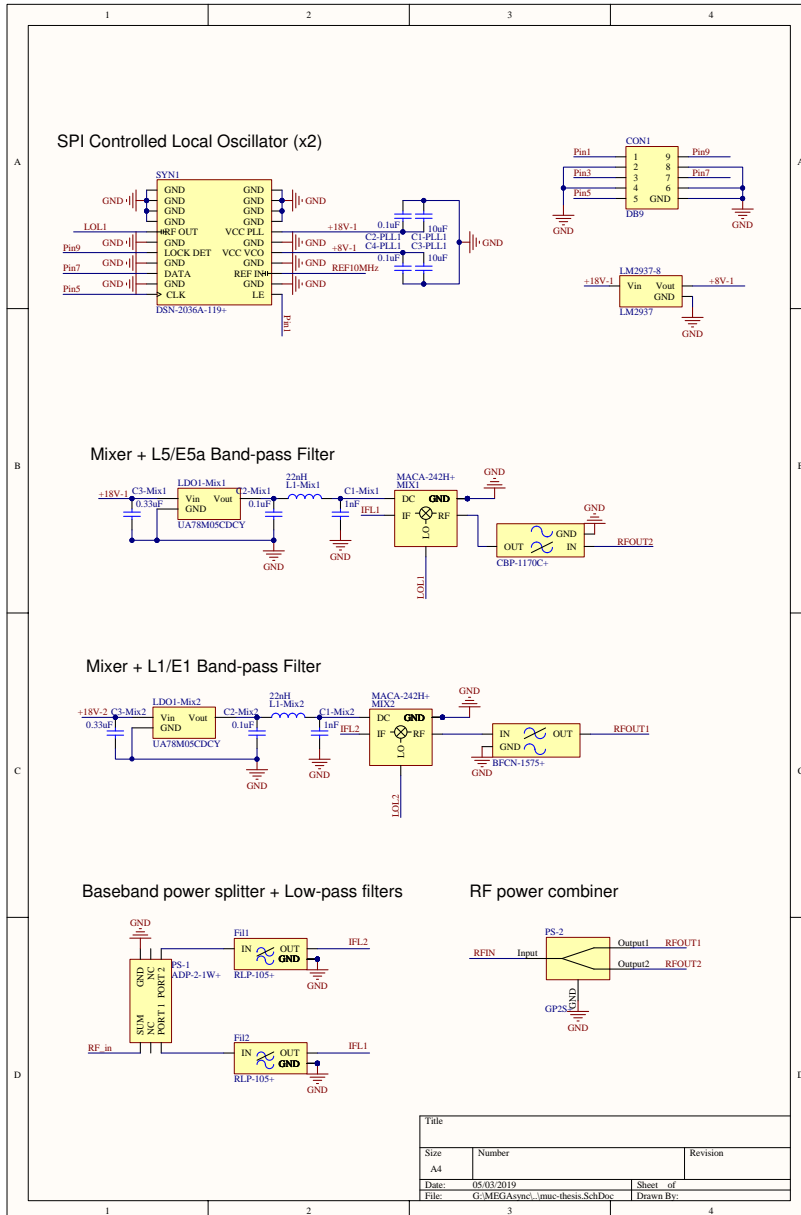


Figure A.19: Calibration system blocks schematics.

The PCB designs can be seen in Fig. A.20. Figs. A.21,A.22,A.23, and A.24 show the CAD design of the enclosures for the base-band power splitter with the low-pass filters, the mixers with the band-pass filters, the SPI controlled oscillators, and the RF power combiners respectively. Last, Fig. A.25 shows how all of the blocks were mounted over the transmitting USRP N210. The orange lines represent SMA to SMA connectors used to connect the different parts. The green line represents the semirigid cable used to connect the N210 output to the baseband power splitter input.

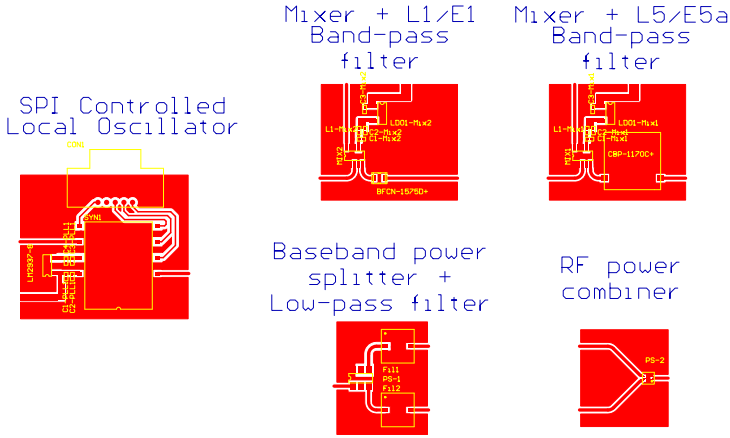


Figure A.20: Calibration system PCB top layers. All bottom layers are ground plane. The Local Oscillator PCB measures 53.6x46 mm, the mixer boards measure 43.6x37 mm, the base-band power splitter measures 29x36 mm, and the RF power combiner measures 28x31 mm.

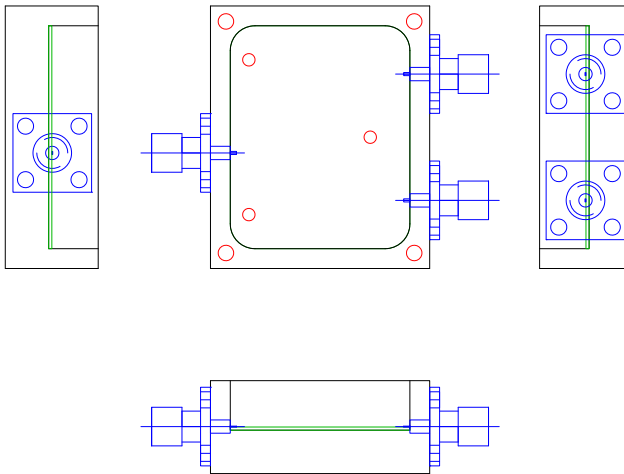


Figure A.21: Base-band power splitter and low-pass filter box CAD design. The box measures 42.4x35.4x15 mm.

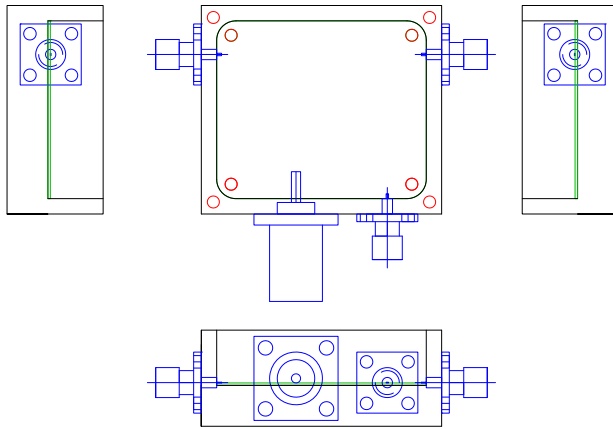


Figure A.22: Mixer and band-pass filter box CAD design. The box measures 43.4x50x15 mm.

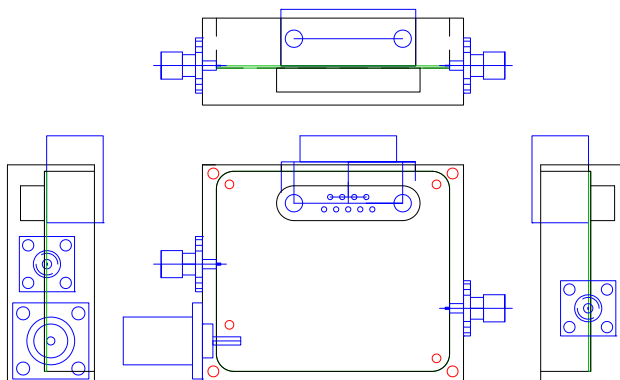


Figure A.23: SPI controlled local oscillators box CAD design. The box measures 50x60x20 mm.

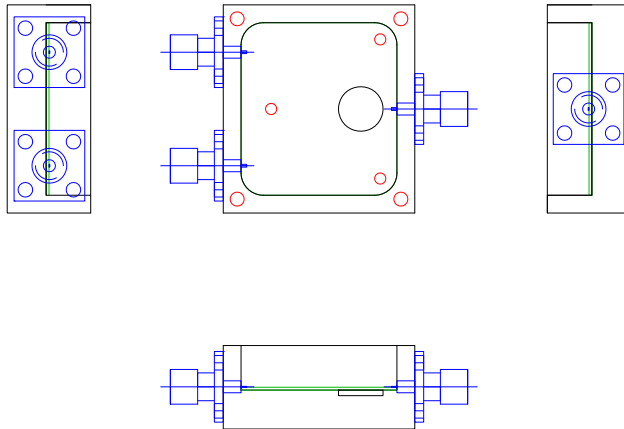


Figure A.24: RF power combiner box CAD design. The box measures 37.4x34.4x15 mm.

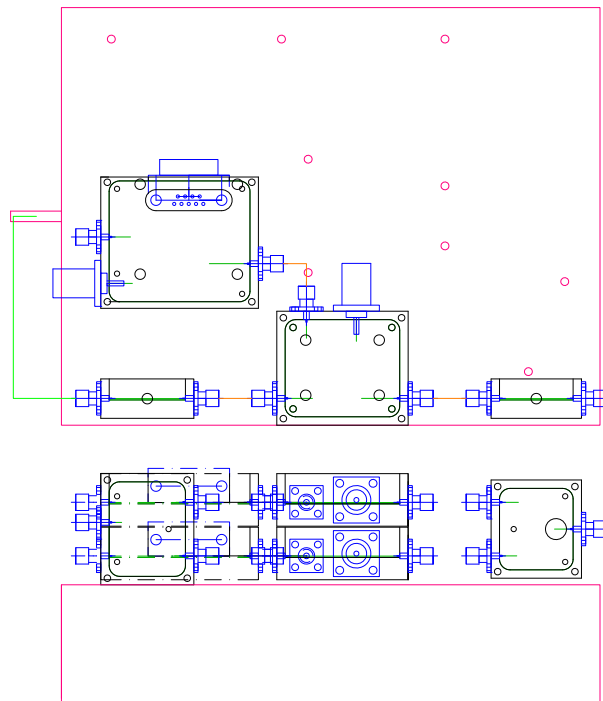


Figure A.25: Calibration system mounted over the USRP N210 CAD design.

A.7 Position and Attitude Determination System

Figures A.26 and A.27 show respectively the schematics, the PCB, and the enclosure CAD design of the power splitter used to feed the auxiliary GNSS antenna and distribute the GNSS signal to the GNSS receiver and the Octoclock. Figures A.28, A.29, and A.30 show the schematic, PCB design, and enclosure CAD design of the ADC sampling board used by the embedded system to sample the analog output of the inclinometer using an SPI ADC.

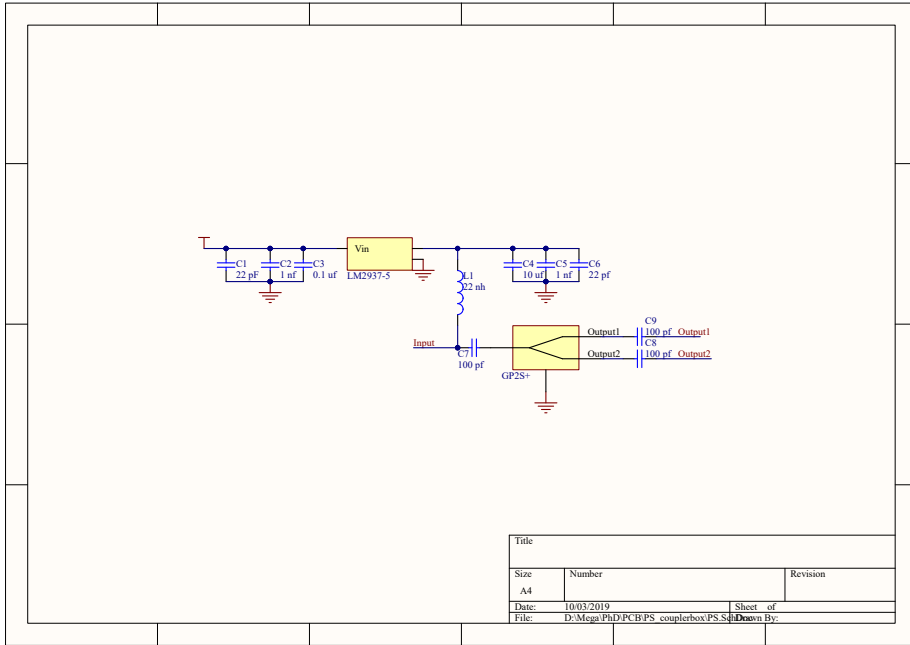


Figure A.26: Schematic of the power splitter used to feed the auxiliary GNSS antenna and distribute the GNSS signal to the GNSS receiver and the Octoclock.

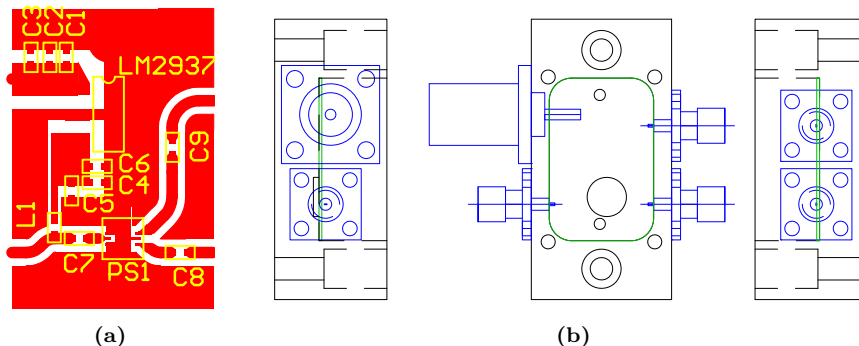


Figure A.27: a) PCB design, and b) enclosure CAD design of the power splitter used to feed the auxiliary GNSS antenna and distribute the GNSS signal to the GNSS receiver and the Octoclock. The PCB measures 18.6x29 mm, and the box 50x25x20 mm.

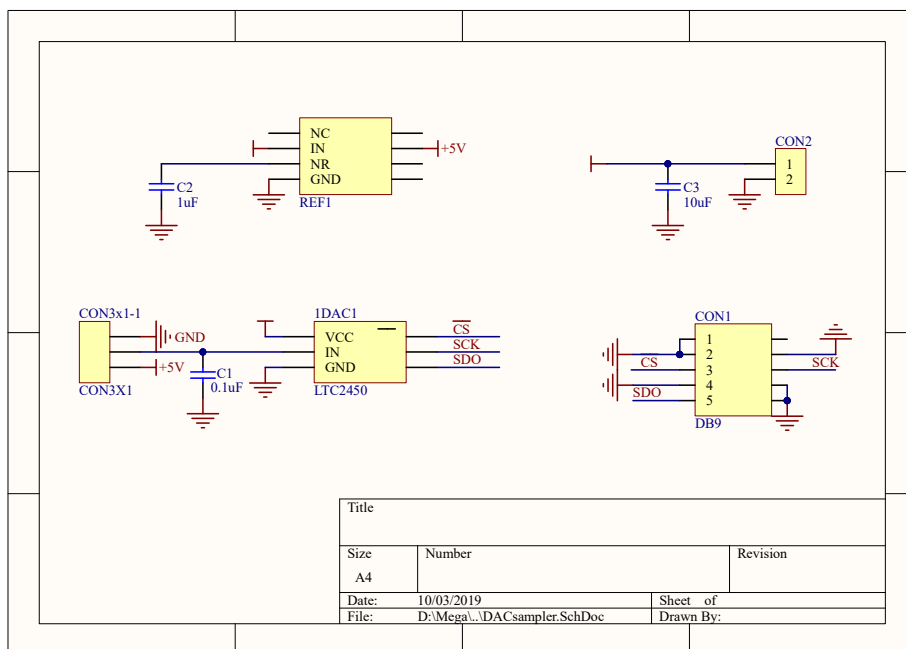


Figure A.28: DAC sampling board schematic.

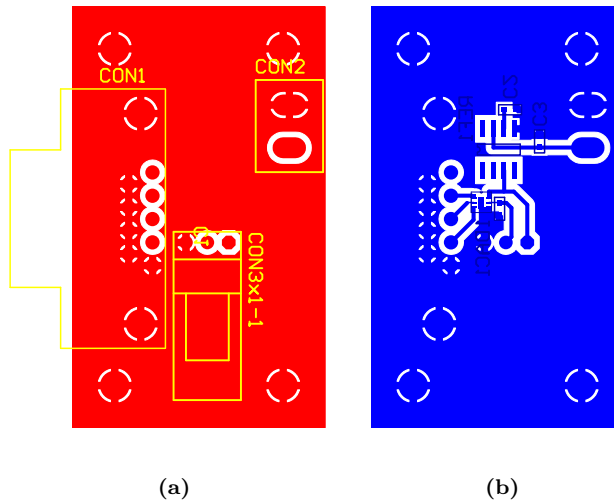


Figure A.29: a) Top, and b) bottom layer of the PCB design of the ADC sampling board. The PCB measures 30x50 mm.

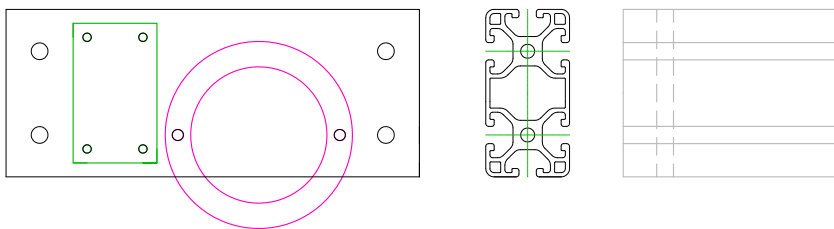


Figure A.30: CAD design of the aluminum slide used to attach the inclinometer and the ADC sampling board to one of the array sides. The slide measures 148x60x6 mm.

A.8 Embedded System

Figures A.31 and A.32 show the schematic and the PCB design of the expansion board.

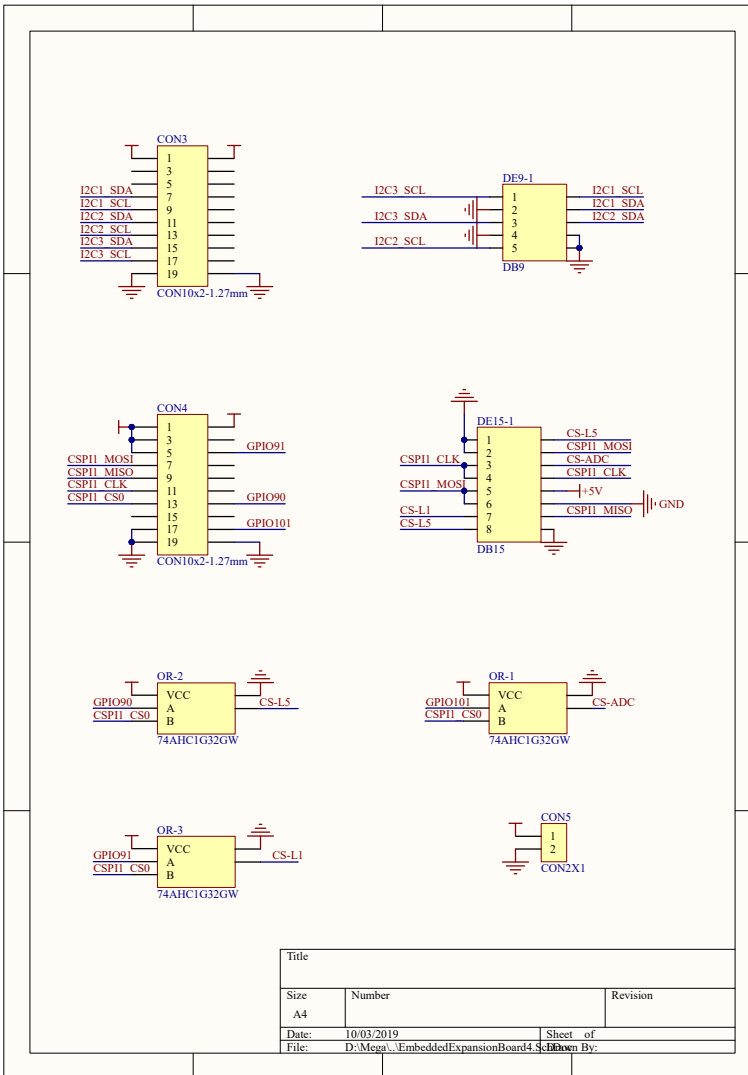


Figure A.31: Expansion board schematic.

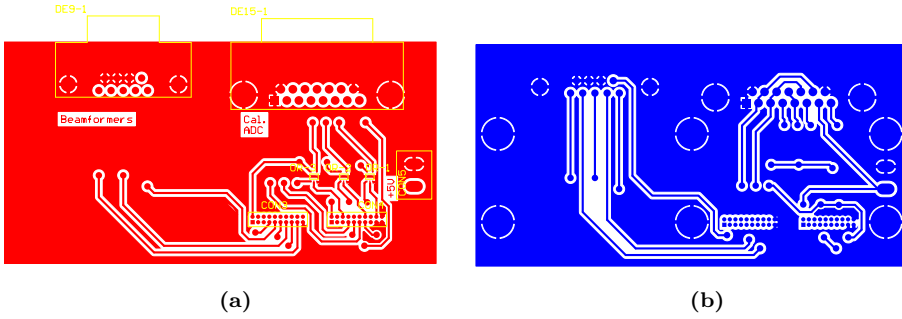


Figure A.32: a) Top layer, and b) Bottom layer of the expansion board PCB. The PCB measures 98x50 mm.

A.9 Extra RF Amplifiers

Figures A.33 and A.34 show the schematic and the PCB design of the extra RF amplifiers used in the down-looking RF channels before the USRPs. The CAD of the two manufactured boxes is shown in Fig. A.35, each one of which has two separate compartments to hold two PCBs inside.

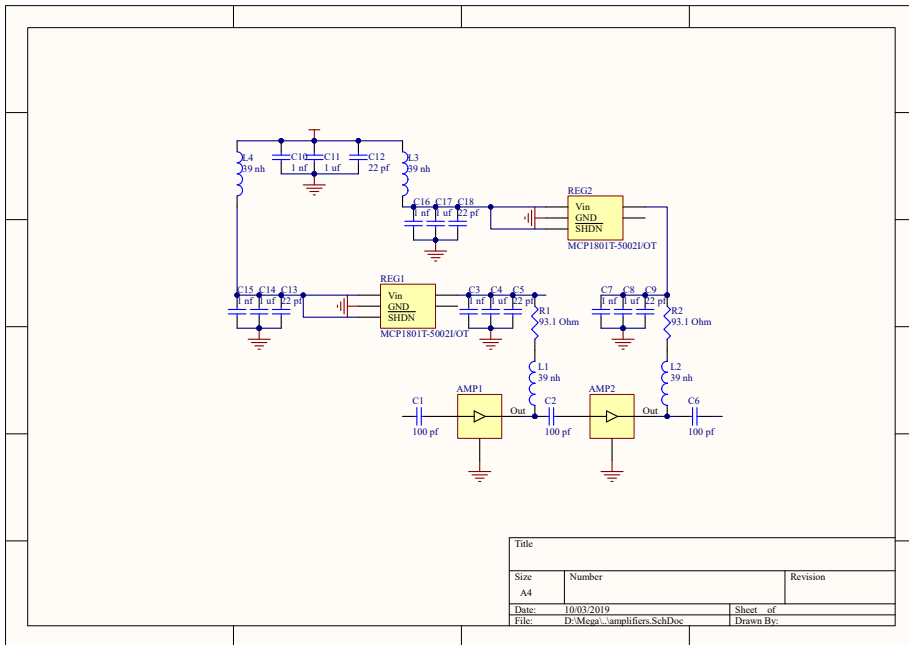


Figure A.33: Extra RF amplifiers schematic.

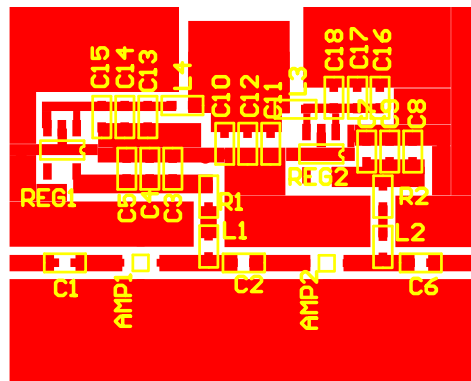


Figure A.34: Extra RF amplifiers PCB top layer. The bottom layer is ground plane. The PCB measures 30.6x25 mm.

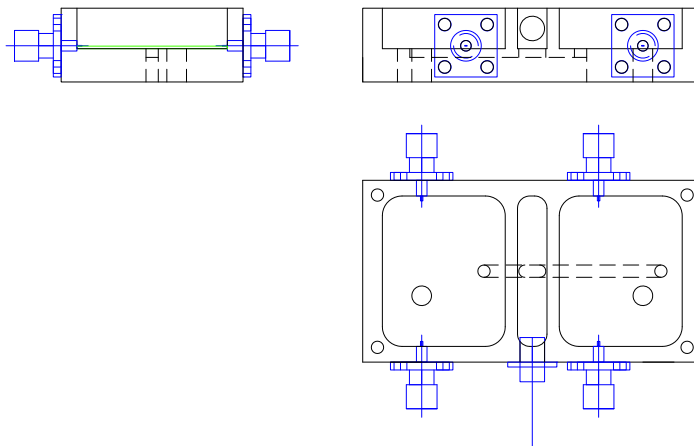


Figure A.35: Extra RF Amplifiers box CAD design. The box measures 66x37x15 mm.

B

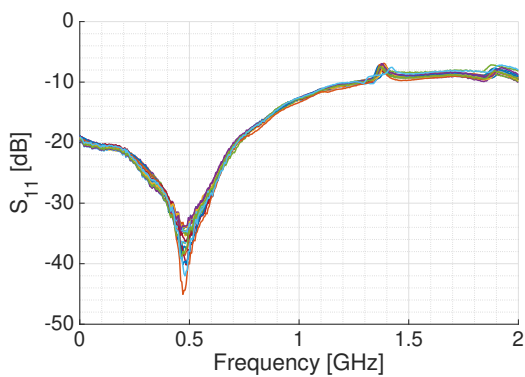
Appendix B

Subsystems Characterization

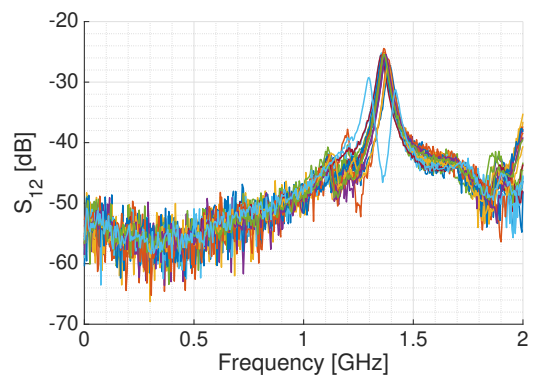
This appendix shows the measured S-Parameters of all subsystems described in Chapter 5.

B.1 RF Front-ends

This section shows the S-Parameters of the 19 RF Front-ends in the up-looking array (see Fig. B.1), and the down-looking array (see Fig. B.2).



(a)



(b)

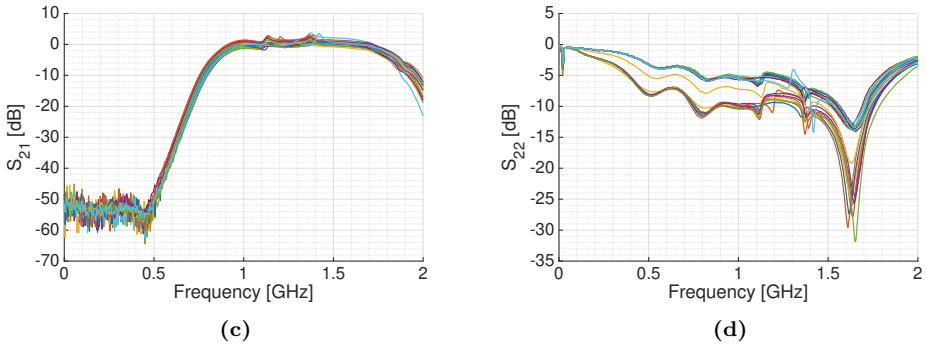


Figure B.1: S-Parameters of the 19 RF Front-ends of the up-looking array.

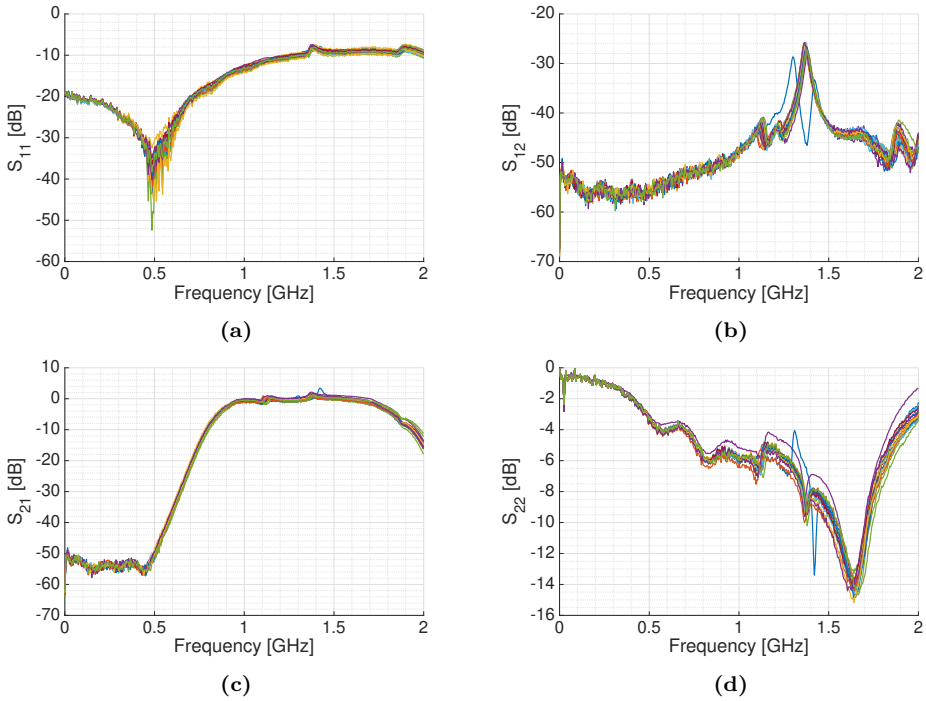


Figure B.2: S-Parameters of the 19 RF Front-ends of the down-looking array.

B.2 19-way Power Combiner

Figure B.3 shows the transmission S-parameter of one of the manufactured 19-way Power combiners, Fig. B.4 shows the input and output matching, and Fig. B.5 shows the coupling between output ports. The rest of the manufactured power combiners were measured to ensure that they worked as expected, but the S-Parameters were not stored.

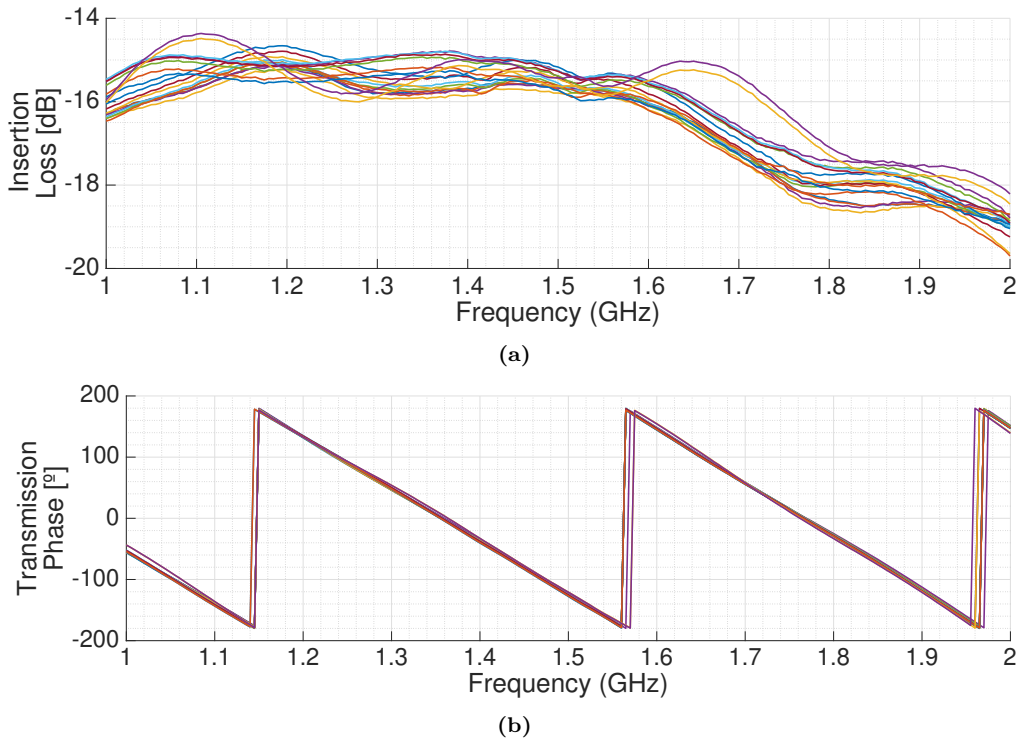


Figure B.3: Measured a) gain, and b) phase of the transmission S-Parameters of a 19-way Power combiner.

B.3 Beamformer Integration

This section shows the measured S-Parameters for the two beamformer blocks. Figure B.6 shows the matching of the 19 inputs. Figure B.7 shows the matching of the 4 outputs of the beamformer block, one for each beam and band. Figures B.8 to B.11 show the transfer function for each particular beam and band. Each graph includes the transfer function obtained when a pair of values $\{I_i = 1, Q_i = 0\}$ was set, and also the transfer function when a pair of values $\{I_i = 0, Q_i = 1\}$ is set.

Figures B.12 and B.13 show the gain in the I and Q component at L1/E1 and E5/E5A in the beamformer 1 and 2 respectively. Figures B.14 and B.15 show the gain difference between the I and Q component at L1/E1 and E5/E5A in the beamformer 1 and 2 respectively. Figures B.16 and B.17 show the phase of I component at L1/E1 and E5/E5A in the beamformer 1 and 2 respectively. Figures B.18 and B.19 show the phase difference between the I and Q component at L1/E1 and E5/E5A in the beamformer 1 and 2 respectively.

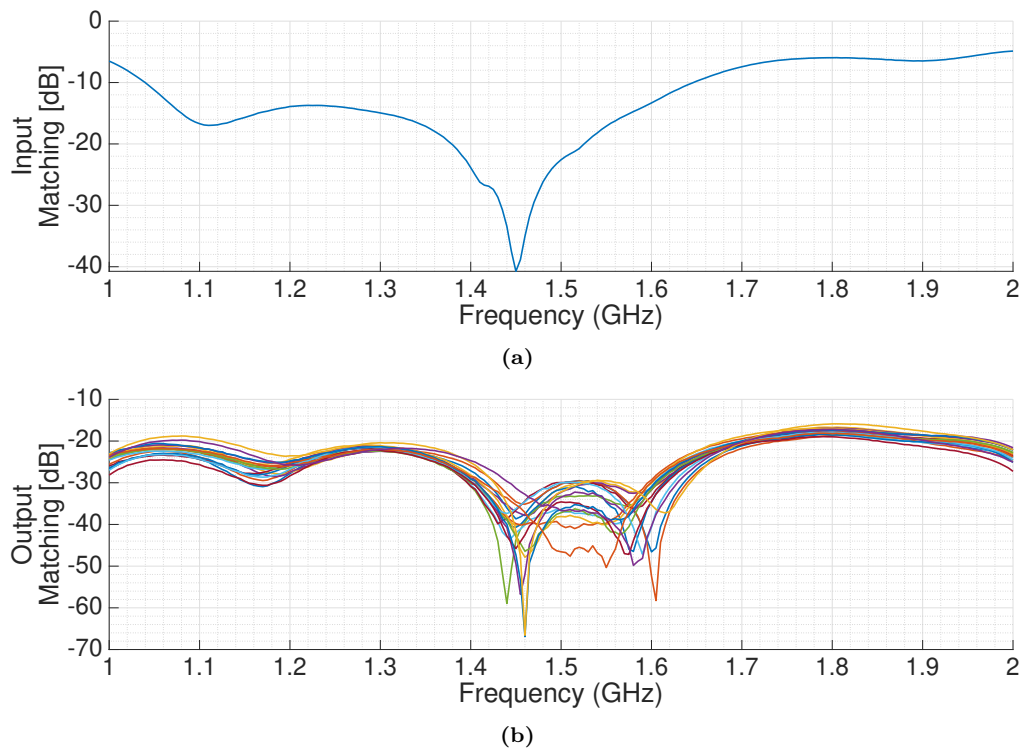


Figure B.4: Measured a) input and b) output matching of a 19-way Power combiner.

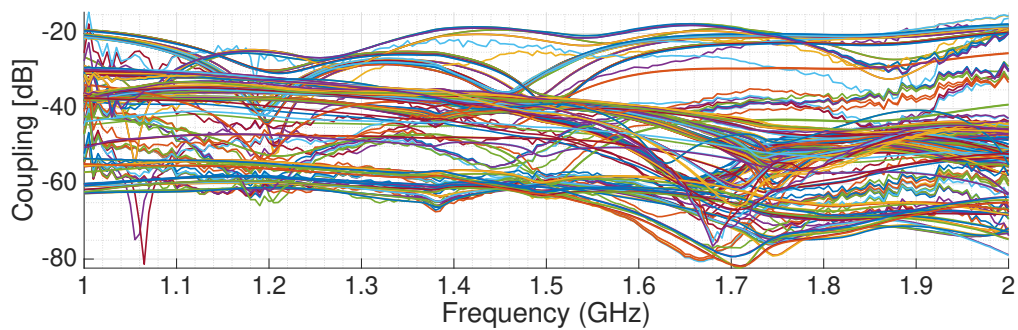


Figure B.5: Measured coupling between ports in of one of the 19-way Power combiners.

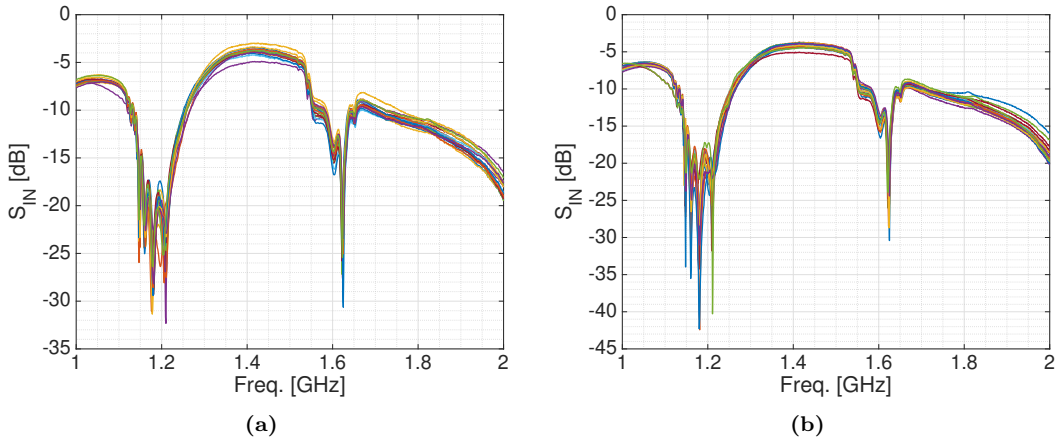


Figure B.6: a) Beamformer 1, and b) beamformer 2 measured input matching.

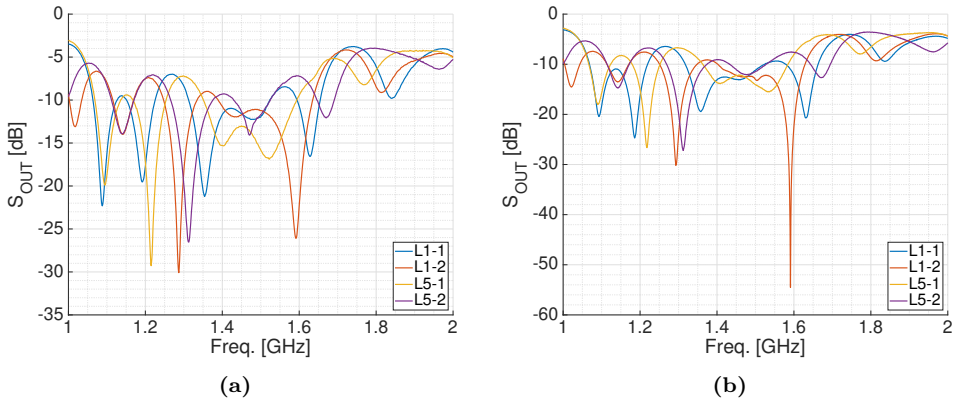


Figure B.7: a) Beamformer 1, and b) beamformer 2 measured output matching.

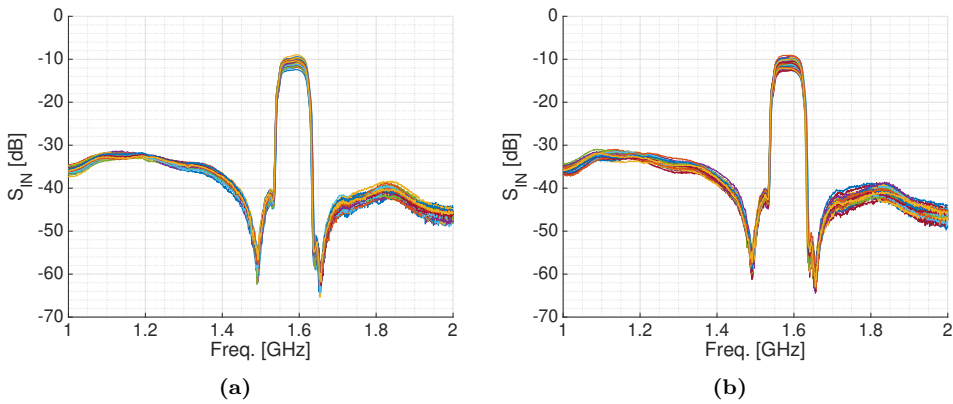


Figure B.8: a) Beamformer 1, and b) beamformer 2 measured transfer function in beam L1-1 for $\{I_i = 1, Q_i = 0\}$ and $\{I_i = 0, Q_i = 1\}$.

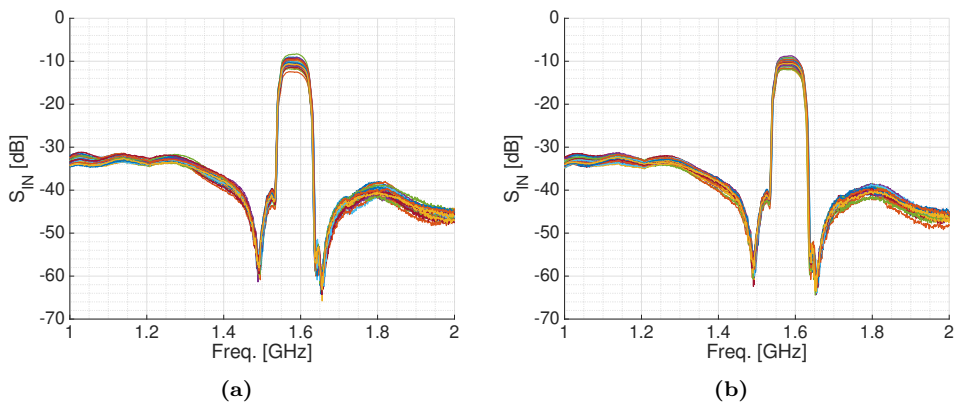


Figure B.9: a) Beamformer 1, and b) beamformer 2 measured transfer function in beam L1-2 for $\{I_i = 1, Q_i = 0\}$ and $\{I_i = 0, Q_i = 1\}$.

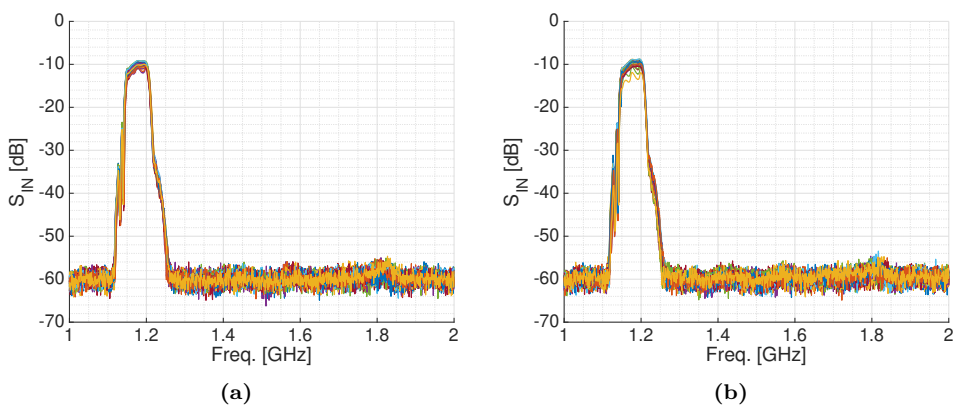


Figure B.10: a) Beamformer 1, and b) beamformer 2 measured transfer function in beam L5-1 for $\{I_i = 1, Q_i = 0\}$ and $\{I_i = 0, Q_i = 1\}$.

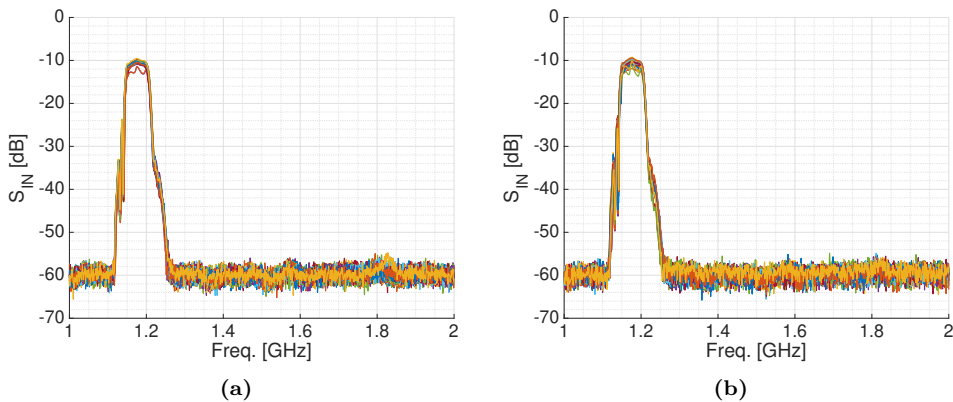


Figure B.11: a) Beamformer 1, and b) beamformer 2 measured transfer function in beam L5-2 for $\{I_i = 1, Q_i = 0\}$ and $\{I_i = 0, Q_i = 1\}$.

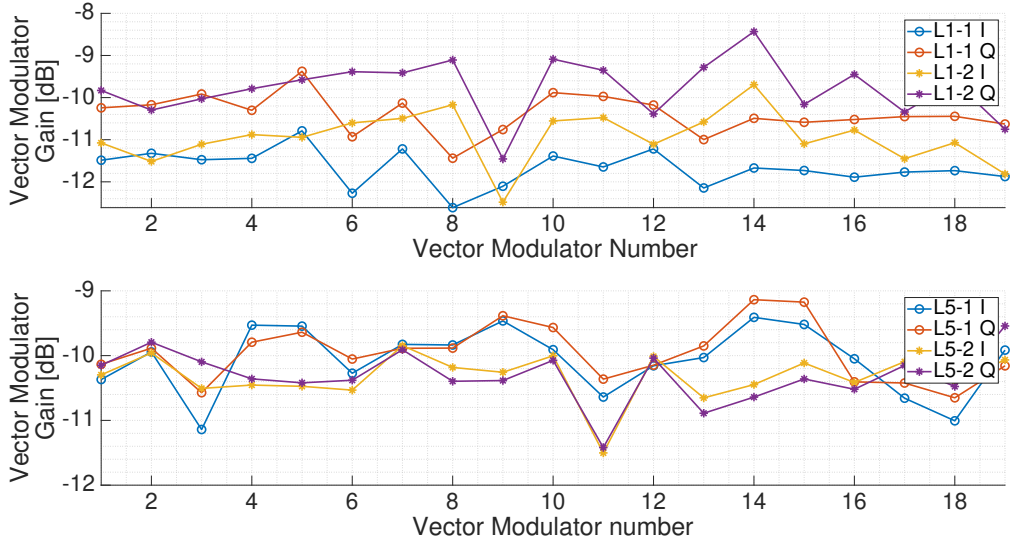


Figure B.12: Beamformer 1 measured I and Q gain.

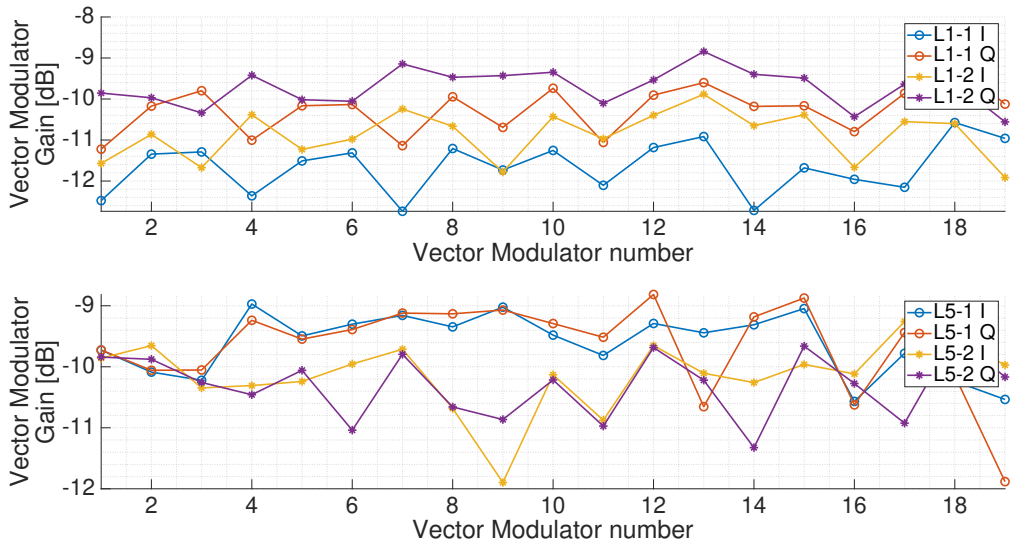


Figure B.13: Beamformer 2 measured I and Q gain.

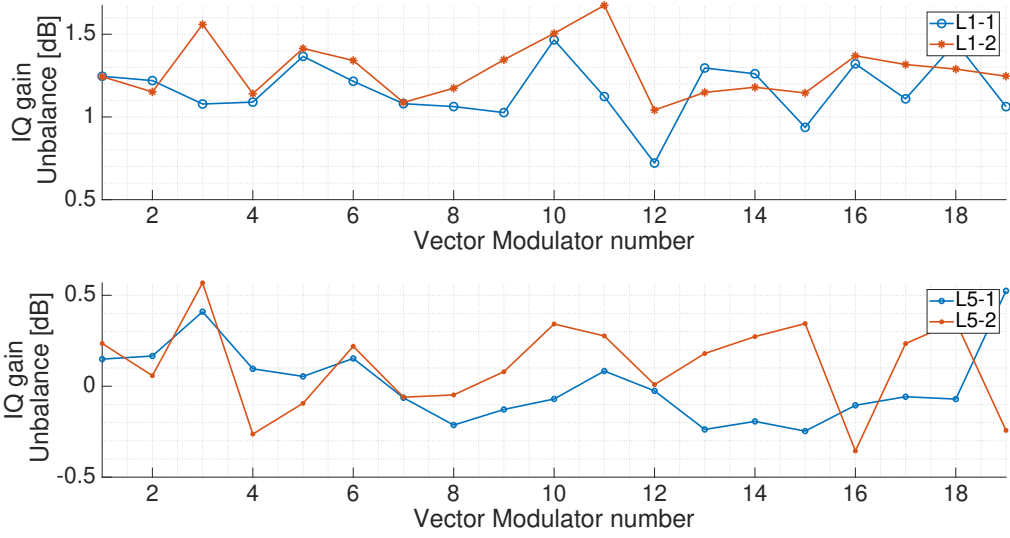


Figure B.14: Beamformer 1 measured gain unbalance.

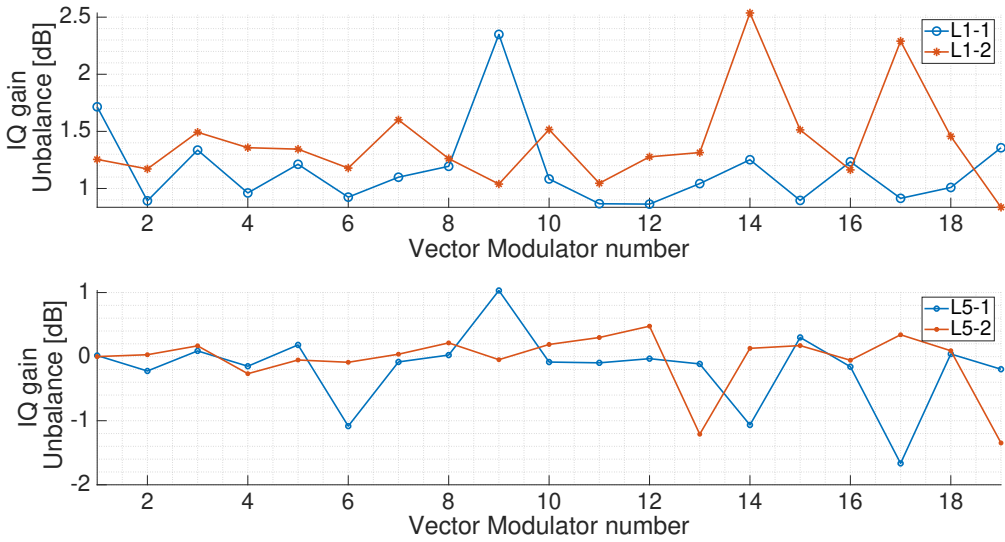


Figure B.15: Beamformer 2 measured gain unbalance.

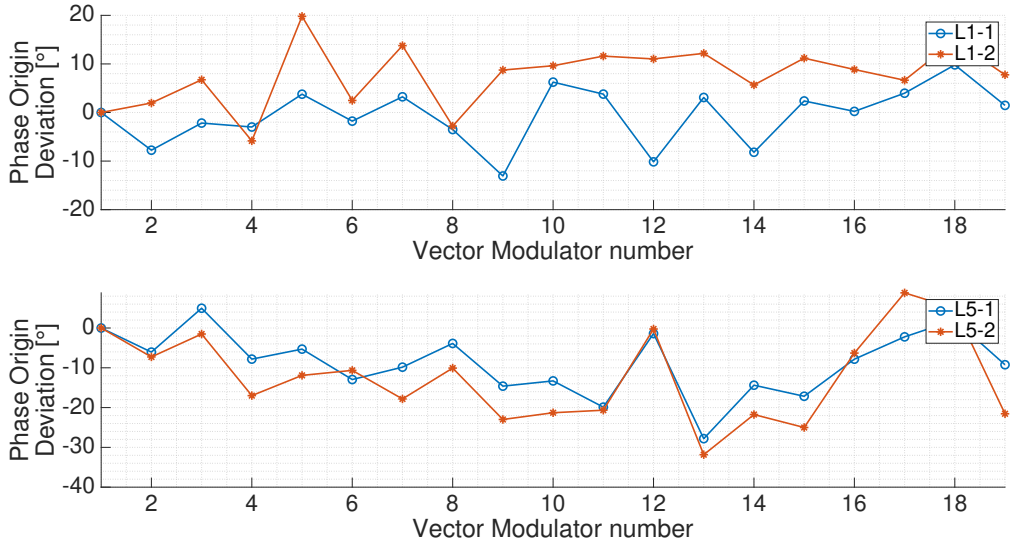


Figure B.16: Beamformer 1 measured I component phase.

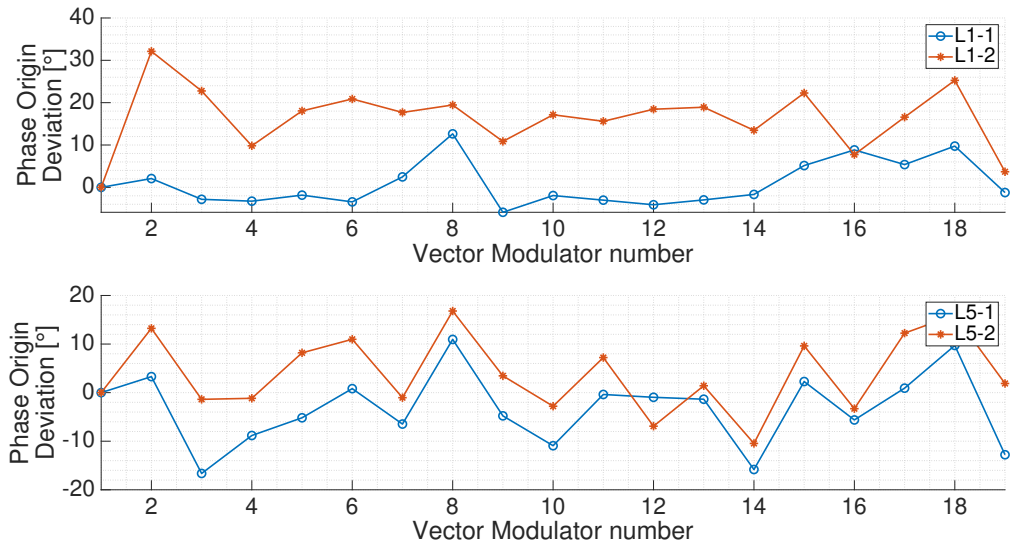


Figure B.17: Beamformer 2 measured I component phase.

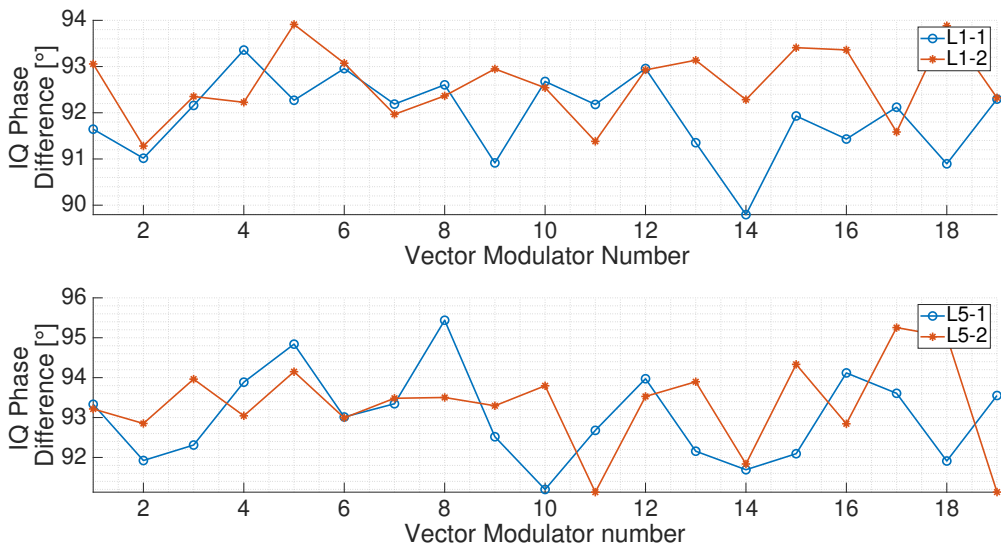


Figure B.18: Beamformer 1 measured phase unbalance.

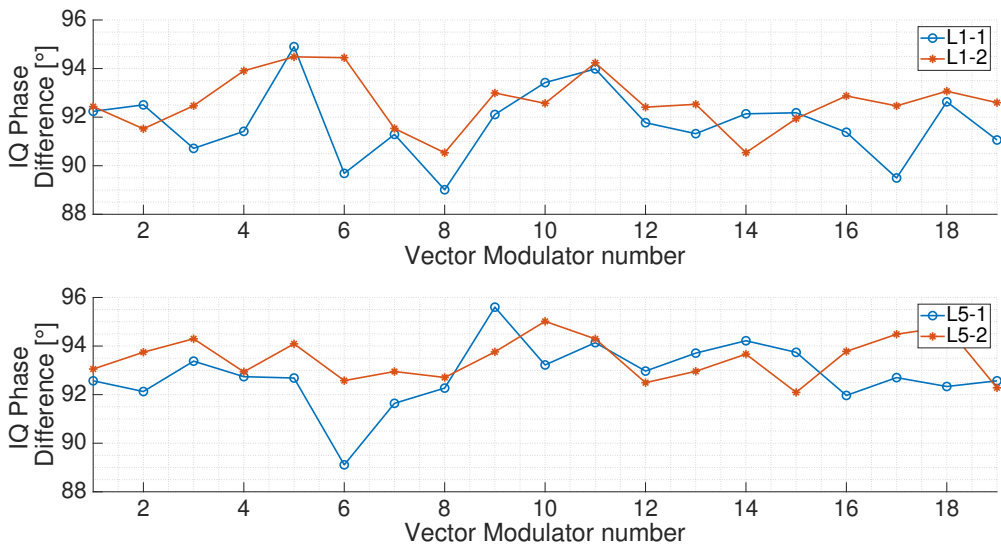


Figure B.19: Beamformer 2 measured phase unbalance.

C

Appendix C

PLMR and Cabin Specifications for the MIR Instrument Design

This appendix includes a cabin sketch (Fig. C.1), and the PLMR size specifications (Fig. C.2) used to design the arrays, the radome, and the instrument rack.

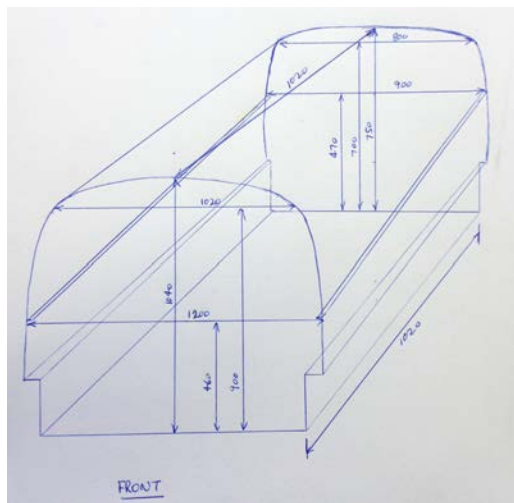



Figure C.1: Cabin sketch used to design the up-looking array and the rack instrument (from [1]).

		PLMR SYSTEM		
Document description:	Date:	Revision:	Page:	
Technical Report	17Feb05	B	31 of 38	

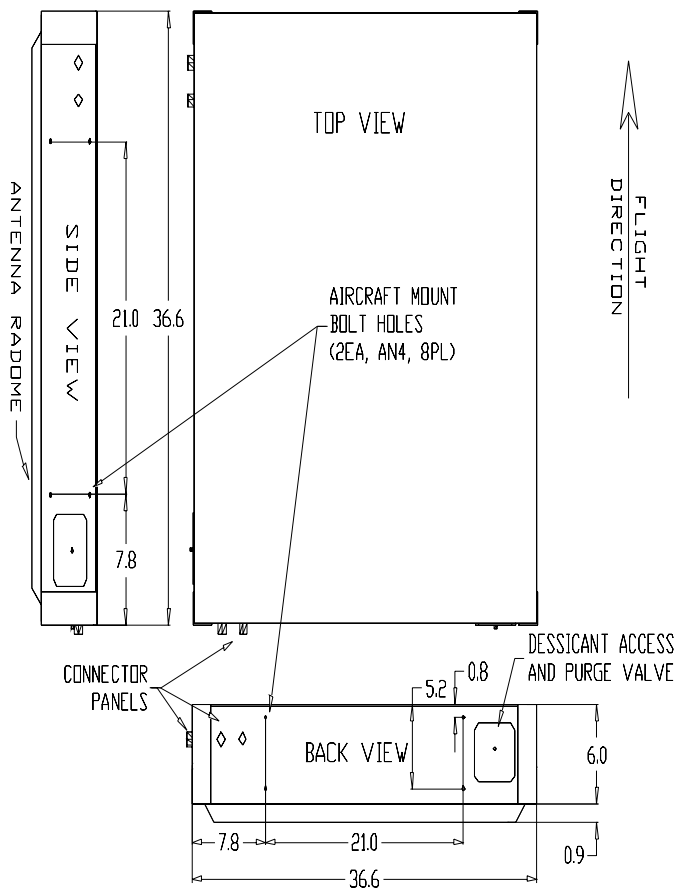


Figure C.2: PLMR specifications used to design the down-looking array. Dimensions are in inches.

D

Appendix D

Integration CADs

This appendix includes some CAD designs of the integration process of the arrays, beamformers, and the MIR rack.

D.1 Arrays

Figure D.1 shows the back view of the CAD design of the up-looking array. Orange represents the aluminum pieces, such as the aluminum profile or some pieces manufactured to hold the calibration power combiner from the structure. In red, the antennas. In purple, the holes for the nylon screws that hold the antennas. In black, the RF Front-ends (in the middle of the antennas) and the calibration power splitter (at the top right corner).

Figure D.2 shows the CAD design of the up-looking antenna ground plane. In orange, D4 holes. In red, D2.5 holes for conical threads. In grey, D3 holes to connect the antennas and the Front-ends using a semirigid SMA cable.

Figure D.3 shows the CAD design of the down-looking array. Orange represents the aluminum pieces, such as the aluminum profile or some pieces manufactured to hold the calibration power combiner from the structure. In red, the antennas and the panel that covers the back side of the array. In purple, the holes for the nylon screws that hold the antennas. In black, the RF Front-ends (in the middle of the antennas) and the calibration power splitter (at the bottom left corner). Note the side pieces of the array that are used to hold the array from the airplane.

Figure D.4 shows the CAD design of the down-looking antenna ground plane. In orange, D4 holes. In red, D2.5 or D4 holes for conical threads. In grey, D3 or D4 holes to connect the antennas and the Front-ends using a semirigid sma cable.

Figure D.5 shows the CAD design of the down-looking radome, and Fig. D.5 shows a

zoom in the side. The material used to manufacture was a custom 3 layer panel made of a 1 mm aluminum plate (bottom), a 38.5 mm extruded polystyrene foam layer (mid), and a 2 mm fiberglass layer (top). Once the panel was ready, it was carved using a drilling machine. The pink holes are the ones used to screw the radome to the ground plane. The dashed lines are the holes where the antennas are allocated. Once the array was manufactured, an adhesive vinyl sheet was stuck to the array to avoid the side wind from stripping off any of the material layers, mainly the top fiberglass one.

Figure D.7 shows the CAD design of the holes in one of the sides of the arrays to pass through the SMA cables and the slide where the SMA panel connectors are hold. Figure D.8 shows the 3D model used in the CNC drilling machine to manufacture the two required slides.

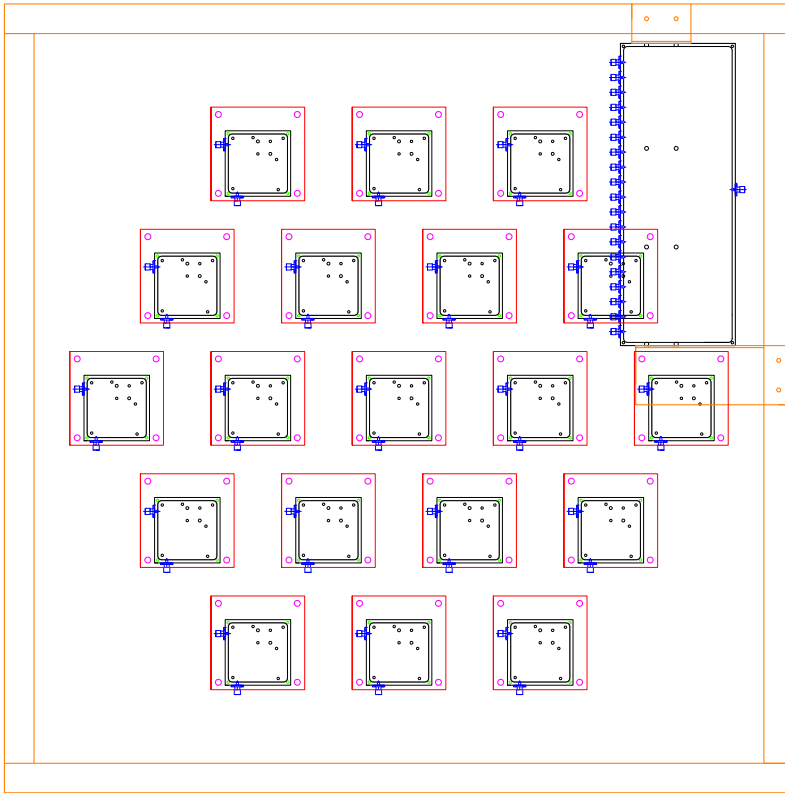


Figure D.1: Back view of CAD Design of the up-looking array with the calibration power splitter attached. The array measures 800x800x60 mm.

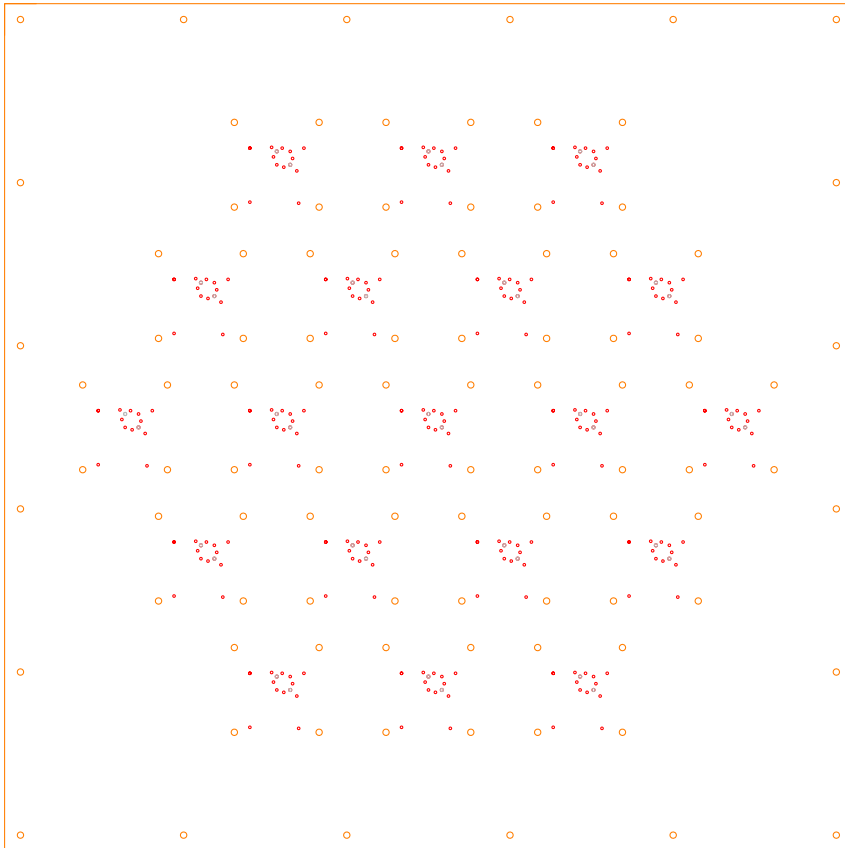


Figure D.2: CAD design ground plane of the up-looking array. The array measures 800x800x60 mm.

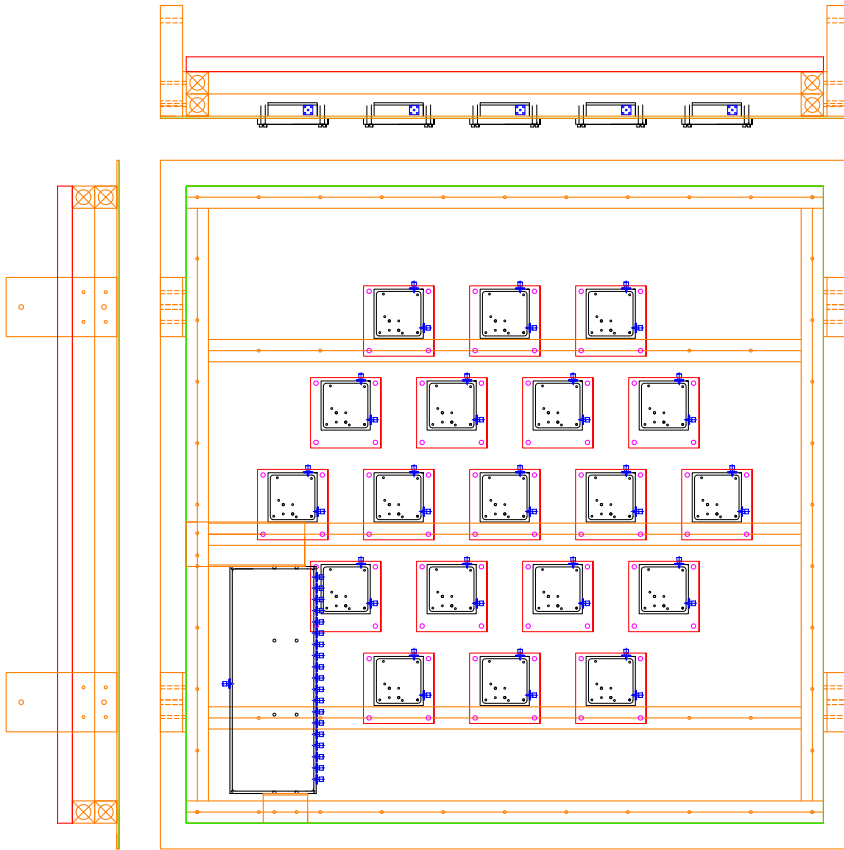


Figure D.3: Back view of CAD Design of the down-looking array and the support holds. The array measures 929.6x929.6x60 mm.

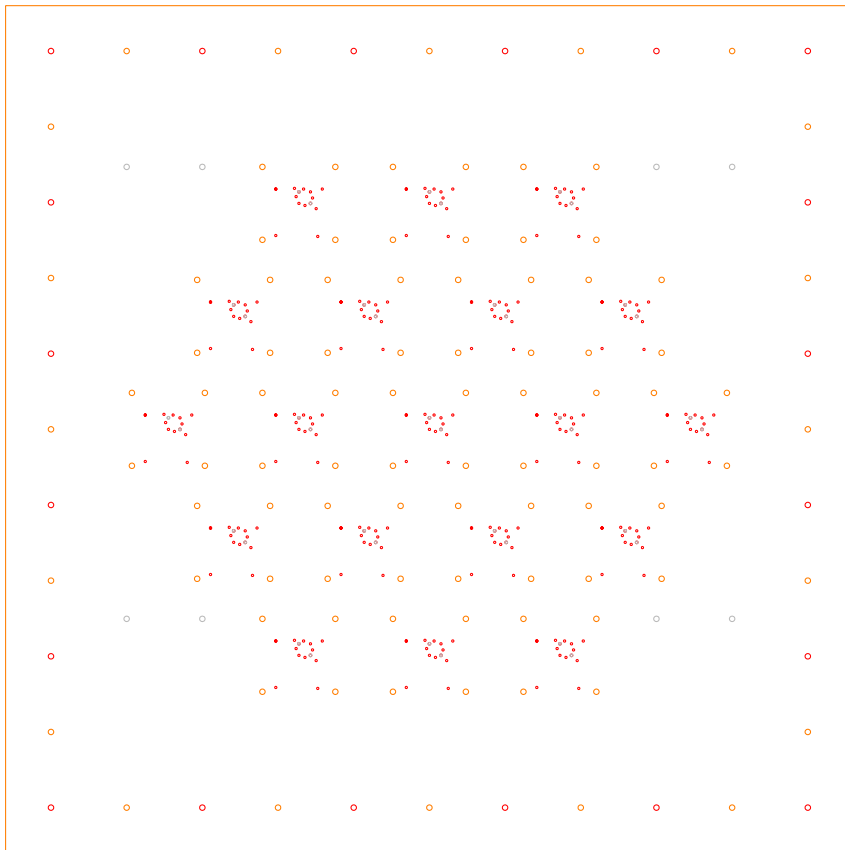


Figure D.4: CAD design ground plane of the down-looking array. The array measures 929.64x929.64x60 mm.

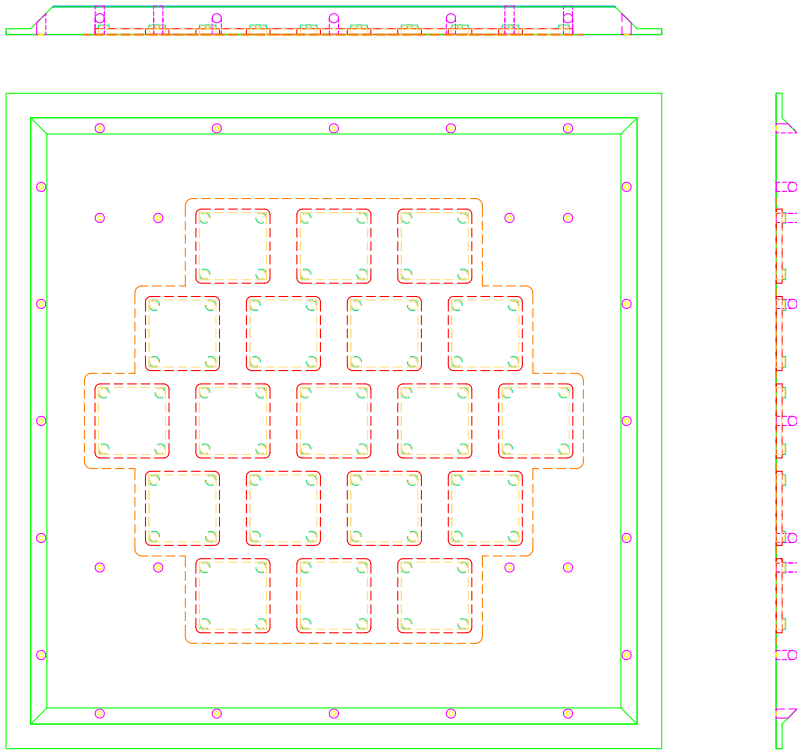


Figure D.5: Designed radome to cover the down-looking array. The radome measures 929.64x929.64x41.2 mm.

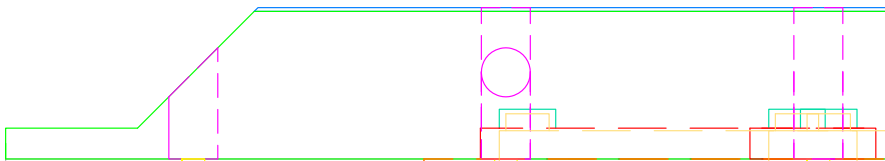


Figure D.6: Detail of one of the sides of the down-looking array radome. It was composed of three layers (from top to bottom): 1mm aluminum + 39.2 mm styrofoam + 1mm FR-4.

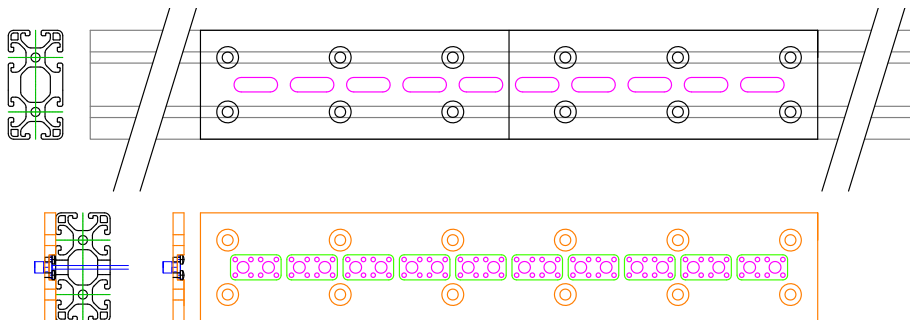


Figure D.7: CAD design of the slide that hold the SMA connectors in one of the sides of each array. The slide measures 340x60x6 mm.



Figure D.8: 3D model of the slide used to manufacture the pieces (down). The slide measures 340x60x6 mm.

D.2 Beamformer

Figure D.9 shows the CAD design of the integrated beamformer. The pieces that were manufactured to put together the phase shifters (in orange, pink, and green)), the power combiners and the motherboard are drawn in a thicker line. Note the U-shaped pieces below the motherboard in orange that hold the whole block in the 30x60 mm standard aluminum profile.

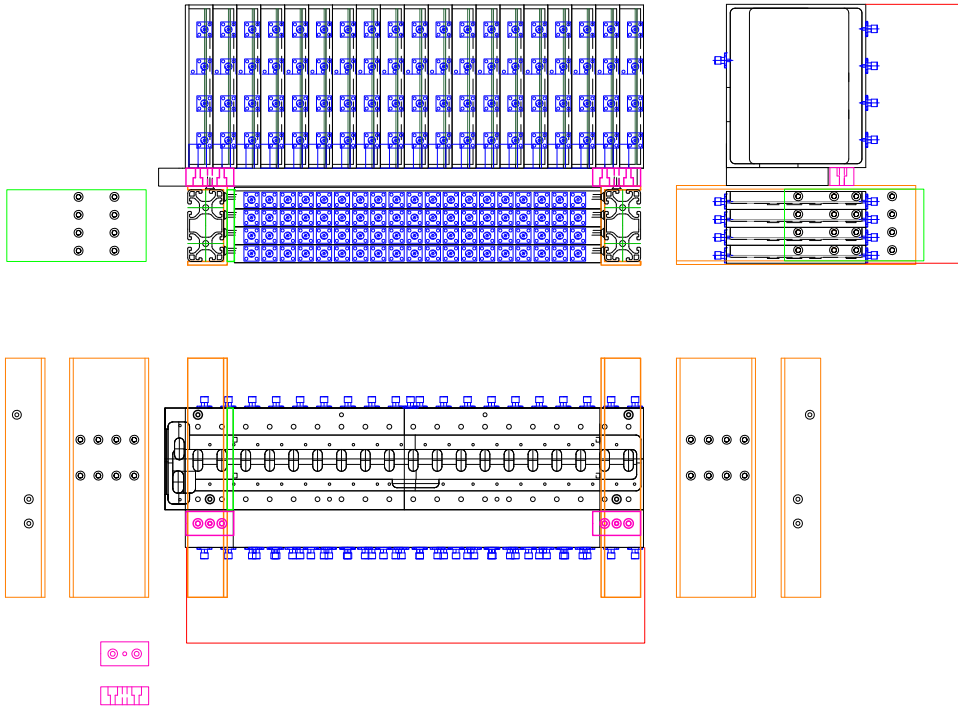


Figure D.9: CAD design of the integrated beamformer. The manufactured pieces to put together all the pieces are drawn at the sides of the whole block. The red area demarcates the space reserved for the cables that connect the phase shifters to the power combiners.

D.3 Rack Integration

Figure D.10 shows the CAD of the integrated rack. On the top left, the top view of the rack's upper floor is shown. This floor has the power supplies, the embedded system, the GNSS receiver, and the USRP N210 with the calibration system over it. On the middle left, the middle floor with the beamformers. On the middle right, the lower floor with the USRPs X310 with the Octoclock and the 1 Gigabit Ethernet switch over them is shown. On the bottom left and right, two of the sides of the rack are shown. The manufactured pieces to put together all the pieces are drawn in orange or purple. The red area delimits the space reserved for the cables that connect the phase shifters to the power combiners.

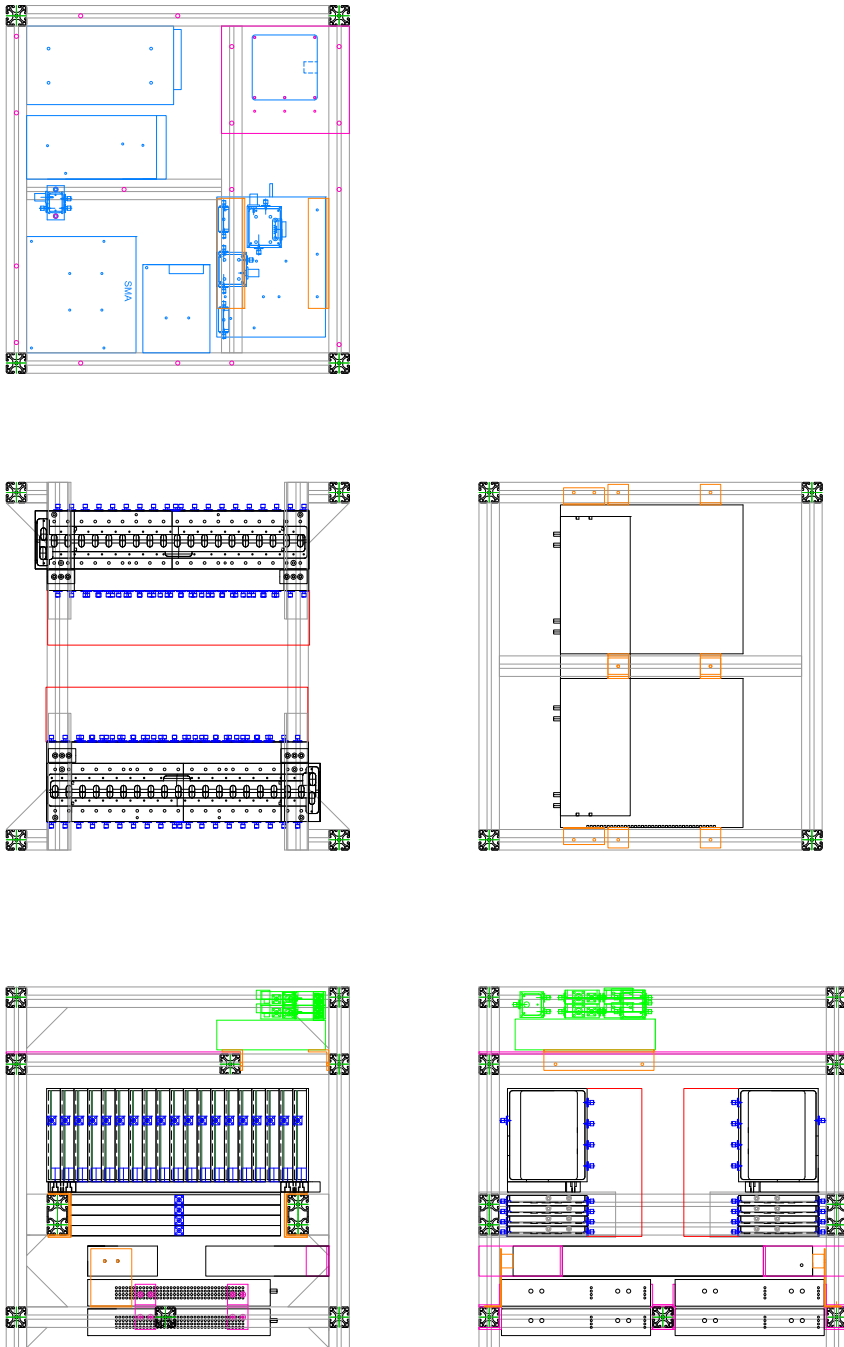


Figure D.10: CAD design of the integrated rack. The figure shows the top views of the top floor (top, left), the middle floor (middle, left), and the lower floor (middle, right), and two side views (bottom, right and left).

E

Appendix E

Coordinate Systems Transformations

This appendix summarizes the coordinate transformations used in the MIR instrument [135]. For all these transformations, the following WGS84 reference ellipsoid parameters are used:

- $R_{EA} = 6,378,137.0$ m is the Semi-major axis
- $R_{EB} = 6,356,752.314245$ m is the Semi-minor axis
- $f = 1/298.257223563$ is the flattening
- $e = 0.0818191908426215$ is the eccentricity
- $ep^2 = e^2/(1 - e^2)$ is the square of the second eccentricity

E.1 LLA Coordinates to ECEF Coordinates

For a given Latitude φ , Longitude λ , and height h , the ECEF coordinates $\{X, Y, Z\}$ are computed as [135]

$$\begin{pmatrix} X \\ Y \\ Z \end{pmatrix} = \begin{pmatrix} (N_e + h) \cdot \cos\varphi \cdot \cos\lambda \\ (N_e + h) \cdot \cos\varphi \cdot \sin\lambda \\ (N_e \cdot (1 - e^2) + h) \cdot \sin\varphi \end{pmatrix}, \quad (\text{E.1})$$

N_e is the radius of curvature in the prime vertical at a given latitude, and is computed as

$$N_e = \frac{a}{\sqrt{1 - e^2 \cdot \sin^2(\varphi)}}. \quad (\text{E.2})$$

E.2 ECEF Coordinates to LLA Coordinates

For a given set of $\{X, Y, Z\}$ values, first the longitude λ is computed as [213]

$$\lambda = \text{atan2}(Y, X), \quad (\text{E.3})$$

where atan2 is the two-argument arctangent function. Then, for the the latitude φ , and height h computation, the Bowring's formula is iterated

$$\rho = \sqrt{X^2 + Y^2} \quad (\text{E.4})$$

$$\beta_0 = \text{atan2}(z, (1 - f) \cdot \rho) \quad (\text{E.5})$$

$$\varphi_0 = \text{atan2}(z + R_{EB} \cdot e p^2 \cdot \sin(\beta_0)^3, \rho - a \cdot e^2 \cdot \cos(\beta_0)^3) \quad (\text{E.6})$$

$$\beta_i = \text{atan2}((1 - f) \cdot \sin(\varphi_{i-1}), \cos(\varphi_{i-1})) \quad (\text{E.7})$$

$$\varphi_i = \text{atan2}(z + R_{EB} \cdot e p^2 \cdot \sin(\beta_{i-1})^3, \rho - a \cdot e^2 \cdot \cos(\beta_{i-1})^3), \quad (\text{E.8})$$

until $|\beta_i - \beta_{i-1}| < 10^{-16}$, which is achieved in typically 2-3 iterations. Then

$$N = \frac{R_{EA}}{\sqrt{1 - e^2 \cdot \sin(\varphi_i)^2}} \quad (\text{E.9})$$

$$h = \rho * \cos(\varphi_i) + (Z \cdot e^2 \cdot N \cdot \sin(\varphi_i)) \cdot \sin(\varphi_i) - N. \quad (\text{E.10})$$

E.3 ECEF Vector from LLA Point to Vehicle Carried NED Coordinates

Given a vehicle with ECEF coordinates $\{X_0, Y_0, Z_0\}$ and LLA coordinates $\{\varphi_0, \lambda_0, h_0\}$, and given a target point with ECEF coordinates $\{X_f, Y_f, Z_f\}$, the coordinates of the target point in the vehicle carried NED coordinate system centered in the reference point are computed as [135]

$$\vec{V} = \begin{pmatrix} V_X \\ V_Y \\ V_Z \end{pmatrix} = \begin{pmatrix} X_f - X_0 \\ Y_f - Y_0 \\ Z_f - Z_0 \end{pmatrix} \quad (\text{E.11})$$

$$\begin{pmatrix} N \\ E \\ D \end{pmatrix} = M_{ECEF}^{NED}(\varphi_0, \lambda_0) \cdot \vec{V}, \quad (\text{E.12})$$

where $M_{ECEF}^{NED}(\varphi_0, \lambda_0)$ is the rotation matrix defined as

$$M_{ECEF}^{NED}(\varphi_0, \lambda_0) = \begin{pmatrix} -\sin\varphi_0 \cdot \cos\lambda_0 & -\sin\varphi_0 \cdot \sin\lambda_0 & \cos\varphi_0 \\ -\sin\lambda_0 & \cos\lambda_0 & 0 \\ -\cos\varphi_0 \cdot \cos\lambda_0 & -\cos\varphi_0 \cdot \sin\lambda_0 & -\sin\varphi_0 \end{pmatrix}. \quad (\text{E.13})$$

E.4 Vehicle Carried NED Coordinates to BODY Coordinates

For a given point in vehicle carried NED coordinates $\{N, E, D\}$ and the yaw, pitch and roll rotation angles $\{\psi, \theta, \phi\}$, the BODY coordinates $\{B_X, B_Y, B_Z\}$ are computed as [135], first rotating the coordinates around the Z axis (yaw), then around the Y axis (pitch), and finally around the X axis (roll):

$$\begin{pmatrix} B_X \\ B_Y \\ B_Z \end{pmatrix} = R_1(\phi) \cdot R_2(\theta) \cdot R_3(\psi) \cdot \begin{pmatrix} N \\ E \\ D \end{pmatrix}, \quad (\text{E.14})$$

where R_1 , R_2 , and R_3 are the following rotation matrices:

$$R_1(\phi) = \begin{pmatrix} 1 & 0 & 0 \\ 0 & \cos\phi & \sin\phi \\ 0 & -\sin\phi & \cos\phi \end{pmatrix} \quad (\text{E.15})$$

$$R_2(\theta) = \begin{pmatrix} \cos\theta & 0 & \sin\theta \\ 0 & 1 & 0 \\ \sin\theta & 0 & \cos\theta \end{pmatrix} \quad (\text{E.16})$$

$$R_3(\psi) = \begin{pmatrix} \cos\psi & \sin\psi & 0 \\ -\sin\psi & \cos\psi & 0 \\ 0 & 0 & 1 \end{pmatrix}. \quad (\text{E.17})$$

F

Appendix F

Satellite Position Determination

This appendix explains how to compute the GNSS satellite position in ECEF coordinates from its orbital parameters [172]:

- t_{oe} is the Ephemerides reference epoch in seconds within the GPS week
- \sqrt{a} is the square root of the semimajor axis
- e is the eccentricity
- M_0 is the mean anomaly at the reference epoch
- ω is the argument of perigee
- i_0 is the inclination at reference epoch
- Ω_0 is the longitude of the ascending node at the beginning of the week
- Δn is the mean motion difference
- \dot{i} is the rate of inclination angle
- $\dot{\Omega}$ is the rate of node's right ascension
- c_{uc} , and c_{us} are the latitude argument correction
- c_{rc} , and c_{rs} are the orbital radius correction
- c_{ic} , and c_{is} are the inclination correction
- a_0 is the SV clock offset

- a_1 is the SV clock drift
- a_2 is the SV clock drift rate

Then, to compute the satellite ECEF position for a given time t , the semimajor axis A , the mean motion n_0 , the time from the ephemeris reference epoch t_k , the time of the reference clock epoch t_{oc} , the corrected mean motion n , and the mean anomaly M are first computed as

$$A = \sqrt{a^2} \quad (\text{F.1})$$

$$n_0 = \sqrt{\frac{\mu}{A^3}} \quad (\text{F.2})$$

$$t_k = t - t_{oe} \quad (\text{F.3})$$

$$t_c = t - t_{oc} \quad (\text{F.4})$$

$$n = n_0 + \Delta n \quad (\text{F.5})$$

$$M = M_0 + n \cdot t_k. \quad (\text{F.6})$$

Note that t_k and t_c must be in the range $\pm 302,400$ s, otherwise 604,800 (the number of seconds in a week) must be added or subtracted accordingly. Then, the Kepler equation for the Eccentric Anomaly E is solved recursively

$$E_i = M + e \cdot \sin(E_{i-1}) \quad (\text{F.7})$$

until $|E_i - E_{i-1}| < 10^{-11}$. After that, the relativistic correction dt_r and the clock bias dt are computed as

$$dt_r = -2 \cdot \frac{\sqrt{\mu}}{c^2} \cdot e \cdot \sqrt{a} \cdot \sin E \quad (\text{F.8})$$

$$dt = a_0 + a_1 \cdot t_c + a_2 \cdot t_c^2 - t_{gd} + dt_r, \quad (\text{F.9})$$

where $\mu = 3.986005 \cdot 10^{14} \text{ m}^3/\text{s}^2$ is the universal gravitational parameter, $c = 2.99792458 \cdot 10^8 \text{ m/s}$ is the speed of light in the vacuum, and t_{gd} is the group delay calculated by the GNSS receiver. The time from the ephemeris reference epoch t_k is now corrected with the clock bias dt (ensuring again that it is in the range $\pm 302,400$ s), and the mean anomaly M , and the eccentric anomaly E are recomputed:

$$t_k = t - t_{oe} + dt \quad (\text{F.10})$$

$$M = M_0 + n \cdot t_k \quad (\text{F.11})$$

$$E_i = M + e \cdot \sin(E_{i-1}). \quad (\text{F.12})$$

Then, the true anomaly v_k , the argument of the latitude u_k , the radial distance r_k ,

and the orbital plane inclination i_k is computed as

$$v_k = \operatorname{atan2}\left(\frac{\sqrt{1-e^2} \cdot \sin(E)}{\cos(E) - e}\right) \quad (\text{F.13})$$

$$u_k = \omega + v_k + c_{uc} \cdot \cos(2 \cdot (\omega + v_k)) + c_{us} \cdot \sin(2 \cdot (\omega + v_k)) \quad (\text{F.14})$$

$$r_k = a \cdot (1 - e \cdot \cos(E)) + c_{rc} \cdot \cos(2 \cdot (\omega + v_k)) + c_{rs} \cdot \sin(2 \cdot (\omega + v_k)) \quad (\text{F.15})$$

$$i_k = i_0 + \dot{i} \cdot t_k + c_{ic} \cdot \cos(2 \cdot (\omega + v_k)) + c_{is} \cdot \sin(2 \cdot (\omega + v_k)). \quad (\text{F.16})$$

Last, the longitude of the ascending node λ_k and the ECEF coordinates of the satellite $\{X, Y, Z\}$ are computed. If the receiver position $\{X_r, Y_r, Z_r\}$ is known, the Sagnac effect can be compensated by iterating the estimated range ρ . Typically 3 iterations are enough for millimetric accuracy. If the receiver position is not known, only one iteration is computed:

$$\rho_0 = 0.07 \cdot c \quad (\text{F.17})$$

$$\lambda_{k_i} = \Omega_0 + \left(\dot{\Omega} - \omega_E\right) + \dot{\Omega} \cdot \left(t_{oe} + \frac{\rho_{i-1}}{c}\right) \quad (\text{F.18})$$

$$\begin{pmatrix} X_i \\ Y_i \\ Z_i \end{pmatrix} = R_3(-\lambda_{k_i}) \cdot R_1(-i_k) \cdot R_3(-u_k) \cdot \begin{pmatrix} X_i \\ Y_i \\ Z_i \end{pmatrix} \quad (\text{F.19})$$

$$\rho_i = \sqrt{(X_i - X_r)^2 + (Y_i - Y_r)^2 + (Z_i - Z_r)^2} \quad (\text{F.20})$$

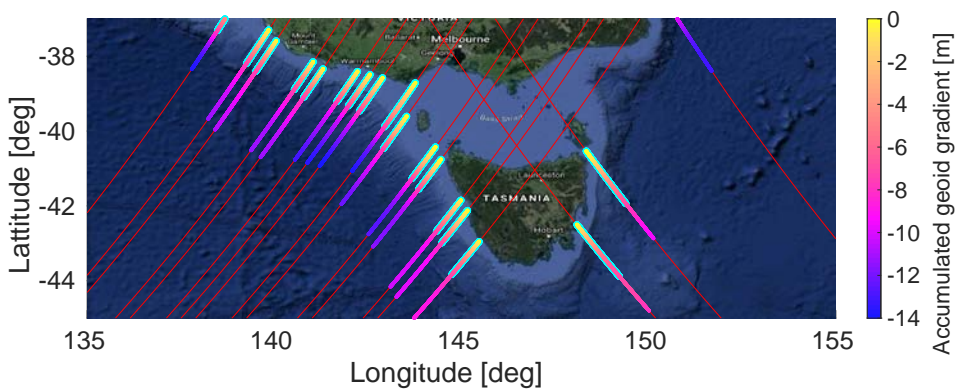
where $\omega_E = 7.2921151467 \cdot 10^{-5} \text{ rad/s}$ is the Earth rotation rate, and R_1 and R_3 are rotation matrices defined in section E.4. A code implementation can be found in the function `getSatECEF` from [214].

G

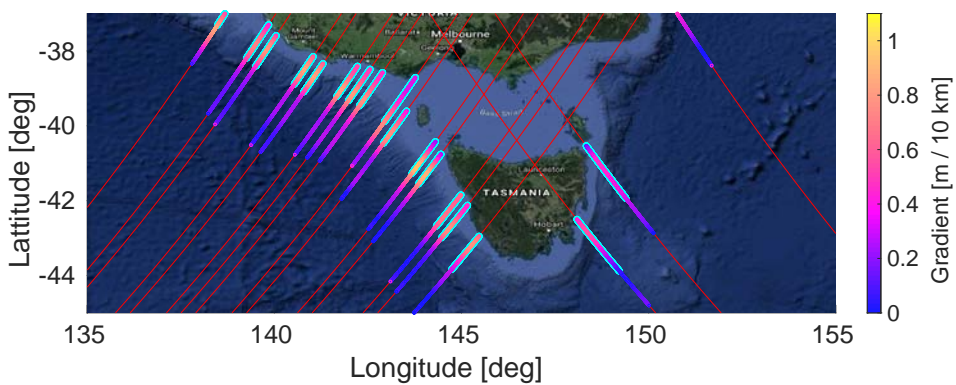
Appendix G

Satellite Overpass Analysis

This appendix shows the satellite overpasses of the four radar altimeters that could have provided sea surface height ground truth for the Bass Strait flight in the period from May 24 2018 to June 29 2018: Jason 2 (see Fig. G.1), Jason 3 (see Fig. G.2), Cryosat-2 (see Fig. G.3), and Sentinel-3a (see fig G.4). Note that the some of the Jason 3 and Sentinel-3a overpasses are overlapped. The required distance to achieve a 7 meter gradient difference is highlighted in bright blue. In green is shown the Cryosat-2 overpass chosen for the Bass Strait flight.

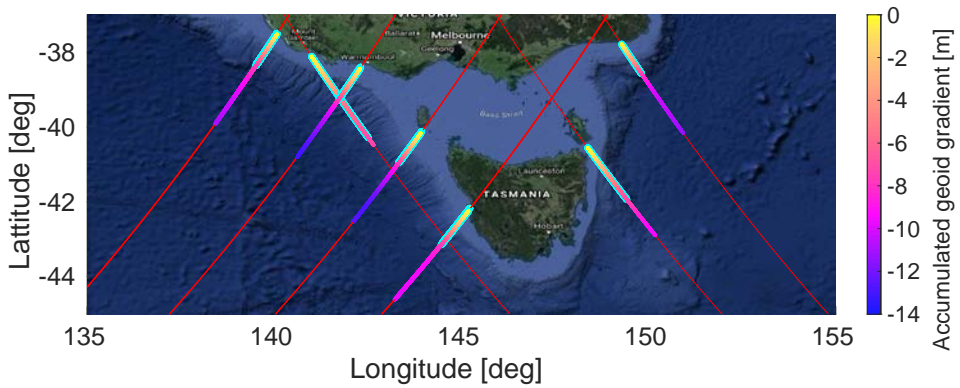


(a)

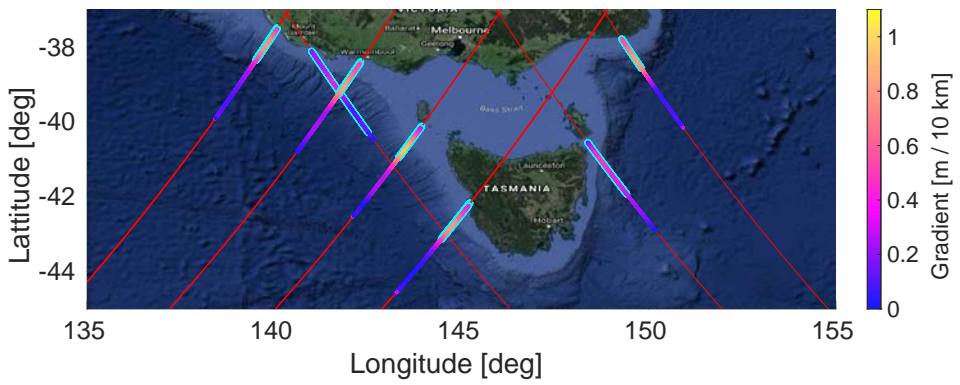


(b)

Figure G.1: a) Accumulated geoid gradient, and b) geoid gradient in 2 minutes of the Jason 2 feasible overpasses during May 2018 and June 2018 in the Bass Strait flight. The red and green lines show the satellite path. The green line shows the chosen one. The flight distance required to reach 7 meters of accumulated geoid gradient is highlighted in bright blue.

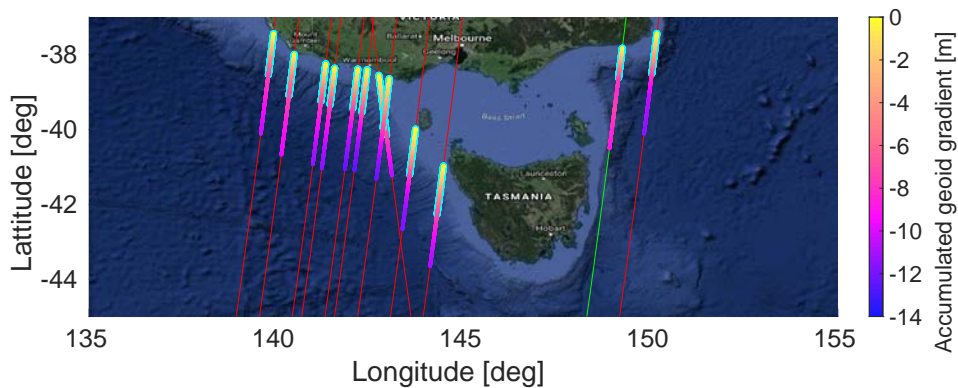


(a)

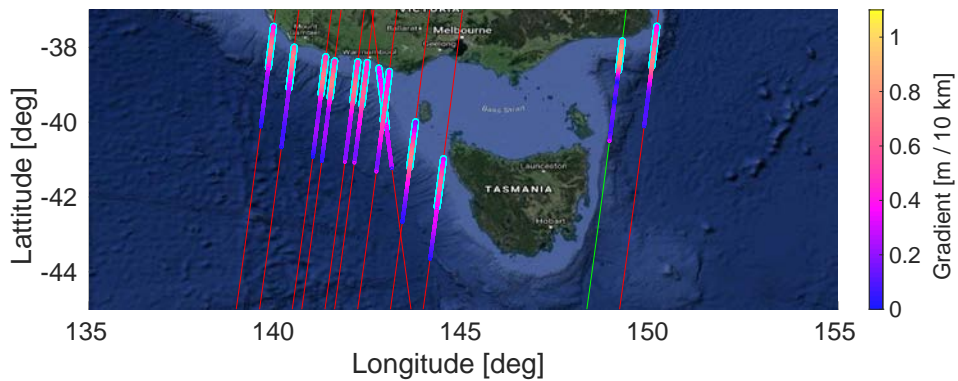


(b)

Figure G.2: a) Accumulated geoid gradient, and b) geoid gradient in 2 minutes of the Jason 3 feasible overpasses during May 2018 and June 2018 in the Bass Strait flight. The red and green lines show the satellite path. The green line shows the chosen one. The flight distance required to reach 7 meters of accumulated geoid gradient is highlighted in bright blue.

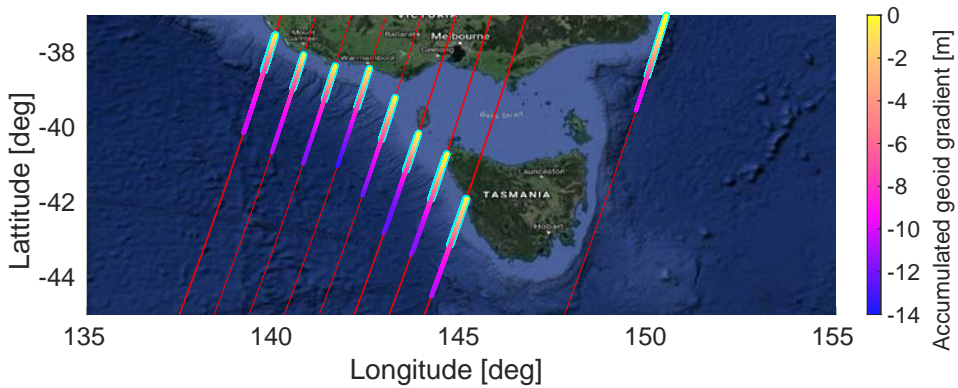


(a)

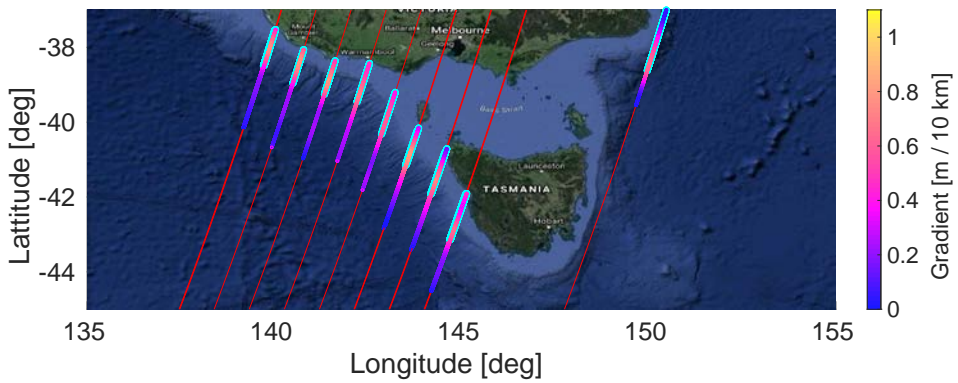


(b)

Figure G.3: a) Accumulated geoid gradient, and b) geoid gradient in 2 minutes of the Cryosat-2 feasible overpasses during May 2018 and June 2018 in the Bass Strait flight. The red and green lines show the satellite path. The green line shows the chosen one. The flight distance required to reach 7 meters of accumulated geoid gradient is highlighted in bright blue.



(a)



(b)

Figure G.4: a) Accumulated geoid gradient, and b) geoid gradient in 2 minutes of the Sentinel-3a feasible overpasses during May 2018 and June 2018 in the Bass Strait flight. The red and green lines show the satellite path. The green line shows the chosen one. The flight distance required to reach 7 meters of accumulated geoid gradient is highlighted in bright blue.

H

Appendix H

Instrument Setup

This appendix is a user manual on how to setup the MIR instrument prior to start the measurements, and how to launch the MIR control software. Once the MIR rack and the arrays have been mounted in the desired location, the following devices and cables need to be mounted:

1. Connect the RF cables from the arrays to the beamformers. Use the 2 meters long cables with labels GCA-151210-1215-XX, where XX is a number from 1 to 42. The cables 1 to 19 should be used for the connectors numbered from 1 to 19 respectively in both the up-looking array and the beamformer. The cables 22 to 40 should be used for the connectors numbered from 1 to 19 respectively in both the down-looking array and the beamformer.
2. Connect the RF calibration cables from the array to the calibration connectors in the rack. Use the 2 meter long cables GCA-151210-1215-41 and GCA-151210-1215-42 for the up- and down-looking arrays and beamformers respectively. Note that a 30 dB attenuator has to be placed in the the rack down-looking calibration connector (see Fig. H.1).
3. Connect the USB cable from the IMU to the USB switch connected to the embedded system (see Fig. H.2).
4. Connect a USB cable from the GNSS receiver (see Fig. H.3) to the the USB switch connected to the embedded system.
5. Mount the two GNSS antennas at the sides of the up-looking array aligned with the y axis of the local coordinate sytem. Connect the RF cables to the two SMA connectors at one of the sides of the GNSS receiver (see Fig. H.4).

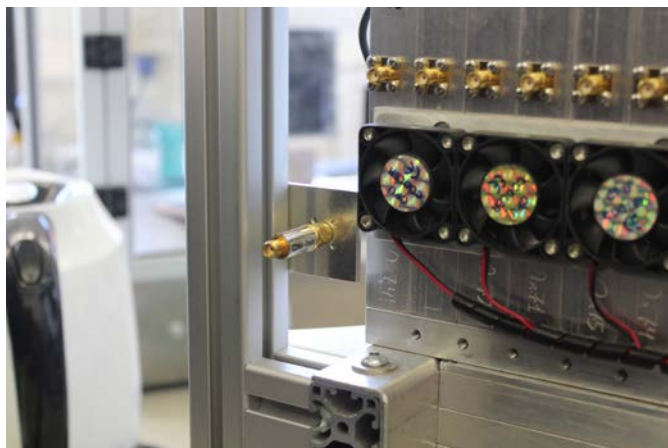


Figure H.1: Down-looking RF chain calibration connector in the MIR rack.



Figure H.2: From left to right, USB switch, power connector, and SPI connector.

6. Mount the inclinometer at the port side of the array. Connect the cable to the DE-9 connector at the side of the power connector.
7. Connect an Ethernet cable from the 1 gigabit Ethernet switch to the MIR laptop. The MIR laptop's network adapter has to be configured with a the static IP address 192.168.2.1.



Figure H.3: GNSS receiver USB connector.

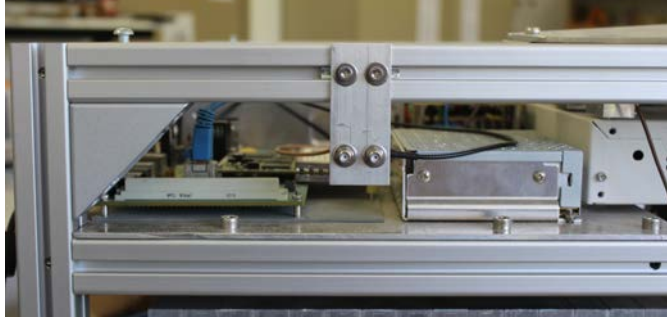


Figure H.4: GNSS receiver input SMA connectors.

8. Connect the power cable to rack and switch the instrument on.
9. (Optional) Ping the GNSS receiver (192.168.2.4), the embedded system (192.168.2.5), and the USRPs (192.168.2.11-14).
10. Using an internet browser open the website <http://192.168.2.4>. In the “Vector - Heading display” tab inside “Receiver status”, check if the “Adjusted Heading” is properly aligned to the North using a compass. If not, add the required “Heading adjustment” in the “Vector” tab inside “Receiver configuration”. Since the instrument is aligned with the airplane, use only multiples of 90°. Note that the GNSS heading points the geographic North, not the magnetic one, so it does not need to match perfectly the heading shown in the compass. In the “I/O configuration tab” configure the following connections:
 - A TCIP/IP connection at port 5018 with GSOFF protocol with the following packets: “Attitude Info”, and “Position Time” at 10 Hz, “Lat, Lon, Ht”, “ECEF position”, “Clock Info”, “Position Sigma”, and “Detail All SV” at 1 Hz.
 - A TCIP/IP connection at port 5019 with GSOFF protocol with the following packets: “Position Time”, “Lat, Lon, Ht”, “ECEF position”, “Clock Info”, and “Position Sigma” at 1 Hz.
 - A USB connection with RT17/RT27 protocol with an Epoch interval of 2 Hz, check the options “Measurements”, “Concise”, “R-T Flag”, “Multi-System Support”, and “Include Doppler”, and set “When new one is available” to all ephemeris.
 - A TCIP/IP connection at port 28004 with RT17/RT27 protocol with an Epoch interval of 1 Hz, check the options “Measurements”, “Positions”, “Send Raw GPS Data”, “Send Raw Galileo Data”, “Multi-System Support”, and “Include Doppler”, and set “10 sec” to all ephemeris and “120 sec to almanac”.
 - A TCIP/IP connection at port 28001 with disabled CMR protocol.
11. Use the software RCAPTURE from Trimble Ltd. to capture GSOFF and RT27 packets by executing in different MS-DOS windows `RCAPTURE.EXE -d192.168.2.4:28004 -n60 -lRT27-` and `RCAPTURE.EXE -d192.168.2.4:5019 -n60 -lGSOFF-`

12. Open a SSH connection to the IP address 192.168.2.5 port 22 using the username and password “ubuntu”.
13. Execute `sudo ./mir-core/cross-hf/mir-core`
14. Once “Ready to calibrate?” is printed, press “Enter”. Once “Ended Calibration?” is printed, use the MIR sampling software to sample in the calibration mode. Using Matlab check that the calibration data is a PRN sequence modulated by a slow tone. Press “Enter” to start the normal functioning mode of the MIR instrument.
15. Once the measurements have ended and the instrument has to be switched off, press “Control + C” in both the RCAPTURE windows, the MIR sampling software and the MIR control software. Then, to shut down the embedded system execute `sudo halt -p`

Part VI

Bibliography and List of Publications

Bibliography

- [1] J. P. Walker, Private Communications, Email, Monash University Clayton Campus, Clayton (Victoria), February 2018. (Cited on pages xvii and 237.)
- [2] W. Emery and A. Camps, “The History of Satellite Remote Sensing,” in *Introduction to Satellite Remote Sensing*. Elsevier, 2017, pp. 1–42. [Online]. Available: <https://linkinghub.elsevier.com/retrieve/pii/B9780128092545000014> (Cited on pages 3 and 4.)
- [3] A. Witze, “A timeline of Earth observation,” *Nature*, dec 2007. (Cited on page 3.)
- [4] “File:Electromagnetic spectrum with sources.svg - Wikimedia Commons,” https://commons.wikimedia.org/wiki/File:Electromagnetic_spectrum_with_sources.svg (Last visited: 10-Oct-2019). (Cited on page 4.)
- [5] “Sonar - Wikipedia,” <https://en.wikipedia.org/wiki/Sonar> (Last visited: 10-Oct-2019). (Cited on page 4.)
- [6] J. Font, A. Camps, A. Borges, M. Martín-Neira, J. Boutin, N. Reul, Y. H. Kerr, A. Hahne, and S. Mecklenburg, “SMOS: The Challenging Sea Surface Salinity Measurement From Space,” *Proceedings of the IEEE*, vol. 98, no. 5, pp. 649–665, may 2010. (Cited on page 4.)
- [7] D. Entekhabi, E. G. Njoku, P. E. O’Neill, K. H. Kellogg, W. T. Crow, W. N. Edelstein, J. K. Entin, S. D. Goodman, T. J. Jackson, J. Johnson, J. Kimball, J. R. Piepmeier, R. D. Koster, N. Martin, K. C. McDonald, M. Moghaddam, S. Moran, R. Reichle, J. C. Shi, M. W. Spencer, S. W. Thurman, L. Tsang, and J. Van Zyl, “The Soil Moisture Active Passive (SMAP) Mission,” *Proceedings of the IEEE*, vol. 98, no. 5, pp. 704–716, may 2010. (Cited on page 4.)
- [8] D. Chaparro, “Applications of L-band missions for environmental research,” Ph.D. dissertation, Universitat Politècnica de Catalunya, <https://www.tdx.cat/handle/10803/663335>, 2018, (Last visit: 01-Dec-2019). (Cited on page 4.)
- [9] “Remote Sensing: a Bit of History - YouTube,” <https://www.youtube.com/watch?v=dQw4w9WgXcQ> (Last visited: 24-Sep-2019). (Cited on page 4.)
- [10] V. U. Zavorotny, S. Gleason, E. Cardellach, and A. Camps, “Tutorial on Remote Sensing Using GNSS Bistatic Radar of Opportunity,” *IEEE Geoscience and Remote Sensing Magazine*, vol. 2, no. 4, pp. 8–45, dec 2014. (Cited on pages 4, 116, and 180.)

- [11] C. S. Ruf, S. Gleason, Z. Jelenak, S. Katzberg, A. Ridley, R. Rose, J. Scherrer, and V. Zavorotny, "The CYGNSS nanosatellite constellation hurricane mission," in *2012 IEEE International Geoscience and Remote Sensing Symposium*. IEEE, jul 2012, pp. 214–216. (Cited on pages 4, 21, and 23.)
- [12] M. Martin-Neira, M. Caparrini, J. Font-Rossello, S. Lannelongue, and C. Vallmitjana, "The PARIS concept: an experimental demonstration of sea surface altimetry using GPS reflected signals," *IEEE Transactions on Geoscience and Remote Sensing*, vol. 39, no. 1, pp. 142–150, 2001. (Cited on pages 4, 22, 25, and 186.)
- [13] "Passive Remote Sensing Group presentation - RSLAB - Departamento de Teoría de la Señal y Comunicaciones - UPC Universitat Politècnica de Catalunya," <https://www.tsc.upc.edu/es/shared/rslab-prs.pdf> (Last visited: 07-Oct-2019). (Cited on page 6.)
- [14] A. Camps, "Application of interferometric radiometry to Earth observation," Ph.D. dissertation, Universitat Politècnica de Catalunya, <https://www.tdx.cat/handle/10803/6885>, 1996, (Last visited: 07-Oct-2019). (Cited on page 6.)
- [15] O. Nogues, A. Sumpsi, A. Camps, and A. Rius, "A 3 GPS-channels Doppler-delay receiver for remote sensing applications," in *IGARSS 2003. 2003 IEEE International Geoscience and Remote Sensing Symposium. Proceedings (IEEE Cat. No.03CH37477)*, vol. 7. IEEE, 2003, pp. 4483–4485. (Cited on page 6.)
- [16] I. Ramos-Perez, E. Valencia, A. Camps, X. Bosch-Lluis, J. F. Marchan-Hernandez, N. Rodriguez-Alvarez, F. Canales-Contador, and M. Donadio, "Initials Results of the Passive Advanced Unit - Synthetic Aperture (PAU-SA)," in *IGARSS 2008 - 2008 IEEE International Geoscience and Remote Sensing Symposium*. IEEE, 2008, pp. II-1148–II-1151. (Cited on page 6.)
- [17] X. Bosch-Lluis, A. Camps, J. Marchan-Hernandez, I. Ramos-Perez, R. Prehn, B. Izquierdo, X. Banque, and J. Yeste, "FPGA-based Implementation of a Polarimetric Radiometer with Digital Beamforming," in *2006 IEEE International Symposium on Geoscience and Remote Sensing*. IEEE, jul 2006, pp. 1176–1179. (Cited on page 6.)
- [18] E. Valencia, A. Camps, M. Vall-llossera, A. Monerris, X. Bosch-Lluis, N. Rodriguez-Alvarez, I. Ramos-Perez, J. F. Marchan-Hernandez, J. Martinez-Fernandez, N. Sanchez-Martin, and C. Perez-Gutierrez, "GNSS-R Delay-Doppler Maps over land: Preliminary results of the GRAJO field experiment," in *2010 IEEE International Geoscience and Remote Sensing Symposium*. IEEE, jul 2010, pp. 3805–3808. (Cited on page 6.)
- [19] A. Camps, J. Marchan, E. Valencia, I. Ramos, X. Bosch-Lluis, N. Rodriguez, H. Park, A. Alcayde, A. Mollfulleda, J. Galindo, P. Martinez, S. Chavero, M. Angulo, and A. Rius, "PAU instrument aboard INTA MicroSat-1: A GNSS-R demonstration mission for sea state correction in L-band radiometry," in *2011 IEEE International Geoscience and Remote Sensing Symposium*. IEEE, jul 2011, pp. 4126–4129. (Cited on page 6.)

- [20] J. M. Tarongi and A. Camps, “Multifrequency experimental radiometer with interference tracking for experiments over land and littoral: Meritxell,” in *2009 IEEE International Geoscience and Remote Sensing Symposium*. IEEE, 2009, pp. IV–653–IV–656. (Cited on page 6.)
- [21] J. Querol, E. M. Julian, **R. Onrubia**, A. Alonso-Arroyo, D. Pascual, and A. Camps, “Preliminary results of FENIX: Front-End GNSS Interference eXcisor,” in *2016 IEEE International Geoscience and Remote Sensing Symposium (IGARSS)*, vol. 2016-Novem. Beijing, China: IEEE, jul 2016, pp. 5627–5630. (Cited on page 6.)
- [22] R. Jove-Casulleras, A. Camps, and J. Ramos, “Cubesat-based demonstrator for optical earth observation,” in *2012 IEEE International Geoscience and Remote Sensing Symposium*. IEEE, jul 2012, pp. 1505–1508. (Cited on page 6.)
- [23] “Missions & Projects — NanoSat Lab — UPC. Universitat Politècnica de Catalunya,” <https://nanosatlab.upc.edu/en/missions-and-projects> (Last visited: 08-Oct-2019). (Cited on page 6.)
- [24] N. Rodriguez-Alvarez, A. Monerris, X. Bosch-Lluis, A. Camps, M. Vall-Llossera, J. F. Marchan-Hernandez, I. Ramos-Perez, E. Valencia, J. Martinez-Fernandez, N. Sanchez-Martin, G. Baroncini-Turricchia, and C. Perez-Gutierrez, “Soil moisture and vegetation height retrieval using GNSS-R techniques,” in *2009 IEEE International Geoscience and Remote Sensing Symposium*, vol. 3. IEEE, 2009, pp. III–869–III–872. (Cited on pages 6, 21, 22, and 25.)
- [25] A. Alonso-Arroyo, A. Camps, A. Monerris, C. Rudiger, J. P. Walker, G. Forte, D. Pascual, H. Park, and **R. Onrubia**, “The light airborne reflectometer for GNSS-R observations (LARGO) instrument: Initial results from airborne and Rover field campaigns,” in *2014 IEEE Geoscience and Remote Sensing Symposium*, IEEE, Ed. Quebec: IEEE, jul 2014, pp. 4054–4057. (Cited on pages 6, 21, 23, and 38.)
- [26] H. Carreno-Luengo, A. Amèzaga, D. Vidal, R. Olivé, J. Munoz, and A. Camps, “First Polarimetric GNSS-R Measurements from a Stratospheric Flight over Boreal Forests,” *Remote Sensing*, vol. 7, no. 10, pp. 13 120–13 138, oct 2015. (Cited on pages 6, 23, and 26.)
- [27] A. Alonso-Arroyo, J. Querol, A. Camps, **R. Onrubia**, H. Park, and D. Pascual, “Can we measure vegetation water content and vegetation opacity at L-band with a single GPS receiver?” in *2016 IEEE International Geoscience and Remote Sensing Symposium (IGARSS)*, vol. 2016-Novem. IEEE, jul 2016, pp. 1985–1988. (Cited on page 6.)
- [28] M. Martin-Neira, S. D’Addio, C. Buck, N. Floury, and R. Prieto-Cerdeira, “The PARIS Ocean Altimeter In-Orbit Demonstrator,” *IEEE Transactions on Geoscience and Remote Sensing*, vol. 49, no. 6, pp. 2209–2237, jun 2011. (Cited on pages 6, 139, 147, and 148.)
- [29] D. Pacual, “Design and Performance Analysis of Advanced GNSS-R Instruments Back-end,” Ph.D. dissertation, Universitat Politècnica de Catalunya, 2020, *To be submitted*. (Cited on pages 7, 8, 87, 96, 109, 120, and 165.)

- [30] D. Pascual, H. Park, A. Camps, A. A. Arroyo, and **R. Onrubia**, “Simulation and Analysis of GNSS-R Composite Waveforms Using GPS and Galileo Signals,” *IEEE Journal of Selected Topics in Applied Earth Observations and Remote Sensing*, vol. 7, no. 5, pp. 1461–1468, may 2014. (Cited on page 7.)
- [31] J. Querol, “Radio Frequency Interference Detection and Mitigation Techniques for Navigation and Earth Observation,” Ph.D. dissertation, Universitat Politècnica de Catalunya, <https://www.tesisenred.net/handle/10803/663905>, 2018, (Last visit: 06-Oct-2019). (Cited on pages 8, 34, 38, 39, and 116.)
- [32] “GNSS signal - Navipedia,” https://gssc.esa.int/navipedia/index.php/GNSS_signal (Last visited: 14-Sep-2019). (Cited on page 12.)
- [33] S. Gleason and D. Gebre-Egziabher, *GNSS Applications and Methods*, 2009. (Cited on pages 12 and 167.)
- [34] P. M. Woodward, *Probability and Information Theory with Applications to Radar*. Elsevier, 1953. (Cited on page 13.)
- [35] “GPS Signal Plan - Navipedia,” https://gssc.esa.int/navipedia/index.php/GPS_Signal_Plan (Last visited: 20-Sep-2019). (Cited on page 16.)
- [36] “Galileo Signal Plan - Navipedia,” https://gssc.esa.int/navipedia/index.php/Galileo_Signal_Plan (Last visited: 20-Sep-2019). (Cited on pages 15 and 17.)
- [37] H.-G. Kahle, M. Cocard, Y. Peter, A. Geiger, R. Reilinger, A. Barka, and G. Veis, “GPS-derived strain rate field within the boundary zones of the Eurasian, African, and Arabian Plates,” *Journal of Geophysical Research: Solid Earth*, vol. 105, no. B10, pp. 23 353–23 370, oct 2000. (Cited on page 14.)
- [38] V. Janssen, “Indirect Tracking of Drop Bears Using GNSS Technology,” *Australian Geographer*, vol. 43, no. 4, pp. 445–452, dec 2012. (Cited on page 14.)
- [39] R. Manson, R. Coleman, P. Morgan, and M. King, “Ice velocities of the Lambert Glacier from static GPS observations,” *Earth, Planets and Space*, vol. 52, no. 11, pp. 1031–1036, jun 2014. (Cited on page 14.)
- [40] G. A. Hajj, R. Ibañez-Meier, E. R. Kursinski, and L. J. Romans, “Imaging the ionosphere with the global positioning system,” *International Journal of Imaging Systems and Technology*, vol. 5, no. 2, pp. 174–187, 1994. (Cited on page 14.)
- [41] C. Rocken, Y.-H. Kuo, W. Schreiner, D. Hunt, S. Sokolovsky, and C. McCormick, “COSMIC System Description,” *Terrestrial, Atmospheric and Oceanic Sciences*, vol. 11, no. 1, pp. 21–52, 2000. (Cited on page 14.)
- [42] C. Hall and R. Cordey, “Multistatic Scatterometry,” in *International Geoscience and Remote Sensing Symposium, 'Remote Sensing: Moving Toward the 21st Century'*, vol. 1. IEEE, 1988, pp. 561–562. (Cited on pages 14 and 21.)
- [43] M. Martin-Neira, “A Passive Reflectometry and Interferometry System (PARIS): Application to Ocean Altimetry,” *ESA Journal*, vol. 17, pp. 331–355, 1993. (Cited on pages 16 and 21.)

-
- [44] S. Katzberg and J. Garrison, "Utilizing GPS To Determine Ionospheric Delay Over the Ocean," *NASA Technical Memorandum 4750*, 1996. (Cited on pages 16 and 18.)
- [45] D. Pascual, H. Park, **R. Onrubia**, A. A. Arroyo, J. Querol, and A. Camps, "Crosstalk Statistics and Impact in Interferometric GNSS-R," *IEEE Journal of Selected Topics in Applied Earth Observations and Remote Sensing*, vol. 9, no. 10, pp. 4621–4630, oct 2016. (Cited on pages 16, 179, 184, and 187.)
- [46] **R. Onrubia**, J. Querol, D. Pascual, A. Alonso-Arroyo, H. Park, and A. Camps, "DME/TACAN Impact Analysis on GNSS Reflectometry," *IEEE Journal of Selected Topics in Applied Earth Observations and Remote Sensing*, vol. 9, no. 10, pp. 4611–4620, oct 2016. (Cited on pages 17 and 137.)
- [47] R. G. Lorenz, R. J. Helkey, and K. K. Abadi, "Global positioning system receiver digital processing technique," jul 1992. [Online]. Available: <http://www.google.com/patents/US5134407> (Cited on page 17.)
- [48] S. T. Lowe, T. Meehan, and L. Young, "Direct Signal Enhanced Semicodeless Processing of GNSS Surface-Reflected Signals," *IEEE Journal of Selected Topics in Applied Earth Observations and Remote Sensing*, vol. 7, no. 5, pp. 1469–1472, may 2014. (Cited on pages 18, 21, 22, and 25.)
- [49] V. Zavorotny and A. Voronovich, "Scattering of GPS signals from the ocean with wind remote sensing application," *IEEE Transactions on Geoscience and Remote Sensing*, vol. 38, no. 2, pp. 951–964, mar 2000. (Cited on pages 18, 19, 20, 181, and 182.)
- [50] E. Valencia, V. U. Zavorotny, D. M. Akos, and A. Camps, "Using DDM Asymmetry Metrics for Wind Direction Retrieval From GPS Ocean-Scattered Signals in Airborne Experiments," *IEEE Transactions on Geoscience and Remote Sensing*, vol. 52, no. 7, pp. 3924–3936, jul 2014. (Cited on pages 19 and 21.)
- [51] A. Camps, G. Forte, I. Ramos, A. Alonso, P. Martinez, L. Crespo, and A. Alcayde, "Recent advances in land monitoring using GNSS-R techniques," in *2012 Workshop on Reflectometry Using GNSS and Other Signals of Opportunity (GNSS+R)*. IEEE, oct 2012, pp. 1–4. (Cited on page 19.)
- [52] G. Ruffini and F. Soulat, "On the GNSS-R Interferometric Complex Field Coherence Time," jun 2004. (Cited on page 20.)
- [53] V. Zavorotny and A. Voronovich, "Bistatic GPS signal reflections at various polarizations from rough land surface with moisture content," in *IGARSS 2000. IEEE 2000 International Geoscience and Remote Sensing Symposium. Taking the Pulse of the Planet: The Role of Remote Sensing in Managing the Environment. Proceedings (Cat. No.00CH37120)*, vol. 7. IEEE, 2000, pp. 2852–2854. (Cited on page 20.)
- [54] A. Kavak, W. Vogel, and G. Xu, "Using GPS to measure ground complex permittivity," *Electronics Letters*, vol. 34, no. 3, p. 254, 1998. (Cited on pages 20, 22, and 25.)

- [55] K. M. Larson, E. E. Small, E. D. Gutmann, A. L. Bilich, J. J. Braun, and V. U. Zavorotny, "Use of GPS receivers as a soil moisture network for water cycle studies," *Geophysical Research Letters*, vol. 35, no. 24, p. L24405, dec 2008. (Cited on page 20.)
- [56] N. Rodriguez-Alvarez, J. Marchan, A. Camps, E. Valencia, X. Bosch-Lluis, I. Ramos-Perez, and J. Nieto, "Soil Moisture Retrieval Using GNSS-R Techniques: Measurement Campaign in a Wheat Field," in *IGARSS 2008 - 2008 IEEE International Geoscience and Remote Sensing Symposium*, vol. 2. IEEE, 2008, pp. II-245–II-248. (Cited on pages 20, 21, 22, and 25.)
- [57] A. Alonso-Arroyo, A. Camps, A. Aguasca, G. Forte, A. Monerris, C. Rudiger, J. P. Walker, H. Park, D. Pascual, and **R. Onrubia**, "Improving the Accuracy of Soil Moisture Retrievals Using the Phase Difference of the Dual-Polarization GNSS-R Interference Patterns," *IEEE Geoscience and Remote Sensing Letters*, vol. 11, no. 12, pp. 2090–2094, dec 2014. (Cited on pages 20, 21, and 22.)
- [58] N. Roussel, G. Ramillien, F. Frappart, J. Darrozes, A. Gay, R. Biancale, N. Striebig, V. Hanquiez, X. Bertin, and D. Allain, "Sea level monitoring and sea state estimate using a single geodetic receiver," *Remote Sensing of Environment*, vol. 171, pp. 261–277, dec 2015. (Cited on pages 20 and 21.)
- [59] J. S. Löfgren and R. Haas, "Sea level measurements using multi-frequency GPS and GLONASS observations," *EURASIP Journal on Advances in Signal Processing*, vol. 2014, no. 1, p. 50, apr 2014. (Cited on page 21.)
- [60] M. Caparrini, A. Egido, F. Soulat, O. Germain, E. Farres, S. Dunne, and G. Ruffini, "Oceanpal@: Monitoring sea state with a GNSS-R coastal instrument," in *2007 IEEE International Geoscience and Remote Sensing Symposium*. IEEE, 2007, pp. 5080–5083. (Cited on page 21.)
- [61] E. Valencia, A. Camps, J. F. Marchan-Hernandez, N. Rodriguez-Alvarez, I. Ramos-Perez, and X. Bosch-Lluis, "Experimental Determination of the Sea Correlation Time Using GNSS-R Coherent Data," *IEEE Geoscience and Remote Sensing Letters*, vol. 7, no. 4, pp. 675–679, oct 2010. (Cited on page 21.)
- [62] C. Zuffada and V. Zavorotny, "A novel technique for characterizing the thickness of first-year sea ice with the GPS reflected signal," dec 2002. (Cited on page 21.)
- [63] M. Semmling, G. Beyerle, J. Beckheinrich, M. Ge, and J. Wickert, "Airborne GNSS reflectometry using crossover reference points for carrier phase altimetry," in *2014 IEEE Geoscience and Remote Sensing Symposium*. IEEE, jul 2014, pp. 3786–3789. (Cited on page 21.)
- [64] J. L. Garrison, S. J. Katzberg, and M. I. Hill, "Effect of sea roughness on bistatically scattered range coded signals from the Global Positioning System," *Geophysical Research Letters*, vol. 25, no. 13, pp. 2257–2260, jul 1998. (Cited on pages 21, 22, and 25.)
- [65] R. Sabia, M. Caparrini, and G. Ruffini, "Potential Synergetic Use of GNSS-R Signals to Improve the Sea-State Correction in the Sea Surface Salinity Estimation:

- Application to the SMOS Mission,” *IEEE Transactions on Geoscience and Remote Sensing*, vol. 45, no. 7, pp. 2088–2097, jul 2007. (Cited on page 21.)
- [66] E. Valencia, A. Camps, H. Park, N. Rodriguez-Alvarez, X. Bosch-Lluis, and I. Ramos-Perez, “Oil slicks detection using GNSS-R,” in *2011 IEEE International Geoscience and Remote Sensing Symposium*. IEEE, jul 2011, pp. 4383–4386. (Cited on page 21.)
- [67] M. Martin-Neira, C. Buck, S. Gleason, M. Unwin, M. Caparrini, E. Farrés, O. Germain, G. Ruffini, F. Soulat, E. D. L, O. Fabra, M. D. Tibidabo, and Spain, “Tsunami Detection Using the PARIS Concept,” in *Progress In Electromagnetics Research Symposium 2005, Hangzhou, China, August 22-26*, aug 2014. (Cited on page 21.)
- [68] J. Beckheinrich, A. Hirrle, S. Schon, G. Beyerle, M. Semmling, and J. Wickert, “Water level monitoring of the Mekong Delta using GNSS reflectometry technique,” in *2014 IEEE Geoscience and Remote Sensing Symposium*, 2014, pp. 3798–3801. (Cited on page 21.)
- [69] N. Rodriguez-Alvarez, X. Bosch-Lluis, A. Camps, I. Ramos-Perez, E. Valencia, H. Park, and M. Vall-llossera, “Water level monitoring using the interference pattern GNSS-R technique,” in *2011 IEEE International Geoscience and Remote Sensing Symposium*. IEEE, jul 2011, pp. 2334–2337. (Cited on pages 21, 22, and 25.)
- [70] N. Kassabian, L. Lo Presti, and G. Falco, “A flight in the Piedmont region for water surface detection and altimetry experimentation,” in *2012 IEEE International Geoscience and Remote Sensing Symposium*. IEEE, jul 2012, pp. 5254–5257. (Cited on page 21.)
- [71] R. Galas, T. Schöne, M. Cokrlc, and M. Semmling, “On Precise GNSS-based Sea Surface Monitoring Systems,” pp. 323–326, 2013. (Cited on page 21.)
- [72] K. D. Anderson, “Determination of Water Level and Tides Using Interferometric Observations of GPS Signals,” *Journal of Atmospheric and Oceanic Technology*, vol. 17, no. 8, pp. 1118–1127, aug 2000. (Cited on pages 21, 22, and 25.)
- [73] A. Alonso-Arroyo, S. Torrecilla, J. Querol, A. Camps, D. Pascual, H. Park, and **R. Onrubia**, “Two dedicated soil moisture experiments using the scatterometric properties of GNSS-reflectometry,” in *2015 IEEE International Geoscience and Remote Sensing Symposium (IGARSS)*, vol. 2015-Novem. IEEE, jul 2015, pp. 3921–3924. (Cited on page 21.)
- [74] D. Masters, V. Zavorotny, S. Katzberg, and W. Emery, “GPS signal scattering from land for moisture content determination,” in *IGARSS 2000. IEEE 2000 International Geoscience and Remote Sensing Symposium. Taking the Pulse of the Planet: The Role of Remote Sensing in Managing the Environment. Proceedings (Cat. No.00CH37120)*, vol. 7. IEEE, 2000, pp. 3090–3092. (Cited on pages 21, 22, and 25.)
- [75] M. S. Grant, S. T. Acton, and S. J. Katzberg, “Terrain Moisture Classification Using GPS Surface-Reflected Signals,” *IEEE Geoscience and Remote Sensing Letters*, vol. 4, no. 1, pp. 41–45, jan 2007. (Cited on page 21.)

- [76] A. Egido, G. Ruffini, M. Caparrini, C. Martin, E. Farres, and X. Banque, “Soil Moisture Monitorization Using GNSS Reflected Signals,” p. 7, may 2008. (Cited on page 21.)
- [77] A. Egido, M. Caparrini, G. Ruffini, S. Paloscia, E. Santi, L. Guerriero, N. Pierdicca, and N. Floury, “Global Navigation Satellite Systems Reflectometry as a Remote Sensing Tool for Agriculture,” *Remote Sensing*, vol. 4, no. 8, pp. 2356–2372, aug 2012. (Cited on pages 21, 23, and 26.)
- [78] K. M. Larson, E. E. Small, E. Gutmann, A. Bilich, P. Axelrad, and J. Braun, “Using GPS multipath to measure soil moisture fluctuations: initial results,” *GPS Solutions*, vol. 12, no. 3, pp. 173–177, aug 2007. (Cited on pages 21, 22, and 25.)
- [79] N. Rodriguez-Alvarez, J. F. Marchan-Hernandez, A. Camps, X. Bosch-Lluis, E. Valencia, I. Ramos-Perez, M. Vall-llossera, A. Monerris, J. Martinez-Fernandez, C. Perez-Gutierrez, G. Baroncini-Turricchia, N. Sanchez-Martin, J. M. Nieto, M. Valf-Llossera, A. Monern, J. Martinez-Fernandez, C. Perez-Gutierrez, G. Baroncini-Turricchia, N. Sanchez-Martin, and J. M. Nieto, “Topographic profile retrieval using the Interference Pattern GNSS-R technique,” in *2009 IEEE International Geoscience and Remote Sensing Symposium*, vol. 3. IEEE, 2009, pp. III-420–III-423. (Cited on page 21.)
- [80] N. Rodriguez-Alvarez, X. Bosch-Lluis, R. Acevo, A. Aguasca, A. Camps, M. Vall-llossera, I. Ramos-Perez, and E. Valencia, “Study of maize plants effects in the retrieval of soil moisture using the interference pattern GNSS-R technique,” in *2010 IEEE International Geoscience and Remote Sensing Symposium*. IEEE, jul 2010, pp. 3813–3816. (Cited on page 21.)
- [81] S. Paloscia, E. Santi, G. Fontanelli, S. Pettinato, A. Egido, M. Caparrini, E. Motte, L. Guerriero, N. Pierdicca, and N. Floury, “GNSS-R sensor sensitivity to soil moisture and vegetation biomass and comparison with SAR data performance,” in *Proceedings of SPIE - The International Society for Optical Engineering*, C. Notarnicola, S. Paloscia, and N. Pierdicca, Eds., vol. 8891, oct 2013, p. 88910I. (Cited on page 21.)
- [82] F. Fabra, E. Cardellach, O. Nogues-Correig, S. Oliveras, S. Ribo, A. Rius, G. Macelloni, S. Pettinato, and S. D’Addio, “An empirical approach towards characterization of dry snowlayers using GNSS-R,” in *2011 IEEE International Geoscience and Remote Sensing Symposium*. IEEE, jul 2011, pp. 4379–4382. (Cited on pages 21, 22, and 25.)
- [83] N. Rodriguez-Alvarez, A. Aguasca, E. Valencia, X. Bosch-Lluis, I. Ramos-Perez, H. Park, A. Camps, and M. Vall-llossera, “Snow monitoring using GNSS-R techniques,” in *2011 IEEE International Geoscience and Remote Sensing Symposium*. IEEE, jul 2011, pp. 4375–4378. (Cited on pages 21, 22, and 25.)
- [84] J.-C. Auber, A. Bibaut, and J.-M. Rigal, “Characterization of Multipath on Land and Sea at GPS Frequencies,” in *Proceedings of the 7th International Technical Meeting of the Satellite Division of The Institute of Navigation (ION GPS 1994)*, sep 1994, pp. 1155–1171. (Cited on page 22.)

- [85] J. Garrison and S. Katzberg, "Detection of ocean reflected GPS signals: theory and experiment," in *Proceedings IEEE SOUTHEASTCON '97. 'Engineering the New Century'*. IEEE, 1997, pp. 290–294. (Cited on page 22.)
- [86] S. T. Lowe, C. Zuffada, Y. Chao, P. Kroger, L. E. Young, and J. L. LaBrecque, "5-cm-Precision aircraft ocean altimetry using GPS reflections," *Geophysical Research Letters*, vol. 29, no. 10, pp. 13–1–13–4, may 2002. (Cited on pages 22 and 25.)
- [87] G. Ruffini, F. Soulat, M. Caparrini, O. Germain, and M. Martín-Neira, "The Eddy Experiment: Accurate GNSS-R ocean altimetry from low altitude aircraft," *Geophysical Research Letters*, vol. 31, no. 12, pp. n/a–n/a, jun 2004. (Cited on pages 22 and 25.)
- [88] S. Gleason, S. Hodgart, C. Gommenginger, S. Mackin, M. Adjrad, and M. Unwin, "Detection and Processing of bistatically reflected GPS signals from low Earth orbit for the purpose of ocean remote sensing," *IEEE Transactions on Geoscience and Remote Sensing*, vol. 43, no. 6, pp. 1229–1241, jun 2005. (Cited on pages 22 and 25.)
- [89] M. Unwin, S. Gleason, and M. Brennan, "The Space GPS Reflectometry Experiment On the UK Disaster Monitoring Constellation Satellite," 2003. (Cited on page 22.)
- [90] M. P. Clarizia, C. P. Gommenginger, S. T. Gleason, M. A. Srokosz, C. Galdi, and M. Di Bisceglie, "Analysis of GNSS-R delay-Doppler maps from the UK-DMC satellite over the ocean," *Geophysical Research Letters*, vol. 36, no. 2, pp. n/a–n/a, jan 2009. (Cited on page 22.)
- [91] A. Helm, O. Montenbruck, J. Ashjaee, S. Yudanov, G. Beyerle, R. Stosius, and M. Rothacher, "GORS - A GNSS Occultation, Reflectometry and Scatterometry Space Receiver," in *Proceedings of the 20th International Technical Meeting of the Satellite Division of The Institute of Navigation (ION GNSS 2007)*, ION, Ed. Fort Worth, Texas: ION, 2007, pp. 2011–2021. (Cited on pages 22 and 25.)
- [92] A. Alonso-Arroyo, A. Camps, H. Park, D. Pascual, **R. Onrubia**, F. Martín, and F. Martín, "Retrieval of Significant Wave Height and Mean Sea Surface Level Using the GNSS-R Interference Pattern Technique: Results From a Three-Month Field Campaign," *IEEE Transactions on Geoscience and Remote Sensing*, vol. 53, no. 6, pp. 3198–3209, jun 2015. (Cited on pages 22 and 25.)
- [93] O. Nogués-Correig, E. Cardellach Gali, J. Sanz Campderros, and A. Rius, "A GPS-Reflections Receiver That Computes Doppler/Delay Maps in Real Time," *IEEE Transactions on Geoscience and Remote Sensing*, vol. 45, no. 1, pp. 156–174, jan 2007. (Cited on page 22.)
- [94] J. F. Marchan-Hernandez, I. Ramos-Perez, X. Bosch-Lluis, A. Camps, N. Rodriguez-Alvarez, and D. Albiol, "PAU-GNSS/R, a real-time GPS-reflectometer for earth observation applications: architecture insights and preliminary results," in *2007 IEEE International Geoscience and Remote Sensing Symposium*. IEEE, 2007, pp. 5113–5116. (Cited on page 22.)
- [95] E. Cardellach, F. Fabra, O. Nogués-Correig, S. Oliveras, S. Ribó, and A. Rius, "GNSS-R ground-based and airborne campaigns for ocean, land, ice, and snow

- techniques: Application to the GOLD-RTR data sets,” *Radio Science*, vol. 46, no. 6, dec 2011. (Cited on pages 22 and 25.)
- [96] F. Fabra, E. Cardellach, O. Nogues-Correig, S. Oliveras, S. Ribo, A. Rius, M. Belmonte-Rivas, M. Semmling, G. Macelloni, S. Pettinato, R. Zasso, and S. D’Addio, “Monitoring sea-ice and dry snow with GNSS reflections,” in *2010 IEEE International Geoscience and Remote Sensing Symposium*. IEEE, jul 2010, pp. 3837–3840. (Cited on pages 22 and 25.)
- [97] F. Fabra, E. Cardellach, A. Rius, S. Ribo, S. Oliveras, O. Nogues-Correig, M. Belmonte Rivas, M. Semmling, and S. D’Addio, “Phase Altimetry With Dual Polarization GNSS-R Over Sea Ice,” *IEEE Transactions on Geoscience and Remote Sensing*, vol. 50, no. 6, pp. 2112–2121, jun 2012. (Cited on pages 22 and 25.)
- [98] A. Rius, O. Nogués-Correig, S. Ribó, E. Cardellach, S. Oliveras, E. Valencia, H. Park, J. M. Tarongí, A. Camps, H. van der Marel, R. van Bree, B. Altena, and M. Martín-Neira, “Altimetry with GNSS-R interferometry: first proof of concept experiment,” *GPS Solutions*, vol. 16, no. 2, pp. 231–241, jun 2011. (Cited on pages 23 and 26.)
- [99] A. Egido, S. Paloscia, E. Motte, L. Guerriero, N. Pierdicca, M. Caparrini, E. Santi, G. Fontanelli, and N. Floury, “Airborne GNSS-R Polarimetric Measurements for Soil Moisture and Above-Ground Biomass Estimation,” *IEEE Journal of Selected Topics in Applied Earth Observations and Remote Sensing*, vol. 7, no. 5, pp. 1522–1532, may 2014. (Cited on pages 23 and 26.)
- [100] S. Powell, D. Akos, and V. Zavorotny, “GPS SBAS L1/L5 bistatic radar altimeter,” in *2014 IEEE Geoscience and Remote Sensing Symposium*. IEEE, jul 2014, pp. 1544–1547. (Cited on pages 23 and 26.)
- [101] F. Fabra, E. Cardellach, S. Ribo, W. Li, A. Rius, J. Praks, E. Rouhe, J. Seppanen, and M. Martin-Neira, “Synoptic capabilities of the GNSS-R interferometric technique with the SPIR instrument,” in *2016 IEEE International Geoscience and Remote Sensing Symposium (IGARSS)*. IEEE, jul 2016, pp. 5600–5602. (Cited on pages 23 and 26.)
- [102] M. Unwin, “TechDemoSat-1 and the GNSS Reflectometry Experiment,” in *GNSS+R 2015 Workshop*, Potsdam, 2015. (Cited on page 23.)
- [103] —, “The SGR-ReSI Experiment on the TechDemoSat-1 Mission,” Surrey Satellite Technology LTD, Tech. Rep., 2015. [Online]. Available: <http://www.merrbys.co.uk:8080/CatalogueData/Documents/TDS-1SGR-ReSIExperiment.pdf> (Cited on page 23.)
- [104] J. Querol, G. F. Forte, and A. Camps, “Study of RFI signals in protected GNSS bands generated by common electronic devices: Effects on GNSS-R measurements,” in *2014 IEEE Geoscience and Remote Sensing Symposium*. IEEE, jul 2014, pp. 4050–4053. (Cited on page 23.)
- [105] R. Rose, W. Wells, J. Redfern, D. Rose, J. Dickinson, C. Ruf, A. Ridley, and K. Nave, “NASA’s Cyclone Global Navigation Satellite System (CYGNSS) Mission

- Temporal Resolution of a Constellation Enabled by Micro-Satellite Technology,” in *27th AIAA/USU Conference, Small Satellite Constellations*, Loga, Utah, 2013. (Cited on page 23.)
- [106] M. Unwin, P. Jales, P. Blunt, S. Duncan, M. Brummitt, and C. Ruf, “The SGR-ReSI and its application for GNSS reflectometry on the NASA EV-2 CYGNSS mission,” in *2013 IEEE Aerospace Conference*. IEEE, mar 2013, pp. 1–6. (Cited on pages 23 and 24.)
- [107] C. Ruf, M. Unwin, J. Dickinson, R. Rose, D. Rose, M. Vincent, and A. Lyons, “CYGNSS: Enabling the Future of Hurricane Prediction [Remote Sensing Satellites],” *IEEE Geoscience and Remote Sensing Magazine*, vol. 1, no. 2, pp. 52–67, jun 2013. (Cited on page 23.)
- [108] C. Ruf, M. Clarizia, S. Gleason, Z. Jelenak, J. Murray, M. Morris, S. Musko, D. Poselt, D. Provost, D. Starkenburg, and V. Zavorotny, *CYGNSS Handbook*, digital ed. Ann Arbor, MI: Michigan Pub., 2016. (Cited on page 23.)
- [109] S. Gleason, C. S. Ruf, M. P. Clarizia, and A. J. O’Brien, “Calibration and Unwrapping of the Normalized Scattering Cross Section for the Cyclone Global Navigation Satellite System,” *IEEE Transactions on Geoscience and Remote Sensing*, vol. PP, no. 99, pp. 1–15, may 2016. (Cited on page 23.)
- [110] N. Rodriguez-Alvarez, D. M. Akos, V. U. Zavorotny, J. A. Smith, A. Camps, and C. W. Fairall, “Airborne GNSS-R Wind Retrievals Using Delay–Doppler Maps,” *IEEE Transactions on Geoscience and Remote Sensing*, vol. 51, no. 1, pp. 626–641, jan 2013. (Cited on pages 23 and 180.)
- [111] M. P. Clarizia, C. S. Ruf, P. Jales, and C. Gommenginger, “Spaceborne GNSS-R Minimum Variance Wind Speed Estimator,” *IEEE Transactions on Geoscience and Remote Sensing*, vol. 52, no. 11, pp. 6829–6843, nov 2014. (Cited on page 23.)
- [112] G. Foti, C. Gommenginger, P. Jales, M. Unwin, A. Shaw, C. Robertson, and J. Roselló, “Spaceborne GNSS reflectometry for ocean winds: First results from the UK TechDemoSat-1 mission,” *Geophysical Research Letters*, vol. 42, no. 13, pp. 5435–5441, jul 2015. (Cited on pages 23 and 26.)
- [113] R. N. Treuhaft, S. T. Lowe, C. Zuffada, and Y. Chao, “2-cm GPS altimetry over Crater Lake,” *Geophysical Research Letters*, vol. 28, no. 23, pp. 4343–4346, dec 2001. (Cited on page 25.)
- [114] W. Li, E. Cardellach, F. Fabra, A. Rius, S. Ribó, and M. Martín-Neira, “First spaceborne phase altimetry over sea ice using TechDemoSat-1 GNSS-R signals,” *Geophysical Research Letters*, vol. 44, no. 16, pp. 8369–8376, aug 2017. (Cited on page 26.)
- [115] F. Said, S. J. Katzberg, and S. Soisuvann, “Retrieving Hurricane Maximum Winds Using Simulated CYGNSS Power-Versus-Delay Waveforms,” *IEEE Journal of Selected Topics in Applied Earth Observations and Remote Sensing*, vol. 10, no. 8, pp. 3799–3809, aug 2017. (Cited on page 26.)

- [116] OACI and ICAO, “Annex 10: Aeronautical Telecommunications,” ICAO - OACI, Tech. Rep. November, 1996. (Cited on pages 27, 28, and 138.)
- [117] Megginson Technologies Ltd., “OurAirports,” (Last visit: 2015-10-25). [Online]. Available: <http://ourairports.com/data/> (Cited on pages 28, 29, and 145.)
- [118] H. Carrenyo Luengo, “Contributions to GNSS-R earth remote sensing from nanosatellites,” Ph.D. dissertation, Universitat Politècnica de Catalunya, <https://www.tesisenred.net/handle/10803/385216>, 2016, (Last visited: 06-Oct-2019). (Cited on page 32.)
- [119] “Sangshin Elecom CO. LTD.” http://sangshinec.com/eng/ant_patchlist1.htm?sub=products&model=ant&msub=1 (Last visited: 22-Jul-2019). (Cited on page 32.)
- [120] H. Carreno-Luengo, A. Camps, J. Querol, G. Forte, **R. Onrubia**, and R. Diez, “A stratospheric balloon GNSS-R experiment: The Cat-2 project in DLR/SNSB BEXUS,” in *2014 IEEE Geoscience and Remote Sensing Symposium*, IEEE, Ed. Quebec: IEEE, 2014, pp. 3626–3629. (Cited on page 33.)
- [121] H. Carreno-Luengo, A. Camps, J. Querol, and G. Forte, “First Results of a GNSS-R Experiment from a Stratospheric Balloon over Boreal Forests,” *IEEE Transactions on Geoscience and Remote Sensing*, 2016. (Cited on page 33.)
- [122] **R. Onrubia**, D. Pascual, J. Querol, J. Castellvi-Esturi, J. Corbera, H. Park, and A. Camps, “Preliminary Altimetry Results of the Malygnss Instrument in the Humit Project,” in *IGARSS 2018 - 2018 IEEE International Geoscience and Remote Sensing Symposium*. IEEE, jul 2018, pp. 3331–3334. (Cited on page 38.)
- [123] A. Alonso-Arroyo, “Contributions to land, sea, and sea ice remote sensing using gnss-reflectometry,” Ph.D. dissertation, Universitat Politècnica de Catalunya, <http://tdx.cat/handle/10803/404062>, 10-Nov-2016, (Last visited: 08-Jan-2018). (Cited on page 38.)
- [124] J. Castellvi-Esturi, A. Camps, J. Corbera, **R. Onrubia**, R. Alamus, D. Pascual, J. Querol, and H. Park, “3CAT-3/MOTS, an Experimental Nanosatellite for Multispectral and GNSS-R Earth Observation: Airborne Optical and GNSS-R Campaign,” in *IGARSS 2018 - 2018 IEEE International Geoscience and Remote Sensing Symposium*. IEEE, jul 2018, pp. 1414–1417. (Cited on page 38.)
- [125] “Sensor Systems 67-1575-96,” <http://www.sensorantennas.com/product/gps-l1l2-antenna-2/> (Last visited: 08-Jan-2018). (Cited on page 39.)
- [126] “Antcom 42G1215RL-AA-XT-1,” <http://www.antcom.com/documents/catalogs/Page/42G1215RL-AA-XT-1.L1L2GPSAntennas.pdf> (Last visited: 08-Jan-2018). (Cited on pages 39 and 90.)
- [127] “Trimble BD982,” <https://www.trimble.com/gnss-inertial/bd982.aspx> (Last visited: 08-Jan-2018). (Cited on pages 39, 46, and 90.)
- [128] “Minicircuits Mar-6+,” <https://www.minicircuits.com/WebStore/dashboard.html?model=MAR-6%2B> (Last visited: 08-Jan-2018). (Cited on page 39.)

- [129] “Antcom 72GNSSA-XX-X-NR,” http://www.antcom.com/documents/catalogs/Page/72GNSSA-XX-X-NR_GNSSAntennas1.pdf (Last visited: 08-Jan-2018). (Cited on page 40.)
- [130] J. C. Kucwaj, G. Stienne, S. Reboul, J.-B. Choquel, and M. Benjelloun, “Accurate Pseudorange Estimation by Means of Code and Phase Delay Integration: Application to GNSS-R Altimetry,” *IEEE Journal of Selected Topics in Applied Earth Observations and Remote Sensing*, vol. PP, no. 99, pp. 1–11, 2016. (Cited on page 40.)
- [131] D. Pascual, **R. Onrubia**, J. Querol, J. Castellvi-Esturi, H. Park, and A. Camps, “Determination of Sea Correlation Time at L-Band with Airborne Reflected New GNSS Signals,” in *IGARSS 2018 - 2018 IEEE International Geoscience and Remote Sensing Symposium*. IEEE, jul 2018, pp. 3185–3188. (Cited on page 40.)
- [132] J. Querol, **R. Onrubia**, D. Pascual, J. Castellvi-Esturi, H. Park, and A. Camps, “RFI Analysis and Mitigation in Airborne GNSS-R Campaign,” in *IGARSS 2018 - 2018 IEEE International Geoscience and Remote Sensing Symposium*. IEEE, jul 2018, pp. 1237–1240. (Cited on page 40.)
- [133] “GPS Space Segment - Navipedia,” https://gssc.esa.int/navipedia/index.php/GPS_Space_Segment (Last visited: 10-Jan-2020). (Cited on page 47.)
- [134] “Galileo Space Segment - Navipedia,” https://gssc.esa.int/navipedia/index.php/Galileo_Space_Segment (Last visited: 10-Jan-2020). (Cited on page 47.)
- [135] G. Cai, B. M. Chen, and T. H. Lee, *Unmanned Rotorcraft Systems*, ser. Advances in Industrial Control. London: Springer London, 2011. (Cited on pages 48, 249, 250, and 251.)
- [136] “Local tangent plane coordinates - Wikipedia,” https://en.wikipedia.org/wiki/Local_tangent_plane_coordinates (Last visited: 23-Mar-2019). (Cited on page 48.)
- [137] N. Imagery and M. Agency, “Department of Defense World Geodetic System 1984 - Technical Report 8350.2, Third Edition, Amendment 1,” Tech. Rep., 2000. (Cited on page 49.)
- [138] “Euler Angles - Wikipedia,” https://en.wikipedia.org/wiki/Euler_angles (Last visited: 23-Mar-2019). (Cited on page 50.)
- [139] J. Benito, A. Andres-Bevide, P. Saameno, A. Olea, and M. Martin-Neira, “PARIS IOD Critical Technology-1 - Radiator Design (TNO-1) - PARIS-CT1-ECE-TN-0015,” European Space Agency, Tech. Rep., 2011. (Cited on page 54.)
- [140] W. L. Stutzman and G. A. Thiele, *Antenna Theory and Design*, 3rd ed. Wiley, 2012. (Cited on page 54.)
- [141] “MACOM MAPS-010143,” <https://cdn.macom.com/datasheets/MAPS-010143.pdf> (Last visited: 05-Apr-2019). (Cited on page 59.)
- [142] “AVAGO AMMP-6640,” <https://datasheet.octopart.com/AMMP-6640-Avago-datasheet-10308915.pdf> (Last visited: 05-Apr-2019). (Cited on page 59.)

- [143] “Yanco, New South Wales December 2010 Daily Weather Observations - Pandora Australia’s web archive,” <http://pandora.nla.gov.au/pan/44065/20110825-0025/www.bom.gov.au/climate/dwo/201012/html/IDCJDW2150.201012.html> (Last visited: 02-May-2019). (Cited on page 62.)
- [144] **R. Onrubia**, D. Pascual, J. Querol, H. Park, and A. Camps, “The Global Navigation Satellite Systems Reflectometry (GNSS-R) Microwave Interferometric Reflectometer: Hardware, Calibration, and Validation Experiments,” *Sensors*, vol. 19, no. 5, p. 1019, feb 2019. (Cited on pages 65 and 105.)
- [145] **R. Onrubia** and A. Camps, “Antena Multibanda Tipo Parche con Sistema de Alimentación Cruzada,” Spain Patent ES 2 540 161 B2, October, 2015. (Cited on pages 66, 67, and 144.)
- [146] “RV-10 - Van’s Aircraft Total Performance,” <https://www.vansaircraft.com/rv-10/> (Last visited: 19-Feb-2019). (Cited on page 72.)
- [147] M. Heron, P. Ridd, A. Prytz, Y. Wang, and J. Hacker, “Salinity Gradients in Coastal Waters by Airborne Microwave Radiometer Remote Sensing,” in *OCEANS 2006 - Asia Pacific*. IEEE, may 2006, pp. 1–5. (Cited on page 72.)
- [148] “Analog Devices ADL5390 Rev. A,” <http://www.analog.com/media/en/technical-documentation/data-sheets/ADL5390.pdf> (Last visited: 06-Sep-2018). (Cited on page 76.)
- [149] “Analog Devices AD5627R,” <https://www.analog.com/en/products/ad5627r.html> (Last visited: 04-Feb-2019). (Cited on page 76.)
- [150] “Texas Instruments LM4041-N-xx Precision Micropower Shunt Voltage Reference,” <http://www.ti.com/lit/ds/symlink/lm4041-n.pdf> (Last visited: 21-Oct-2019). (Cited on page 77.)
- [151] “Texas Instruments PCA9546A,” <http://www.ti.com/product/pca9546a?qgpn=pca9546a> (Last visited: 04-Feb-2019). (Cited on page 77.)
- [152] S. Ipc, “IPC 2221 Generic Standard on Printed Board Design,” 1998. (Cited on page 79.)
- [153] “Fluke VT02 Visual IR Thermometer User Manual,” https://dam-assets.fluke.com/s3fs-public/VT0204A_umspa0200.pdf (Last visited: 08-Feb-2019). (Cited on page 81.)
- [154] A. Alonso-Arroyo, A. Camps, A. Moneris, C. Rudiger, J. P. Walker, **R. Onrubia**, J. Querol, H. Park, and D. Pascual, “On the Correlation Between GNSS-R Reflectivity and L-Band Microwave Radiometry,” *IEEE Journal of Selected Topics in Applied Earth Observations and Remote Sensing*, vol. 9, no. 12, pp. 5862–5879, dec 2016. (Cited on pages 84 and 105.)
- [155] “Ettus Research USRP X310,” https://www.ettus.com/content/files/X300_X310_Spec_Sheet.pdf (Last visited: 19-Feb-2019). (Cited on page 85.)
- [156] “Ettus Research DBSRX2,” <https://www.ettus.com/product/details/DBSRX2> (Last visited: 08-Feb-2018). (Cited on page 86.)

-
- [157] “Ettus Research Octoclock,” <https://www.ettus.com/content/files/Octoclock-Spec.Sheet.pdf> (Last visited: 06-Sep-2018). (Cited on page 87.)
- [158] I. Pérez, X. Bosch-Lluis, A. Camps, N. Alvarez, J. F. Hernandez, E. Domènech, C. Vernich, S. De la Rosa, and S. Pantoja, “Calibration of Correlation Radiometers Using Pseudo-Random Noise Signals,” *Sensors*, vol. 9, no. 8, pp. 6131–6149, aug 2009. (Cited on pages 87 and 114.)
- [159] “Ettus Research USRP X210,” https://www.ettus.com/content/files/Ettus-N200-210_DS_Flyer_HR_2.pdf (Last visited: 21-Feb-2019). (Cited on page 87.)
- [160] “Analog Devices ADF4153,” <https://www.analog.com/en/products/adf4153.html> (Last visited: 05-Mar-2019). (Cited on page 88.)
- [161] “Minicircuits DSN-2036A-119+,” <https://www.minicircuits.com/WebStore/dashboard.html?model=DSN-2036A-119%2B> (Last visited: 05-Mar-2019). (Cited on page 88.)
- [162] “Minicircuits BFCN-1575+,” <https://www.minicircuits.com/WebStore/dashboard.html?model=BFCN-1575%2B> (Last visited: 05-Mar-2019). (Cited on page 88.)
- [163] “Minicircuits CBP-1170C+,” <https://www.minicircuits.com/WebStore/dashboard.html?model=CBP-1170C%2B> (Last visited: 05-Mar-2019). (Cited on page 88.)
- [164] “Seika NG-4,” http://www.seika.de/english/html_e/NG_e.htm (Last visited: 07-Nov-2018). (Cited on page 90.)
- [165] “9 Degrees of Freedom - Razor IMU,” <https://www.sparkfun.com/products/retired/10736> (Last visited: 25-Oct-2018). (Cited on page 91.)
- [166] “Wandboard Quad (IMX6),” <https://www.wandboard.org/products/wandboard/WB-IMX6Q-BW/> (Last visited: 25-Oct-2018). (Cited on page 92.)
- [167] “Wandboard Baseboard Schematics,” <http://download.wandboard.org/wandboard-imx6/documentation/wand-rev-c1.pdf> (Last visited: 08-Mar-2019). (Cited on page 93.)
- [168] “Wandboard Linux on ARM eewiki,” <https://www.digikey.com/eewiki/display/linuxonarm/Wandboard> (Last visited: 08-Mar-2019). (Cited on page 93.)
- [169] “Wandboard CPU Board Schematics,” <http://download.wandboard.org/wandboard-imx6/documentation/wb-edm-imx6-rev-c1.pdf> (Last visited: 08-Mar-2019). (Cited on page 94.)
- [170] “Device Tree Reference eLinux.org,” https://elinux.org/Device_Tree_Reference (Last visited: 08-Mar-2019). (Cited on page 94.)
- [171] “Using spidev on the Wandboard Luis notes,” <http://blog.luisdearquer.net/index.php/2016/04/28/using-spidev-on-the-wandboard/> (Last visited: 08-Mar-2019). (Cited on page 94.)
- [172] “The Essential GNSS Project,” <http://gnsstk.sourceforge.net/index.html> (Last visited: 27-Mar-2019). (Cited on pages 97 and 253.)

- [173] L. Ma and S. Zhou, “Positional Accuracy of Gps Satellite Almanac,” *Artificial Satellites*, vol. 49, no. 4, pp. 225–231, jan 2014. (Cited on page 102.)
- [174] A. Camps, X. Bosch-Lluis, and H. Park, “Impact of receiver’s frequency response in GNSS reflectometers,” in *2010 IEEE International Geoscience and Remote Sensing Symposium*. IEEE, jul 2010, pp. 3817–3820. (Cited on page 107.)
- [175] A. S. Goldberger, *Econometric Theory*, I. John Wiley and Sons, Ed., New York, 1964. (Cited on page 111.)
- [176] R. Butora, M. Martín-Neira, and A.-L. Rivada-Antich, “Fringe-washing function calibration in aperture synthesis microwave radiometry,” *Radio Science*, vol. 38, no. 2, pp. n/a–n/a, apr 2003. (Cited on page 114.)
- [177] J. G. Proakis and D. G. Manolakis, “Digital Signal Processing Principles, Algorithms and Applications,” 1996. (Cited on pages 114 and 117.)
- [178] “R&S SMU200A Vector Signal Generator — Overview — Rohde & Schwarz,” https://www.rohde-schwarz.com/us/product/smu200a-productstartpage_63493-7555.html (Last visited: 19-Jun-2019). (Cited on page 120.)
- [179] A. Camps, H. Park, E. Valencia i Domenech, D. Pascual, F. Martin, A. Rius, S. Ribo, J. Benito, A. Andres-Beivide, P. Saameno, G. Staton, M. Martin-Neira, S. DAddio, and P. Willemsen, “Optimization and Performance Analysis of Interferometric GNSS-R Altimeters: Application to the PARIS IoD Mission,” *IEEE Journal of Selected Topics in Applied Earth Observations and Remote Sensing*, vol. 7, no. 5, pp. 1436–1451, may 2014. (Cited on pages 126 and 140.)
- [180] **R. Onrubia**, D. Pascual, J. Querol, H. Park, A. Camps, C. Rudiger, and J. Walker, “Preliminary End-to-End Results of the MIR Instrument: the Microwave Interferometric Reflectometer,” in *IGARSS 2018 - 2018 IEEE International Geoscience and Remote Sensing Symposium*. IEEE, jul 2018, pp. 2027–2030. (Cited on pages 132 and 133.)
- [181] M. De Angelis, R. Fantacci, S. Menci, and C. Rinaldi, “Analysis of air traffic control systems interference impact on galileo aeronautics receivers,” in *IEEE International Radar Conference, 2005*. IEEE, 2005, pp. 585–595. (Cited on page 139.)
- [182] F. DAVIS, L. Musumeci, and J. Samson, “Performance assessment of pulse blanking mitigation in presence of multiple Distance Measuring Equipment/Tactical Air Navigation interference on Global Navigation Satellite Systems signals,” *IET Radar, Sonar and Navigation*, vol. 8, no. 6, pp. 647–657, jul 2014. (Cited on page 139.)
- [183] E. D. Kaplan and C. J. Hegarty, *Understanding GPS. Principles and Applications*, 2nd ed., Artech House, Ed., 2005. (Cited on page 139.)
- [184] J. W. Betz, “Effect of partial-band interference on receiver estimation of C/N0: Theory,” in *The Institute of Navigation’s National Technical Meeting*, 2001, pp. 716–723. (Cited on page 139.)

- [185] B. Roturier, "Report on DME interference on GPS/L5," Eurocontrol, Tech. Rep., 2001, (Last visit: 2015-10-25), Available: https://www.eurocontrol.int/sites/default/files/field_tabs/content/documents/communications/071999-dgac-report-dme-interference-on-gps-l5.pdf. (Cited on page 139.)
- [186] J. Querol, A. Alonso-Arroyo, **R. Onrubia**, D. Pascual, H. Park, and A. Camps, "SNR Degradation in GNSS-R Measurements Under the Effects of Radio-Frequency Interference," *IEEE Journal of Selected Topics in Applied Earth Observations and Remote Sensing*, vol. 9, no. 10, pp. 4865–4878, oct 2016. (Cited on pages 139, 142, 143, and 181.)
- [187] T. Elfouhaily, D. Thompson, and L. Linstrom, "Delay-Doppler analysis of bistatically reflected signals from the ocean surface: theory and application," *IEEE Transactions on Geoscience and Remote Sensing*, vol. 40, no. 3, pp. 560–573, mar 2002. (Cited on page 140.)
- [188] H. Park, D. Pascual, A. Camps, F. Martin, A. Alonso-Arroyo, and H. Carreno-Luengo, "Analysis of Spaceborne GNSS-R Delay-Doppler Tracking," *IEEE Journal of Selected Topics in Applied Earth Observations and Remote Sensing*, vol. 7, no. 5, pp. 1481–1492, may 2014. (Cited on pages 141, 142, and 146.)
- [189] W. Martin and P. Flandrin, "Wigner-Ville spectral analysis of nonstationary processes," *IEEE Transactions on Acoustics, Speech, and Signal Processing*, vol. 33, no. 6, pp. 1461–1470, dec 1985. (Cited on page 143.)
- [190] Ettus Research. (2015) Ettus Research. (Last visit: 2015-10-25). [Online]. Available: <http://www.ettus.com> (Cited on page 144.)
- [191] J. Wickert, O. Andersen, G. Beyerle, B. Chapron, E. Cardellach, S. D'Addio, C. Foerste, C. Gommenginger, T. Gruber, A. Helm, M. Hess, P. Hoeg, A. Jaeggi, N. Jakowski, M. Kern, T. Lee, M. Martin-Neira, O. Montenbruck, N. Pierdicca, A. Rius, M. Rothacher, C. Shum, C. Zuffada, J. Wickert, O. B. Andersen, G. Beyerle, B. Chapron, E. Cardellach, S. D'Addio, C. Foerste, C. Gommenginger, T. Gruber, A. Helm, M. Hess, P. Hoeg, A. Jaeggi, N. Jakowski, M. Kern, T. Lee, M. Martin-Neira, O. Montenbruck, N. Pierdicca, A. Rius, M. Rothacher, C. Shum, and C. Zuffada, "GEROS-ISS: Innovative GNSS reflectometry/occultation payload onboard the International Space Station for the Global Geodetic Observing System," in *American Geophysical Union*, Nov. 4-7, ESTEC, Noordwijk, 2013. (Cited on page 145.)
- [192] ITU-R, "P.452-15: Prediction procedure for the evaluation of interference between stations on the surface of the Earth at frequencies above about 0.1 GHz," <http://www.itu.int/rec/R-REC-P.452-15-201309-I/en>, Tech. Rep., (Last visit: 2015-10-25). (Cited on page 145.)
- [193] —, "P.526-13: Propagation by diffraction," <http://www.itu.int/rec/R-REC-P.526-13-201311-I/es>, Tech. Rep., (Last visit: 2015-10-25). (Cited on page 145.)
- [194] F. Moreno, ENAIRE, Private communication - Email, February 2016. (Cited on page 145.)

- [195] dB Systems Inc., “Omni-Directional dBs 5100A DME Antenna.” [Online]. Available: <http://www.dbsant.com/5100A.php> (Cited on page 145.)
- [196] J. Querol, D. Pascual, **R. Onrubia**, and A. Camps, “GEROS-ISS Performance and Error Budget Report: Part 1/3 Assessment of RFI Effects in GNSS-R GEROS-ISS-PhA-IEEC-UPC-TN-D26-1/3,” Tech. Rep., 2015. (Cited on pages 145, 146, and 150.)
- [197] B. Forssell, *Radionavigation Systems*. Prentice Hall, 1991, pp. 166-175. (Cited on page 147.)
- [198] **R. Onrubia**, D. Pascual, H. Park, A. Camps, C. Rüdiger, J. P. Walker, and A. Moneris, “Satellite Cross-Talk Impact Analysis in Airborne Interferometric Global Navigation Satellite System-Reflectometry with the Microwave Interferometric Reflectometer,” *Remote Sensing*, vol. 11, no. 9, p. 1120, may 2019. (Cited on pages 154 and 179.)
- [199] J. P. Walker, Private Communications - Flight planning meetings, Monash University Clayton Campus, Clayton (Victoria), May 2018. (Cited on page 155.)
- [200] A. B. Smith, J. P. Walker, A. W. Western, R. I. Young, K. M. Ellett, R. C. Pipunic, R. B. Grayson, L. Siriwardena, F. H. S. Chiew, and H. Richter, “The Murrumbidgee soil moisture monitoring network data set,” *Water Resources Research*, vol. 48, no. 7, jul 2012. (Cited on page 156.)
- [201] “Daily rainfall - Narrandera Airport AWS - Bureau of Meteorology,” http://www.bom.gov.au/jsp/ncc/cdio/weatherData/av?p_nccObsCode=136&p_display_type=dailyDataFile&p_startYear=2018&p_c=-1099598755&p_stn_num=074148 (Last visited: 08-Apr-2019). (Cited on page 156.)
- [202] “List of GPS Satellites - Wikipedia,” https://en.wikipedia.org/wiki/List_of_GPS_satellites (Last visited: 28-Jun-2019). (Cited on page 162.)
- [203] J.-H. Lee and D.-S. Shim, “Fast acquisition of GPS L5 PRN and NH code using L1 signal for software receivers,” *International Journal of Control, Automation and Systems*, vol. 14, no. 4, pp. 1133–1139, aug 2016. (Cited on page 163.)
- [204] “Earth Gravitational Model 2008 (EGM2008),” <https://earth-info.nga.mil/GandG/wgs84/gravitymod/egm2008/> (Last visited: 03-Jul-2019). (Cited on page 166.)
- [205] “WebGIS - Geographic Information Systems Resource - GIS,” <http://www.webgis.com/srtm3.html> (Last visited: 03-Jul-2019). (Cited on page 166.)
- [206] “Tide Predictions for Australia, South Pacific, and Antartica - Bureau of Meteorology,” <http://www.bom.gov.au/australia/tides/> (Last visited: 22-Aug-2019). (Cited on page 171.)
- [207] A. Camps, “Spatial Resolution in GNSS-R Under Coherent Scattering,” *IEEE Geoscience and Remote Sensing Letters*, pp. 1–5, 2019. (Cited on page 173.)
- [208] F. Martín, “Interferometric GNSS-R processing : modeling and analysis of advanced processing concepts for altimetry,” Ph.D. dissertation, Universitat Politècnica de Catalunya, <https://www.tdx.cat/handle/10803/316583>, 2015, (Last visit: 08-Jan-2020). (Cited on page 179.)

- [209] “The Multi-GNSS Experiment and Pilot Project (MGEX),” <http://mgex.igs.org/> (Last visited: 28-Jan-2019). (Cited on page 179.)
- [210] A. Rius, E. Cardellach, and M. Martin-Neira, “Altimetric Analysis of the Sea-Surface GPS-Reflected Signals,” *IEEE Transactions on Geoscience and Remote Sensing*, vol. 48, no. 4, pp. 2119–2127, apr 2010. (Cited on page 182.)
- [211] B. Hofmann-Wellenhof, H. Lichtenegger, and E. Wasle, *GNSS Global Navigation Satellite Systems; GPS, Glonass, Galileo and More*. Springer Wien New York, 2008. (Cited on page 182.)
- [212] E. Cardellach, A. Rius, M. Martin-Neira, F. Fabra, O. Nogues-Correig, S. Ribo, J. Kainulainen, A. Camps, and S. D’Addio, “Consolidating the Precision of Interferometric GNSS-R Ocean Altimetry Using Airborne Experimental Data,” *IEEE Transactions on Geoscience and Remote Sensing*, vol. 52, no. 8, pp. 4992–5004, aug 2014. (Cited on page 182.)
- [213] “Convert Earth-centered Earth-fixed (ECEF) coordinates to geodetic coordinates - MATLAB ecef2lla - MathWorks España,” <https://es.mathworks.com/help/aerotbx/ug/ecef2lla.html> (Last visited: 26-Mar-2019). (Cited on page 250.)
- [214] **R. Onrubia**, “GPS/Galileo/Beidou/IRNSS/QZSS Satellite Position Calculator for MATLAB,” <https://github.com/onrubia/computeSatellitePosition/blob/master/getSatECEF.m> (Last visited: 27-Mar-2019). (Cited on page 255.)

H

List of Publications

Granted Patents

- [GP1] **R. Onrubia** and A. Camps, “Antena Multibanda Tipo Parche con Sistema de Alimentación Cruzada,” Spanish Patent ES 2 540 161 B2, October 2015, [Online]. Available: http://www.oepm.es/pdf/ES/0000/000/02/54/01/ES-2540161_A1.pdf.

Open-source software

- [SO1] **R. Onrubia**, “GPS/Galileo/Beidou/IRNSS/QZSS Satellite Position Calculator for MATLAB,” <https://github.com/onrubia/computeSatellitePosition/blob/master/getSatECEF.m> (Last visited: 27-Mar-2019).

Journal Articles

- [JA1] **R. Onrubia**, J. Querol, D. Pascual, A. Alonso-Arroyo, H. Park, and A. Camps, “DME/TACAN impact analysis on GNSS reflectometry,” *IEEE Journal of Selected Topics in Applied Earth Observations and Remote Sensing*, vol. 9, no. 10, pp. 4611–4620, oct 2016.
- [JA2] **R. Onrubia**, D. Pascual, J. Querol, H. Park, and A. Camps, “The Global Navigation Satellite Systems Reflectometry (GNSS-R) Microwave Interferometric Reflectometer: Hardware, Calibration, and Validation Experiments,” *Sensors*, vol. 19, no. 5, p. 1019, feb 2019.

- [JA3] **R. Onrubia**, D. Pascual, H. Park, A. Camps, C. Rüdiger, J. P. Walker, and A. Monerri, “Satellite Cross-Talk Impact Analysis in Airborne Interferometric Global Navigation Satellite System-Reflectometry with the Microwave Interferometric Reflectometer,” *Remote Sensing*, vol. 11, no. 9, p. 1120, may 2019.
- [JA4] A. Alonso-Arroyo, A. Camps, A. Aguasca, G. Forte, A. Monerri, C. Rüdiger, J. P. Walker, H. Park, D. Pascual, and **R. Onrubia**, “Improving the accuracy of soil moisture retrievals using the phase difference of the dual-polarization GNSS-R interference patterns,” *IEEE Geoscience and Remote Sensing Letters*, vol. 11, no. 12, pp. 2090–2094, dec 2014.
- [JA5] A. A. Arroyo, A. Camps, A. Aguasca, G. F. Forte, A. Monerri, C. Rüdiger, J. P. Walker, H. Park, D. Pascual, and **R. Onrubia**, “Dual-polarization GNSS-R interference pattern technique for soil moisture mapping,” *IEEE Journal of Selected Topics in Applied Earth Observations and Remote Sensing*, vol. 7, no. 5, pp. 1533–1544, may 2014.
- [JA6] D. Pascual, A. Camps, F. Martín, H. Park, A. A. Arroyo, and **R. Onrubia**, “Precision bounds in GNSS-R ocean altimetry,” *IEEE Journal of Selected Topics in Applied Earth Observations and Remote Sensing*, vol. 7, no. 5, pp. 1416–1423, may 2014.
- [JA7] D. Pascual, H. Park, A. Camps, A. A. Arroyo, and **R. Onrubia**, “Simulation and analysis of GNSS-R composite waveforms using GPS and galileo signals,” *IEEE Journal of Selected Topics in Applied Earth Observations and Remote Sensing*, vol. 7, no. 5, pp. 1461–1468, may 2014.
- [JA8] A. Alonso-Arroyo, A. Camps, H. Park, D. Pascual, **R. Onrubia**, and F. Martín, “Retrieval of significant wave height and mean sea surface level using the GNSS-R interference pattern technique: Results from a three-month field campaign,” *IEEE Transactions on Geoscience and Remote Sensing*, vol. 53, no. 6, pp. 3198–3209, jun 2015.
- [JA9] D. Pascual, H. Park, **R. Onrubia**, A. A. Arroyo, J. Querol, and A. Camps, “Crosstalk Statistics and Impact in Interferometric GNSS-R,” *IEEE Journal of Selected Topics in Applied Earth Observations and Remote Sensing*, vol. 9, no. 10, pp. 4621–4630, oct 2016.
- [JA10] J. Querol, A. Alonso-Arroyo, **R. Onrubia**, D. Pascual, H. Park, and A. Camps, “SNR Degradation in GNSS-R Measurements under the Effects of Radio-Frequency Interference,” *IEEE Journal of Selected Topics in Applied Earth Observations and Remote Sensing*, vol. 9, no. 10, pp. 4865–4878, oct 2016.
- [JA11] A. Alonso-Arroyo, A. Camps, A. Monerri, C. Rüdiger, J. P. Walker, **R. Onrubia**, J. Querol, H. Park, and D. Pascual, “On the Correlation between GNSS-R Reflectivity and L-Band Microwave Radiometry,” *IEEE Journal of Selected Topics in Applied Earth Observations and Remote Sensing*, vol. 9, no. 12, pp. 5862–5879, dec 2016.

-
- [JA12] H. Park, A. Camps, D. Pascual, Y. Kang, **R. Onrubia**, J. Querol, and A. Alonso-Arroyo, “A Generic Level 1 Simulator for Spaceborne GNSS-R Missions and Application to GEROS-ISS Ocean Reflectometry,” *IEEE Journal of Selected Topics in Applied Earth Observations and Remote Sensing*, vol. 10, no. 10, pp. 4645–4659, 2017.
- [JA13] J. Querol, **R. Onrubia**, A. Alonso-Arroyo, D. Pascual, H. Park, and A. Camps, “Performance Assessment of Time-Frequency RFI Mitigation Techniques in Microwave Radiometry,” *IEEE Journal of Selected Topics in Applied Earth Observations and Remote Sensing*, vol. 10, no. 7, pp. 3096–3106, 2017.
- [JA14] A. Alonso-Arroyo, J. Querol, C. Lopez-Martinez, V. U. Zavorotny, H. Park, D. Pascual, **R. Onrubia**, and A. Camps, “SNR and standard deviation of cGNSS-R and iGNSS-R scatterometric measurements,” *Sensors (Switzerland)*, vol. 17, no. 1, p. 183, jan 2017.
- [JA15] D. Guan, H. Park, A. Camps, Y. Wang, **R. Onrubia**, J. Querol, and D. Pascual, “Wind direction signatures in GNSS-R observables from space,” *Remote Sensing*, vol. 10, no. 2, p. 198, jan 2018.

Conference Proceedings

- [CP1] **R. Onrubia**, D. Pascual, A. Camps, A. Alonso-Arroyo, and H. Park, “MIR: The microwave interferometric reflectometer, a new airborne sensor for GNSS-R advanced research,” in *International Geoscience and Remote Sensing Symposium (IGARSS)*. IEEE, jul 2013, pp. 109–112.
- [CP2] **R. Onrubia**, D. Pascual, A. Camps, A. Alonso-Arroyo, and H. Park, “The Microwave Interferometric Reflectometer. Part I: Front-end and beamforming description,” in *International Geoscience and Remote Sensing Symposium (IGARSS)*. IEEE, jul 2014, pp. 4046–4049.
- [CP3] **R. Onrubia**, L. Garrucho, D. Pascual, H. Park, J. Querol, A. Alonso-Arroyo, and A. Camps, “Advances in the MIR instrument: Integration, control subsystem and analysis of the flight dynamics for beamsteering purposes,” in *International Geoscience and Remote Sensing Symposium (IGARSS)*, vol. 2015-Novem. IEEE, jul 2015, pp. 4765–4768.
- [CP4] **R. Onrubia**, J. Querol, D. Pascual, H. Park, A. Alonso-Arroyo, and A. Camps, “Assessment of DME/TACAN RFI mitigation techniques in GNSS-R,” in *International Geoscience and Remote Sensing Symposium (IGARSS)*, vol. 2016-Novem. IEEE, jul 2016, pp. 4811–4814.
- [CP5] **R. Onrubia**, D. Pascual, J. Querol, H. Park, and A. Camps, “Beamformer characterization of the MIR instrument: The microwave interferometric reflectometer,” in *International Geoscience and Remote Sensing Symposium (IGARSS)*, vol. 2017-July, 2017, pp. 5026–5029.

- [CP6] **R. Onrubia**, D. Pascual, J. Querol, J. Castellvi-Esturi, J. Corbera, H. Park, and A. Camps, "Preliminary altimetry results of the MALYGNSS instrument in the HUMIT project," *2018 IEEE International Geoscience and Remote Sensing Symposium (IGARSS)*, pp. 3331–3334, jul 2018.
- [CP7] **R. Onrubia**, D. Pascual, J. Querol, H. Park, A. Camps, C. Rudiger, and J. Walker, "Preliminary End- to-End Results of the MIR Instrument: the Microwave Interferometric Reflectometer," *IGARSS 2018 - 2018 IEEE International Geoscience and Remote Sensing Symposium*, pp. 2027–2030, jul 2018.
- [CP8] A. Alonso-Arroyo, G. Forte, A. Camps, H. Park, D. Pascual, **R. Onrubia**, and R. Jove-Casulleras, "Soil moisture mapping using forward scattered GPS L1 signals," in *International Geoscience and Remote Sensing Symposium (IGARSS)*. IEEE, jul 2013, pp. 354–357.
- [CP9] D. Pascual, H. Park, A. Camps, A. Alonso, and **R. Onrubia**, "Comparison of GPS L1 and Galileo E1 signals for GNSS-R ocean altimetry," in *International Geoscience and Remote Sensing Symposium (IGARSS)*. IEEE, jul 2013, pp. 358–361.
- [CP10] H. Carreno-Luengo, A. Camps, I. Perez-Ramos, G. Forte, **R. Onrubia**, and R. Diez, "3Cat-2: A P(Y) and C/A GNSS-R experimental nano-satellite mission," in *2013 IEEE International Geoscience and Remote Sensing Symposium - IGARSS*. IEEE, jul 2013, pp. 843–846.
- [CP11] D. Pascual, **R. Onrubia**, A. Alonso-Arroyo, H. Park, and A. Camps, "The microwave interferometric reflectometer. Part II: Back-end and processor descriptions," in *International Geoscience and Remote Sensing Symposium (IGARSS)*. IEEE, jul 2014, pp. 3782–3785.
- [CP12] A. Alonso-Arroyo, A. Camps, A. Monerri, C. Rudiger, J. P. Walker, G. Forte, D. Pascual, H. Park, and **R. Onrubia**, "The light airborne reflectometer for GNSS-R observations (LARGO) instrument: Initial results from airborne and Rover field campaigns," in *International Geoscience and Remote Sensing Symposium (IGARSS)*. IEEE, jul 2014, pp. 4054–4057.
- [CP13] A. Camps, J. F. Marchan-Hernandez, X. Bosch-Lluis, N. Rodriguez-Alvarez, I. Ramos-Perez, E. Valencia, J. M. Tarongi, H. Park, H. Carreno-Luengo, A. Alonso-Arroyo, D. Pascual, **R. Onrubia**, G. Forte, and J. Querol, "Review of GNSS-R instruments and tools developed at the Universitat Politecnica de Catalunya-Barcelona tech," in *International Geoscience and Remote Sensing Symposium (IGARSS)*. Institute of Electrical and Electronics Engineers Inc., 2014, pp. 3826–3829.
- [CP14] H. Park, A. Camps, D. Pascual, A. Alonso-Arroyo, F. Martin, H. Carreno-Luengo, and **R. Onrubia**, "Simulation study on tropical cyclone tracking from the ISS using GNSS-R measurements," in *International Geoscience and Remote Sensing Symposium (IGARSS)*. IEEE, jul 2014, pp. 4062–4065.

- [CP15] A. Alonso-Arroyo, A. Camps, A. Monerris, C. Ruudiger, J. P. Walker, G. Forte, D. Pascual, H. Park, and **R. Onrubia**, “The dual polarization GNSS-R interference pattern technique,” in *International Geoscience and Remote Sensing Symposium (IGARSS)*. IEEE, jul 2014, pp. 4058–4061.
- [CP16] H. Carreno-Luengo, A. Camps, J. Querol, G. Forte, **R. Onrubia**, and R. Diez, “A stratospheric balloon GNSS-R experiment: The Cat-2 project in DLR/SNSB BEXUS,” in *2014 IEEE Geoscience and Remote Sensing Symposium*, IEEE, Ed. Quebec: IEEE, 2014, pp. 3626–3629.
- [CP17] J. Querol, A. Alonso-Arroyo, **R. Onrubia**, D. Pascual, and A. Camps, “Assessment of back-end RFI mitigation techniques in passive remote sensing,” in *International Geoscience and Remote Sensing Symposium (IGARSS)*, vol. 2015-Novem. IEEE, jul 2015, pp. 4746–4749.
- [CP18] A. Alonso-Arroyo, S. Torrecilla, J. Querol, A. Camps, D. Pascual, H. Park, and **R. Onrubia**, “Two dedicated soil moisture experiments using the scatterometric properties of GNSS-reflectometry,” in *International Geoscience and Remote Sensing Symposium (IGARSS)*, vol. 2015-Novem. IEEE, jul 2015, pp. 3921–3924.
- [CP19] H. Park, A. Camps, D. Pascual, **R. Onrubia**, A. Alonso-Arroyo, and F. Martin, “Evolution of PAU/PARIS End-to-end Performance Simulator (P2EPS) towards GNSS reflectometry, radio occultation and Scatterometry simulator (GEROS-SIM),” in *International Geoscience and Remote Sensing Symposium (IGARSS)*, vol. 2015-Novem. IEEE, jul 2015, pp. 4757–4760.
- [CP20] D. Pascual, **R. Onrubia**, J. Querol, A. Alonso-Arroyo, H. Park, and A. Camps, “First Delay Doppler Maps obtained with the Microwave Interferometric Reflectometer (MIR),” in *International Geoscience and Remote Sensing Symposium (IGARSS)*, vol. 2016-Novem. IEEE, jul 2016, pp. 1993–1996.
- [CP21] J. Querol, **R. Onrubia**, D. Pascual, A. Alonso-Arroyo, H. Park, and A. Camps, “Comparison of real-time time-frequency RFI mitigation techniques in microwave radiometry,” in *14th Specialist Meeting on Microwave Radiometry and Remote Sensing of the Environment, MicroRad 2016 - Proceedings*. IEEE, apr 2016, pp. 68–70.
- [CP22] J. Querol, A. Alonso-Arroyo, **R. Onrubia**, D. Pascual, and A. Camps, “SNR degradation in conventional GNSS-R measurements under the effects of radio frequency interference,” *8th Workshop on GNSS Reflectometry*, p. 1, 2015.
- [CP23] H. Park, A. Camps, I. Sekulic, J. M. Rius, D. Pascual, A. Alonso-Arroyo, J. Querol, and **R. Onrubia**, “Impact of multi-path by ISS structure on GEROS-ISS measured waveforms,” in *International Geoscience and Remote Sensing Symposium (IGARSS)*, vol. 2016-Novem. IEEE, jul 2016, pp. 5603–5606.
- [CP24] A. Alonso-Arroyo, J. Querol, A. Camps, **R. Onrubia**, H. Park, and D. Pascual, “Can we measure vegetation water content and vegetation opacity at L-band

- with a single GPS receiver?” in *International Geoscience and Remote Sensing Symposium (IGARSS)*, vol. 2016-Novem. IEEE, jul 2016, pp. 1985–1988.
- [CP25] A. Camps, H. Park, **R. Onrubia**, D. Pascual, J. Querol, A. Alonso-Arroyo, J. Benito, A. Andres-Beivide, S. Moreno, X. Ballesteros, M. Segarra, R. Vilaseca, A. Rius, and M. Martin-Neira, “Altimetric performance of the GEROS experiment at the ISS,” *International Geoscience and Remote Sensing Symposium (IGARSS)*, vol. 2016-Novem, pp. 5621–5624, 2016.
- [CP26] H. Park, A. Camps, D. Pascual, A. Alonso-Arroyo, J. Querol, and **R. Onrubia**, “Improvement of PAU/PARIS end-to-end performance simulator (P2EPS): Land scattering including topography,” *International Geoscience and Remote Sensing Symposium (IGARSS)*, vol. 2016-Novem, pp. 5607–5610, 2016.
- [CP27] D. Pascual, **R. Onrubia**, J. Querol, H. Park, and A. Camps, “Calibration of GNSS-R receivers with PRN signal injection: Methodology and validation with the microwave interferometric reflectometer (MIR),” in *International Geoscience and Remote Sensing Symposium (IGARSS)*, vol. 2017-July, 2017, pp. 5022–5025.
- [CP28] J. Querol, **R. Onrubia**, D. Pascual, H. Park, and A. Camps, “A radio-frequency interference detector for GNSS navigation and GNSS-reflectometry applications,” in *International Geoscience and Remote Sensing Symposium (IGARSS)*, vol. 2017-July, 2017, pp. 1266–1269.
- [CP29] D. Pascual, **R. Onrubia**, J. Querol, J. Castellvi-Esturi, H. Park, and A. Camps, “Determination of Sea Correlation Time at L-Band with Airborne Reflected New GNSS Signals,” *IGARSS 2018 - 2018 IEEE International Geoscience and Remote Sensing Symposium*, pp. 3185–3188, jul 2018.
- [CP30] J. Querol, **R. Onrubia**, D. Pascual, J. Castellvi-Esturi, H. Park, and A. Camps, “RFI Analysis and Mitigation in Airborne GNSS-R Campaign,” *2018 IEEE International Geoscience and Remote Sensing Symposium (IGARSS)*, pp. 1237–1240, jul 2018.
- [CP31] J. Castellvi-Esturi, A. Camps, J. Corbera, **R. Onrubia**, R. Alamús, D. Pascual, J. Querol, and H. Park, “3CAT-3/MOTS, An Experimental Nanosatellite for Multispectral and GNSS-R Earth Observation: Airborne Optical and GNSS-R Campaign,” in *2018 IEEE International Geoscience and Remote Sensing Symposium (IGARSS)*. IEEE, jul 2018, pp. 1414–1417.
- [CP32] H. Park, A. Camps, D. Pascual, J. Querol, and **R. Onrubia**, “Spaceborne GNSS-R End-To-End Simulator: Topography and Vegetation Effects,” in *IGARSS 2018 - 2018 IEEE International Geoscience and Remote Sensing Symposium*. IEEE, jul 2018, pp. 3157–3160.

Co-directed Bachelor Final Degree Projects

- [DP1] L. Garrucho, “Attitude Determination System for a Phased Array Beamformer,” B.Sc. Thesis, Universitat Politècnica de Catalunya, 2015.